FLORIDA STATE UNIVERSITY

COLLEGE OF ARTS AND SCIENCES

NUMERICAL AND EXPERIMENTAL STUDIES OF TURBULENCE IN QUANTUM FLUIDS

By

TOSHIAKI KANAI

A Dissertation submitted to the
Department of Physics
in partial fulfillment of the
requirements for the degree of
Doctor of Philosophy

2023

Toshiaki Kanai defended this dissertation on November 14, 2023.
The members of the supervisory committee were:

Wei Guo
Professor Co-directing Dissertation

David Collins
Professor Co-directing Dissertation

Mark Sussman
University Representative

Jorge Piekarewicz
Committee Member

Sean Dobbs
Committee Member

The Graduate School has verified and approved the above-named committee members, and certifies that the dissertation has been approved in accordance with university requirements.

ACKNOWLEDGMENTS

I am immensely grateful to my major advisor, Prof. Wei Guo, for his unwavering support during my Ph.D. program at Florida State University. Prof. Guo provided invaluable guidance and mentorship on all my research projects, which helped me develop my research skills and knowledge in the field. I would also like to thank my committee members, Prof. David Collins, Prof. Jorge Piekarewicz, Prof. Sean Dobbs, and Prof. Mark Sussman, for their valuable feedback and constructive criticism throughout my Ph.D. journey. I am incredibly grateful to Prof. Collins for co-chairing. I would also like to express my appreciation to Dr. Kun Yang, Dr. William Joe Vinen, Dr. Dafei Jin, and Dr. Satoshi Yui for their valuable comments. In addition, I would like to thank the past and present members of the Cryolab, especially Dr. Shiran Bao for guiding me in my experimental projects, and Dr. Hamid Sanavandi, Dr. Nathaniel Garceau, Dr. Yuan Tang, and Mr. Mikai Hulse for helping me to develop my skills.

This work has been supported by the National Science Foundation under Grant No. DMR-1507386, No. DMR-1807291, and No. DMR-2100790 and the Gordon and Betty Moore Foundation through Grant GBMF11567. Also, this work has been conducted at the National High Magnetic Field Laboratory at Florida State University, which is supported by National Science Foundation Cooperative Agreement No. DMR-1644779 and No. DMR-2128556 and the state of Florida.

TABLE OF CONTENTS

LIST OF TABLES

LIST OF FIGURES

ABSTRACT

In inviscid quantum fluids like superfluid ^{4}He (He II) and Bose-Einstein condensates (BECs), rotational motion can occur when quantized vortex lines are present. A chaotic tangle of vortices then induces quantum turbulence (QT), turbulent flows in the quantum fluids. QT has become increasingly important in various physical systems, such as superfluid neutron stars, holographic superfluid models of gravity, and complex light fields. Many unanswered questions remain despite past studies on QT in He II and BECs. In this dissertation, we discuss four research projects, three of which are numerical and experimental studies on selected questions in the quantum fluids field, and the other is a numerical study on electron qubits floated on solid neon (Ne).

The first numerical study involves the merging process of a stationary BEC with a rotating BEC. In classical fluid drops, rotational motion is transferred by viscous shear flow during the merging process. However, BEC is inviscid, and the corresponding mechanism is less clear. Our results reveal that soliton sheets play an important role in transferring angular momentum during the BEC merging processes.

In the second numerical study, we study the two-dimensional (2D) QT in a spherical shell BEC. Although Onsager vortex (OV) clusters, which are persistent clusters of like-signed vortices, can form in the evolution of decaying 2D flat superfluid turbulence, our search for exotic OV patterns in a boundaryless 2D spherical BEC shows that OV clusters never form despite the annihilation of vortex pairs.

The third topic is the numerical and experimental study of the anisotropy in thermal counterflow turbulence of He II. While turbulence in classical fluids generally becomes more homogeneous and isotropic as the scale reduces, it is theoretically predicted that counterflow turbulence can become more anisotropic in He II as the length scale reduces. Our experimental results support this idea, but our simulation results suggest the need to revise past theoretical models for this turbulence.

Lastly, we numerically study electron qubits floating in a vacuum above solid neon, which is under development and has recently achieved a coherent time long enough for practical usage. We study the interaction between the electron and a small protrusion on the neon surface. Our results indicate the possibility of novel electron states spontaneously bound around the surface bump and the prospect of utilizing these states as a qubit.

CHAPTER 1

INTRODUCTION

Turbulence, a complicated and ever-changing flow, is common in our daily lives. This phenomenon has been extensively studied in various research fields, such as mathematics, physics, and mechanical engineering. Nevertheless, controlling and predicting its dynamics remains challenging due to its strong nonlinearity and non-equilibrium [4]. In the field of condensed matter physics, quantum hydrodynamics has been studied since the discovery of superfluid helium in the late 1930s [5] (e.g., Kapitza [6] and Allen and Misener [7] in 1938). Quantum turbulence (QT), which refers to turbulence in quantum fluids, is one of the central topics in this field of study. The significant systems to study QT are superfluid ^{4}He and atomic Bose–Einstein condensate (BEC). The defining features of quantum fluids are the superfluidity and quantization of vortices, where the term 'superfluidity' was introduced by Kapitza in the analogy of superconductivity [6]. This area of study is pertinent to a wide range of research topics, including axion BEC dark matter [8], cosmic strings in the Higgs field (e.g., Kibble–Zurek mechanism [9, 10]), Hawking radiation [11, 12], holographic superfluid model of gravity [13–15], and neutron stars [16]. This dissertation presents our studies regarding flows in superfluid ^{4}He or atomic BEC. This chapter introduces the fundamentals of QT in superfluid ^{4}He and atomic BEC.

1.1 Bose–Einstein Condensate

Einstein [17, 18] predicted a surprising quantum state, Bose–Einstein condensate (BEC), in thermally equilibrium ideal Bose gas, and Penrose and Onsager [19] expanded the definition of BEC. The following introduces the fundamentals of BEC. It should be noted that this dissertation does not take into account the spin degree of freedom in Bose systems; however, the following discussion can be readily extended to spinor Bose systems [20].

1.1.1 Ideal Bose Gas

As the first step, this section examines the traits of ideal (i.e., non-interacting) Bose gases in thermal equilibrium. The absence of interactions leads to a loss of nonlinearity, making it impossible for non-equilibrium states to achieve equilibrium. Nevertheless, the ideal gas approximation proves

helpful in describing weakly interacting gases in thermal equilibrium, as the contribution of such interactions for thermodynamics functions becomes negligible after the system reaches equilibrium [21]. In Bose systems, there is no limit to the number of particles that can occupy a state, which sets it apart from Fermi systems, where only one particle can occupy each state. The free energy F in thermal equilibrium is given by [22]

$$F = \frac{1}{\beta}\sum_j \log\left(1 - e^{-\beta(\varepsilon_j - \mu)}\right). \tag{1.1}$$

Here, $\beta := 1/k_B T$ is the inverse temperature with the Boltzmann constant k_B, ε_j stands for the energy of the j-th state, and μ denotes the chemical potential. Under the periodic boundary condition with the box size L^3, the discretized wave number vector $\boldsymbol{k}$ can be expressed as

$$\boldsymbol{k} = \frac{2\pi}{L}(n_x, n_y, n_z) \qquad \forall n_x, n_y, n_z \in \mathbb{Z} \tag{1.2}$$

$$=: \Delta k\,(n_x, n_y, n_z)\,. \tag{1.3}$$

and the free energy is then expressed as

$$F = \frac{1}{\beta}\left(\frac{L}{2\pi\hbar}\right)^3 \sum_j \Delta p^3 \log\left(1 - e^{-\beta(\varepsilon_j - \mu)}\right). \tag{1.4}$$

Here, $\Delta p = \hbar \Delta k = 2\pi\hbar/L$ and $\varepsilon_j = \boldsymbol{p}_j/2m$ with the momentum of the j-th state $\boldsymbol{p}_j$. If the energy difference between the levels is significantly lower than the average energy, the Thomas–Fermi (TF) approximation is applicable. Then, the free energy can be approximated as

$$F = \frac{1}{\beta}\left(\frac{L}{2\pi\hbar}\right)^3 \int dp^3 \log\left(1 - e^{-\beta(\varepsilon - \mu)}\right), \tag{1.5}$$

with $\varepsilon := p^2/2m$, and the total number of particles N is given by

$$N = -\frac{\partial F}{\partial \mu} \tag{1.6}$$

$$= V\left(\frac{m k_B T}{2\pi\hbar^2}\right)^{3/2} \zeta_{3/2}(\alpha_B)\,, \tag{1.7}$$

where $\alpha_B := e^{\beta\mu}$ and $\zeta_r(\alpha_B) := \sum_{n=i}^{\infty} \alpha_B^r/n^r$ is the Riemann zeta function, which diverges when $\alpha_B > 1$. It is pertinent to note that the derivative of $\zeta_r(\alpha_B)$ with α_B is given by $\partial\zeta_r(\alpha_B)/\partial\alpha_B = \zeta_{r-1}(\alpha_B)/\alpha_B$. At $\alpha_B = 1$, the total particle number is represented as

$$N = V\left(\frac{m k_B T_c}{2\pi\hbar^2}\right)^{3/2} \zeta_{3/2}(1), \tag{1.8}$$

where T_c is the BEC critical temperature and can be written as

$$T_c = \frac{2\pi\hbar^2}{mk_B}\left(\frac{N}{V\zeta_{3/2}(1)}\right)^{2/3}. \tag{1.9}$$

Above the critical temperature, the energy is given by

$$\begin{aligned} E_{T>T_c} &= \frac{\partial(\beta F)}{\partial\beta} + \mu\langle N\rangle \\ &= V\int\frac{d^3\boldsymbol{p}}{(2\pi\hbar)^3}\frac{p^2/2m}{\alpha_B^{-1}e^{p^2/2mk_BT}-1} \\ &= \frac{3}{2}k_BT\left(\frac{mk_BT}{2\pi\hbar^2}\right)^{3/2}V\zeta_{5/2}(\alpha), \end{aligned} \tag{1.10}$$

and the specific heat is expressed as

$$\begin{aligned} C_{v,T<T_c} &:= \left(\frac{\partial E}{\partial T}\right)_{V=\text{const.}} \\ &= \frac{15}{4}k_B\left(\frac{mk_BT}{2\pi\hbar^2}\right)^{3/2}V\zeta_{5/2}(\alpha_B) + \frac{3}{2}k_BT\left(\frac{mk_BT}{2\pi\hbar^2}\right)^{3/2}V\frac{\partial\alpha_B}{\partial T}\frac{\zeta_{3/2}(\alpha_B)}{\alpha_B} \\ &= \frac{15}{4}k_B\left(\frac{mk_BT}{2\pi\hbar^2}\right)^{3/2}V\zeta_{5/2}(\alpha_B) - \frac{9}{4}Nk_B\frac{\zeta_{3/2}(\alpha_B)}{\zeta_{1/2}(\alpha_B)} \end{aligned} \tag{1.11}$$

where Equation 1.7 is applied to derive $\partial\alpha_B/\partial T$ as

$$\frac{1}{\alpha_B}\frac{\partial\alpha_B}{\partial T} = -\frac{3}{2}\left(\frac{2\pi\hbar^2}{mk_B}\right)^{3/2}\frac{N}{V}\frac{1}{\zeta_{1/2}(\alpha)T^{5/2}}. \tag{1.12}$$

Below the critical temperature, a macroscopic number of particles occupy the ground state, and the TF approximation may not apply. In such cases, the free energy and total particle number are expressed as

$$F = \frac{1}{\beta}\sum_j \log\left(1-e^{-\beta\varepsilon_j}\alpha_B\right) \tag{1.13}$$

$$\begin{aligned} N &= -\frac{\partial F}{\partial\mu} = \sum_j\frac{1}{\alpha_B^{-1}e^{\beta\varepsilon_j}-1} \\ &=: \sum_j\langle n_j\rangle. \end{aligned} \tag{1.14}$$

Here, $\langle n_j\rangle$ is the particle number in the j-th state. At very low temperatures, the particle numbers of the ground and first excited states have a relation

$$\langle n_1\rangle = \frac{1}{\alpha_B^{-1}e^{\beta\varepsilon_1}-1} \ll \frac{1}{\alpha_B^{-1}e^{\beta\varepsilon_0}-1} = \langle n_0\rangle. \tag{1.15}$$

Given $\varepsilon_0 = 0$, the chemical potential can be calculated as

$$\begin{aligned} \langle n_0 \rangle &= \frac{1}{e^{-\beta\mu} - 1} && (1.16) \\ \Leftrightarrow \mu &= -k_B T \log\left(1 + \frac{1}{\langle n_0 \rangle}\right). && (1.17) \end{aligned}$$

Therefore, the chemical potential can be considered negligible at very low temperatures. We can apply the TF approximation to calculate the particle number of the excitation N_{ex} when the number of the excitation is small. Below the critical temperature, the excitation particle number $N_{\text{ex},T<T_c}$ and the condensation particle number $N_{\text{cond},T<T_c}$ can be expressed as

$$\begin{aligned} N_{\text{ex},T<T_c} &= \sum_{i=1}^{\infty} \frac{1}{e^{\beta\varepsilon_i} - 1} \\ &\approx V \int \frac{d^3\boldsymbol{p}}{(2\pi\hbar)^3} \frac{1}{e^{p^2/2mk_BT} - 1} \\ &= N \left(\frac{T}{T_c}\right)^{3/2} && (1.18) \\ N_{\text{cond},T<T_c} &= 1 - N_{\text{ex},T<T_c} \\ &= N \left[1 - \left(\frac{T}{T_c}\right)^{3/2}\right], && (1.19) \end{aligned}$$

showing that the particle number of the condensation becomes an order of N below the critical temperature. Since the ground state has zero energy, the total energy and the specific heat can be calculated as[1]

$$\begin{aligned} E_{T<T_c} &= V \int \frac{d^3\boldsymbol{p}}{(2\pi\hbar)^3} \frac{p^2/2m}{e^{p^2/2mk_BT} - 1} \\ &= \frac{3}{2} \frac{\zeta_{5/2}(1)}{\zeta_{3/2}(1)} N k_B T \left(\frac{T}{T_c}\right)^{3/2} \\ &\approx 0.77 N k_B T \left(\frac{T}{T_c}\right)^{3/2} && (1.20) \\ C_{v,T<T_c} &= \frac{15}{4} \frac{\zeta_{5/2}(1)}{\zeta_{3/2}(1)} N k_B \left(\frac{T}{T_c}\right)^{3/2} \\ &\approx 1.93 N k_B \left(\frac{T}{T_c}\right)^{3/2}, && (1.21) \end{aligned}$$

where $\Gamma(x) := \int_0^\infty t^{x-1} e^{-t} dt$ is the Gamma function. The derivative of the specific heat is discontinuous at $T = T_c$, which indicates that the BEC phase transition is a second-order phase transition [23, 24].

[1] $\zeta_{3/2}(1) \approx 2.612$, $\zeta_{5/2}(1) \approx 1.341$

1.1.2 Bose Field Operator and Macroscopic Wave Function

For a system of N identical bosons, in which $n_j \in \mathbb{N}_0$ bosons occupy the j-th state, the state basis can be established by $|N\rangle := |n_0, n_1, \cdots\rangle$ and the creation and annihilation operators $\hat{a}_j^\dagger$ and $\hat{a}_j$ are defined by

$$\begin{aligned} \langle N'|\, \hat{a}_j^\dagger \,|N\rangle &= \langle n_0', n_1', \cdots |\, \hat{a}_j^\dagger \,|n_0, n_1, \cdots\rangle \\ &= \sqrt{n_j}\delta_{n_j', n_{j-1}} \prod_{k\neq j} \delta_{n_k', n_k} \qquad (1.22) \\ \langle N'|\, \hat{a}_j \,|N\rangle &= \sqrt{n_j+1}\delta_{n_j', n_{j+1}} \prod_{k\neq j} \delta_{n_k', n_k}. \qquad (1.23) \end{aligned}$$

These operators satisfy the commutation relations as

$$\begin{aligned} \left[\hat{a}_j, \hat{a}_{j'}\right] = \left[\hat{a}_j^\dagger, \hat{a}_{j'}^\dagger\right] &= 0, \qquad \forall j, j' \in \mathbb{N} \qquad (1.24) \\ \left[\hat{a}_j, \hat{a}_{j'}^\dagger\right] &= \delta_{jj'}. \qquad (1.25) \end{aligned}$$

With the vacuum state $|\text{vac}\rangle := |0, \cdots, 0, \cdots\rangle$, the N-body state may be written as

$$|N\rangle = \prod_j \frac{\left(\hat{a}_j^\dagger\right)^{n_j}}{\sqrt{n_j!}} |\text{vac}\rangle\,. \qquad (1.26)$$

The Hamiltonian of a bosonic system with a two-body interaction is given by [25]

$$\hat{\mathcal{H}} = \sum_j \frac{\hbar^2 k_j^2}{2m} \hat{a}_j^\dagger \hat{a}_j + \frac{1}{2}\sum_{ijkl} V_{ijkl} \hat{a}_i^\dagger \hat{a}_j^\dagger \hat{a}_k \hat{a}_l, \qquad (1.27)$$

where the first term is the kinetic term, and the second term represents the interactions among particles with the interaction matrix V_{ijkl}.

The transformation from the single-particle basis $|j\rangle$ to a new complete orthonormal basis, eigenstates $|\boldsymbol{r}\rangle$ of the coordinate operator, is written as

$$|\boldsymbol{r}\rangle = \sum_j U_{\mu j}^* \,|j\rangle \qquad (1.28)$$

with a unitary matrix $\hat{U}$. The annihilation operator is then transformed as

$$\hat{\psi}(\boldsymbol{r}) := \sum_j U_{\mu j} \hat{a}_j \qquad (1.29)$$

where $\hat{\psi}$ is the Bose field operator satisfying the commutation relations:

$$\begin{aligned} \left[\hat{\psi}(\boldsymbol{r}), \hat{\psi}(\boldsymbol{r}')\right] = \left[\hat{\psi}^\dagger(\boldsymbol{r}), \hat{\psi}^\dagger(\boldsymbol{r}')\right] &= 0, \qquad \forall \boldsymbol{r}, \boldsymbol{r}' \in \mathbb{R}^3 \qquad (1.30) \\ \left[\hat{\psi}(\boldsymbol{r}), \hat{\psi}^\dagger(\boldsymbol{r}')\right] &= \delta(\boldsymbol{r} - \boldsymbol{r}'). \qquad (1.31) \end{aligned}$$

With the Bose field operator, the kinetic term $\hat{K}$ and external potential term $\hat{U}$ may be written as [20, 25]

$$\hat{K} := -\frac{\hbar^2}{2m}\sum_j \nabla_j^2 = -\frac{\hbar^2}{2m}\int \hat{\psi}^\dagger(\boldsymbol{r})\nabla^2\hat{\psi}(\boldsymbol{r})d\boldsymbol{r} \tag{1.32}$$

$$\hat{U} := \sum_j U(\boldsymbol{r}_j) = \int \hat{\psi}^\dagger(\boldsymbol{r})U(\boldsymbol{r})\hat{\psi}(\boldsymbol{r})d\boldsymbol{r}, \tag{1.33}$$

and the two-body interaction term is given by

$$\begin{aligned}\hat{V}_{\text{int}} &:= \frac{1}{2}\sum_{i\neq j} V(\boldsymbol{r}_i, \boldsymbol{r}_j) \\ &= \frac{1}{2}\int\int d\boldsymbol{r}d\boldsymbol{r}' V(\boldsymbol{r}, \boldsymbol{r}')\hat{\psi}^\dagger(\boldsymbol{r})\hat{\psi}(\boldsymbol{r})\hat{\psi}^\dagger(\boldsymbol{r}')\hat{\psi}(\boldsymbol{r}').\end{aligned} \tag{1.34}$$

For a pure N-body state $\Psi_N(\boldsymbol{r}_1, \boldsymbol{r}_2, \cdots, \boldsymbol{r}_N; t)$, we can define the single-particle density matrix ρ_1 as

$$\rho_1(\boldsymbol{r}, \boldsymbol{r}'; t) := \langle \hat{\psi}^\dagger(\boldsymbol{r}, t)\, \hat{\psi}\left(\boldsymbol{r}', t\right)\rangle . \tag{1.35}$$

Since the system is Bosonic, the wave function is symmetric under the exchange of any pair of particle positions, and the single-particle density matrix is Hermitian, i.e., $\rho_1(\boldsymbol{r}, \boldsymbol{r}'; t) = \rho_1^*(\boldsymbol{r}', \boldsymbol{r}; t)$. Therefore, the single-particle density matrix can be diagonalized, such as

$$\rho_1(\boldsymbol{r}, \boldsymbol{r}'; t) := \sum_j n_j(t)\chi_j^*(\boldsymbol{r}, t)\,\chi_j\left(\boldsymbol{r}', t\right) \tag{1.36}$$

where the eigenvalues n_j evolve with time, and the eignfunctions $\chi_j(\boldsymbol{r}, t)$ are called single-particle states.

The BEC appears below the critical temperature when the eigenvalue n_0 of the ground single-particle state χ_0 becomes $\mathcal{O}(N)$ in the thermodynamic limit[2]. The $U(1)$ gauge symmetry is then broken, and the condensate obtains an order parameter called the macroscopic wave function defined by

$$\Psi(\boldsymbol{r}, t) := \sqrt{n_0}\chi_0. \tag{1.37}$$

The velocity $\boldsymbol{v}$ in the BEC is given by

$$\boldsymbol{v}(\boldsymbol{r}, t) = \frac{\hbar}{m}\boldsymbol{\nabla}\phi(\boldsymbol{r}, t) \tag{1.38}$$

[2]There are cases where several eigenvalues χ_j become $\mathcal{O}(N)$ in the thermodynamic limit. Such a state is called 'fragmented BEC' [20].

where m is the mass of the particle, $\hbar$ is the Dirac constant (i.e., the Planck constant h divided by 2π), and ϕ is the phase of the macroscopic wave function Ψ. It is worth noting that the macroscopic wave function $\Psi(\boldsymbol{r}, t)$ is a classical wave function whose amplitude n_0 and phase ϕ are determined simultaneously.

1.1.3 Quantized Vortex

From Equation 1.38, the vorticity $\boldsymbol{\omega}$ is given by

$$\begin{aligned} \boldsymbol{\omega} &:= \boldsymbol{\nabla} \times \boldsymbol{v} && (1.39) \\ &= \frac{\hbar}{m} \boldsymbol{\nabla} \times \boldsymbol{\nabla} \phi && (1.40) \\ &= \mathbf{0}, && (1.41) \end{aligned}$$

which means the flow in the condensate is irrotational, and the circulation Γ along a closed contour $\mathcal{C}$ around a closed area $\mathcal{S}$ having no singular is given by

$$\Gamma := \oint_{\mathcal{C}} \boldsymbol{v} \cdot d\boldsymbol{l} = \int_{\mathcal{S}} \boldsymbol{\omega} \cdot d\boldsymbol{S} = 0 \tag{1.42}$$

where the Stokes theorem is applied. On the other hand, if the area $\mathcal{S}$ has a singular, the circulation may have a finite value. In BECs, vortices appear as topological phase defects, i.e., singular points. In such cases, the Stokes theorem is not applicable, and the phase gradient integrated along $\mathcal{C}$ may have a finite value:

$$\oint_{\mathcal{C}} \boldsymbol{\nabla} \phi \cdot d\boldsymbol{r} = [\phi] = 2\pi l_v. \qquad \forall\, l_v \in \mathbb{N}_0 \tag{1.43}$$

Here, the phase difference along the closed contour must be 2π times an integer l_v due to the single-valuedness of the macroscopic wave function. As a result, the circulation Γ around a closed contour may be a finite value quantized in the unit of $\kappa = h/m$ as[3]

$$\Gamma = \oint_{\mathcal{C}} \boldsymbol{v} \cdot d\boldsymbol{l} = l_v \kappa, \tag{1.44}$$

where l_v is called the vortex charge. Onsager theoretically proposed the quantization of vortices in 1949 [26], and Vinen first experimentally observed a quantized vortex in superfluid ^{4}He in 1961 [27]. The vortices with multiple quanta of circulation are unstable and can be quickly split into single-charged vortices. For example, when a l_v-charged vortex is located at the center of a rotating cylindrical condensate of the radius R, the velocity is given by

$$\boldsymbol{v}_s = \frac{l_v \kappa}{2\pi r} \hat{\boldsymbol{\phi}}, \tag{1.45}$$

[3] In superfluid helium, $\kappa \approx 9.97 \times 10^{-8} \mathrm{m}^2/\mathrm{s}$

where r is the radial distance from the center axis and $\hat{\boldsymbol{\phi}}$ is the unit vector in the azimuth direction. Then, the vortex energy per unit length is calculated as

$$E_{SV}(l_v) = \int_{a_0}^{R} \frac{1}{2}\rho_s \boldsymbol{v}_s^2 2\pi r dr = l_v^2 \frac{\rho_s \kappa^2}{4\pi} \ln\left(\frac{R}{a_0}\right), \tag{1.46}$$

where a_0 is the vortex core size[4]. The vortex energy of a single vortex with vortex-charge of l_v (i.e., $E_{SV}(l_v) = {l_v}^2 E_{SV}(1)$) is higher than that of l_v single-charged vortices (i.e., $l_v E_{SV}(1)$) when $l_v \geq 2$. Therefore, multi-charged vortices quickly split into single-charged vortices [28] .

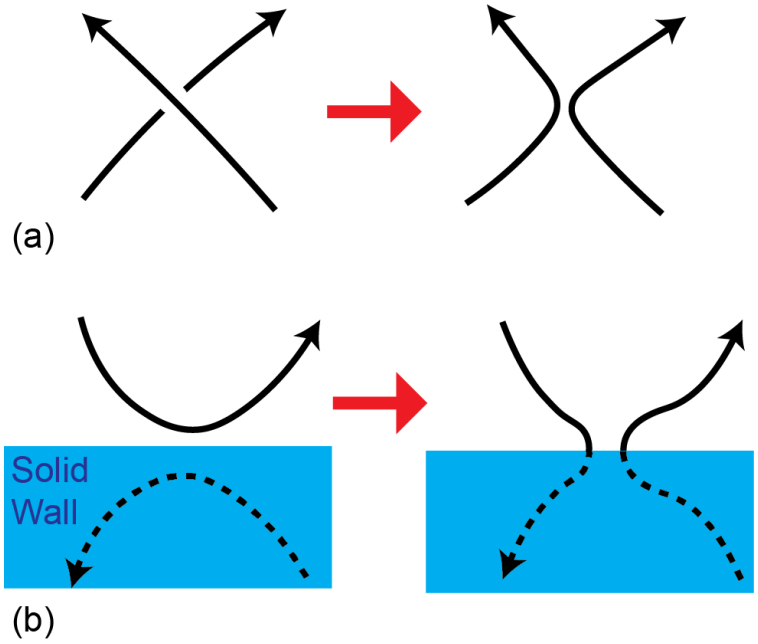

Figure 1.1: Schematic of vortex reconnection. (a) Vortex reconnection between two vortex lines. (b) Vortex reconnection between a vortex line and its imaginary vortex line in the solid wall.

When two vortex lines approach each other closer than a threshold distance Δ_{rec}, they reconnect (Figure 1.1a. Vortex reconnection may happen with its imaginary vortex on the boundary (Figure 1.1b). The vortex reconnection process emits sound waves [29] and excites Kelvin waves, the distortion waves traveling along vortex lines [30]. In superfluid ^{4}He, Schwarts [31] estimated the threshold distance about $\Delta_{\mathrm{rec}} \approx 2R/\ln(R/c_{\mathrm{rec}}a_0)$ where R is the radius of curvature and c_{rec} is a constant on the order of 1. The Kelvin wave induces the sound wave radiation [32–34].

[4] $a_0 \approx 0.5$ Å in superfluid helium.

1.2 Atomic Bose–Einstein Condensates

Atomic BECs (i.e., BECs in ultracold atomic gases) are significant systems in quantum fluid research. Ultracold atomic gas is a dilute group of atoms cooled down to about zero Kelvin in a vacuum by lasers [35]. Since BECs were realized in dilute atomic gas of rubidium [36], sodium [37], and lithium [38,39] in 1995, many theoretical and experimental techniques have been developed [40].

1.2.1 Weakly Interacting Bose System

Considering a neutral atomic BEC without any external potential in a system of the size L^3, each state has a momentum $\boldsymbol{p} = \Delta p\,(n_x, n_y, n_z)$ with $\forall n_z, n_y, n_z \in \mathbb{N}$. In BECs at about absolute zero temperature, the s-wave scattering is dominant, and the interparticle interaction can be effectively written as

$$V_{\mathrm{int}}(\boldsymbol{r} - \boldsymbol{r}') = U_0 \delta(\boldsymbol{r} - \boldsymbol{r}') \tag{1.47}$$

with $U_0 = 4\pi\hbar^2 a_s/m$ and the s-wave scattering length a_s. From Equation 1.27, the Hamiltonian is given by

$$\hat{\mathcal{H}} = \sum_{\boldsymbol{p}} \frac{p^2}{2m} \hat{a}^\dagger_{\mathrm{p}} \hat{a}_{\mathrm{p}} + \frac{U_0}{2V} \sum_{\boldsymbol{p}_1+\boldsymbol{p}_2=\boldsymbol{p}_3+\boldsymbol{p}_4} \hat{a}^\dagger_{\boldsymbol{p}_1} \hat{a}^\dagger_{\boldsymbol{p}_2} \hat{a}_{\boldsymbol{p}_3} \hat{a}_{\boldsymbol{p}_4}. \tag{1.48}$$

In BECs, the expected particle number in the single-particle ground state (i.e., $\boldsymbol{p} = \boldsymbol{0}$) should be $\mathcal{O}(N)$ in the thermodynamics limit, i.e., in the limit $V, N \to \infty$ with a constant density N/V. Since $\left[\hat{a}_0, \hat{a}_0^\dagger\right] = 1 \ll N$, the operators $\hat{a}_0$ and $\hat{a}_0^\dagger$ may be approximated as a c-number $\sqrt{N_0}$, where $N_0 = n_0 V$ is the particle number of the ground state. Bogoliubov first introduced this approach [40]. The particle number operator $\hat{N}$ and the Hamiltonian can be then written as

$$\hat{N} := \sum_{\boldsymbol{p}} \hat{a}^\dagger_{\boldsymbol{p}} \hat{a}_{\boldsymbol{p}} = N_0 + \sum_{\boldsymbol{p}\neq\boldsymbol{0}} \hat{a}^\dagger_{\boldsymbol{p}} \hat{a}_{\boldsymbol{p}} \tag{1.49}$$

$$\hat{\mathcal{H}} = \frac{N_0^2 U_0}{2V} + \sum_{\boldsymbol{p}\neq\boldsymbol{0}} \left(\frac{p^2}{2m} + 2U_0 n_0 \right) \hat{a}^\dagger_{\boldsymbol{p}} \hat{a}_{\boldsymbol{p}} + \frac{U_0 n_0}{2} \sum_{\boldsymbol{p}\neq\boldsymbol{0}} \left(\hat{a}^\dagger_{\boldsymbol{p}} \hat{a}^\dagger_{-\boldsymbol{p}} + \hat{a}_{\boldsymbol{p}} \hat{a}_{-\boldsymbol{p}} \right), \tag{1.50}$$

where we have retained the terms up to the second order on the operators because the particle number of the excitations is assumed to be small within the Bogoliubov approach. By combining these equations, we may rewrite the Hamiltonian as

$$\hat{\mathcal{H}} = \frac{\hat{N}^2 U_0}{2V} + \sum_{\boldsymbol{p}\neq\boldsymbol{0}} \left(\frac{p^2}{2m} + U_0 n_0 \right) \hat{a}^\dagger_{\boldsymbol{p}} \hat{a}_{\boldsymbol{p}} + \frac{U_0 n_0}{2} \sum_{\boldsymbol{p}\neq\boldsymbol{0}} \left(\hat{a}^\dagger_{\boldsymbol{p}} \hat{a}^\dagger_{-\boldsymbol{p}} + \hat{a}_{\boldsymbol{p}} \hat{a}_{-\boldsymbol{p}} \right). \tag{1.51}$$

where we have again retained the terms up to the second order on the operators. The Hamiltonian $\hat{\mathcal{H}}$ has been written in a quadratic form and can be diagonalized by the normalized Bogoliubov

transformation defined by [5]:

$$\hat{b}_{\boldsymbol{p}} := u_{\boldsymbol{p}}\hat{a}_{\boldsymbol{p}} + v_{\boldsymbol{p}}\hat{a}^{\dagger}_{-\boldsymbol{p}} \tag{1.52}$$

$$\hat{b}^{\dagger}_{\boldsymbol{p}} := u_{\boldsymbol{p}}\hat{a}_{-\boldsymbol{p}} + v_{\boldsymbol{p}}\hat{a}^{\dagger}_{\boldsymbol{p}} \tag{1.53}$$

with

$$u^2_{\boldsymbol{p}} = \frac{1}{2}\left(\frac{\frac{p^2}{2m} + U_0 n_0}{\varepsilon_{\boldsymbol{p}}} + 1\right) \tag{1.54}$$

$$v^2_{\boldsymbol{p}} = \frac{1}{2}\left(\frac{\frac{p^2}{2m} + U_0 n_0}{\varepsilon_{\boldsymbol{p}}} - 1\right), \tag{1.55}$$

$$\varepsilon_{\boldsymbol{p}} = \sqrt{\left(\frac{p^2}{2m}\right)^2 + \frac{p^2}{2m}2U_0 n_0}, \tag{1.56}$$

where $\varepsilon_{\boldsymbol{p}}$ is called the Bogoliubov spectrum. The diagonalized formula of the Hamiltonian is then given by

$$\hat{\mathcal{H}} = \frac{\hat{N}^2 U_0}{2V} + \sum_{\boldsymbol{p}\neq 0}\varepsilon_{\boldsymbol{p}}\hat{b}^{\dagger}_{\boldsymbol{p}}\hat{b}_{\boldsymbol{p}} - \frac{1}{2}\sum_{\boldsymbol{p}\neq 0}\left(\frac{p^2}{2m} + U_0 n_0 - \varepsilon_{\boldsymbol{p}}\right). \tag{1.57}$$

The formula is equivalent to that for a non-interacting Bose system with the Bogoliubov spectrum. The non-interacting quasi-particles associated with the operator $\hat{b}_{\boldsymbol{p}}$ are called Bogolons.

With the Bogoliubov formula, the particle number operator can be written as

$$\hat{N} = N_0 + \sum_{\boldsymbol{p}\neq 0} v^2_p + \sum_{\boldsymbol{p}\neq 0}\left(u^2_{\boldsymbol{p}} + v^2_{\boldsymbol{p}}\right)\hat{b}^{\dagger}_{\boldsymbol{p}}\hat{b}_{\boldsymbol{p}}. \tag{1.58}$$

When thermal excitations are absent, the third term becomes zero, and the second term corresponds to the particle number of the non-condensed part, which occupies finite wave-number states at absolute zero temperature. Therefore, the ratio between the non-condensed particle number $N_{\rm ex}$ and the total particle number N can be evaluated as

$$\begin{aligned}\frac{N_{\rm ex}}{N} &= \frac{V}{N}\sum_{\boldsymbol{p}\neq 0} v^2_p \\ &= \frac{1}{3\pi^2 n}\left(\frac{mc_{\rm s}}{\hbar}\right)^3 \\ &= \frac{8}{3\sqrt{\pi}}\sqrt{na_s^3},\end{aligned} \tag{1.59}$$

where $c_{\rm s} = \sqrt{U_0 n/m}$ is the sound speed in weak-interacting BECs. This result indicates that most particles are in the identical single-particle ground state when $na_s^3 \ll 1$, called the diluteness condition.

[5] The normalization condition is $u^2_{\boldsymbol{p}} - v^2_{\boldsymbol{p}} = 1$.

1.2.2 Gross–Pitaevskii Equation

Neutral dilute atomic gases usually satisfy the diluteness condition $na_s \ll 1$ at very low temperatures, and the N-body wave function in atomic BEC may be approximated by the mean-field (Hartree) approximation as

$$\Psi_N(\boldsymbol{r}_1, \boldsymbol{r}_2, \cdots, \boldsymbol{r}_N; t) = \prod_{i=1}^{N} \chi_0(\boldsymbol{r}_i, t). \tag{1.60}$$

where $\chi_0(\boldsymbol{r}, t)$ is the normalized single-particle wave function in the ground state. The effective interaction potential between the two particles at $\boldsymbol{r}$ and $\boldsymbol{r}'$ is a constant U_0 in the momentum representation and a delta function $U_0\delta(\boldsymbol{r}-\boldsymbol{r}')$ in the coordinate representation. Then, the effective Hamiltonian of neutral dilute BECs is written as

$$\mathcal{H} = \sum_{i=1}^{N} \left[\frac{\boldsymbol{p}_i^2}{2m} + U(\boldsymbol{r}_i) \right] + U_0 \sum_{i<j} \delta(\boldsymbol{r}_i - \boldsymbol{r}_j), \tag{1.61}$$

here $U(\boldsymbol{r})$ is the external potential. Introducing the macroscopic wave function

$$\Psi(\boldsymbol{r}, t) = \sqrt{N}\chi_0(\boldsymbol{r}, t), \tag{1.62}$$

the action is given by

$$\begin{aligned}
\mathcal{S} &= \int \left[\frac{i\hbar}{2} \left(\Psi_N^* \frac{\partial \Psi_N}{\partial t} - \Psi_N \frac{\partial \Psi_N^*}{\partial t} \right) - \Psi_N^* H \Psi \right] d\boldsymbol{r}_1 d\boldsymbol{r}_2 \cdots d\boldsymbol{r}_N dt \\
&= N \int \left[\frac{i\hbar}{2} \left(\chi_0^* \frac{\partial \chi_0}{\partial t} - \chi_0 \frac{\partial \chi_0^*}{\partial t} \right) \right. \\
&\quad \left. - \frac{\hbar^2}{2m} |\boldsymbol{\nabla}\chi_0|^2 - U |\chi_0|^2 - \frac{N-1}{2} U_0 |\chi_0|^4 \right] d\boldsymbol{r} dt \\
&= \int \left[\frac{i\hbar}{2} \left(\Psi^* \frac{\partial \Psi}{\partial t} - \Psi \frac{\partial \Psi^*}{\partial t} \right) \right. \\
&\quad \left. - \frac{\hbar^2}{2m} |\boldsymbol{\nabla}\Psi|^2 - U |\Psi|^2 - \frac{1}{2} U_0 |\Psi|^4 + \mathcal{O}(1/N) \right] d\boldsymbol{r} dt
\end{aligned} \tag{1.63}$$

Ignoring the $\mathcal{O}(1/N)$ term and applying the the action principle $\delta\mathcal{S}[\Psi, \Psi^*]/\delta\Psi^* = 0$, we obtain the Gross–Pitaevskii equation (GPE):

$$i\hbar \frac{\partial \Psi}{\partial t} = \left[-\frac{\hbar^2}{2m}\nabla^2 + U(\boldsymbol{r}) + U_0 |\Psi|^2 - \mu \right] \Psi. \tag{1.64}$$

In static BEC bulk, the spatial and time derivatives of the macroscopic wave function are zero. Therefore, in the absence of any external potential, the chemical potential is

$$\mu = U_0 n_0 \tag{1.65}$$

where n_0 is the bulk density. The GPE has a coherent length defined as

$$\xi = \frac{\hbar}{\sqrt{2m\mu}}, \tag{1.66}$$

which characterizes the length of competition between the kinetic and interaction energies.

The following derives the hydrodynamic formula of the GP equation. The action can be written in terms of the density n and the phase ϕ as

$$\mathcal{S}[n,\phi] = \int \left[\hbar n \frac{\partial \phi}{\partial t} - \frac{\hbar^2}{2m}\left[\left(\boldsymbol{\nabla}\sqrt{n}\right)^2 + \left(\boldsymbol{\nabla}\phi\right)^2 n\right] - Un - \frac{1}{2}U_0 n^2\right] d\boldsymbol{r}dt, \tag{1.67}$$

and from the action principle, we obtain

$$\begin{aligned}
\frac{\delta \mathcal{S}}{\delta n} &= \int \left[\hbar \frac{\partial \phi}{\partial t} - \frac{\hbar^2}{2m}\left[\frac{1}{\sqrt{n}}\nabla^2\sqrt{n} + \left(\boldsymbol{\nabla}\phi\right)^2\right] - U - U_0 n\right] d\boldsymbol{r}dt = 0 \\
\Rightarrow -\hbar\frac{\partial \phi}{\partial t} &= -\frac{\hbar^2}{2m\sqrt{n}}\nabla^2\sqrt{n} + \frac{1}{2}mv^2 + U + U_0 n \qquad (1.68) \\
\frac{\delta \mathcal{S}}{\delta \phi} &= \int \left[-\hbar\frac{\partial n}{\partial t} + \frac{\hbar^2}{m}\boldsymbol{\nabla}\cdot\left(n\boldsymbol{\nabla}\phi\right)\right] d\boldsymbol{r}dt = 0 \\
\Rightarrow \frac{\partial n}{\partial t} &= -\frac{\hbar}{m}\boldsymbol{\nabla}\cdot\left(n\boldsymbol{\nabla}\phi\right). \qquad (1.69)
\end{aligned}$$

Equation 1.69 corresponds to the continuity equation:

$$\frac{\partial n}{\partial t} + \boldsymbol{\nabla}\cdot\left(n\boldsymbol{v}\right) = 0. \tag{1.70}$$

By taking the gradient of Equation 1.68, we obtain

$$\frac{\partial \boldsymbol{v}}{\partial t} + \boldsymbol{\nabla}\left(\frac{v^2}{2}\right) = -\boldsymbol{\nabla}\left(U_0 n - \frac{\hbar^2}{2m\sqrt{n}}\nabla^2\sqrt{n}\right) - \boldsymbol{\nabla}U, \tag{1.71}$$

corresponding to the Euler equation. The first pressure term $U_0 n$ corresponds to the traditional pressure in classical fluids, and the second is called the quantum pressure. The quantum pressure term becomes negligible in the bulk but plays a critical role in the generation of quantized vortices [41].

1.2.3 Imaginary Time Propagation

The GP equation conserves the total energy and total particle number. In real experiments, however, the atomic BEC system is not at zero temperature and has small thermal excitations, dampening the energy in atomic BECs. Imaginary time propagation is introduced to model the energy damping [42]:

$$\left(i-\gamma\right)\hbar\frac{\partial \Psi}{\partial t} = \left[-\frac{\hbar^2}{2m}\nabla^2 + V(\boldsymbol{r}) + U_0|\Psi|^2 - \mu\right]\Psi. \tag{1.72}$$

Where γ is a fitting parameter and may be estimated by the experimental results [43–45]. When we prepare the initial state in our simulations, we apply the imaginary time propagation method by damping the energy from an approximated initial state. This method may suppress not only the total energy but also the total particle number as

$$\frac{\partial N}{\partial t} = \int d^3r \left[\Psi^* \frac{\partial \Psi}{\partial t} + \Psi \frac{\partial \Psi^*}{\partial t}\right] \tag{1.73}$$

$$= -\frac{2}{\gamma\hbar} \int d^3r \left[\frac{\hbar^2}{2m}|\nabla\Psi|^2 + U|\Psi|^2 + U_0|\Psi|^4 - \mu|\Psi|^2\right]. \tag{1.74}$$

To impose the conservation of the particle number, the chemical potential is evolved as

$$\mu(t) = \frac{1}{N} \int d^3r \left[\frac{\hbar^2}{2m}|\nabla\Psi|^2 + U|\Psi|^2 + U_0|\Psi|^4\right]. \tag{1.75}$$

The evolution with the imaginary time propagation might be trapped in a metastable state. For example, the circular BEC with a quantized vortex at the center is metastable, requiring enough perturbation to reach the static ground state. The long decay time allows us to numerically prepare the initial state with rotational motion by the imaginary time method.

1.2.4 Solition

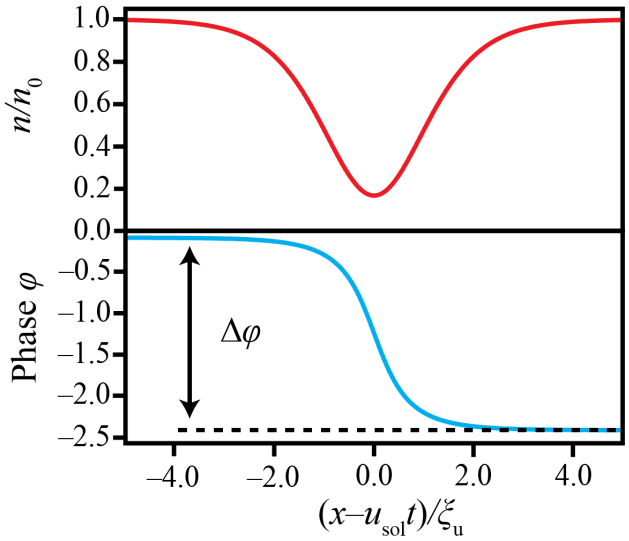

Figure 1.2: The density and phase profile of a gray soliton with $u/c_s = 0.4$.

The GPE has soliton solutions, localized non-linear waves propagating toward a direction. If the interaction is attractive, the soliton has an increment of density and is called a bright soliton.

In our case, the interaction is always repulsive, and we consider the opposite case, called the gray soliton. The one-dimensional wave function of gray solitons can be written as

$$\Psi(x,t) = \sqrt{n_0}\left[i\frac{u_{\rm sol}}{c_s} + \sqrt{1-\frac{u_{\rm sol}^2}{c_s^2}}\tanh\left(\frac{x-u_{\rm sol}t}{\sqrt{2}\xi_u}\right)\right], \tag{1.76}$$

where $u_{\rm sol}$ is the soliton speed, n_0 is the bulk density, and $\xi_u = \xi/\sqrt{1-(u_{\rm sol}/c_{\rm s})^2}$. The density and the velocity are

$$\begin{aligned} n(x,t) &= n_0 - \frac{n_0 - n_{\rm min}}{\cosh^2\left[(x-u_{\rm sol}t)/\sqrt{2}\xi_u\right]}, & (1.77)\\ v(x,t) &= u_{\rm sol}\left(1-\frac{n_0}{n}\right), & (1.78) \end{aligned}$$

where $n_{\rm min} = n_0 u_{\rm sol}^2/c_{\rm s}^2$. Figure 1.2 shows a typical profile of density and velocity. The phase change across the soliton $\Delta\phi$ is related to the soliton speed as

$$\begin{aligned} \Delta\phi &= \phi(\infty) - \phi(-\infty) \\ &= -2\cos^{-1}\left(\frac{u_{\rm sol}}{c_{\rm s}}\right) \end{aligned} \tag{1.79}$$

If the phase change is $\Delta\phi = \pi$, the soliton does not move (i.e., $u_{\rm sol} = 0$) and is called the dark soliton.

1.3 Superfluid Helium-4

Superfluid ^{4}He or He II is the most traditional system in quantum fluid study. In most matters, all atoms should rest to minimize the potential energy at sufficiently low temperatures, and it becomes solid. On the other hand, the interaction among helium atoms is relatively weak. Although the helium may be solidified at high pressure[6], quantum effects appear before the solidification at the atmospheric pressure. When liquid ^{4}He reaches a temperature below $T_\lambda := 2.172$K, it undergoes a phase transition into a superfluid state called He II, vanishing the viscosity. The specific heat has a sharp peak at $T = T_\lambda$, which is called the λ-point. London [47] suggested the relation between superfluidity and the existence of a condensate based on the similarity of the specific heat jump in an ideal BEC (Equations 1.11 and 1.21). The strong connection between superfluidity and BEC is still believed, but one is neither a sufficient nor necessary condition for the other. For instance, an ideal BEC cannot possess superfluidity since the critical velocity is zero. Additionally, superfluidity can appear in lower-dimensional systems that do not involve a BEC state.

[6]The solid state has the hexagonal close packing (hcp) and the face-centered cubic (fcc) phases. [46]

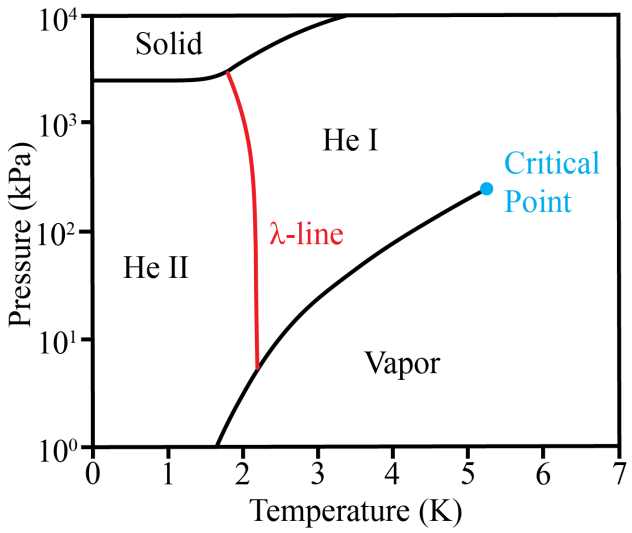

Figure 1.3: Phase diagram of helium

1.3.1 Two-Fluid Model

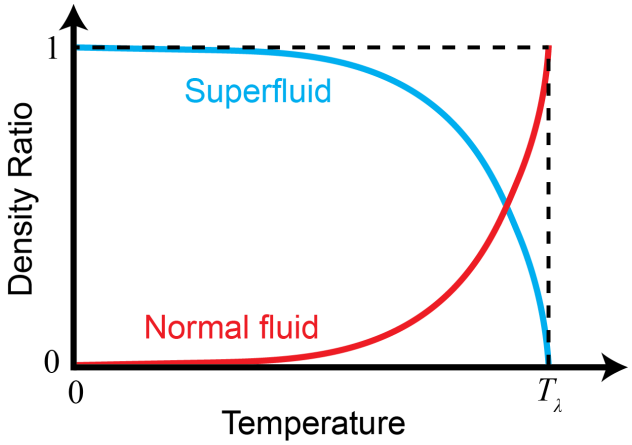

Figure 1.4: Temperature dependence of the density ratio:ρ_s/ρ for the superfluid component and ρ_n/ρ for the normal fluid compoent.

The dynamics in He II can be phenomenologically described by the two-fluid model, which treats He II as a mixture of two fluid components, an inviscid and zero-entropy superfluid component and a viscous normal-fluid component (i.e., the collection of thermal excitations). The total density is $\rho = \rho_s + \rho_n$ where ρ_s and ρ_n are superfluid and normal fluid densities, respectively (Figure 1.4). The momentum per unit volume is $\boldsymbol{j} = \rho_s \boldsymbol{v}_s + \rho_n \boldsymbol{v}_n$ where $\boldsymbol{v}_s$ and $\boldsymbol{v}_n$ are superfluid and normal fluid velocities, respectively. The superfluid has no entropy, and the normal fluid carries the total

entropy per density s. Then the conservation equations of mass ρ, momentumj_l, and entropy s with no dissipation are given as [48, 49]:

$$\frac{\partial \rho}{\partial t} + \boldsymbol{\nabla} \cdot \boldsymbol{j} = 0, \tag{1.80}$$

$$\frac{\partial j_l}{\partial t} + \frac{\partial \Pi_{lk}}{\partial x_l} = 0, \tag{1.81}$$

$$\frac{\partial \rho s}{\partial t} + \boldsymbol{\nabla} \cdot (\rho s \boldsymbol{v}_n) = 0 \tag{1.82}$$

where Π_{ik} is the momentum flux tensor. The simplest formula of the two-fluid velocity equations neglecting the thermal conductivity and bulk viscosity is given by [50]

$$\begin{aligned} \frac{\partial \boldsymbol{v}_s}{\partial t} &= -\frac{1}{\rho}\boldsymbol{\nabla} p + s\boldsymbol{\nabla} T \\ &\quad + \frac{\rho_n}{2\rho}\boldsymbol{\nabla}\left(\boldsymbol{v}_n - \boldsymbol{v}_s\right)^2 - \frac{1}{\rho_n}\boldsymbol{F}_{ns} \end{aligned} \tag{1.83}$$

$$\begin{aligned} \frac{\partial \boldsymbol{v}_n}{\partial t} &= -\frac{1}{\rho}\boldsymbol{\nabla} p - \frac{\rho_s}{\rho_n} s\boldsymbol{\nabla} T + \nu_n \nabla^2 \boldsymbol{v}_n \\ &\quad - \frac{\rho_s}{2\rho}\boldsymbol{\nabla}\left(\boldsymbol{v}_n - \boldsymbol{v}_s\right)^2 + \frac{1}{\rho_s}\boldsymbol{F}_{ns}, \end{aligned} \tag{1.84}$$

where $\nu_n := \eta_n/\rho_n$ is the kinematic viscosity of the normal fluid component and $\boldsymbol{F}_{ns}$ is a mutual friction force between the two fluids [51], caused by the scattering between the thermal excitations and the quantized vortices. This model is often called Hall-Vinen-Bekarevich-Khalatnikov (HVBK) model.

It is important to note two facts about the two-fluid model. Firstly, the normal fluid velocity $\boldsymbol{v}_n$ is not the mean velocity of the non-condensed part and is defined as [20]

$$\boldsymbol{v}_n(\boldsymbol{r}) = \frac{\delta F}{\delta \left\langle \hat{J}(\boldsymbol{r}) \right\rangle}, \tag{1.85}$$

where F is the free energy of the system and $\hat{J}$ is the mass current operator.

Secondly, the superfluid density ρ_s is not that of the condensate. According to a measurement by the neutron scattering measurements [52], the condensate fraction in ^{4}He at the saturated pressure is written as

$$\frac{N_0(T)}{N} = A\left(1 - \left(\frac{T}{T_\lambda}\right)^\gamma\right) \tag{1.86}$$

where $A = (7.25 \pm 0.75) \times 10^{-2}$ and $\gamma = 5.5 \pm 1.0$, which is consistent with the result of a numerical study [53]. The behavior is similar to that of the ideal Bose system (Equation 1.19), but the

condensate fraction at the zero-temperature is less than 10%, which is much smaller than the fraction of the superfluid component in the two-fluid model[7].

1.3.2 First and Second Sound Waves

In He II, several kinds of sound waves can be observed [48, 55]. When the velocities are small enough, the Equations 1.80, 1.81, 1.82, and 1.83 can be linearized as:

$$\frac{\partial \rho}{\partial t} + \boldsymbol{\nabla} \cdot \boldsymbol{j} = 0 \tag{1.87}$$

$$\frac{\partial \boldsymbol{j}}{\partial t} + \boldsymbol{\nabla} p = 0 \tag{1.88}$$

$$\frac{\partial \rho s}{\partial t} + \rho s \boldsymbol{\nabla} \cdot \boldsymbol{v}_n = 0 \tag{1.89}$$

$$\frac{\partial \boldsymbol{v}_s}{\partial t} + \frac{1}{\rho} \boldsymbol{\nabla} p + s \boldsymbol{\nabla} T = 0 \tag{1.90}$$

where the entropy ρs is supposed to be constant. From Equations 1.87 and 1.88, the propagation equation for the normal sound wave called the first sound wave is obtained as:

$$\frac{\partial^2 \rho}{\partial t^2} = \nabla^2 p. \tag{1.91}$$

The speed of the first sound u_1 is given by

$$u_1^2 \approx \left. \frac{\partial p}{\partial \rho} \right|_s \approx \frac{C_p}{C_V} \frac{1}{\rho \kappa}, \tag{1.92}$$

where C_p and C_V are the heat capacities at constant pressure and at constant volume, respectively.

In He II, there is another type of sound wave called the second sound wave, which is a wave of entropy and temperature. Under a constant density and pressure, we obtain the propagation equation from Equations 1.89 and 1.90 as:

$$\frac{\partial^2 s}{\partial t^2} = \frac{\rho_s s^2}{\rho_n} \nabla^2 T. \tag{1.93}$$

The speed of the second sound u_2 is given by

$$u_2^2 \approx \frac{s^2 \rho_s}{\rho_n} \left. \frac{\partial T}{\partial s} \right|_\rho \approx \frac{\rho_s}{\rho_n} \frac{T s^2}{C_V}. \tag{1.94}$$

1.3.3 Thermal Excitations in Superfluid Helium-4

At low temperatures, the normal fluid is composed of two types of thermal excitations at low temperatures, i.e., phonons and rotons. The expected energy spectrum (Figure 1.5) was observed

[7] There are other experimental or numerical studies showing slightly larger values of A [53, 54], but they are much smaller than 1

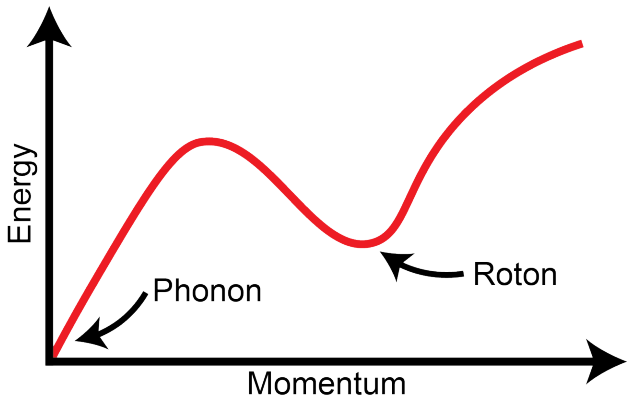

Figure 1.5: Energy spectrum of the thermal excitations in He II.

by the neutron scattering [56,57]. Phonons are the primary excitations at low momentum; however, at higher momentum, rotons emerge as the dominant component. Phonons are the quantized sound waves and have an energy spectrum of $\mathcal{E} = c_s p$. On the other hand, the roton energy has a minimum Δ_R at $p = p_0$ given by

$$\frac{\Delta_R}{k_B} = 8.6 \text{ K} \tag{1.95}$$

$$\frac{p_0}{\hbar} = 1.9 \text{ Å}^{-1}. \tag{1.96}$$

Near the minimum, the energy spectrum can be approximated as

$$\mathcal{E} = \Delta_R + \frac{(p - p_0)^2}{0.3 m_4} \tag{1.97}$$

with the mass of a ^{4}He atom $m_4 \sim 6.65 \times 10^{-27}$kg.

The identity of the roton is still controversial. In the original idea of Feynman, roton was considered as the rotational motion around a vortex ring with an atomic-scale radius. Noziéres [58] later proposed that roton might be a precursor mode of solidification. In this context, roton modes are studied in dipolar BECs in which the gas may spontaneously obtain a discretized symmetry due to their long-distance dipolar interactions [59–67].

The energy of the thermal excitations decreases with the superfluid velocity $\boldsymbol{v}_s$ and becomes negative below a critical superfluid velocity, making He II unstable. At $T = 0$ K, the energy spectrum with the superfluid velocity v_s is given by

$$\mathcal{E}' = \mathcal{E} + \boldsymbol{p} \cdot \boldsymbol{v}_s, \tag{1.98}$$

where $\mathcal{E}$ is the energy spectrum at $v_s = 0$. The superfluid becomes unstable when $\mathcal{E}' < 0$, and the critical speed v_c is calculated as

$$v_c = \min\left(\frac{\mathcal{E}}{\hbar k}\right). \tag{1.99}$$

The minimum value of $\mathcal{E}/\hbar k$ is given at the roton minimum, and the critical velocity is $v_c \approx 60$ m/s.

1.3.4 Capillary Wave: Ripplon

Another type of wave propagates along a free surface of He II, similar to a capillary wave, known as a ripplon [49]. Defining that the z-axis is the perpendicular direction to the liquid surface and the displacement from the equilibrium height in the z-direction is denoted by $\zeta(x, y)$, the flux, entropy, and surface force equations across the surface are given by

$$\rho_s v_{s,z} + \rho_n v_{n,z} - \rho\frac{\partial\zeta}{\partial t} = 0, \tag{1.100}$$

$$v_{n,z} - \frac{\partial\zeta}{\partial t} = 0, \tag{1.101}$$

$$p - \sigma_\zeta\left(\frac{\partial^2}{\partial x^2} + \frac{\partial^2}{\partial y^2}\right)\zeta = 0, \tag{1.102}$$

where σ_ζ is the surface tension [48]. Equations 1.100 and 1.101 show that the velocities of both components in the z-direction are equal to the surface velocity (i.e., $v_{n,z} = v_{s,z} = \partial\zeta/\partial t$)[8].

In the following, the flow is supposed to be incompressible ($\boldsymbol{\nabla}\cdot\boldsymbol{v} = 0$) and irrotational ($\boldsymbol{v} = \boldsymbol{\nabla}\phi_R$ with the velocity potential ϕ_R). Also, the temperature is assumed to be low enough so that evaporation is negligible. The Hamiltonian of the ripplon system is then given by [68–70]

$$\begin{aligned}\mathcal{H} = {} & \frac{\rho_0}{2}\int dS\int_{-\infty}^{\zeta} dz v^2 + \frac{\rho_0 g}{2}\int dS\zeta^2 \\ & + \sigma_\zeta\int dS\left[\left(1 + \left(\frac{\partial\zeta}{\partial x}\right)^2 + \left(\frac{\partial\zeta}{\partial y}\right)^2\right)^{1/2} - 1\right].\end{aligned} \tag{1.104}$$

The displacement ζ may be expanded by the Fourier series as

$$\zeta(\boldsymbol{r}) = \sum_{\boldsymbol{k}}\check{\zeta}(\boldsymbol{k})e^{i\boldsymbol{k}\cdot\boldsymbol{r}}. \tag{1.105}$$

[8] For ripplons propagating along a helium film where the normal fluid component may not flow (i.e., $\boldsymbol{v}_s = \boldsymbol{0}$), Equation 1.100 is modified as

$$\rho_s v_{s,z} - \rho\frac{\partial\zeta}{\partial t} = 0. \tag{1.103}$$

Such waves are called the third sound wave. It is worth noting that the spatial varying of the fraction ρ_n/ρ_s causes local evaporation and condensation and may dampen the ripplon at finite temperatures.

where the wave vector $\boldsymbol{k}$ is restricted in the $x-y$ plane on the helium surface. Similarly, from the incompressible and irrotational conditions $\nabla^2\phi_R = 0$, the flow potential ϕ_R may be expanded as

$$\phi_R(\boldsymbol{r}) \;=\; \sum_{\boldsymbol{k}} \check{\phi}_R(\boldsymbol{k}) e^{i\boldsymbol{k}\cdot\boldsymbol{r}} e^{qz}. \tag{1.106}$$

By considering up to the third order with the small quantities ζ and ϕ_R, the Hamiltonian may be written as $\mathcal{H} = \mathcal{H}_0 + \mathcal{H}_1$ where

$$\mathcal{H}_0 \;=\; \frac{\rho_0}{2}\sum_{\boldsymbol{k}} k\left|\check{\phi}(\boldsymbol{k})\right|^2 + \frac{1}{2}\sum_{\boldsymbol{k}}\left(\sigma_\zeta k^2 + \rho_0 g\right)\left|\check{\zeta}(\boldsymbol{k})\right|^2 \tag{1.107}$$

$$\mathcal{H}_1 \;=\; \frac{\rho_0}{2}\sum_{\boldsymbol{k},\boldsymbol{k}'}\left(kk' - \boldsymbol{k}\cdot\boldsymbol{k}'\right)\check{\phi}_R(\boldsymbol{k})\check{\zeta}(-\boldsymbol{k}-\boldsymbol{k}')\check{\phi}(\boldsymbol{k}'). \tag{1.108}$$

We may quantize the Hamiltonian $\mathcal{H}$ by introducing the canonical commutation relations with ϕ_R and ζ [49, 68, 70] as

$$\left[\hat{\zeta}(\boldsymbol{k}), \hat{\phi}_R(\boldsymbol{k}')\right] = \frac{i\hbar}{\rho_0}\delta(\boldsymbol{k}-\boldsymbol{k}'). \tag{1.109}$$

Defining a characteristic dispersion relationship

$$\omega_0(k) = \sqrt{\frac{\sigma_\zeta}{\rho_0}k^3 + gk} \tag{1.110}$$

and Bosonic creation and annihilation operators

$$\hat{a}(\boldsymbol{k}) := \sqrt{\frac{\rho_0\omega_0}{2\hbar k}}\left[\hat{\zeta}(\boldsymbol{k}) + i\frac{k}{\omega_0(k)}\hat{\phi}(-\boldsymbol{k})\right] \tag{1.111}$$

$$\hat{a}^\dagger(\boldsymbol{k}) := \sqrt{\frac{\rho_0\omega_0}{2\hbar k}}\left[\hat{\zeta}(-\boldsymbol{k}) - i\frac{k}{\omega_0(k)}\hat{\phi}(\boldsymbol{k})\right], \tag{1.112}$$

the Hamiltonians $\mathcal{H}_0$ and $\mathcal{H}_1$ can be simplified as

$$\mathcal{H}_0 \;=\; \sum_{\boldsymbol{k}}\hbar\omega_0(k)\left[\hat{a}^\dagger(\boldsymbol{k})\hat{a}(\boldsymbol{k}) + \frac{1}{2}\right] \tag{1.113}$$

$$\mathcal{H}_1 \;=\; \sum_{\boldsymbol{k},\boldsymbol{k}'}\Lambda_R(\boldsymbol{k},\boldsymbol{k}')\left[\hat{a}(\boldsymbol{k}) - \hat{a}^\dagger(-\boldsymbol{k})\right]\left[\boldsymbol{a}(-\boldsymbol{k}-\boldsymbol{k}') + \boldsymbol{a}^\dagger(\boldsymbol{k}+\boldsymbol{k}')\right]\left[\hat{a}(\boldsymbol{k}') - \hat{a}^\dagger(-\boldsymbol{k}')\right] \tag{1.114}$$

with

$$\Lambda_R(\boldsymbol{k},\boldsymbol{k}') = \frac{1}{2}\left[\frac{\boldsymbol{k}\cdot\boldsymbol{k}'}{qq'} - 1\right]\sqrt{\frac{\hbar^3\omega_0(k)\omega_0(k')}{8\rho_0\omega_0(|\boldsymbol{k}+\boldsymbol{k}'|)}kk'\,|\boldsymbol{k}+\boldsymbol{k}'|}. \tag{1.115}$$

$\mathcal{H}_0$ corresponds to the unperturbed oscillation of ripplons with energy $\hbar\omega_0(k)$, and $\mathcal{H}_1$ shows the scattering among ripplons. We emphasize that ripplon and the first sound wave are different excitations. For example, we may assume incompressibility to find ripplon, whereas compressibility is not negligible for the first sound wave.

1.4 Turbulence

Our main subject is turbulence in quantum fluids, and this section introduces the theory of classical turbulence. It is known that the flows $\boldsymbol{v}$ in incompressible viscous classical fluids (i.e., $\boldsymbol{\nabla} \cdot \boldsymbol{v} = 0$) are well described by the Navier–Stokes equation [4]:

$$\frac{\partial v_i}{\partial t} + (\boldsymbol{v} \cdot \boldsymbol{\nabla}) v_i = -\frac{1}{\rho}\frac{\partial p}{\partial x_i} + \frac{1}{\rho}\frac{\partial \tau_{ij}}{\partial x_j} \tag{1.116}$$

$$\tau_{ij} := \rho\nu \left[\frac{\partial v_i}{\partial x_j} + \frac{\partial v_j}{\partial x_i}\right] \tag{1.117}$$

where p is the pressure, ρ is the density, ν is the kinematic viscosity, and τ_{ij} is the stress tensor. Due to the similarity of the equation, the flow is characterized by a non-dimensional quantity called the Reynolds number:

$$Re := \frac{UL}{\nu} \tag{1.118}$$

where U and L are the characteristic speed and length of the flow, respectively. At small Reynolds numbers (e.g., $Re < 1.70 \times 10^3$ [4]), the flow has high symmetry and is known as laminar flow. However, at high Reynolds numbers (e.g., $Re > 1.70 \times 10^3$), the flow causes instability and loses its symmetries, resulting in turbulence.

Turbulent flows are characterized by their chaotic nature, making them unpredictable and lacking repeatability. Nevertheless, the averaged quantities in turbulent flows have high symmetries, and hence the statistical quantities are critical for understanding the physics of turbulence. Statistical theory in homogeneous isotropic turbulence in the steady state has been successfully developed, with the Kolmogorov scale being a significant milestone [71, 72]. It is important to note that isotropy guarantees homogeneity but not necessarily vice versa.

From the Navier–Stokes equation (Equation 1.116) with the Dirichlet boundary condition (i.e., $\boldsymbol{u} = 0$ on the boundary), the conservation equation of the kinematic energy per unit volume is derived as

$$\begin{aligned}
\frac{d}{dt}\int \frac{1}{2}v^2 dV_u &= -\int \left(\frac{1}{2}\frac{\partial v_i v_j v_j}{\partial x_i} + \frac{1}{\rho} v_i \frac{\partial p}{\partial x_i}\right) dV_u + \nu \int v_i \nabla^2 v_i dV_u \\
&= -\frac{\nu}{2}\int \left(\frac{\partial v_i}{\partial x_j} + \frac{\partial u_j}{\partial x_i}\right)^2 dV_u \\
&= -\nu \int |\omega|^2 \, dV_u \qquad (1.119) \\
&=: -\int \epsilon_d(\boldsymbol{r}, t) dV_u =: -\bar{\epsilon}_d \qquad (1.120)
\end{aligned}$$

where the integral is taken in the unit volume V_u, and $\bar{\epsilon}_d$ is called the energy dissipation rate per unit volume.

1.4.1 Time-Averaged Navier–Stokes Equations

There are three methods of average a quantity $A(\boldsymbol{r}, t)$ that varies in space and time:

- Time average involves integrating the quantity over a period of time T_{ave} as $\int_t^{t+T_{\text{ave}}} A(\boldsymbol{r}, t)dt$.
- Spatial average involves integrating the quantity over a volume V_{ave} as $\int A(\boldsymbol{r}, t)dV_{\text{ave}}$.
- Ensemble average involves taking the average of a number of samples N_{ave} as $\frac{1}{N_{\text{ave}}} \sum_{j=1}^{N_{\text{ave}}} A_j(\boldsymbol{r}, t)$, where A_j indicates the quantity of the j-th sample.

It is known that these methods provide identical results in static and homogeneous turbulence when the number of samples N_{ave}, sampling time T_{ave}, and sampling space V_{ave} are large enough.

In turbulence theories, the velocity is usually decomposed as

$$\boldsymbol{v} = \bar{\boldsymbol{v}} + \boldsymbol{u} \tag{1.121}$$

where $\bar{\boldsymbol{v}}$ is the time-averaged velocity and $\boldsymbol{u}$ is the velocity fluctuation, whose average is zero (i.e., $\bar{\boldsymbol{u}} = 0$). The Navier–Stokes equation (Equation 1.116) can be time-averaged as

$$(\bar{\boldsymbol{v}} \cdot \boldsymbol{\nabla})\bar{v}_i = -\frac{1}{\rho}\frac{\partial \bar{p}}{\partial x_i} + \frac{1}{\rho}\frac{\partial}{\partial x_j}\left[\bar{\tau}_{ij} - \rho\overline{v_i v_j}\right]. \tag{1.122}$$

This averaged equation cannot be fully solved by the averaged quantities of the same order because it is not closed due to the additional stresses $-\rho\overline{v_i v_j} =: \tau_{ij}^R$, which are called Reynolds stresses and correspond to the mean momentum fluxes induced by the turbulence. This problem is general for averaged turbulence equations and is known as the closure problem [73]. Phenomenological equations are necessary to close the equations and are dependent on the configuration and problems to be solved [74].

1.4.2 Kolmogorov 1941

In 1941, Kolmogorov [71, 72] established important statistical laws, called the K41 theory, from the following two hypotheses of similarity:

1. When the Raynolds number Re is sufficiently high, the statistical quantities are uniquely determined by the scale length $l = 2\pi/k$, the kinematic viscosity ν, and the energy dissipation rate $\bar{\epsilon}_d$.

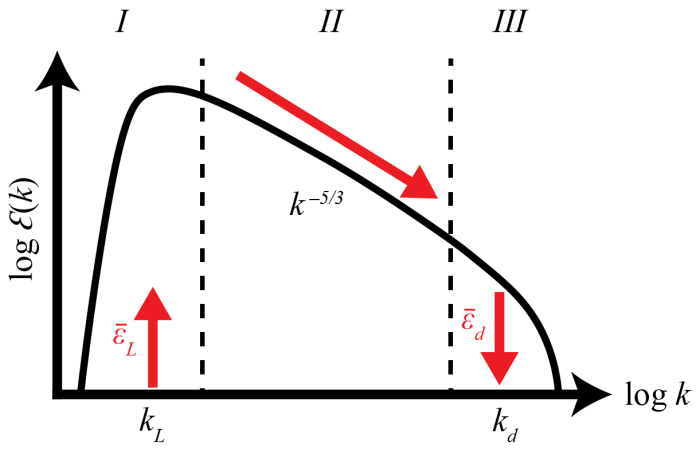

Figure 1.6: Schematic of the energy spectrum in three-dimensional turbulence. The ranges I, II, and III are the energy-containing range, the inertial range, and the dissipation range, respectively.

2. At the scale much larger than the Kolmogorov length $l_K = \left(\nu^3/\bar{\epsilon}\right)^{1/4}$, the statistical quantities are uniquely determined by the scale l and the energy dissipation rate $\bar{\epsilon}_d$ and do not depend on the kinematic viscosity ν.

From the first hypothesis, the energy spectrum in a system of the size L^3 is written as

$$\mathcal{E}(k) = \bar{\epsilon}_d^{1/4}\nu^{5/4} f(k/k_K), \qquad (k_L \ll k, \qquad k_L := 2\pi/L) \tag{1.123}$$

where $k_K := 2\pi/l_K$ is the Kolmogorov wave number and f is a non-dimensional function. Then, applying the second hypothesis, we obtain

$$\mathcal{E}(k) = K\bar{\epsilon}_d^{2/3}k^{-5/3}, \qquad (k_L \ll k \ll k_K), \tag{1.124}$$

where K is a universal constant called the Kolmogorov constant and estimated as $K = 1.62 \pm 0.17$ by experiments [75]. The energy spectrum is proportional to $k^{-5/3}$ in the inertial range ($k_L \ll k \ll k_K$). This scaling law is called the Kolmogorov scaling (Figure 1.6) and agrees with various experiments, but this theory still has some issues. Firstly, the intermittency observed in experiments does not agree with the results predicted by the K41. According to the K41 theory, the p-th order normalized structure function

$$K_p(\boldsymbol{r}) := \frac{\langle |u(\boldsymbol{x}+\boldsymbol{r}) - u(\boldsymbol{x})|^p \rangle}{\langle |u(\boldsymbol{x}+\boldsymbol{r}) - u(\boldsymbol{x})|^2 \rangle^{p/2}} \tag{1.125}$$

is constant, but experiments show that K_p increases with L/r and p [76]. Secondly, the K41 theory ignores the fluctuation of the energy dissipation ϵ_d and considers only the mean value $\bar{\epsilon}_d$ [48]. In

1962, Kolmogorov proposed a revised theory assuming a spatial fluctuation of a lognormal distribution [77], and the theory describes the low-order structure functions. However, this assumption has many issues (e.g., [78–80]) and modeling ϵ_d is still a challenging problem. The behavior of ϵ_d depends on the system, and we cannot simply apply the Navier–Stokes equations to model the general behavior of ϵ_d because the Navier–Stokes equations ignore the thermal fluctuation and cannot describe the dissipation range well (e.g., in gas turbulence [81]).

1.4.3 Two-Dimensional Turbulence

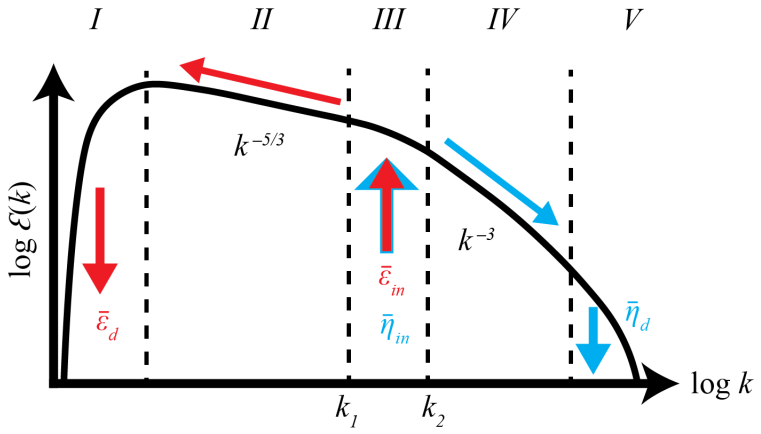

Figure 1.7: Schematic of the energy spectrum in two-dimensional turbulence. The ranges I and V are the dissipation ranges. The ranges II and IV are the inertial ranges. The range III is the energy-containing range.

The K41 theory is rooted in the conservation of energy cascades in k-space, which renders it independent of the system's dimension. In 2D turbulence, the enstrophy per unit volume

$$G := \int \frac{\omega^2}{2} dV_u \tag{1.126}$$

is similarly conserved in the non-viscous range as

$$\frac{dG}{dt} = \frac{d}{dt}\int \frac{\omega^2}{2} dV_u \tag{1.127}$$

$$= -\nu \int |\boldsymbol{\nabla} \times \boldsymbol{\omega}|^2 \, dV_u$$

$$=: -\int \eta_d(\boldsymbol{r}, t) dV_u =: -\bar{\eta}_d, \tag{1.128}$$

where η_d is the enstrophy dissipation rate per volume. A similar energy spectrum for the enstrophy is then obtained as

$$\mathcal{E}(k) = K' \bar{\eta}_d^{2/3} k^{-3}. \qquad (k_L \ll k \ll k_K) \tag{1.129}$$

The above results indicate the existence of the double cascades in 2D turbulence (Figure 1.7), but the directions of these cascades are still unknown at this stage. The following discusses the directions [82]. When comparing two energy spectra of quantities $A(k)$ and $B(k)$, the spectral equations can be expressed as:

$$\frac{\partial A}{\partial t} + \frac{\partial \Pi_A(k)}{\partial k} = -D_A(k) + F_A(k) \tag{1.130}$$

$$\frac{\partial B}{\partial t} + \frac{\partial \Pi_B(k)}{\partial k} = -D_B(k) + F_B(k), \tag{1.131}$$

where $P_A(k)$ and $P_B(k)$ are the fluxes, $D_A(k)$ and $D_B(k)$ are the (positive) dissipation terms, and $F_A(k)$ and $F_B(k)$ are the forcing terms. The forcing spectra are supposed to be confined to a narrow range as

$$F_A(k) = F_B(k) = 0, \qquad \forall k \in (0, k_1) \cup (k_2, \infty). \tag{1.132}$$

Furthermore, since the spectra $A(k)$ and $B(k)$ satisfy a relation: $B(k) = L_{\text{Leith}}(k)A(k)$, and we obtain

$$\frac{\partial \Pi_B(k)}{\partial k} = L_{\text{Leith}}(k) \frac{\partial \Pi_A(k)}{\partial k}, \tag{1.133}$$

which relation is called Leith constraint [83]. The time derivative term is ignored to study the steady state. By integrating Equations 1.130, 1.131, and 1.133, we obtain

$$\begin{aligned} \Pi_A(k) &= \int_k^\infty \left[D_A(k') - F_A(k')\right] dk' \\ &= -\int_0^k \left[D_A(k') - F_A(k')\right] dk' \end{aligned} \tag{1.134}$$

$$\begin{aligned} \Pi_B(k) &= \int_k^\infty \left[D_B(k') - F_B(k')\right] dk' \\ &= \int_k^\infty L_{\text{Leith}}(k') \left[D_A(k') - F_A(k')\right] dk' \\ &= -\int_0^k L_{\text{Leith}}(k') \left[D_A(k') - F_A(k')\right] dk', \end{aligned} \tag{1.135}$$

which show

$$\Pi_A(k) > 0 \quad \text{and} \quad \Pi_B(k) > 0, \qquad \forall k \in (k_2, +\infty) \tag{1.136}$$

$$\Pi_A(k) < 0 \quad \text{and} \quad \Pi_B(k) < 0, \qquad \forall k \in (0, k_1), \tag{1.137}$$

meaning that both fluxes flow downward in the range *II* and upward in the range *III* in Figure 1.7. However, experiments have demonstrated that the energy cascade occurs in the range *II*, and the

enstrophy cascade appears in the range III. The following shows that this observation is because the energy flux is dominant in the range II, but the enstrophy flux is in the range III.

From the Leith constraint (Equation 1.133), we obtain

$$\begin{aligned}
\Pi_A(k) &= \int_k^\infty \frac{1}{L_{\rm Leith}(k')} \frac{\partial \Pi_B(k')}{\partial k'} dk' \\
&= L_{\rm Leith}^{-1}(k)\Pi_B(k) - \int_k^\infty L_{\rm Leith}^{-2}(k') \frac{dL_{\rm Leith}(k')}{dk'} \Pi_B(k') dk' \qquad (1.138) \\
\Pi_B(k) &= \int_0^k L_{\rm Leith}(k') \frac{\partial \Pi_A(k')}{\partial k'} dk' \\
&= L_{\rm Leith}(k)\Pi_A(k) - \int_0^k \frac{dL_{\rm Leith}(k')}{dk'} dk', \qquad (1.139)
\end{aligned}$$

and then,

$$\begin{aligned}
\int_0^k \frac{dL_{\rm Leith}(k')}{dk'} \Pi_A(k') dk' &= L_{\rm Leith}(k)\Pi_A(k) - \Pi_B(k) \\
&= \int_k^\infty \left[L_{\rm Leith}(k) - L_{\rm Leith}(k')\right] \left[D_A(k') - F_A(k')\right] dk' \\
&< 0 \qquad \forall k \in (k_2, \infty) \qquad (1.140) \\
\int_k^\infty L_{\rm Leith}^{-2}(k') \frac{dL_{\rm Leith}(k')}{dk'} \Pi_B(k') dk' &= -\frac{L_{\rm Leith}(k)\Pi_A(k) - \Pi_B(k)}{L_{\rm Leith}(k)} \\
&= L_{\rm Leith}^{-1}(k) \int_0^k \left[L_{\rm Leith}(k) - L_{\rm Leith}(k')\right] \left[D_A(k') - F_A(k')\right] dk' \\
&> 0 \qquad \forall k \in (0, k_1) \qquad (1.141)
\end{aligned}$$

because the coefficient $L_{\rm Leith}(k) - L_{\rm Leith}(k')$ is positive in $0 < k' < k_1$ and negative in $k_2 < k' < +\infty$ [9]. In 2D turbulence, the Leith function is $L_{\rm Leith}(k) = k^2$ and $A(k)$ and $B(k)$ correspond to the kinetic energy $E(k)$ and the enstrophy $G(k)$, respectively. We then obtain

$$\int_0^k \frac{dL_{\rm Leith}(k')}{dk'} \Pi_A(k') dk' = 2 \int_0^k k'^1 \Pi_A(k') dk' < 0 \qquad \forall k \in (k_2, \infty) \quad (1.143)$$

$$\int_k^\infty L_{\rm Leith}^{-2}(k') \frac{dL_{\rm Leith}(k')}{dk'} \Pi_B(k') dk' = 2 \int_k^\infty k'^{-3} \Pi_B(k') dk' > 0. \qquad \forall k \in (0, k_1) \quad (1.144)$$

According to Equation 1.143, the integral of the flux Π_A with a weight function having a large value in the high-k range becomes negative, meaning that the kinetic energy tends to cascade into low-k modes. Similarly, from Equation 1.144, the integral of the flux Π_B with a weight function having a large value in the low-k range becomes positive, meaning that the enstrophy tends to cascade into high-k modes.

[9] You may find an inequality

$$L_{\rm Leith}(k)\Pi_A(k) - \Pi_B(k) < 0, \qquad \forall k \in (0, k_1) \cup (k_2, +\infty) \qquad (1.142)$$

which is called the Danilov inequality [84].

1.4.4 Anisotropic Turbulence

In 1935, Taylor proposed isotropic turbulence, where statistical averages of functions of velocity and its derivatives are invariant to axis rotation [85]. This assumption allows great simplification of the statistical theory and is usually justified at small scales. However, anisotropy of flows at large scales may remain at small scales [86–90]. Furthermore, thermal counterflow turbulence in He II may spontaneously obtain anisotropy, as discussed later. Therefore, turbulence theories for anisotropic flows are needed [91].

1.4.5 Quantum Turbulence

QT is turbulent flows in quantum fluids (e.g., superfluid helium and atomic BEC) [10]. It is known that vortices play a critical role in turbulence [4]. In classical turbulence, vortices have wide core sizes, and the circulation may become of any real value. On the other hand, in QT, vortices have an identical circulation with a tiny core size; therefore, it is theoretically easier to discuss turbulence in quantum fluids than in classical fluids.

1.5 Thermal Counterflow Turbulence in Superfluid Helium-4

The study of turbulence in He II often employs the thermal counterflow involving the normal fluid carrying the heat away from the heat source while the superfluid flows in the opposite direction to conserve the total mass. Supposed the velocity is one-dimensional in the direction from the heater to the helium bath $\hat{x}$, the speed of the normal and superfluid components are given by

$$v_n = \frac{W}{\rho s T} \tag{1.145}$$

$$v_s = -\frac{\rho_n}{\rho_s} v_n, \tag{1.146}$$

where W is the injected heat flux. Then, the relative speed is written as

$$v_{ns} := v_n - v_s = \frac{W}{\rho_s s T}. \tag{1.147}$$

When the relative speed is small enough and both flows are laminar, the velocity equations (Equations 1.83 and 1.84) are written as

$$\mathbf{0} = -\frac{\rho_s}{\rho}\boldsymbol{\nabla} p + \rho_s s \boldsymbol{\nabla} T - \boldsymbol{F}_{ns} \tag{1.148}$$

$$\mathbf{0} = -\frac{\rho_n}{\rho}\boldsymbol{\nabla} p - \rho_s s \boldsymbol{\nabla} T + \boldsymbol{F}_{ns} + \eta_n \nabla^2 \boldsymbol{v}_n. \tag{1.149}$$

[10] QT in superfluid helium-3 is also studied, e.g., [92].

By combining these two equations, we obtain:

$$\mathbf{0} = -\boldsymbol{\nabla} p + \eta_n \nabla^2 \boldsymbol{v}_n. \tag{1.150}$$

Supposed that the flow is one-dimensional in the $\hat{x}$ direction in a circular pipe of the radius R, the velocity is obtained as

$$u_x(r) = \frac{1}{4\eta_n} \frac{dp}{dx} \left(R^2 - r^2\right) \tag{1.151}$$

which is called the Hagen–Poiseuille flow [48].

On the other hand, when the relative speed between the two fluid components exceeds a small critical value, turbulence is generated in the superfluid as a tangle of quantized vortex lines even though the normal fluid flow is laminar, which is called the T-1 turbulent state [50]. Once the relative speed exceeds the second critical value, the normal fluid component also becomes turbulent, which is called the T-II turbulent state [93–95]. These vortex lines all have identical cores with a thickness of about 1Å, each carrying a single quantum of circulation $\kappa = h/m_4$. Despite tremendous progress in studying counterflow turbulence, unsolved problems remain and require careful consideration.

1.5.1 Vortex Dynamics

When a cylinder with circulation Γ is placed in a flow $\boldsymbol{v}_\infty$, it experiences a lift force $\rho \boldsymbol{v}_\infty \times \Gamma$ which is known as the Magnus effect. H. E. Hall and W. F. Vinen [96] introduced a Magnus force for the quantized vortex in a similar manner. Considering a vortex segment located at $\boldsymbol{s}$ and moving with the velocity $\boldsymbol{v}_L$, the Magnus force is written as

$$\boldsymbol{f}_{\mathrm{M}} = \rho_s \kappa \boldsymbol{s}' \times (\boldsymbol{v}_L - \boldsymbol{v}_{\mathrm{sl}}) \tag{1.152}$$

where $\boldsymbol{v}_{\mathrm{sl}}$ is the local superfluid velocity and $\boldsymbol{s}' := \partial \boldsymbol{s} / \partial \xi_v$ is the derivative of $\boldsymbol{s}$ with the arc length along the vortex line ξ_v. The mutual friction $\boldsymbol{F}_{ns}$ is believed to occur due to roton-like collisions above 1K. Hence, the drag force $\boldsymbol{f}_{\mathrm{D}}$ may be approximated as

$$\boldsymbol{f}_{\mathrm{D}} = -\alpha \rho_s \kappa \boldsymbol{s}' \times \left[\boldsymbol{s}' \times (\boldsymbol{v}_n - \boldsymbol{v}_{\mathrm{sl}})\right] - \alpha' \rho_s \kappa \boldsymbol{s}' \times (\boldsymbol{v}_n - \boldsymbol{v}_{\mathrm{sl}}), \tag{1.153}$$

where α and α' are the temperature-dependent parameters.

It is known that the effective mass of a quantized vortex is fairly small [26, 48], and the inertia of the vortex core should be negligible. As a result, the total force acting on a vortex segment should be balanced as:

$$\boldsymbol{f}_{\mathrm{D}} + \boldsymbol{f}_{\mathrm{M}} = \rho_s \kappa \boldsymbol{s}' \times \left[(\boldsymbol{v}_L - \boldsymbol{v}_{\mathrm{sl}}) - \alpha \boldsymbol{s}' \times (\boldsymbol{v}_n - \boldsymbol{v}_{\mathrm{sl}}) - \alpha' (\boldsymbol{v}_n - \boldsymbol{v}_{\mathrm{sl}})\right] = 0. \tag{1.154}$$

We then obtain

$$\boldsymbol{v}_L = \boldsymbol{v}_{\rm sl} + \alpha \boldsymbol{s}' \times (\boldsymbol{v}_n - \boldsymbol{v}_{\rm sl}) - \alpha' \boldsymbol{s}' \times \left[\boldsymbol{s}' \times (\boldsymbol{v}_n - \boldsymbol{v}_{\rm sl})\right]. \tag{1.155}$$

This equation is employed to describe the motion of the quantized vortices in three-dimensional He II.

1.5.2 Energy Dissipation in Superfluid Component

The normal fluid energy dissipates to thermal energy by viscosity. However, this is not the case in superfluids, where viscosity is absent. Instead, energy loss may be caused in counterflow turbulence mostly due to the Kelvin waves emission on the order of the inter vortex distance scale $l = \mathcal{L}^{-1/2}$ [97, 98]. The energy loss rate can be approximated by $\nu_s \kappa^2 \mathcal{L}^2$ with an effective viscosity denoted as ν_s. The effective viscosity is roughly of order κ [99] and can be incorporated into the equation of $\boldsymbol{v}_s$ (Equation 1.83) as

$$\begin{aligned} \frac{\partial \boldsymbol{v}_s}{\partial t} &= -\frac{1}{\rho}\boldsymbol{\nabla} p + s\boldsymbol{\nabla} T + \nu_s \nabla^2 \boldsymbol{v}_s \\ &\quad + \frac{\rho_n}{2\rho}\nabla \left(\boldsymbol{v}_n - \boldsymbol{v}_s\right)^2 - \frac{1}{\rho_s}\boldsymbol{F}_{ns}. \end{aligned} \tag{1.156}$$

1.5.3 Vinen Equation

In principle, we can model counterflow turbulence by numerically tracking quantized vortices' movements using Equation 1.155. However, this approach demands significant computational resources and becomes impractical with high VLD. Vinen proposed a time-evolution equation of the averaged VLD $\mathcal{L}$ by using dimensional analysis [51, 100–102]. Firstly, such an equation should be expressed as

$$\frac{d\mathcal{L}}{dt} = \mathcal{G} + \mathcal{D} \tag{1.157}$$

where $\mathcal{G}$ and $\mathcal{D}$ denote the generation and decay terms, respectively. Since the mutual friction increases VLD, the terms should consist of the mutual speed $V_{ns} := |\boldsymbol{v}_n - \boldsymbol{v}_s|$ and the averaged VLD $\mathcal{L}$. Then, the generation term formula is given by

$$\mathcal{G} = \chi_1 \alpha V_{ns} \mathcal{L}^{3/2} \tag{1.158}$$

where χ_1 is a non-dimensional const of order unity. On the opposite, the vortex reconnection causes the dissipation of VLD $\mathcal{L}$. The typical time scale of the vortex collision is l/v_s, and each collision

dissipates the energy of the order of v_s^2. The velocity v_s induced by a vortex tangle of the length scale l is roughly $v_s \approx \kappa/2\pi l$. Therefore, the dissipation term $\mathcal{D} \approx v_s^3/l$ can be expressed as

$$\mathcal{D} = -\chi_2 \frac{\kappa}{2\pi} \mathcal{L}^2 \tag{1.159}$$

where χ_2 is a non-dimensional constant of order unity. Thus, the time evolution equation can be written as

$$\frac{d\mathcal{L}}{dt} = \chi_1 \alpha V_{ns} \mathcal{L}^{3/2} - \chi_2 \frac{\kappa}{2\pi} \mathcal{L}^2 \tag{1.160}$$

which is called the Vinen equation.

In the steady state $d\mathcal{L}/dt = 0$, the averaged VLD is given by

$$\mathcal{L}^{1/2} = \gamma V_{ns}, \tag{1.161}$$

$$\gamma := \frac{2\pi}{\kappa} \frac{\alpha \chi_1}{\chi_2}. \tag{1.162}$$

This result shows that the averaged VLD at the steady state $\mathcal{L}$ is proportional to the square of the counterflow velocity V_{ns}, which has been confirmed by many experiments.

1.5.4 Mutual Friction

To close the HVBK equations, the formula of $\boldsymbol{F}_{ns}$ is needed. Gorter and Mellink [103] proposed an empirical formula in thermal counterflow turbulence of He II as

$$\bar{\boldsymbol{F}}_{ns} = A_{\mathrm{GM}} \rho_n \rho_s \bar{v}_{ns}^2 \bar{\boldsymbol{v}}_{ns}, \tag{1.163}$$

where $\boldsymbol{v}_{ns} := \boldsymbol{v}_n - \boldsymbol{v}_s$, A_{GM} is the Gorter–Mellink coefficient depending on the temperature and tube shape, and the notation of bar ($\bar{}$) means averaging. Vinen later modified it as

$$\bar{\boldsymbol{F}}_{ns} = \alpha \rho_s \kappa \mathcal{L} \bar{\boldsymbol{v}_{ns}}, \tag{1.164}$$

where $\alpha(T)$ is a temperature-dependent parameter [104] and $\mathcal{L}$ is the averaged vortex line density (VLD), i.e., length of vortices per unit volume. The above equations are about the averaged mutual friction $\bar{F}_{ns}$, but the local force formula F_{ns} is still under discussion. So far, the well-accepted formula is [105, 106]

$$\boldsymbol{F}_{ns} = \alpha \rho_s \kappa \mathcal{L} \boldsymbol{v}_{ns}, \tag{1.165}$$

which is the natural extension of Equation 1.164. In rotating He II, all vortices are polarized in the direction of the vorticity; hence the averaged VLD may be expressed as $\mathcal{L} = |\boldsymbol{\nabla} \times \boldsymbol{v}_s| / \kappa$. The mutual friction force F_{ns} is important for the counterflow turbulence in He II, and we will discuss the details later.

CHAPTER 2

ANGULAR MOMENTUM TRANSFER DURING MERGING OF ROTATING BOSE–EINSTEIN CONDENSATES

Vortices play a critical role in turbulence, and rotational motion is usually associated with vortices [4, 48]. Angular momentum conservation can cause exciting effects in the rotating fluid systems, for example, eddies in the ocean flow [107] and accretion discs [108, 109]. The merging of rotating classical drops leads to the Kelvin-Helmholtz instability generating spiral vortices at the interface [110]. The viscous shear stress then transfers the angular momentum in classical fluids [48]. On the other hand, quantum fluids have no viscosity and have a wave property that may lead the merging to wave interference. Therefore, the corresponding mechanism is little known.

The merging dynamics of isolated BECs have been a comprehensive topic including matter-wave interferometry [111–114], nonlinear quantum hydrodynamics [115, 116], galactic dark matter [117], superfluid helium droplet [118–120], and the creation of quantized vortices [121–123] or dark solitons [124–126]. Past studies mainly research BEC merging in the context of the Kibble–Zurek mechanism [127–130], which describes the formation of phase defects (e.g., quantized vortex in BECs) following the merging of isolated condensates with random phases during a rapid second-order phase transition [131,132]. Such past studies assumed static condensates with uniform phases. However, if the BEC has a vortex, velocity and phase gradient exist. We have conducted two-dimensional (2D) and three-dimensional (3D) GP simulations to study how the angular momentum is transferred from the initially rotating condensate to the initially static condensate. This chapter summarizes our published works regarding the BEC merging [1, 2, 133]. Our 2D simulations of concentric condensates show the emergence of a spiral dark soliton having a sharp endpoint in the merging process. We have revealed that this endpoint behaves like a fractional vortex [134, 135] and can induce angular momentum transfer even without quantized vortices. Furthermore, our 3D simulations present that rapid angular momentum transfer accompanies a corkscrew-shaped soliton-like structure at the interface of the two BECs. This transfer does not need fluid advection or shift of quantized vortices. Instead, the solitonic corkscrew can exert a torque that directly

creates or annihilates angular momentum in BECs. To understand this fascinating dynamic, we have systematically studied the merging process under various conditions in 2D and 3D spaces.

2.1 Two-Dimensional Merging

2.1.1 Method

Two-Dimensional Gross–Pitaevskii Equation. In the long cylindrical potential [136] or the pancake-shaped potential [137], we may approximate the system as a 2D system. The following briefly discusses the derivation of the 2D GP equation in those two cases.

In the cylindrical potential, we may assume translational symmetry in the z-direction and ignore the z-dependence. The GP equation may be written as

$$i\hbar\frac{\partial\psi(x,y;t)}{\partial t} = \left[-\frac{\hbar^2}{2m}\nabla_{\rm 2D}^2 + U(x,y;t) + U_0|\psi(x,y;t)|^2 - \mu\right]\psi(x,y;t). \tag{2.1}$$

where $\nabla_{\rm 2D}^2 = \frac{\partial^2}{\partial x^2} + \frac{\partial^2}{\partial y^2}$.

In the pancake-shaped potential

$$\begin{aligned} U(x,y,z;t) &= \frac{1}{2}m\left[\omega_\perp^2\left(x^2+y^2\right) + \omega_z^2 z^2\right] \\ &= U_{\rm 2D}(x,y) + U_z(z), \end{aligned} \tag{2.2}$$

the excitation in the z-direction is negligible, and the wave function may be approximated as $\psi(x,y,z;t) = \psi_{\rm 2D}(x,y;t)Z(z)$ where Z is the ground state in the z-direction and is normalized as $\int |Z|^2 dz = 1$. By taking an integral with z, we may rewrite the GP equation (Equation 1.64) into the 2D formula as

$$\begin{aligned} i\hbar\frac{\partial\psi_{\rm 2D}}{\partial t}Z &= -\frac{\hbar^2}{2m}\left[Z\nabla_{\rm 2D}^2\psi_{\rm 2D} + \psi_{\rm 2D}\frac{\partial^2 Z}{\partial z^2}\right] \\ &\quad + \left[U_{\rm 2D}(x,y) + U_z(z) + U_0|\psi_{\rm 2D}|^2|Z|^2 - \mu\right]\psi_{\rm 2D}Z \end{aligned} \tag{2.3}$$

$$\begin{aligned} \rightarrow i\hbar\frac{\partial\psi_{\rm 2D}}{\partial t} &= -\frac{\hbar^2}{2m}\nabla_{\rm 2D}^2\psi_{\rm 2D} + \left[U_{\rm 2D}(x,y;t) + U_0\left(\int |Z|^4 dz\right)|\psi_{\rm 2D}|^2\right]\psi_{\rm 2D} \\ &\quad + \left[\frac{\hbar^2}{2m}\int\left|\frac{\partial Z}{\partial z}\right|^2 dz + \int U_z(z)|Z|^2 dz - \mu\right]\psi_{\rm 2D} \\ &= \left[-\frac{\hbar^2}{2m}\nabla_{\rm 2D}^2 + U_{\rm 2D}(x,y) + U_{0,\rm 2D}|\psi_{\rm 2D}|^2 - \mu_{\rm 2D}\right]\psi_{\rm 2D} \end{aligned} \tag{2.4}$$

where

$$U_{0,\rm 2D} = U_0\int |Z|^4 dz, \tag{2.5}$$

$$\mu_{\rm 2D} = \mu - \frac{\hbar^2}{2m}\int\left|\frac{\partial Z}{\partial z}\right|^2 dz - \int U_z(z)|Z|^2 dz. \tag{2.6}$$

The coherent length (Equation 1.66) is then expressed as

$$\xi = \sqrt{\frac{\hbar^2}{2m\mu_{2D}}} \tag{2.7}$$

where $\mu_{2D} = U_{0,2D} n_{0,2D}$ and $n_{0,2D}$ is the bulk density of the 2D wave function ψ_{2D}. The Equations 2.1 and 2.4 are the 2D GP equations. In this section, we omit the notation of '2D' as

$$i\hbar \frac{\partial \psi}{\partial t} = \left[-\frac{\hbar^2}{2m}\nabla^2 + U(x,y) + U_0|\psi|^2 - \mu \right] \psi. \tag{2.8}$$

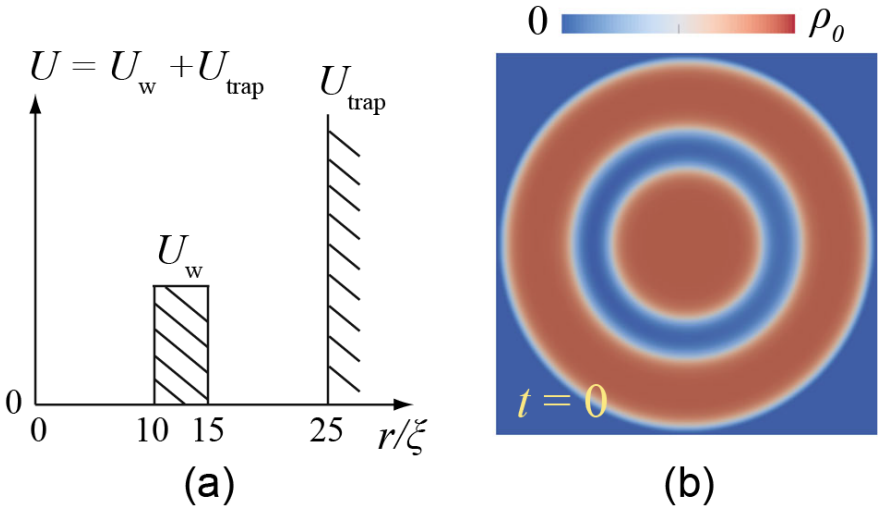

Figure 2.1: (a) Schematic of the potential $U(r,t)$ for the 2D GPE simulation. (b) The initial density profile of the condensates in the absence of rotational motion in the condensates. Adapted from Figure 1 in T. Kanai et al. [1]

Configuration for Numerical Simulation. To observe the merging dynamics of two concentric BECs with different rotational velocities in 2D space, we set the potential $U = U_{\text{trap}} + U_w$, where U_{trap} represents the cylindrical-shaped box potential trapping the condensates, and U_w is the coaxial barrier separating the ring and disk condensates (Figure 2.1a). We set the radius of U_{trap} as 25ξ because the range of typical condensate sizes in real experiments is about $10\xi - 10^2\xi$ [122, 130, 138, 139]. The potential barrier U_{w} has a square shape with a width of 5ξ in the radial direction and has a height in the range of $\mu - 10\mu$, where the typical values in the past experiments are in the range of $\mu - 10^2\mu$ [121, 130, 138–141].

We use a computational region $\mathbf{r} \in [-25\xi, 25\xi] \times [-25\xi, 25\xi]$ with a mesh grid of 500×500 nodes for our simulations. The time step is $\Delta t = 10^{-4}\tau$, where τ is the characteristic time of the sound

speed defined by

$$\tau = \frac{\hbar}{\mu}. \tag{2.9}$$

Figure 2.1b shows a typical initial density profile of static BECs. We introduce rotational motion by printing a phase on the wave function and apply the imaginary time propagation method to prepare the initial state (Section 1.2.3). The circulation associated with the supercurrent can be any integer m multiplied by the quantum circulation $\kappa = h/m$. At $t = 0$, we suddenly remove the energy barrier U_{w} and let the two condensates merge. The dynamical evolution of the condensate wavefunction during merging can be obtained by numerically integrating the GP equation (Equation 2.8) using an implicit method in an alternating direction [142].

2.1.2 Simulation Results

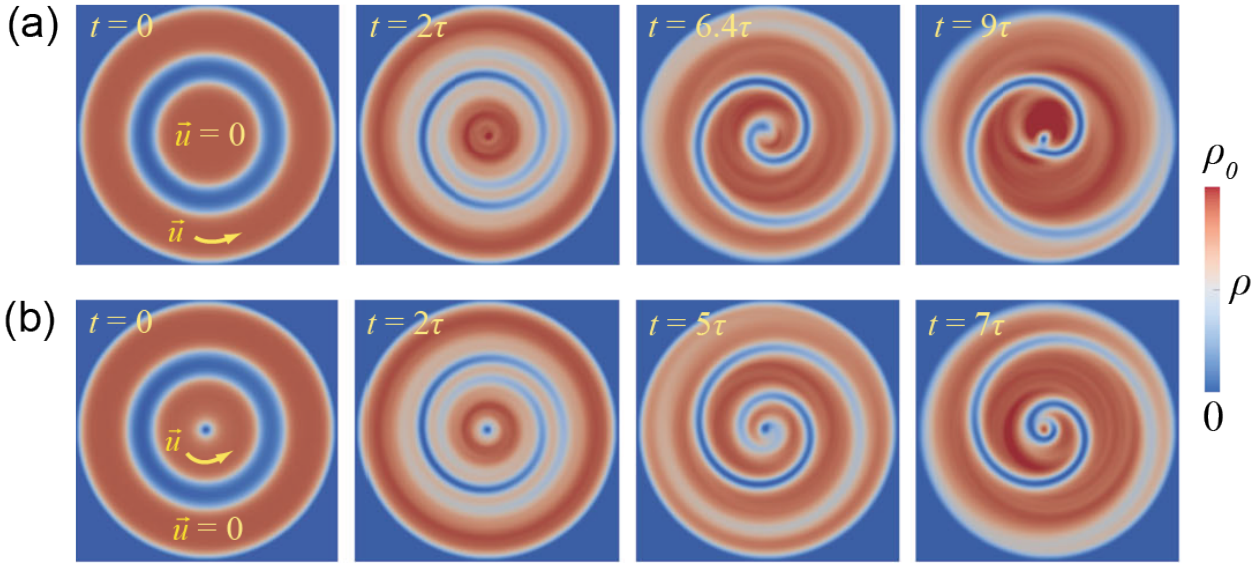

Figure 2.2: Representative snapshots showing the time evolution of the BEC density ρ for $U_{\mathrm{w}} = \mu$. Here $\rho_0 = 8 \times 10^{-4}\xi^{-2}$. (a) The initial state is a static inner disk condensate with a rotating outer ring condensate carrying a circulation of κ. (b) The initial state is a static outer ring condensate with a rotating inner disk condensate having a single vortex point at the center. Adapted from Figures 2 and 3 in T. Kanai et al. [1]

Figure 2.2 shows representative images of the time evolution of the condensate density $\rho = |\psi|^2$ with $U_{\mathrm{w}} = \mu$. Figure 2.2a shows the case that the inner disk condensate is static and the outer ring condensate rotates with a circulation of κ at $t = 0$. Figure 2.2b is for the case in that the outer disk condensate is static and the inner ring condensate rotates with a circulation of κ containing a single vortex point at the center at $t = 0$. A spiral stripe characterized by a depleted condensate

density appears in both scenarios. Across this stripe, there is an abrupt phase step $\Delta\phi$. This stripe corresponds to a gray soliton, similar to the ring gray solitons observed during the expansion of 2D disks and annular condensates [124–126]. Since the soliton velocity is controlled by the phase step $\Delta\phi$ as Equation 1.79, a dark soliton with complete density depletion (i.e., $\rho = 0$ at the center) has $\Delta\phi = \pi$ and zero soliton velocity with a thickness on the order of ξ. When $\Delta\phi$ decreases, the soliton becomes wider and shallower, increasing its velocity. At the dark soliton point ($\Delta\phi = \pi$), the relative phase between the inner and the outer condensates changes sign. The soliton then develops two ends, with one end spiraling in and the other extending out. The difference in the chirality of the spiral solitons between those cases reflects the distinction of the relative phase winding between the two condensates.

The spiral soliton stripe has an exciting interaction with quantized vortex points. Firstly, besides the actual vortices, the endpoint of the phase branch-cut behaves as a phase vortex with a phase winding of 2π around it but does not induce rotational flow. The soliton stripe rapidly evolves a sharp inner end spiraling toward the center in the condensate. In the case of Figure 2.2a, as the sharp inner end of the soliton stripe approaches the center, snake instability occurs where the local curvature radius of the inner end becomes comparable to ξ [122,138,139], resulting in the nucleation of a quantized vortex near the center. In Figure 2.2b, as the inner end of the soliton stripe approaches the center, the vortex point merges with the soliton stripe, resulting in a vortex-free condensate. This vortex-free structure can be observed in Figure 2.11b, specifically at $t = 7\tau$. During the long-term evolution, the solitons in both cases eventually decay into quantized vortices via snake instability.

Effect of Potential Barrier Height. We examine the effect of the potential barrier height U_{w} in the condensate merging dynamics. Figure 2.3 shows representative pictures of the time evolution of the condensate density with $U_{\mathrm{w}} = 10\mu$. By comparing the soliton profiles in the snapshots for $U_{\mathrm{w}} = \mu$ (Figure 2.2) and $U_{\mathrm{w}} = 10\mu$ (Figure 2.3), it is apparent that the spiral soliton develops a sharp inner endpoint that spirals toward the condensate center in both cases. Here the length of the soliton stripe is longer for $U_{\mathrm{w}} = 10\mu$ than that for $U_{\mathrm{w}} = \mu$. This result is likely due to the steep drop in the initial condensate density in the potential barrier area for the $U_{\mathrm{w}} = 10\mu$ case. This significant density gradient provides more potential energy for the soliton formation once U_{w} is removed.

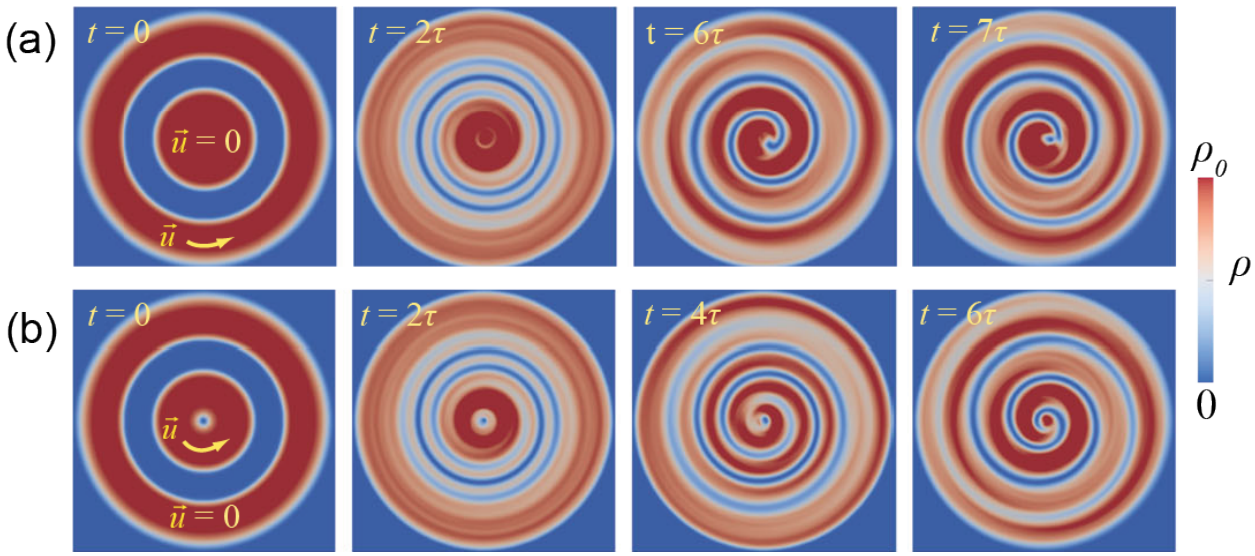

Figure 2.3: Representative snapshots showing the time evolution of the BEC density ρ for $U_{\rm w} = 10\mu$. Here $\rho_0 = 8 \times 10^{-4}\xi^{-2}$. (a) The initial state is a static inner disk condensate with a rotating outer ring condensate carrying a circulation of κ. (b) The initial state is a static outer ring condensate with a rotating inner disk condensate having a single vortex point at the center. Adapted from Figures 2 and 3 in T. Kanai et al. [1]

Angular Momentum Transfer. To analyze the transfer of the rotational motion, we calculate the angular momentum density per particle defined as

$$L_z(\mathbf{r}, t) = \frac{1}{N}\left(\psi^* \hat{L}_z \psi\right). \tag{2.10}$$

For example, Figure 2.4a shows some snapshots of the condensate density, phase, and angular momentum of the case in Figure 2.2a. The angular momentum initially contained in the outer condensate can spread to the internal condensate along the spiral channel formed by the soliton stripe. Interestingly, quantized vortices are absent during this angular momentum transfer while conserving the total angular momentum. An intriguing observation becomes apparent by closely analyzing the depicted flow in Figure 2.4a. The counterclockwise direction of the flow within the initially rotating condensate prevents it from entering the outward spiral channel created by the soliton. Consequently, the rotational movement observed in the initially stationary disk condensate must be triggered by an alternative mechanism that operates independently of quantized vortices.

We have identified this novel mechanism as due to the rotational flow induced by the sharp endpoint of the spiral soliton. As depicted in Figure 2.4a, due to the phase change across the boundary of the soliton, the sharp inner endpoint has a phase winding of $\Delta\phi$ around it. This phase

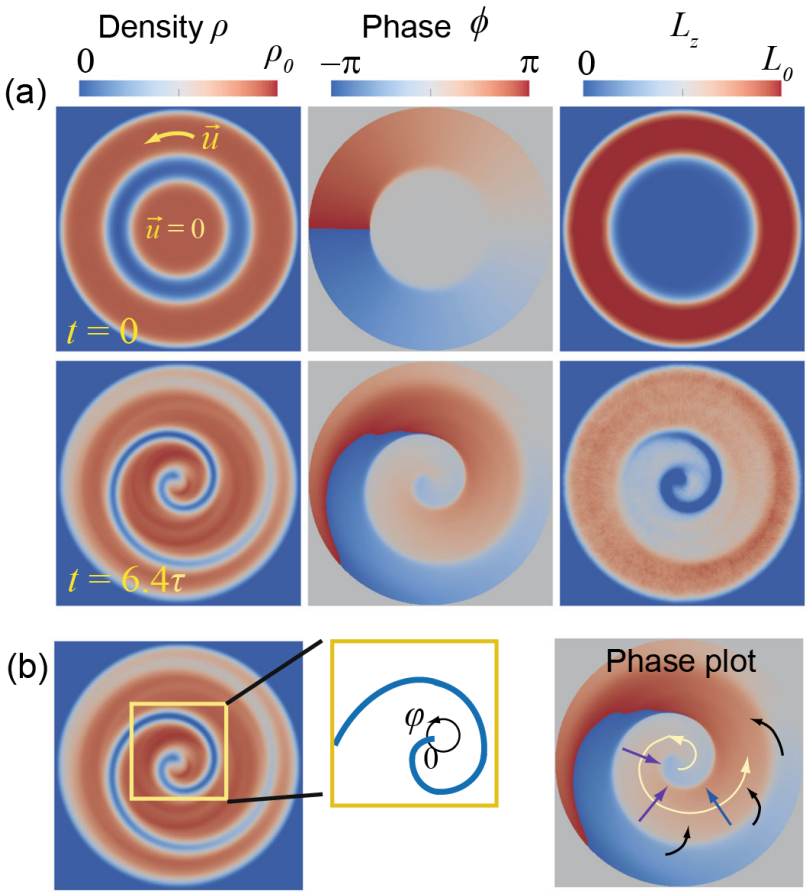

Figure 2.4: (a) Snapshots of the condensate density, phase, and angular momentum density L_z for the case shown in Figure 2.2a. Here $\rho_0 = 8 \times 10^{-4}\xi^{-2}$ and $L_0 = 7 \times 10^{-4}m/\tau$. (b) Schematics illustrating the underlying mechanism for the mass and angular momentum transfer. Adapted from Figure 4 in T. Kanai et al. [1]

winding leads to a rotational motion in the condensate, making the sharp endpoint effectively a 'vortex point' that carries a fraction of a quantized circulation given by $\kappa\Delta\phi/2\pi$. It is essential to highlight that the circulation, which is the integral of velocity along a closed contour around the endpoint, remains zero due to the presence of opposite phase velocities within the soliton's density-depleted region. The motion induced by the endpoint results in mass transportation within the condensate from the inner to the outer region, guided by the spiral channel. Consequently, a phase increases along the boundary of the soliton. This phase increment generates a radial phase gradient within the condensate, which in turn drives an inward flow of mass. In the shallow section of the soliton stripe, where the condensate density is not depleted, there is a significant mass flow from the outer region through the soliton boundary towards the inner part. This mechanism results

in the establishment of a mass circulation that effectively mixes the condensates and facilitates the transport of angular momentum.

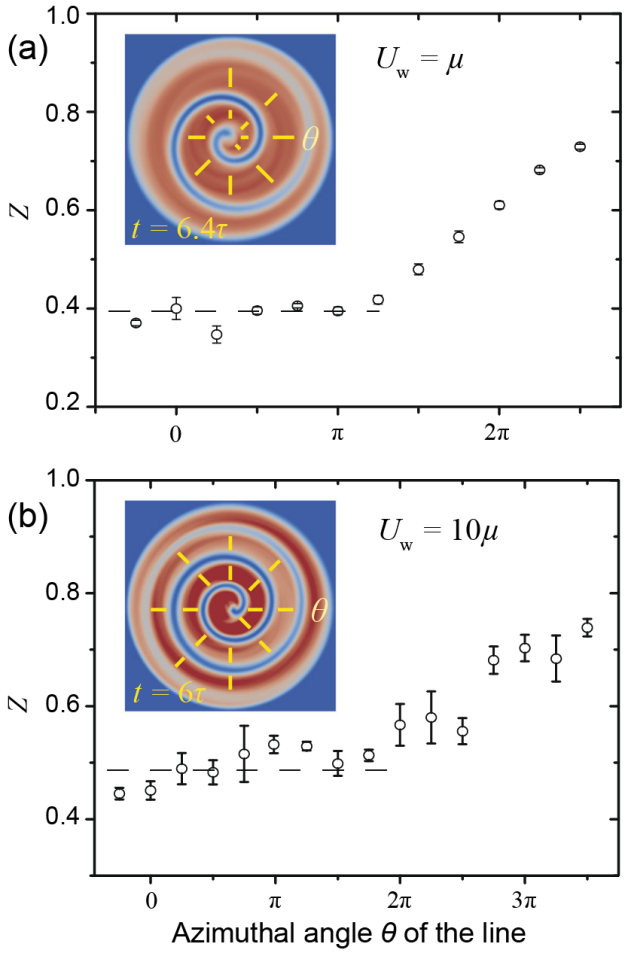

Figure 2.5: Calculated vortex charge Z in the condensate along the radial lines represented by the solid yellow lines shown in the inset for (a) $U_w = \mu$ and (b) $U_w = 10\mu$. Adapted from Figure 5 in T. Kanai et al. [1]

To show that the inner endpoint behaves like a fractional vortex point, we introduce a vortex charge parameter Z, defined as $Z = \frac{m}{\hbar}|r \times v(r)| = \frac{m}{\hbar} r v_\theta$, where v_θ is the velocity along the azimuth angle direction. When a vortex point is located at the center, Z is a constant and equals the winding number of the vortex. Figure 2.5 shows the calculated Z values along some radial lines in the condensate when the inner endpoint of the spiral soliton is located around the center. Near the endpoint around the center, the Z values are nearly 0.4 for the $U_w = \mu$ case and nearly 0.48 for the $U_w = 10\mu$ case, which matches well with the measured phase step across the soliton boundary near the inner endpoint (i.e., $\Delta\phi \simeq 0.8\pi$ for $U_w = \mu$ and $\Delta\phi \simeq 0.95\pi$ for $U_w = 10\mu$). In the tail

part of the soliton line, there are palpable mass flows across the soliton boundary from the outer region. Then Z increases toward one, which is expected for the flow in the initial ring condensate.

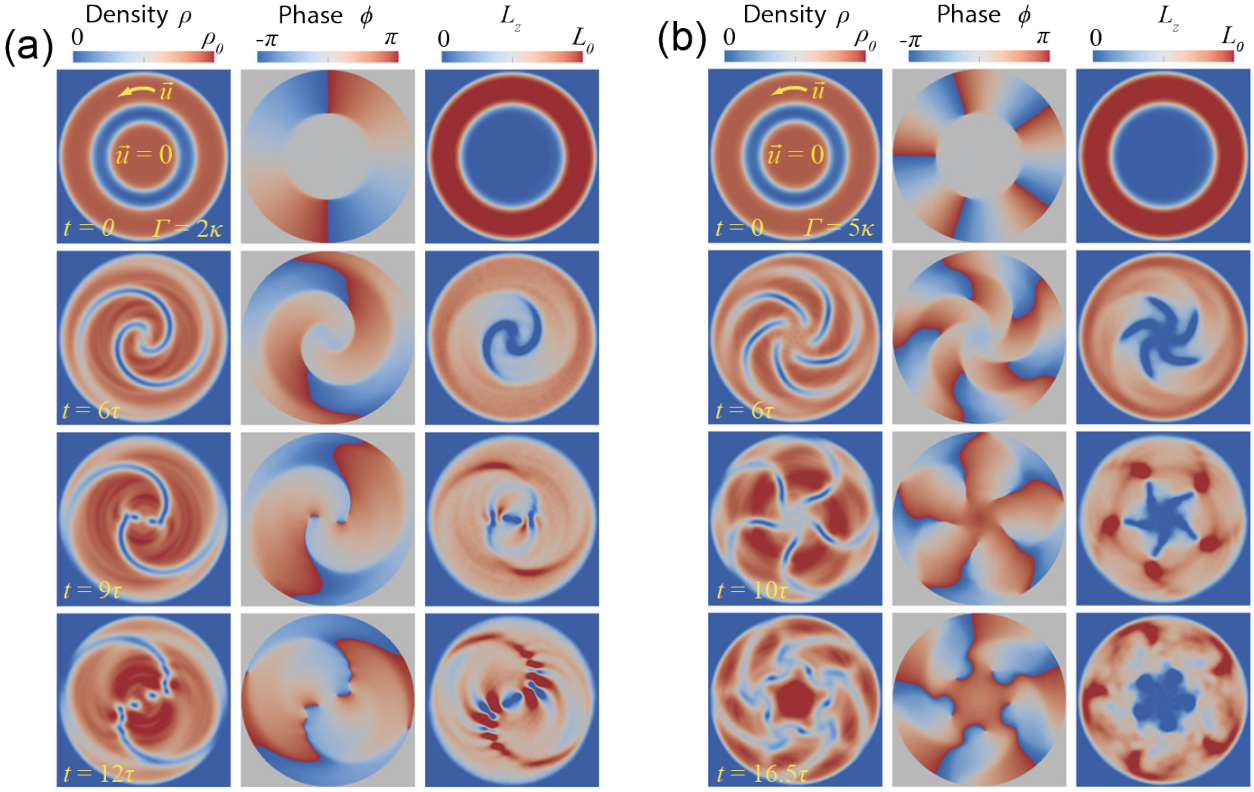

Figure 2.6: Time evolution of the condensate density ρ, phase ϕ, and angular momentum density L_z when the static inner disk condensate merges with the rotating outer ring condensate that carries a circulation of (a) 2κ and (b) 5κ. The potential barrier $U_{\rm w} = \mu$. The maximum angular momentum L_0 is (a) $1.4 \times 10^{-3} m/\tau$ and (b) $3.5 \times 10^{-3} m/\tau$. Adapted from Figure 6 in T. Kanai et al. [1]

Multiple Quantum Circulation Cases. We have also investigated the merging dynamics between a stationary inner disk condensate and a rotating outer ring condensate with an axially symmetric supercurrent with multiple quantum circulations. Figure 2.6 shows typical snapshots of the time evolution of ρ, ϕ, and L_z for the outer ring condensate having a circulation of 2κ (in Figure 2.6a) and 5κ (in Figure 2.6b) with $U_{\rm w} = \mu$. Notably, multiple spiral dark solitons are observed in these cases, where the number of soliton stripes matches the flow's winding number, equivalent to the number of quantum circulations present in the initial ring condensate. Similar to the mechanism discussed in the previous section, each soliton develops a sharp inner endpoint that induces rotational motion in the initially static disk condensate, facilitating angular momentum

transfer. As the local curvature radius near the inner ends of the solitons decreases, vortex points detach from the inner ends of the solitons. It is important to note that when multiple soliton stripes and vortices are present in the condensate, the flow field becomes highly complex. The flows induced by neighboring solitons and vortices can significantly influence soliton stripes. As a result, snake instability occurs more quickly, breaking the inner ends of the solitons into segments and vortices as shown in Figure 2.6a at $t = 12\tau$. In both cases presented in Figure 2.6, the net vorticity, considering both positive and negative vortices, in the condensate always matches the quantum circulation number in the initial outer ring condensate. Additionally, we have conducted tests where a static outer ring condensate merges with a rotating inner disk condensate with multiple vortex points. Similarly, spiral solitons emerge during the merging process, and the number of soliton stripes corresponds to the number of vortices initially present in the disk condensate. It appears that the formation of spiral soliton stripes during condensate merging is determined by the relative winding number (i.e., relative circulation) between the two condensates. The underlying mechanism responsible for this exciting soliton formation process shall be discussed in Section 2.2.3.

Merging of Condensates with Constant Phase Difference. The previous subsection presents the observations indicating that the relative winding number between the disk and the ring condensates determines the number of spiral solitons. Consequently, one may wonder about the outcome when the two condensates merge from an initial configuration without any relative motion. One might expect that no spiral soliton should emerge in this situation. We have examined two representative scenarios, as depicted in Figure 2.7. The first case (Figure 2.7a) involves merging a static ring condensate with a static disk condensate. The second case (Figure 2.7b) entails merging a rotating ring condensate with a corotating disk condensate containing a single quantized vortex point at the center. In both cases, ring-shaped dark solitons are created at the interface between the two condensates following merging. These gray ring solitons undergo expansion in radius, bounce from the trap boundary, and then shrink towards the center of the condensate. This expansion-shrinking cycle can occur many times. This observed soliton behavior is similar to the formation and propagation of planar solitons observed during the merging of 3D condensates with constant phase differences [143]. Over time, fluctuations in the simulation accumulate, leading to snake instability. In both cases, the ring solitons finally break up into vortex pairs (e.g., see Figure 2.7a at $t = 40\tau$ and Figure 2.7b at $t = 32\tau$). One notable distinction between the ring solitons and the spiral solitons described earlier is that the spiral solitons possess distinct inner endpoints that

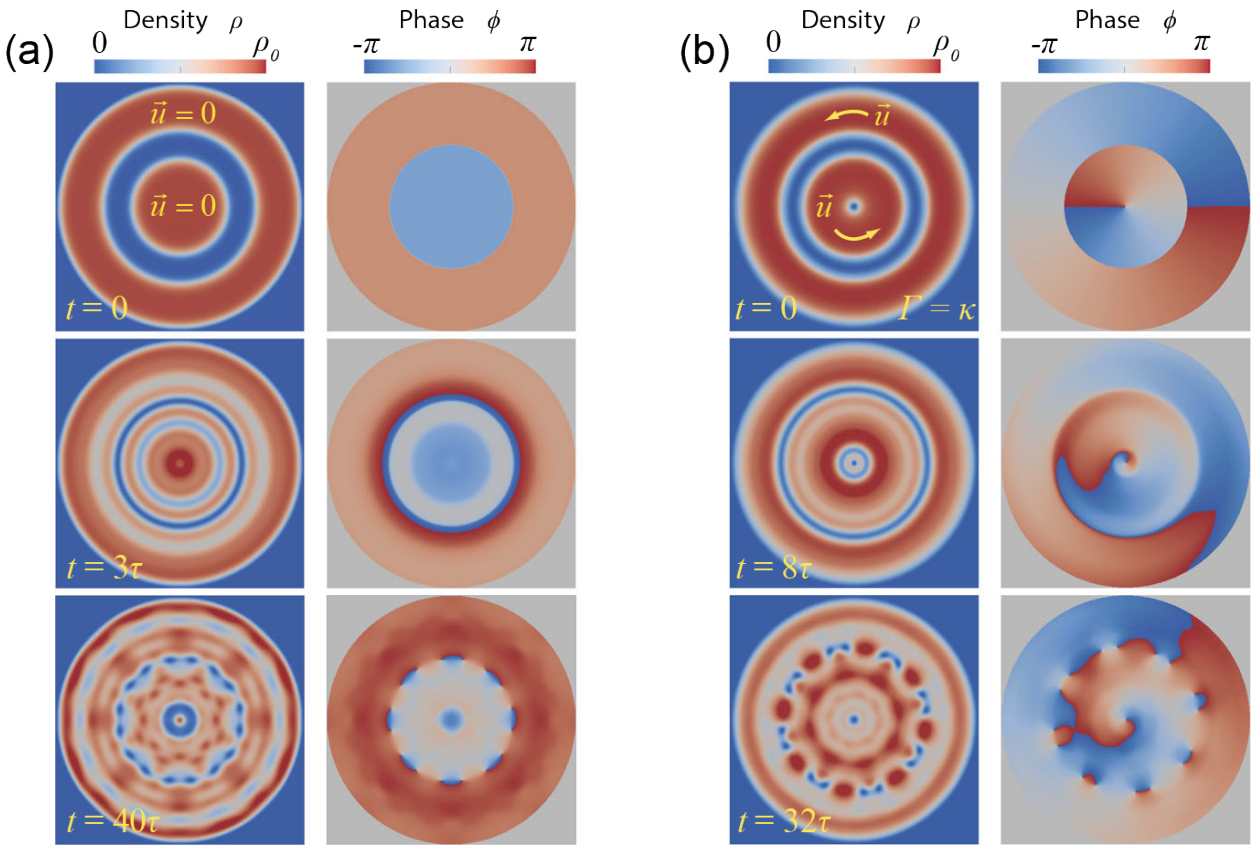

Figure 2.7: Time evolution of the BEC density ρ and phase ϕ when the initial phase difference between the ring and the disk condensates is constant across their interface with the potential barrier $U_{\rm w} = \mu$. (a) Both condensates are initially static. (b) The rotating ring condensate carries a circulation of κ merging with a corotating disk condensate with a single charged quantized vortex point at the center. Adapted from Figure 7 in T. Kanai et al. [1]

can induce rotational motion, resembling vortices, within the condensate. These sharp endpoints enable angular momentum transfer between the two regions of the condensate. However, when the two condensates are static or exhibit corotation without relative motion, the angular momentum transfer between them becomes unnecessary. Consequently, the ring solitons remain unbroken, unlike the spiral shape soliton. It is important to emphasize that while soliton formation during the merging of condensates is a well-known phenomenon, the current simulation has confirmed a crucial point: it is the relative motion between the condensates before merging that triggers the breaking of solitons and the development of sharp endpoints. This novel characteristic of solitons would not have been observed in earlier simulation studies that focused on condensate merging with uniform phases or no relative motion.

2.1.3 Discussion

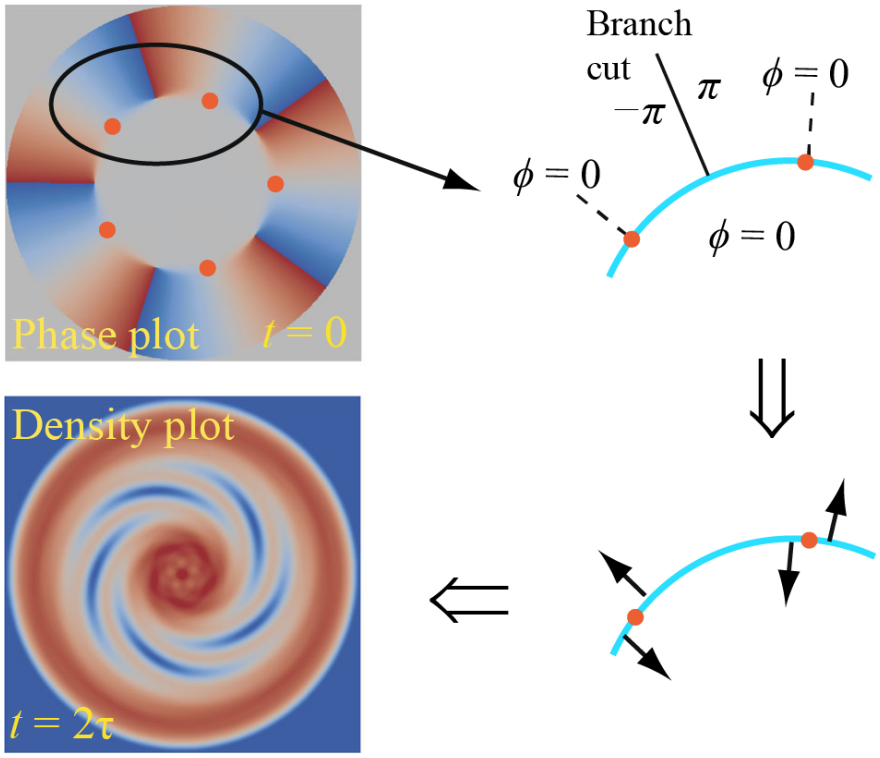

Figure 2.8: Schematics illustrating the underlying mechanism on how a soliton at the interface of the two BEC domains breaks up and develops multiple spiral stripes. Adapted from Figure 8 in T. Kanai et al. [1]

The simulation results explained in the previous sections provide valuable insights into understanding the formation of spiral solitons with the exact number of soliton stripes matching the relative winding number of the two condensates. As an illustration, we can examine the phase profile at the initial time ($t = 0$) for the scenario in which the outer ring condensate possesses a supercurrent with a circulation of 5κ, as depicted in Figure 2.8. The inner disk condensate initially has a constant phase (i.e., $\phi = 0$), while the phase in the outer ring condensate progressively increases in the counter-clockwise direction between the branch-cut lines. Consequently, the phase difference $\Delta\phi$ across the interface between the two condensates varies along the interface. Notably, there are five points (highlighted as red dots in the schematics) across which the phase difference $\Delta\phi$ changes sign. It is worth noting that, as seen from Equation 1.79, a soliton stripe moves in the opposite direction to the phase step $\Delta\phi$ across the soliton boundary. For a soliton stripe created at the interface between the ring and the disk condensates, the stripe on either side of a red dot

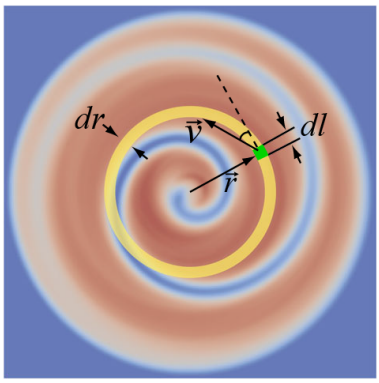

Figure 2.9: Schematic for estimating the angular momentum density possessed by the merged condensate in the axially symmetric trap. Adapted from Figure 9 in T. Kanai et al. [1]

tends to move in opposite directions due to the change in sign of the phase step, breaking up the stripe at these locations. Notably, the breakup of the soliton stripe occurs concurrently with its formation. Consequently, instead of witnessing the formation of a complete ring soliton followed by its subsequent breakup into five pieces, what transpires is the gradual development of five soliton stripes that possess two ends, with one end spiraling inward and the other end extending outward. Our simulation results demonstrate that quantized vortices are unnecessary for angular momentum transfer in the merged condensate in the axially symmetric potential trap. This observation may appear counterintuitive; therefore, we want to clarify the relevant concepts below.

Considering the angular momentum held by the ring part between r and $r + dr$ as shown in the yellow ring in Figure 2.9, it can be calculated as

$$dL_z(r) = \int \left[\hat{e}_z \cdot (\mathbf{r} \times \mathbf{v})\right] \rho dl dr = r dr \left[\oint \rho d\mathbf{l} \cdot \mathbf{v}\right], \tag{2.11}$$

where the integral is taken only with $d\mathbf{l}$. In a highly incompressible quantum fluid, the integral in the square brackets in Equation 2.11 reduces to $\rho\Gamma$, where ρ is the density and Γ is the circulation along the closed ring, which equals the quantum circulation κ multiplied by the number of quantized vortices inside the enclosed area. If there is no vortex in the condensate, the angular momentum contained in the yellow ring area in Figure 2.9 should be zero. Repeating this procedure for all concentric rings in the axially symmetric condensate, one can find that the incompressible condensate cannot hold finite angular momentum without quantized vortices. However, highly compressible superfluids may evolve with time and can have spatially non-uniform density, letting the integral in Equation 2.4 have non-zero, even when the circulation Γ is zero. For our case in

Figure 2.9, most of the yellow ring carries a flow with a tangential velocity in the counterclockwise direction. On the other hand, the velocity of the yellow ring segment inside the soliton is clockwise because the phase gradient is opposite. Consequently, when integrating the velocity along the entire ring, the contributions cancel out while the circulation is zero. Nevertheless, since the condensate density is nearly depleted in the soliton region but remains finite in the rest part of the ring, the integral in the square brackets in Equation 2.4 for calculating angular momentum is finite.

2.2 Three-Dimensional Merging

2.2.1 Method

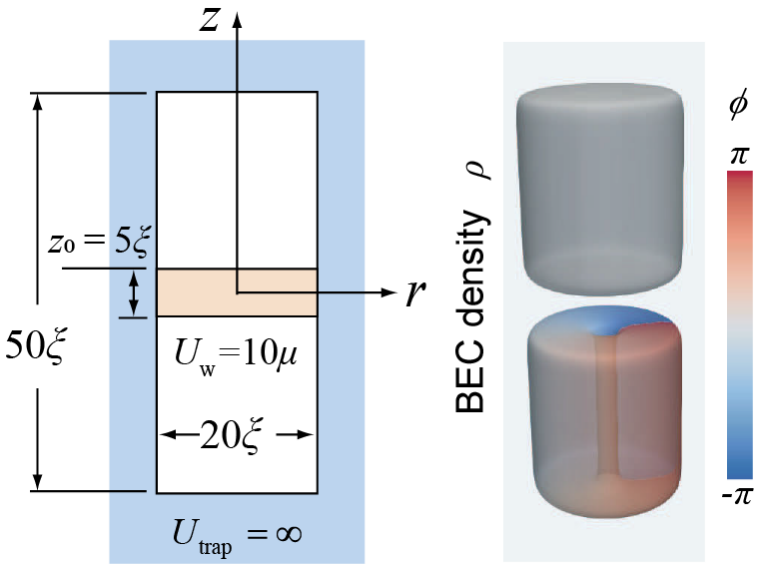

Figure 2.10: (a) Schematic of the potential $U(\mathbf{r})$ used in our three-dimensional GP simulation. (b) Initial profile of the BEC density and phase with a single vortex line at the center in the lower condensate. The density isosurface corresponds to 50% of the bulk density. Adapted from Figure 1 in T. Kanai et al. [2]

Configuration for Numerical Simulation. To investigate the merging of BECs along the rotational axis, we examine two cylindrical BECs that have the same size and are aligned along the z-axis. This arrangement is achieved by the external potential $U = U_{\text{trap}} + U_{\text{w}}$, where U_{trap} denotes a cylindrical hard-wall box potential to trap the condensates and U_{w} represents the potential separating the two BECs from each other, as shown in Figure 2.10a. The hard-wall potential U_{trap} has a length of 50ξ and a diameter of 20ξ. The potential U_{w} is located at the center of the hard-wall trap with a thickness $z_0 = 5\xi$ and has a uniform height of $U_{\text{w}} = 10\mu$. The imaginary time method

in Section 1.2.3 prepares the initial state. Each condensate may have quantized vortex lines in it. Figure 2.10b shows an example of the initial condensate density profile having a single vortex line at the center in the lower part. We then instantaneously remove the energy barrier U_{w} at $t = 0$, allowing the two condensates to merge. The time evolution of the condensate wave function can be obtained by numerically integrating the GP equation (Equation 1.64) with spatial steps $\Delta x = \Delta y = \Delta z = 0.2\xi$ and a time step $\Delta t = 4 \times 10^{-5}\tau$.

2.2.2 Simulation Results

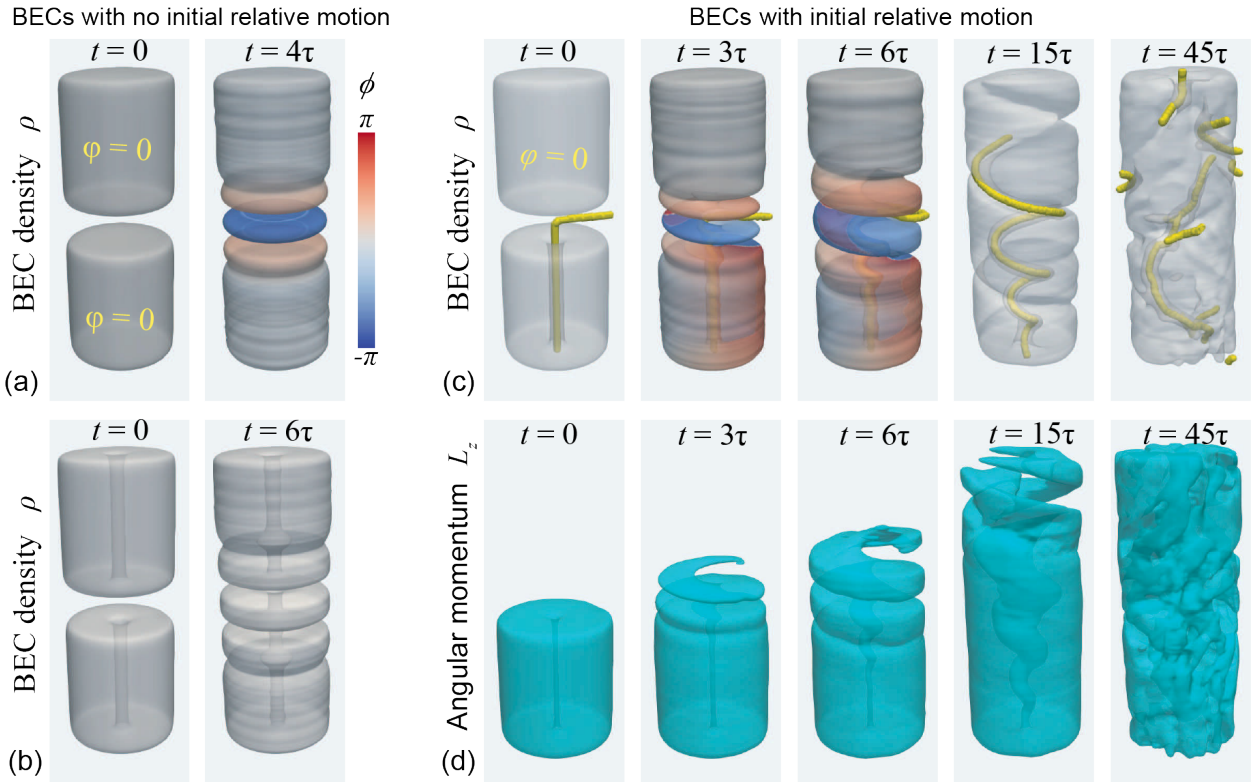

Figure 2.11: Merging dynamics of the two condensates when they are (a) static and (b) corotate at $t = 0$. (c) BEC density evolution when only the lower condensate contains a vortex line at $t = 0$. The color plots at $t = 3\tau$ and 6τ show the phase profiles. The solid yellow lines correspond to the locations of the vorticity singularities. (d) Time evolution of the angular-momentum density L_z corresponding to (c). The plot pictures the L_z isosurface at 10% of the initial bulk value. Adapted from Figure 2 in T. Kanai et al. [2]

Constant Phase. We initially examine the BEC merging at $t = 0$ with no relative motion. Figures 2.11a and b display two scenarios where the condensates are static and corotate with a vortex line placed at the center, respectively, at $t = 0$. Upon removing the potential barrier,

interference fringes emerge at the interface between the condensates. These fringes swiftly develop into disk-shaped gray solitons that propagate towards the upper and lower ends of the trap. Similar to the 2D case, the direction of the phase step $\Delta\phi$ across the density-depleted region is opposite to the soliton speed (Equation 1.79) [143–145]. The soliton disks eventually break up into vortices due to the snake instability [146–149].

Angular Momentum Transfer. We now shift our attention to the angular-momentum transfer during BEC merging. Figure 2.11c displays a representative case. At the initial time ($t = 0$), the upper condensate is static with a uniform phase $\phi = 0$, while the lower condensate, which carries angular momentum, rotates with a vortex line positioned at the center. Because of the phase winding in the lower condensate, the phase difference between the two condensates across the barrier gap varies around the z-axis. Due to the phase winding in the lower part, the phase gap between the two condensates across the barrier $U_{\rm w}$ varies around the z-axis. Intriguing new characteristics appear during evolution. A soliton-like structure having a corkscrew-like shape initially appears at the interface of the BECs around $z = 0$ and then extends to both ends of the cylindrical condensate. This structure reaches the ends at about $t \approx 15\tau$ and bounces back, inducing complex density and velocity fields in the condensate. The yellow lines in Figure 2.11c correspond to the locations of the vorticity singular lines. The propagation of the helical soliton sheet in the lower condensate causes Kelvin waves [26, 150, 151] along the vortex line. Surprisingly, in a relatively early stage of the evolution (i.e., $t < 12\tau$), the vortices are almost confined to the lower region ($z < 0$). Later, these vortices shift to the upper region ($z > 0$) accompanied by the local flows [26]. Eventually, as shown in Figure 2.11c at $t \approx 45\tau$, quantum turbulence [99] carrying angular momentum appears through the soliton decay.

Angular Momentum Density. This section is devoted to quantitative analysis of the angular momentum transfer by an angular-momentum density L_z defined for the 3D wave function in a similar manner as Equation 2.10. Figure 2.11d shows the time evolution of L_z for the case illustrated in Figure 2.11c. The angular momentum initially possessed by the lower rotating condensate quickly flows to the upper region along the helical channel created by the soliton sheet. Figure 2.12a shows the total angular momentum integrated over each region as $L_T = \int L_z dV$.

One may ask what the mechanism inducing the angular momentum transfer before the vortices drift into the upper condensate region ($t \lesssim 12\tau$) is. Figure 2.11d may give an impression that the fluid advection controls this transfer. To examine this appearance, we calculate the

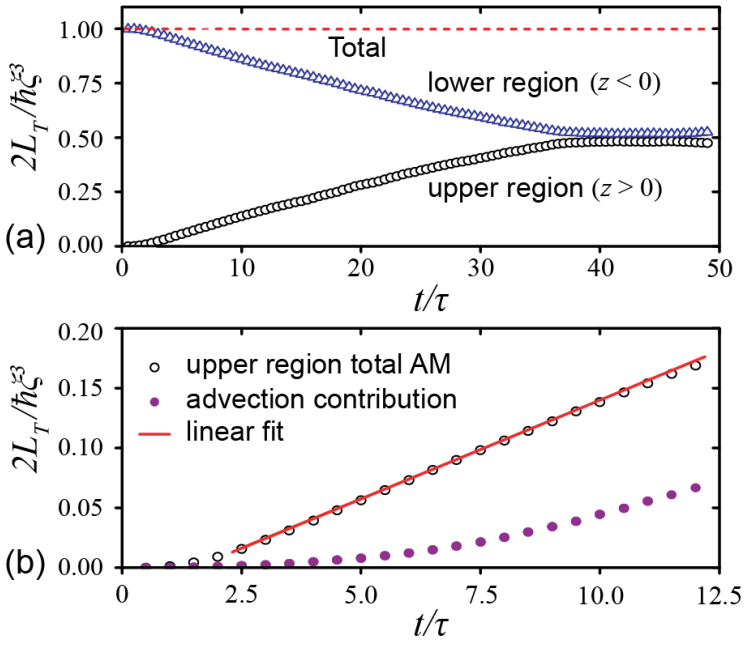

Figure 2.12: (a) Time evolution of the total angular momentum L_T in the upper and lower BECs. (b) The contribution of the fluid advection to the angular momentum in the upper condensate before vortices drift to this region. Adapted from Figure 3 in T. Kanai et al. [2]

angular momentum advection across the $z = 0$ plane as $\int_0^t dt' \int_{z=0} d^2r \; v_z(r,t') L_z(r,t')$, where $v_z = \frac{\hbar}{2im}\left(\psi^* \frac{\partial \psi}{\partial z} + \psi \frac{\partial \psi^*}{\partial z}\right)$ is the momentum density along the z-axis divided by the mass. Figure 2.12b shows that this advection contribution is minor for the total angular momentum gained by the upper condensate. This observation is because the flow in the lower condensate is initially perpendicular to the merging direction. The progressive rise of the advection contribution during the time interval $t \lesssim 7.5\tau$ can be explained in the following manner: the Kelvin waves propagating along the vortex line within the lower condensate cause the line to deform, adopting a coiled configuration. This coiled shape subsequently generates a vertical flow passing through the coil, leading to an effective advection of angular momentum towards the upper region.

2.2.3 Discussion

As shown in the previous section, fluid advection cannot be the mechanism of the observed rapid angular-momentum transfer at short evolution times. The key is the free edge that the helical soliton sheet has. Similarly to the 2D case, a phase step across the soliton sheet induces a phase winding around this edge line, which generates flows in the BEC like a fractional vortex line.

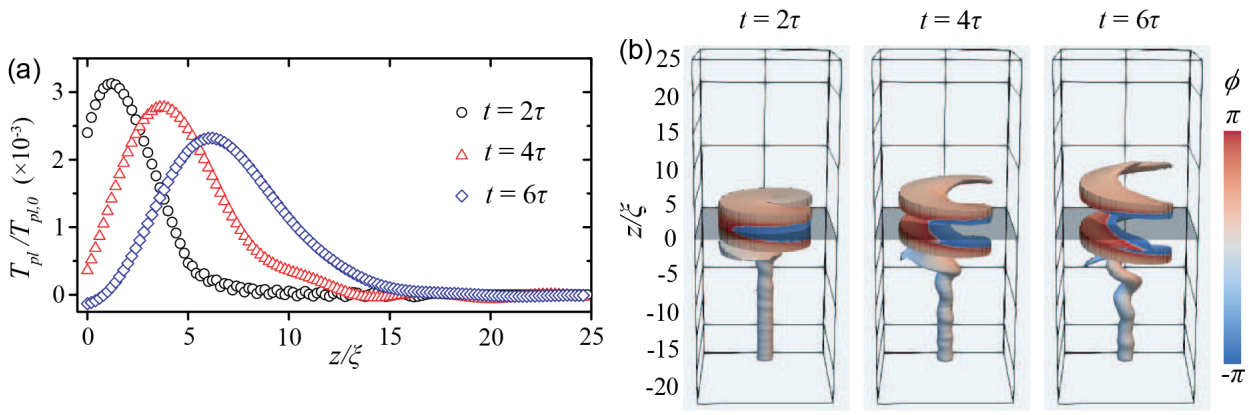

Figure 2.13: (a) Profiles of the integrated torque exerted by the soliton sheet in the upper BEC. (b) The plot shows the density isosurface at 50% of the bulk density, showing the soliton sheet and the vortex line. Adapted from Figure 4 in T. Kanai et al. [2]

As the soliton propagates, its phase profile can cause force and generate torque in both the upper and lower condensates. The torque per unit volume in the BEC concerning the z-axis is written as $T_z = (\mathbf{r} \times \mathbf{f}) \cdot \hat{e}_z$, where the force per unit volume $\tilde{\mathbf{f}}$ can be calculated based on the change rate of the momentum density, $\mathbf{f} = d\mathbf{P}/dt = d\left(m\,|\psi|^2\,\mathbf{v}\right)/dt$. Figure 2.13a shows the total torque T_{pl} integrated over the x-y plane and over a step length $\Delta z = 0.2\xi$ in the z-direction. This torque profile shifts to the condensate's top end associated with the soliton sheet's propagation. Figure 2.13b presents the corresponding profiles of the soliton sheet and verifies that the peak of the torque profile roughly coincides with the middle of the soliton profile in the upper BEC region. We have also confirmed that the angular momentum created by the total torque in the upper condensate region is the same as the difference between the two curves in Figure 2.12b, which is the remaining after subtracting the advection contribution from the total angular momentum increment in the upper region. These results confirm that the spatial extent of the torque matches the soliton profile, and the torque is the missing mechanism for the angular-momentum transfer. We note that the soliton sheet also exerts torque to the lower condensate and annihilates the angular momentum in this region because the phase step of the soliton sheet reverts its direction across the $z = 0$ plane (see Figure 2.11a) resulting in the negative torque in the lower condensate. The existence of the vortices makes plotting the exact torque profile in the lower condensate difficult. Still, the magnitude of the total torque in the lower condensate matches that in the upper condensate, which conserves the total angular momentum.

We have also calculated the rate of angular-momentum transfer in the early stage, where the torque mechanism plays a critical role. Figure 2.12b shows how we linearly fit the total angular momentum to calculate this rate. The almost linear time dependence of L_T can be understood by examining the torque profile shown in Figure2.13a. While the torque profile changes with time, the total torque exerted in the upper BEC region, equal to the total area below the profile curve, remains nearly constant. Therefore, the angular-momentum transfer rate becomes nearly constant.

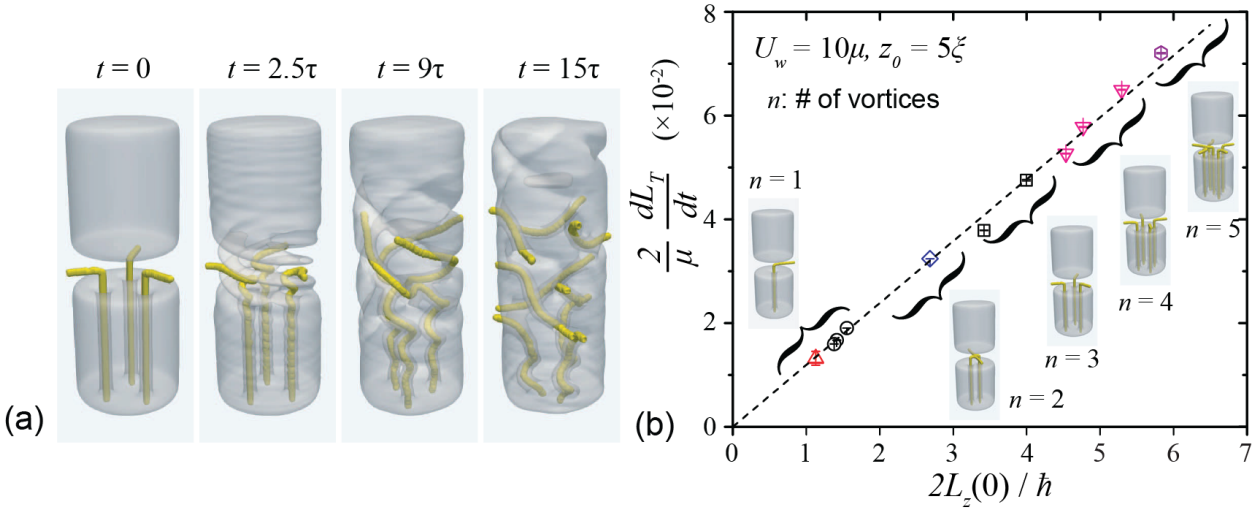

Figure 2.14: (a) Evolution of the BEC density when the lower part contains three vortex lines. (b) The angular-momentum transfer rate dL_T/dt with the initial angular-momentum density $L_z(0)$ for cases with various initial vortex configurations. The barely visible error bars represent the uncertainties of the linear fit, as shown in Figure 2.12b. The dashed line is a linear fit to the data. Adapted from Figure 5 in T. Kanai et al. [2]

We also wonder how this rate may depend on the initial angular-momentum density difference $L_z(0)$ between the two condensates. To investigate this effect, we vary the initial angular-momentum density difference $L_z(0)$ by introducing multiple vortex lines in the lower condensate while keeping the upper condensate static. Furthermore, for a given number of vortex lines in the lower condensate, $L_z(0)$ can be further tuned by varying the distance between the vortices and the z-axis. Figure 2.14a shows an example case with three vortex lines in the lower condensate at $t = 0$. Instead of having one soliton sheet, three solitonic corkscrews emerge and twist together. A constant angular-momentum transfer rate dL_T/dt is again observed at short evolution times, and this indeed holds for every case we have studied. In Figure 2.14b, we plot the obtained dL_T/dt against the initial angular-momentum density difference $L_z(0)$ for all the cases. It is remarkable to observe that the rate dL_T/dt is universally proportional to the initial angular-momentum density difference

$L_z(0)$ regardless of the vortex configurations. This universality may be understood qualitatively as follows. The initial angular-momentum density difference $L_z(0)$ depends on the exact vortex configuration. Meanwhile, for any vortex configuration, the solitonic corkscrews are always initiated at locations where the vortex lines are. Therefore, the solitonic corkscrews' spatial arrangement mimics the vortex lines' geometric configuration. The resulting total torque depends on this spatial arrangement, similar to the dependence of the initial angular-momentum density difference $L_z(0)$ on the vortex configuration. Therefore, the total torque (which equals dL_T/dt when the torque mechanism dominates) appears to be consistently proportional to the initial angular-momentum density difference $L_z(0)$ at short evolution times.

2.3 Conclusion

We have conducted numerical studies on the BEC merging process in 2D and 3D spaces. Our 2D simulation results of concentric disk and ring BECs show that relative motion between the two condensates induces spiral solitons whose sharp inner endpoints can cause rotational motion like a fractional vortex. The soliton stripe length depends on the height of the potential barrier initially separating the BEC. These spiral solitons can boost the angular momentum transfer between the two BECs, allowing the merged condensate to carry angular momentum even without quantized vortices. Moreover, the number of spiral solitons emerging during the merging process matches precisely the initial relative winding number between the two concentric BECs. The relative shear flows of the condensates at the interface can induce the underlying mechanism for which the solitons can break up at the condensate interface and the observed exact matching. It is well known in classical fluids that velocity shear in a single fluid or a velocity difference across the interface between two fluids causes the so-called Kelvin–Helmholtz (KH) instability, leading to the formation of periodic vortical structures at the interface [141, 152]. In superfluid systems, KH instability appears at the interfaces between two superfluid components, e.g., at the interface between superfluid ^{3}He-A and superfluid ^{3}He-B [144, 153], and in two-component BECs [143, 145]. The identified mechanism should be responsible for the KH instability in a single component superfluid. This angular momentum redistribution is a general mechanism that should be able to apply to condensates in 3D when the BEC merging and the flow occur in the same plane.

We have also studied 3D merging in which the merging direction is perpendicular to the initial flow. Our work has revealed that the soliton-like corkscrew structures formed at the interface enable

angular-momentum transfer by exerting torques on the BECs. This transfer rate is universally proportional to the initial angular-momentum density difference. These discoveries enrich our understanding of BEC merging dynamics and benefit the study of other rotating coherent matter-wave systems.

We want to emphasize that the configurations adopted in our simulations can be realized in BEC experiments. For example, there are past experiments studying the Kibble-Zurek mechanism and superfluid weak link utilizing the interference patterns of a ring condensate and a disk condensate during free expansion [130, 154]. Their setup can be adapted to realize the configuration for our 2D simulation. Indeed, there are past experiments implementing the 3D box potential [155, 156], and separating the BEC in a box geometry like in Figure 2.10 using tailored optical potentials is straightforward. The size of our BECs and the height of the potential barrier are typical in the experiments (i.e., typical BEC size of about $10\xi - 10^2\xi$ [122,130,138,139], and typical U in the range of $\mu - 100\mu$ [122, 130, 138, 140, 141]). Furthermore, the phase imprinting method can be applied to create the rotational motion in BECs [157]. We would also like to note that our 3D configuration is similar to that used in the experiment studying interface instability between superfluid ^{3}He-A and ^{3}He-B phases [152, 153], even though that experiment utilized two immiscible superfluids and the merging dynamics was not directly related to our case.

CHAPTER 3

TWO-DIMENSIONAL QUANTUM TURBULENCE

In 2D turbulence, large-scale persistent vortex structures are often observed, e.g., soap film vortex [158] and gigantic vortex in Jupiter's atmosphere [159]. To understand the emergence of these large-scale persistent vortex clusters, L. Onsager [160] introduced a simplified point-vortex model and showed that energy injection to a finite-sized 2D fluid containing many pointlike vortices might form persistent clusters of like-signed vortices, i.e., Onsager vortex (OV) clusters, having the high kinetic energy. This OV state is ordered with less entropy and higher energy; hence, the temperature associated with the OV state should be negative. The point vortex model has provided worthwhile understandings about general 2D turbulence [161, 162] and is particularly relevant to 2D superfluids, such as planar BECs [163, 164] and superfluid helium films [165, 166], where the vortices are pointlike topological defects with a quantized circulation [26].

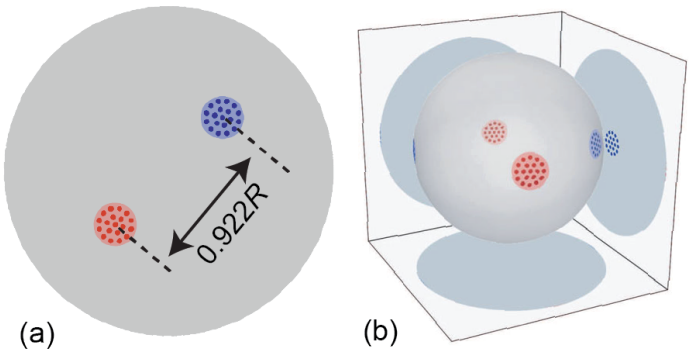

Figure 3.1: Schematics of the limiting two-dimensional OV cluster configuration with zero angular momentum in (a) planar disk-shaped BEC and (b) spherical shell BEC. The red and blue points represent vortices and antivortices, respectively. Adapted from Figure 1 in T. Kanai et al. [3]

T. Simula et al. [167] and T.P. Billam et al. [168] numerically discovered that a pair of OV clusters with opposite signs could form without any energy input during the evolution of 2D superfluid turbulence in a uniform 2D BEC. This fascinating spontaneous emergence of order from disorder has stimulated vast research [169–176]. They explained that this remarkable spontaneous order is due to the vortex evaporative heating mechanism, i.e., vortex-antivortex pair annihilation.

Such pairs of vortices induce negligible flows in the BEC and have relatively small energy in the vortex system. Those annihilations thus decrease the number of vortices but mostly keep the total energy of the vortex system, thereby boosting the mean energy per vortex. Specifically, their initial state contains many vortices and antivortices in a disk-shaped BEC with a radius R carrying zero angular momentum. During the evolution of the BEC, the vortices keep annihilating, and the vortex system goes into a negative temperature state, eventually approaching a limiting configuration illustrated in Figure 3.1a consisting of two vortex clusters separated symmetrically around the disk center [169]. This limiting configuration corresponds to the state having the highest kinetic energy per vortex.

Spherical shell BECs have recently attracted much interest [177–181]. Creating such a 2D BEC manifold in a spherical bubble trap was proposed in 2001 [182], but later research showed that uniform spherical shell BEC could be achieved only in a microgravity environment because the atoms would fall to the bottom of the trap by gravity [183, 184]. Nevertheless, the NASA cold atom laboratory recently installed an experimental setup at the International Space Station and observed small BEC bubbles [185–187]. In a spherical shell BEC with zero angular momentum, any dipole OV cluster configuration is always associated with a finite angular momentum; therefore, the formation of OV clusters is prohibited. We may then expect a quadrupole limiting configuration containing two pairs of the same signed OV clusters across perpendicular diameters (Figure 3.1 b) because the quadrupole state carries the highest kinetic energy with zero angular momentum.

The vortex evaporative heating mechanism should be general in 2D BECs. Nevertheless, our search for exotic OV states shows that OV clusters do not appear in a boundaryless 2D spherical BEC despite the vortex pair annihilations. Our analysis shows that contrary to prevailing thought, vortex-pair annihilation emits intense sound waves, dampening all vortices' motion and suppressing the formation of OV clusters. Uncovering this mechanism advances our understanding of spontaneous emergent vortex orders in 2D superfluid manifolds driven far from equilibrium. This chapter explains our published study about 2D turbulence [3].

3.1 Numerical Method

We simulate quasi-2D BECs in the disk and the spherical shell geometries by the three-dimensional GP equation (Equation 1.64). Note that r is the radius in the radial plane in the disk case and in the 3D space in the spherical shell case in this chapter. We apply the confining

potential used in Reference [167] to create a disk-shaped BEC:

$$U(\mathbf{r}) = U_{wall}\left[\tanh\left(\frac{r_{2D}-R}{a_{osc}}\right)+1\right]+\frac{1}{2}m\omega^2 z^2, \tag{3.1}$$

where r_{2D} is the radius in the radial plane in the disk case, and U_{wall} and ω are parameters relevant to the trap strength in the radial plane and along the z-axis. $a_{osc}=\sqrt{\hbar/m\omega}$ is the characteristic length of the trapping potential in the z direction that controls the thickness of the disk, and R sets the disk's radius. To create a spherical BEC shell, we apply the radial potential:

$$U(\mathbf{r}) = \frac{1}{2}m\omega^2\left(r-R\right)^2. \tag{3.2}$$

We set the parameters as $U_0N/\hbar\omega a_{osc}^3=\sqrt{125}\times10^4$ and $U_{wall}/\hbar\omega=64$, matching with those in the past theoretical and experimental studies [167, 188]. We choose the radius for the disk-shaped BEC as $R=30a_{osc}$ so that Kelvin waves along the quantized vortices are suppressed enough [189] [1]. Also, we take the radius for the spherical BEC shell as R = 15 a so that it has the same surface area as that of the disk-shaped BEC. We then apply the phase imprinting method [2, 133, 179] to create 80 vortices and 80 antivortices in the BECs while keeping their angular momentum nearly zero [167]. Equation 1.64 evolves in imaginary time for a short period for the vortex-core density structure [190]. We then obtain the dynamical evolution of the macroscopic wave function by numerically integrating Equation 1.64 with a time step of 10^{-3} and spatial resolutions $\Delta x=\Delta y=\Delta z=0.1a_{osc}$ using the fourth-order Runge-Kutta method [142].

3.2 Simulation Results and Discussions

Figure 3.2a and b are snapshots of the BEC density during the time evolution on the $z=0$ plane for the disk-shaped BEC and on the $r=R$ surface for the spherical BEC shell, respectively. We prepare typical initiate states in these geometries. In the disk-shaped BEC, the identical sign vortices form ephemeral clusters growing with time, eventually leading to two large persistent OV clusters. The frequency of vortex pair annihilation decreases with time and becomes extremely low upon forming the OV clusters. These observations are similar to those of past studies, e.g., [167].

[1] We want to note that this thin BEC behaves as two-dimensional for vortex system but three-dimensional for wave system. Therefore, the ideal-2D GP simulation implicitly supposes zero-thickness BEC in turbulence studies containing many waves.

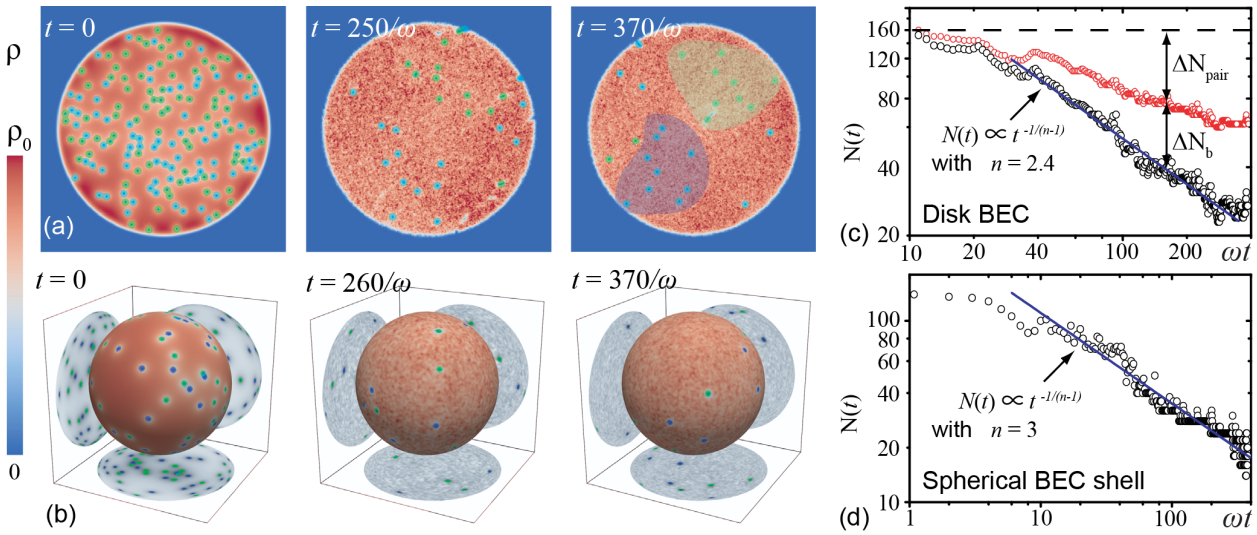

Figure 3.2: (a) and (b) show the evolution of the condensate density $\rho = |\psi|^2$ for the quasi-two-dimensional BEC in the disk geometry and the spherical shell geometry, respectively. The green and cyan dots correspond to the location of vortices and antivortices, respectively. The shaded areas in the disk BEC visualize coherent OV clusters. (c) and (d) show the time evolution of the total vortex number $N(t)$ (black circles). The red circles in the disk BEC case illustrate the division of decaying vortices, separating the contribution from pair annihilation process ΔN_{pair} and that from vortices exiting the boundaries ΔN_b. Adapted from Figure 2 in T. Kanai et al. [3]

3.2.1 Decay Scaling of Vortex Number

Figures 3.2c and d show the total vortex number $N(t)$ in the disk-shaped BEC and spherical shell BEC, respectively. The vortex-pair annihilations result in a more rapid decay of the total vortex number in the spherical BEC shell. Note that in ideal 2D BECs, two vortices annihilate essentially via a multi-vortex interaction process [191–194]. In ideal 2D BECs, vortex-antivortex pair annihilation requires a third vortex due to energy conservation. Otherwise, the pair becomes stable and moves at a constant velocity [26]. This annihilation generates a long-lived nonlinear density wave, which Nazarenko and Onorato first identified as a soliton [191] and was later called "crescent-shaped" wave [192] or "vortexonium" [170]. This nonlinear wave may decay into phonons when it collides with a fourth vortex [170, 193]. Baggaley and Barenghi [194] numerically substantiated examined decaying homogeneous turbulence in a boundaryless ideal 2D square BEC with periodic boundaries and confirmed that the anticipated vortex decay through a four-vortex process. Generally speaking, when an n-vortex process dominates the vortex decay, the time evolution of the total vortex number is $dN(t)/dt \propto -N^n$, and hence we can expect a scaling of $N(t) \propto t^{-(1/n-1)}$.

Baggaley and Barenghi [194] discovered that the total vortex number scales as $N(\tilde{t}) \propto t^{-1/3}$ at large decay times, suggesting a four-vortex process. Furthermore, some dissipation intentionally added to the ideal 2D BEC can change the decay scaling to $n = 3$ because the dissipation can dampen the soliton wave without a fourth vortex. We will show additional results of square BECs supporting our argument later.

Our result in Figure 3.2c and d shows that at a later time but before the OV clusters form in the quasi-2D BECs, $N(t)$ can be fitted well by this scaling with $n = 2.4$ for the disk-shaped BEC and $n = 3$ for the spherical shell BEC. The interaction between the sound waves and the vortices becomes stronger in quasi-2D BECs than in ideal 2D BECs [167], inducing effective damping in ideal 2D BECs. Therefore, the $n = 3$ decay scaling in boundaryless quasi-2D BECs corresponds to the vortex-antivortex pair annihilation. We can then interpret that the $n = 2.4$ decay scaling in the quasi-2D disk BEC is due to the interplay of the vortex-pair annihilation process ($n = 3$) and vortex exiting process ($n = 2$). Figure 3.2c shows that 1/3 of the decayed vortices in the disk BEC result from the vortex exiting process.

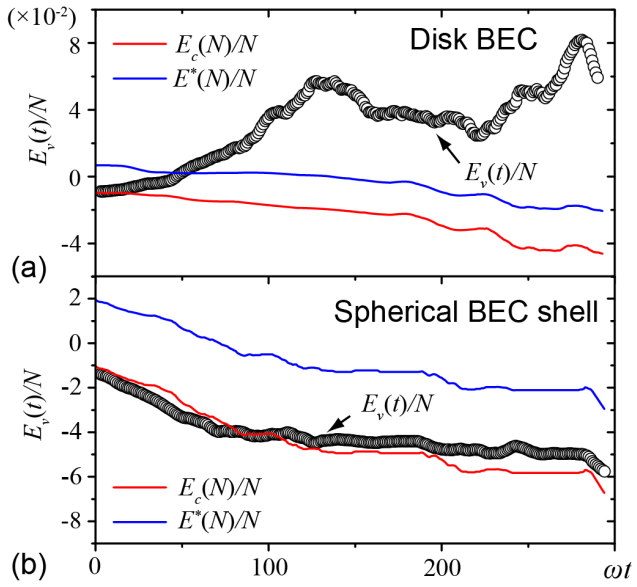

Figure 3.3: Time evolution of the incompressible kinetic energy E_V in (a) the disk-shaped BEC and (b) the spherical shell BEC. $E^*(N)$ is a reference energy above which vortex clusters are readily observable and $E_c(N)$ is the threshold energy for transition to the negative temperature state. Adapted from Figure 3 in T. Kanai et al. [3]

According to Figure 3.2b, regardless of the more quick decay of vortex number through the pair annihilation in the spherical BEC shell, no clear vortex clusters appear at any time. For more

concrete evidence to judge whether or not OV clusters ever form in a BEC, we evaluate the vortex energy [195]. The total kinetic energy of a BEC consists of three parts [40]:

- Incompressible kinetic energy due to the flow field induced by the vortices
- Compressible kinetic energy due to sound waves
- Compressible kinetic energy due to quantum pressure.

The following explains how to estimate the incompressible part by the point vortex model.

3.2.2 Point Vortex Thermodynamics

The incompressible kinetic energy can be evaluated by first determining the vortex locations of all vortices and then applying the point-vortex Hamiltonian [167–169, 172, 173]:

$$\begin{aligned}\mathcal{H} &= -\frac{\rho_0\kappa^2}{4\pi}\left[\sum_{i<j} s_i s_j \ln\left(\left|\mathbf{r}'_i - \mathbf{r}'_j\right|^2\right) - \sum_i s_i^2 \ln\left(1 - r'^2_i\right)\right. \\ &\quad \left. - \sum_{i<j} \ln\left(1 - 2\mathbf{r}'_i \cdot \mathbf{r}'_j + \left|r'_i\right|^2 \left|r'_j\right|^2\right)\right]. \end{aligned} \tag{3.3}$$

where ρ_0 is the mean density, $\kappa = h/m$ is the quantized circulation, and $\mathbf{r}'_i = \mathbf{r}_i/R$ is the normalized position vector of the i-th vortex with a winding number $s_i = \pm 1$. For vortices in the spherical shell, we adopt the same procedures with the Hamiltonian [196, 197]:

$$\mathcal{H} = -\frac{\rho_0\kappa^2}{4\pi}\sum_{i<j} s_i s_j \ln\left(1 - \mathbf{r}'_i \cdot \mathbf{r}'_j\right). \tag{3.4}$$

Figure 3.3 displays the normalized incompressible kinetic energy variations $E_V = (4\pi/\rho_0\kappa^2)H$ in both BEC geometries and also shows the threshold energy $E_c(N)$ above which the corresponding 2D neutral N-vortex system becomes the negative temperature state. We use the Markov chain Monte-Carlo method [198] to derive this $E_c(N)$ using the above Hamiltonians [169]. To apply the Monte Carlo method evaluating the thermodynamic properties of the vortex system, we consider a neutral point-vortex system with a total vortex number N in a disk-shaped BEC ($R = 30a_{osc}$) and in a spherical BEC shell ($R = 15a_{osc}$) having zero angular momentum. We use the Markov chain to generate a considerable ensemble (i.e., 5×10^6) of vortex configurations with a given temperature T based on the Boltzmann distribution $e^{-E_V T_0/NT}$ as detailed in Reference [198], where $T_0 = N\rho_0\kappa^2/4\pi k_B$ is a characteristic temperature. Note that the generated vortex configurations are restricted to have nearly zero BEC angular momentum (i.e., negligible vortex dipole moment

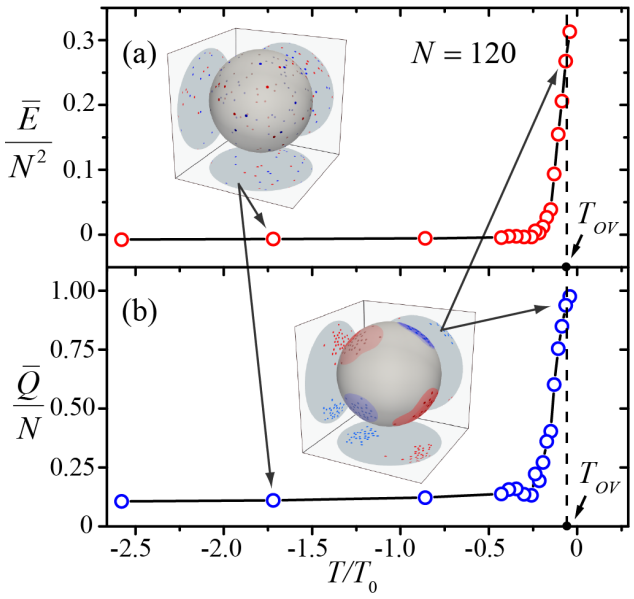

Figure 3.4: Temperature dependence of (a) the mean energy $\bar{E}$ and (b) the mean quadrupole moment $\bar{Q}$ for neutral point-vortex systems in a spherical shell with $N = 120$ vortices and zero BEC angular momentum. $T_{OV} = T_0/16$ corresponds to the transition temperature for the ideal point-vortex super-condensation. Adapted from Figure S1 in T. Kanai et al. [3]

$\mathbf{d} = \sum_i s_i \mathbf{r}'_i$ for the spherical BEC shell case). The mean energy of the vortex system $\bar{E}(T)$ is obtained as the average of E_V overall vortex configurations.

The following shows the results of the spherical shell case. Figure 3.4a plots $\bar{E}$ versus T for a representative vortex system with $N = 120$. We have also calculated the quadrupole moment Q for each vortex configuration, defined as $Q = (\sum_l q_l^2)^{1/2}$ where $q_l (l = x, y, z)$ are the eigenvalues of the quadrupole tensor:

$$Q_{ll'} = \frac{1}{2} \sum_i s_i \left[3 \left(\mathbf{r}'_i \cdot \hat{e}_l \right) \left(\mathbf{r}'_i \cdot \hat{e}'_l \right) - \delta_{ll'} \right]. \tag{3.5}$$

The limiting vortex configuration (as shown in Figure 3.1b) has four compact vortex clusters, each containing $N/4$ like-signed vortices, and achieves the maximum quadrupole moment$Q_{Max}/N \simeq 3\sqrt{2}/4$. Figure 3.4b shows the mean quadrupole moment $\bar{Q}(T)$ determined as the ensemble average of Q at different T. $\bar{E}(T)$ and $\bar{Q}(T)$ rise quickly as $T \to -0$, indicating a transition to the Onsager-vortex phase. Applying an energy-entropy balancing analysis [195] to estimate T_{OV} above which the vortex system undergoes a super-condensation transition, we can obtain $T_{OV} = -T_0/4$ for the disk BEC [167–169] and $T_{OV} = -T_0/16$ for the spherical BEC shell. Figure 3.4 also includes two representative microcanonical vortex configurations at temperatures much lower or close to T_{OV}.

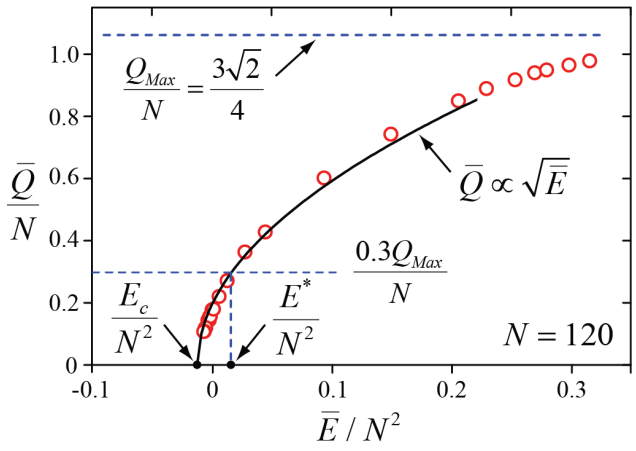

Figure 3.5: The mean quadrupole moment $\bar{Q}$ as a function of the mean vortex energy $\bar{E}$. The reference energies E_c and E^* are determined as the main text explains. Adapted from Figure S2 in T. Kanai et al. [3]

Next, we evaluate two key reference energies, E_c and E^*. The threshold energy E_c is the value of $\bar{E}$ in the limit of $\tilde{T} \to -\infty$. We apply the method discussed in Reference [169] to determine E_c reliably, and Figure 3.5 plots $\bar{Q}(T)$ versus $\bar{E}(T)$, where the data near $\bar{Q}(T) = 0$ follows a $\sqrt{\bar{E}}$ scaling [169]. The intersect of this scaling curve with the $\tilde{E}$-axis corresponds to E_c. Since the OV clusters can emerge at temperatures slightly lower than T_{OV}, we also introduce a phenomenological reference energy $E^*(N)$ at which the mean vortex quadrupole moment (dipole moment for the disk case) equals 30% of the value for the limiting configuration illustrated in Figure 3.1. Comparing Figure 3.4 and Figure 3.5 shows that the E^* corresponds to the level where the $\bar{E}$ curve starts to rise quickly.

We repeat this analysis with different N and collect the obtained E_c and E^* in Figure 3.6. We then perform a polynomial fit with the form $\bar{E} = \sum_{i=0}^{7} a_i N^i$ to the E_c and E^* data to determine the dependence on the vortex number N. Figure 3.3 shows that in the disk BEC the vortex energy E_V quickly increases to above $E^*(N)$, which agrees that clear OV clusters emerge. We note that $E_c(N)$ and $E^*(N)$ change with time since the total vortex number $N(t)$ decays. On the other hand, E_V for the spherical BEC shell barely reaches above $E_c(N)$ and is always lower than $E^*(N)$, thereby verifying that we can hardly observe the formation of OV clusters in the spherical BEC shell.

The contrasting fate comes from the difference in the vortex decay processes in the disk BEC and the spherical BEC shell, which calls for an explanation. The vortex-pair annihilation process

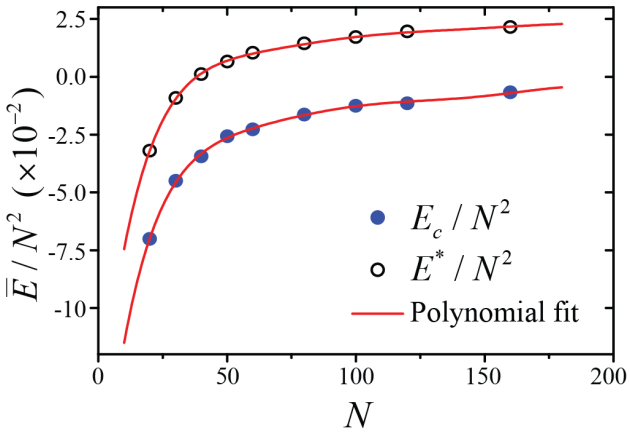

Figure 3.6: Vortex number dependence of the E_c and E^*. The solid red curves are polynomial fits with the form $E = \sum_{i=0}^{7} a_i N^i$. Adapted from Figure S3 in T. Kanai et al. [3]

works in both geometries, but the vortex-exiting process can occur only in the disk geometry. To understand what this difference causes, we simulate ideal cases of these processes. For the annihilation process, we first place a vortex-antivortex pair at close separation in bulk and then evolve the GP equation with a small added damping through the imaginary time propagation so that the two vortices approach each other while propagating [194]. When the vortex separation is around the coherent length, we set $t = 0$ and remove the artificial damping so that the dissipation does not influence the following annihilation process. For the exiting process, We adopt similar procedures for the initial state having a single vortex near the BEC boundary. Figure 3.7 displays the results. We can see that the pair annihilation in bulk BEC generates intense sound waves due to the linear momentum conservation. Conversely, during the vortex exiting process, the vortex merges into the zero-density area, resulting in a much fewer generation of sound waves. Sound waves can dampen the vortex motion and dissipate the incompressible kinetic energy in the BEC. [191]. This process is similar in nature to superfluid helium in that the normal-fluid component dampens the quantized vortices in the superfluid component through the mutual friction [199–201]. Therefore, we conclude:

1. The vortex pair annihilation process alone does not lead to the OV cluster formation because of the intense sound emission

2. The vortex exiting process on the BEC boundaries, which boosts the mean vortex energy with minimum sound wave emission, is responsible for the spontaneous OV orders.

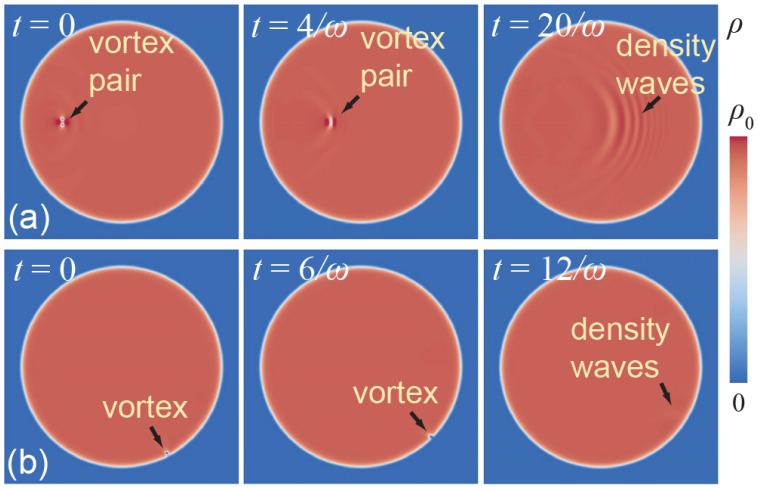

Figure 3.7: Time evolution of the condensate density in the disk-shaped BEC when (a) a vortex-antivortex pair undergoes annihilation and (b) a vortex exits from the disk boundary. Adapted from Figure 4 in T. Kanai et al. [3]

The following presents three complementary tests that can produce unequivocal supporting evidence to verify these conclusions.

3.2.3 Point Vortex Dynamics on Sphere

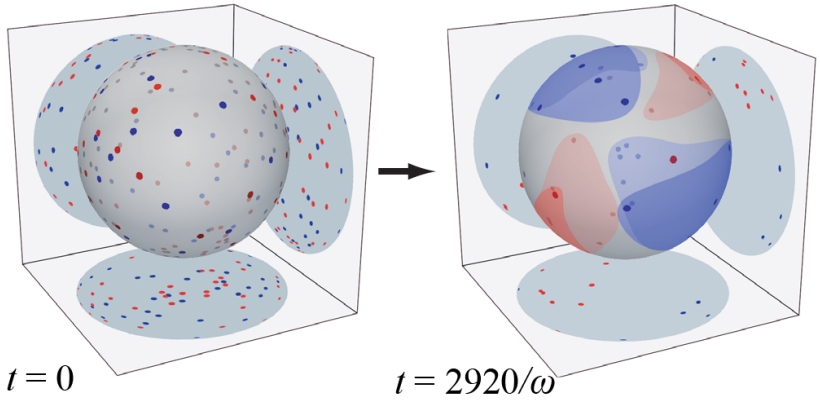

Figure 3.8: Time evolution of the vortex dynamics on a two-dimensional spherical surface with the point-vortex model. The initial state is the same as in our GPE simulation. Adapted from Figure 5 in T. Kanai et al. [3]

The first test examines the ideal vortex dynamics on the spherical surface ($R = 15a_{osc}$). This system has no sound waves, and removing a vortex pair with a short separation distance subtracts a large negative value from the Hamiltonian in Equation 3.4, resulting in the increment of the

point-vortex energy with time. Therefore, We can expect the limiting OV configuration in Figure 3.1b. We evolve point vortices by the equation of motion derived from the Hamiltonian in Equation 3.4 [196, 197]:

$$\frac{\partial \mathbf{r'}_i}{dt} = \frac{\omega}{2\left(R/a_{osc}\right)^2} \sum_{j \neq i} \frac{\mathbf{r'}_i \times \mathbf{r'}_j}{1 - \mathbf{r'}_i \cdot \mathbf{r'}_j}. \tag{3.6}$$

where the initial distribution is the same as in our GP equation simulation (Figure 3.2b). We remove vortex-antivortex pairs if the arc-length separation between the two vortices with different signs is less than $0.03R/a_{osc}$ to imitate the vortex-pair annihilation process [167]. Figure 3.8 shows that four vortex clusters spontaneously form at large t, eventually evolving toward the limiting configuration as expected. The exact time toward the OV clusters' emergence depends on the threshold separation for vortex-pair removal. This simulation result indicates that the evaporative-heating mechanism will work if the sound waves are absent. Our finding also suggests the need for careful consideration when employing the point-vortex model to understand the vortex dynamics in BECs.

3.2.4 Onsager Vortex State in Square-Shaped Bose–Einstein Condensates

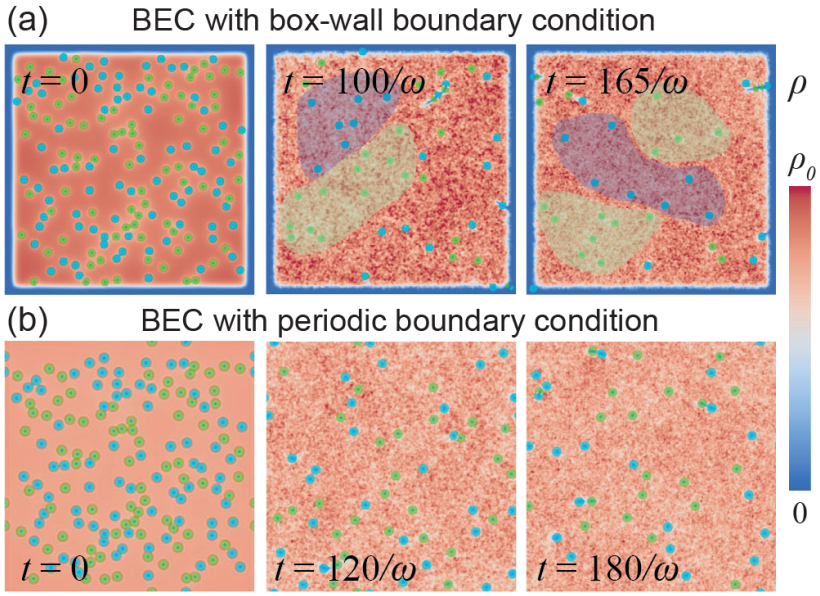

Figure 3.9: GPE simulation of the vortex dynamics in quasi-2D square BEC with (a) box-wall boundary condition and (b) periodic boundary condition. The green and cyan dots correspond to the location of vortices and antivortices, respectively. Adapted from Figure 6 in T. Kanai et al. [3]

The second test simulates a square-shaped planar quasi-2D BEC with 80 vortices and 80 antivortices at random initial positions by the GP equation (Equation 1.64). We choose the identical trapping parameters, U_0 and ω, as those used for the disk BEC case and set the square's side length to $R = 50a_{osc}$ to achieve a comparable area. We then apply either the box-wall boundaries with the hyperbolic tangent potential or the periodic boundaries [194] to directly compare the vortex dynamics in the same BEC geometry with and without the vortex exiting mechanism. According to Figure 3.9, showing representative snapshots of the BEC density from the same initial state with the two different boundary conditions, large-scale OV clusters emerge only in the box-wall boundaries case.

To substantiate our perspective regarding vortex decay scaling, we have investigated the vortex number decay in these quasi-two-dimensional square BECs (Figure 3.10). The vortex number decay with the periodic boundary condition shows the $n = 3$ decay scaling at late times, which agrees with our viewpoint about vortex-number decay in boundaryless quasi-2D BECs. Furthermore, a decay scaling with the box-wall boundary is $n = 2.3$, close to that in the disk-shaped BEC bounded by the same type of boundary. Here, we want to mention that we simulated an ideal 2D square-shaped

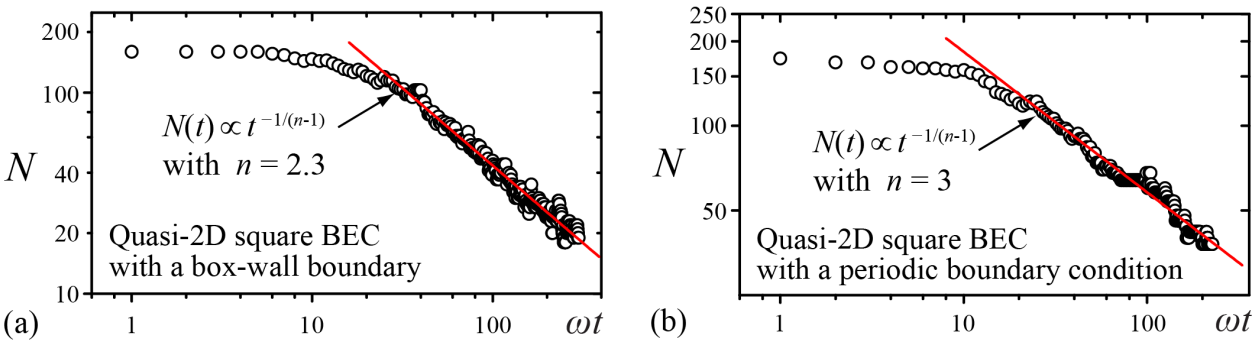

Figure 3.10: Time evolution of the total vortex number $N(t)$ in the GPE simulations with a square BEC with (a) a box-wall boundary condition and (b) a periodic boundary condition. These results are related to the cases shown in Figure 3.9. Adapted from Figure 2 in T. Kanai et al. [3]

BEC with the periodic boundary condition and observed the $n = 4$ decay scaling as reported by Baggaley and Barenghi [194]. Therefore, these observations substantiate our perspective that the transition from zero to finite thickness in BEC leads to an intensified interaction between sound and vortices, causing a shift in the decay scaling from $n = 4$ to $n = 3$ for pair annihilation.

3.2.5 Onsager Vortex State in Spherical-Cap-Shaped Bose–Einstein Condensates

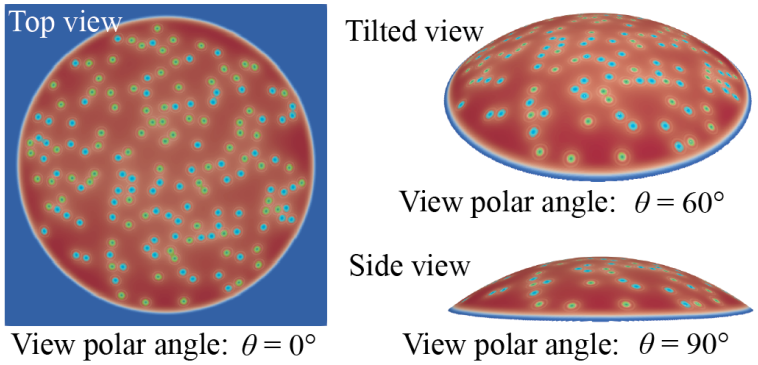

Figure 3.11: Initial density profile of the quasi-two-dimensional spherical BEC cap at $r = R$. The green and cyan dots represent the location of vortices and antivortices, respectively. Adapted from Figure S5 in T. Kanai et al. [3]

The third test simulates the vortex evolution in a curved BEC with a boundary (i.e., a quasi-2D spherical BEC cap). We have associated the spontaneous emergence of OV clusters with vortices exiting from the BEC boundaries, a process decreasing the vortex number with fewer sound waves.

Then, we consider that the absence of such boundaries causes the OV clusters to be absent in the quasi-2D spherical BEC shell. However, confirming that OVs can emerge on the curved surface when solid-wall boundaries are restored is worthwhile because the curvature may affect the vortex dynamics [181]. For this purpose, we have conducted supplementary simulations of the vortex dynamics in a quasi-2D spherical BEC cap using the GP equation. This spherical BEC cap is generated by utilizing the following potential:

$$U(\mathbf{r}) = \frac{1}{2}m\omega^2(r-R)^2 + U_{wall}\left[\tanh\left\{\frac{R}{a_{osc}}(\theta-\theta_{\max})\right\}+1\right], \tag{3.7}$$

where we choose the curvature radius as $R = 45a_{osc}$ and the maximum polar angle as $\theta_{max} = 0.216\pi$ such that the cup surface area is the same as that for the disk and the spherical shell BECs. As the other cases, we apply the same coupling constant U_0 and potential parameters U_{wall} and ω in the GP equation. We introduce 80 vortices and 80 antivortices into the initial BEC cap at random positions, ensuring the initial angular momentum is close to zero. Figure 3.11 illustrates the initial density profile on the cross-section at $r = R$ from various polar angles. Figure 3.12

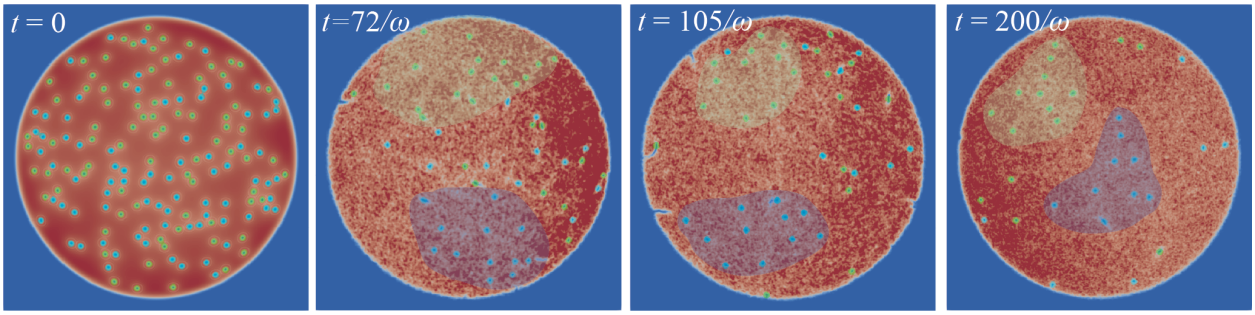

Figure 3.12: Time evolution of the condensate density at $r = R$ for the spherical BEC cap, viewed from the top. The shaded regions correspond to the persistent OV clusters. Adapted from Figure S6 in T. Kanai et al. [3]

shows the representative top-view images of the BEC density during the GP equation evolution and illustrates two persistent OV clusters observed at large times, similar to those in the disk BEC case. This result confirms our perspective that the vortex-exiting process through the solid-wall boundaries is essential for the spontaneous formation of the OVs. These findings undeniably showcase the vital significance of the boundaries where vortices exit in the spontaneous emergence of OV orders.

3.3 Conclusion

We have examined the evolution of vortices in both planar and spherical 2D BECs. In a disk-shaped quasi-2D BEC, we have observed the OV cluster state, which has a high incompressible kinetic energy and entropy. On the other hand, our results show that OV clusters do not appear in a spherical shell quasi-2D BEC. This difference is due to the existence of the BEC boundary and the amount of sound waves. The quantized vortices may decay through two processes: vortex-antivortex pair annihilation process and vortex exiting process. The vortex-antivortex annihilation process emits intense sound waves even though the vortex-exiting process produces fewer sound waves. In a boundaryless spherical shell quasi-2D BEC, vortices may decay only through the vortex-antivortex pair annihilation process, which emits fewer sound waves, damping the vortex energy. A comprehensive understanding of the mechanism underlying the spontaneous vortex orders is achieved, representing significant progress in studying the far-from-equilibrium dynamics of 2D superfluids. Our findings may also motivate future experiments in 2D spherical BECs at the International Space Station.

CHAPTER 4

ANISTROPY OF THERMAL COUNTERFLOW TURBULENCE IN SUPERFLUID HELIUM-4

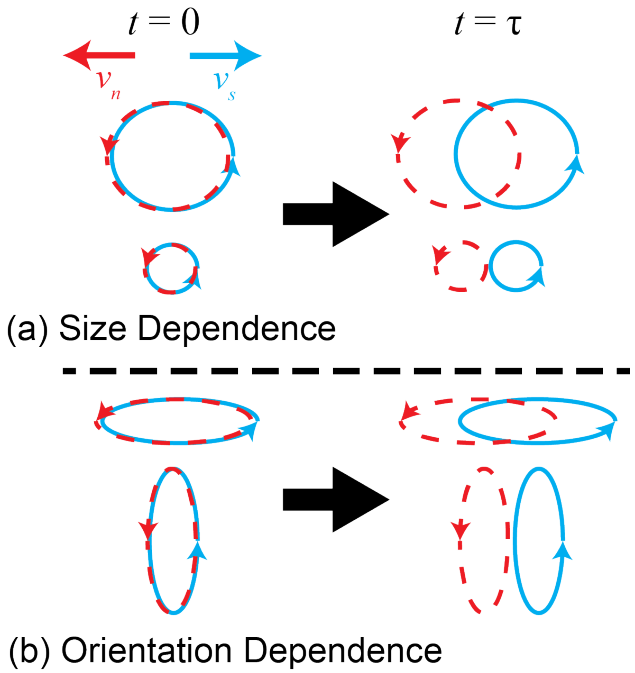

Figure 4.1: Schematic of turbulent eddies in counterflow turbulence. (a) and (b) show the size dependency and orientation dependency, respectively.

Turbulence in classical fluids tends to become more homogeneous and isotropic as the scale decreases, even if it is highly anisotropic at large energy injection scales [91]. However, Biferale et al. [202] predicted that counterflow turbulence can become more anisotropic in He II as the length scale reduces. Turbulent He II counterflow is influenced by a mutual friction force (Equation 1.165), which is balanced by the chemical potential gradient established due to the applied heat current in He II on average [55]. Turbulent eddies can cause velocity fluctuations in the two fluids as $\boldsymbol{u}_s$ and $\boldsymbol{u}_n$. When these eddies have no overlapping and no correlation (i.e., $\boldsymbol{u}_s \neq \boldsymbol{u}_n$), unbalanced mutual friction effectively damps out these eddies. However, if turbulent eddies are correlated in the two fluids, mutual friction dissipation remains small, allowing these eddies to survive for sufficient time to maintain an energy cascade. This energy dissipation mechanism has two effects on the

distribution of the coupled turbulent eddies. Turbulent eddies initially coupled are swept apart due to the opposite mean flows. First, the population of the coupled eddies must be suppressed as the scale reduces because larger eddies can remain correlated for longer times, while smaller eddies become uncorrelated quickly and are promptly damped, as illustrated in Figure 4.1a. J. Gao et al. [203] and Bao et al. [204] have verified this phenomenon by measuring the streamwise energy spectrum via molecular tagging velocimetry (MTV). Secondly, Biferale et al. [202] have theoretically suggested that coupled eddies being initially elongated along with the mean flow or the perpendicular directions have different suppression magnitude, leading to anisotropy in counterflow. As shown in Figure 4.1b, the eddy elongated to the mean flow direction has a longer overlap time and is more weakly suppressed than that elongated to the perpendicular direction. Quantitative measurement of this anisotropy is critical to develop the theoretical framework of counterflow turbulence.

4.1 Experimental Method

Measuring the thermal counterflow is commonly achieved through second-sound attenuation, which provides the averaged vortex line density (VLD), i.e., total vortex line length per unit volume. Our Cryogenics team has devised a state-of-the-art experimental setup that merges laser optics with helium cryogenics to enhance comprehension of velocity fluctuation and correlation. Our innovative system utilizes laser beams to generate metastable helium molecules, which allows for flow visualization. The optical system originates the required laser beams, which are then transmitted to the cryogenics system. These lasers generate a trace line in the thermal counterflow within a helium channel. A. Marakov and J. Gao, former members of our Cryogenics lab, built the original system for their 1D measurement in the mean flow direction [95, 199, 203, 205–208], and we have developed the cryostat for our 2D measurements.

4.1.1 Vortex Line Density Measurement

We first briefly explain the measurement of the averaged VLD by the second-sound attenuation. In our system, the second sound wave is stranded between two oscillating superleak transducers (OSTs) [209], each consisting of a porous membrane and a plastic membrane (Figure 4.2). When the plastic membrane is pulled, only the superfluid can follow it, while the normal fluid cannot pass through the porous membrane. Conversely, when the plastic membrane is pushed, the stored superfluid flows into the helium channel. As a result, the vibration of the plastic membrane moves

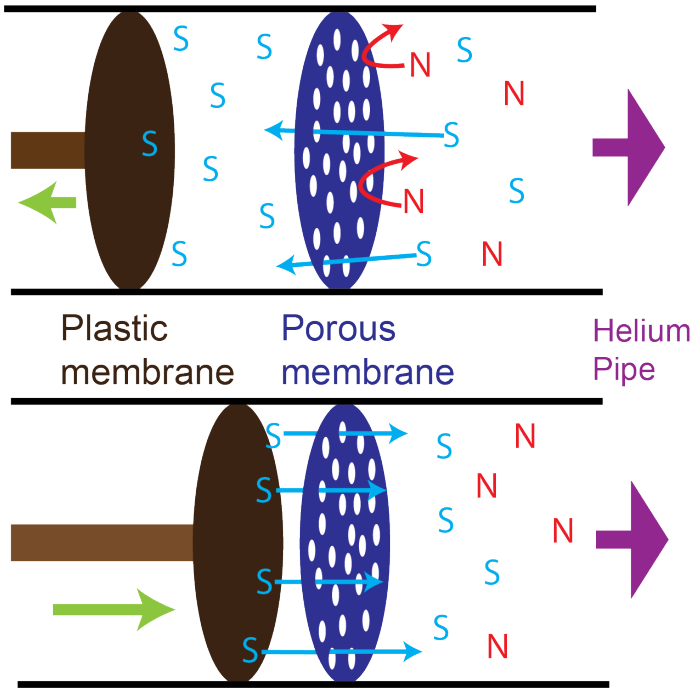

Figure 4.2: Schematic of the membrane for the second sound generation and measurement.

the variations of ρ_s and ρ_n out of phase, causing the second wave to stand. The other transducer can measure the attenuation of the second sound. Quantum turbulence in He II is a tangle of vortex cores attenuating the second sound by mutual friction [96], and the decay of the second sound depends on the VLD as [210]:

$$\mathcal{L} = \frac{6\pi\Delta_0}{B\kappa}\left(\frac{A_0}{A} - 1\right). \tag{4.1}$$

Here, A is the amplitude of a Lorentzian resonant peak in the second sound frequency spectrum, A_0 is the amplitude in the absence of vortices, B is a mutual friction coefficient depending on the temperature [211], and Δ_0 is the full width at half maximum (FWHM) of the resonant peak.

4.1.2 Metastable Helium Triplet Molecules

Our experiment uses the MTV method with metastable helium molecules He_2^* to visualize normal fluid flows in He II. These molecules are formed by exciting or ionizing ground-state helium atoms using a femtosecond regenerative amplifier laser with a wavelength of 800 nm through the

following processes:

$$\mathrm{He}^+ + \mathrm{e}^- + \mathrm{He} \rightarrow \mathrm{He}_2^* \tag{4.2}$$

$$\mathrm{He}^* + \mathrm{He} \rightarrow \mathrm{He}_2^*, \tag{4.3}$$

where the notation of '$*$' means the excited electronic state. The excited He_2^* can exist in spin-singlet or triplet states. Once generated, the molecules emit scintillation photons as they quench to their singlet ground state ($A^1\sum_u^+$) or triplet ground state ($a^3\sum_u^+$) [212]. The singlet ground state ($A^1\sum_u^+$) radiatively decays in the order of nanoseconds, which is much shorter than our observation time scale [213]. Therefore, we utilize the triplet ground state ($a^3\sum_u^+$) with a long radiative lifetime of roughly 13 s because the radiative transition to two free helium atoms of the ground state necessitates spin flipping [214]. These He_2^* molecules form tiny bubbles with a radius a_p of about 6 Å in liquid helium. The motion of a tiny particle can be described by an equation of motion:

$$\rho_\mathrm{p}\Theta\frac{d\boldsymbol{u}_\mathrm{p}}{dt} = \boldsymbol{F}_\mathrm{p} \tag{4.4}$$

where ρ_p is the particle density, $\Theta = \frac{4}{3}\pi a_\mathrm{p}^3$ is the particle volume, and $\boldsymbol{u}_\mathrm{p}$ is the velocity of the particle. The force $\boldsymbol{F}_\mathrm{p}$ acting on this tiny particle mainly consists of six forces [215, 216].

- $\boldsymbol{F}^{(g)}$: The gravitational force given by $\boldsymbol{F}^{(g)} = (\rho_\mathrm{p} - \rho)\,\Theta\boldsymbol{g}$, where $\boldsymbol{g}$ is the gravitational acceleration vector.
- $\boldsymbol{F}_n^{(d)}$: The viscous drag force from the normal fluid.
- $\boldsymbol{F}_c^{(i)}$: The inertial force from the normal fluid ($c = n$) and the superfluid ($c = s$) given by $\boldsymbol{F}_c^{(i)} = \rho_c\Theta\frac{D\boldsymbol{v}_c}{Dt}$
- $\boldsymbol{F}_c^{(a)}$: The added mass force from the normal fluid ($c = n$) and the superfluid ($c = s$) given by $\boldsymbol{F}_c^{(a)} = \frac{1}{2}\rho_c\Theta\left(\frac{D\boldsymbol{v}_c}{Dt} - \frac{d\boldsymbol{u}_\mathrm{p}}{dt}\right)$

The particle Raynolds number is small (i.e., $Re_p = 2\rho_n a_\mathrm{p}\left|\boldsymbol{v}_n - \boldsymbol{u}_\mathrm{p}\right|/\eta_n << 1$), and the viscous drag force for a spherical particle can be approximated as $\boldsymbol{F}_n^{(d)} \approx 6\pi a_\mathrm{p}\eta_n\left(\boldsymbol{v}_n - \boldsymbol{u}_\mathrm{p}\right)$. Therefore, the

equation of motion is written as

$$\rho_{\rm p}\Theta\frac{d\boldsymbol{u}_{\rm p}}{dt} = 6\pi a_{\rm p}\eta_n\left(\boldsymbol{v}_n-\boldsymbol{u}_{\rm p}\right)+\left(\rho_{\rm p}-\rho\right)\Theta\boldsymbol{g} \tag{4.5}$$

$$+\sum_{c=\{n,s\}}\rho_c\Theta\left(\frac{3}{2}\frac{D\boldsymbol{v}_c}{Dt}-\frac{1}{2}\frac{d\boldsymbol{u}_{\rm p}}{dt}\right) \tag{4.6}$$

$$\Leftrightarrow \frac{d\boldsymbol{u}_{\rm p}}{dt} = \frac{9\eta_n}{2\left(\rho_{\rm p}+\rho/2\right)a_{\rm p}^2}\left(\boldsymbol{v}_n-\boldsymbol{u}_{\rm p}\right)+\frac{\rho_{\rm p}-\rho}{\rho_{\rm p}+\rho/2}\boldsymbol{g} \tag{4.7}$$

$$+\sum_{c=\{n,s\}}\frac{3\rho_c}{2\left(\rho_{\rm p}+\rho/2\right)}\frac{D\boldsymbol{v}_c}{Dt} \tag{4.8}$$

Then, the viscous relaxation time τ_p is expressed as

$$\tau_{\rm p}=\frac{2\rho_{\rm p}+\rho}{9\eta_n}a_{\rm p}^2, \tag{4.9}$$

which is fairly small at our experimental temperatures (e.g., $\tau_{\rm p}\approx 4.5$ ps at $T=1.65$ K). Therefore, the viscous normal fluid fully entrains the molecules, and they are ideal tracer particles for normal fluid flow above $T=1$ K. On the other hand, these particles are trapped by quantized vortices at adequately low temperatures (i.e., $T<0.6$ K); the quantized vortices may be directly visualized in that temperature region [217].

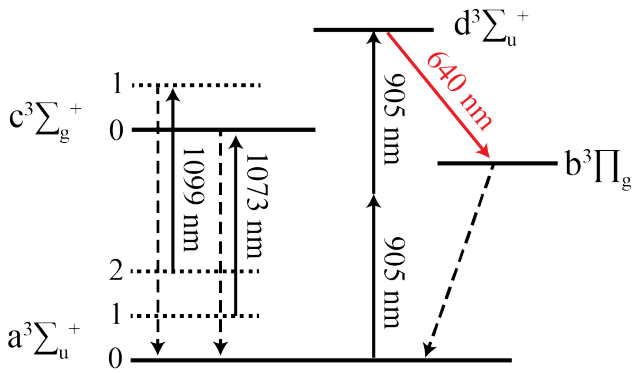

Figure 4.3: Schematic diagram illustrating the relevant metastable states of the He_2^* triplet molecules and the optical transitions related to the flow visualization. The labels of 0, 1, and 2 correspond to the vibrational levels for each electronic state.

He_2^* molecules can be barely seen, and we employ a technique called cycling-transition laser-induced fluorescence (LIF) to visualize He_2^* molecules [218, 219]. Figure 4.3 illustrates the relevant metastable states of the He_2^* triplet molecules and their low-lying optical transitions. The triplet ground state $a^3\sum_u^+$ can be excited to the electronic state $d^3\sum_u^+$ by two infrared photons of 905 nm wavelength. Over 90% of the molecules in the $d^3\sum_u^+$ state then emit red photons of 640 nm

and decay to the $b^3\Pi_g$ state within 10 ns. We detect these red photons using intensified charge-coupled device (ICCD) cameras. The $b^3\Pi_g$ state decays to the $a^3\sum_u^+$ state through the rotational and vibrational levels between these states, and the $a(1)$ and $a(2)$ states have a long vibrational-relaxation time (i.e., about 1 s). Two lasers having 1073 nm and 1099 nm wavelengths are applied to excite these two states to the $c^3\sum_u^+$ states, which quickly decay to the $a(0)$ state [219, 220].

4.1.3 Laser Optical System

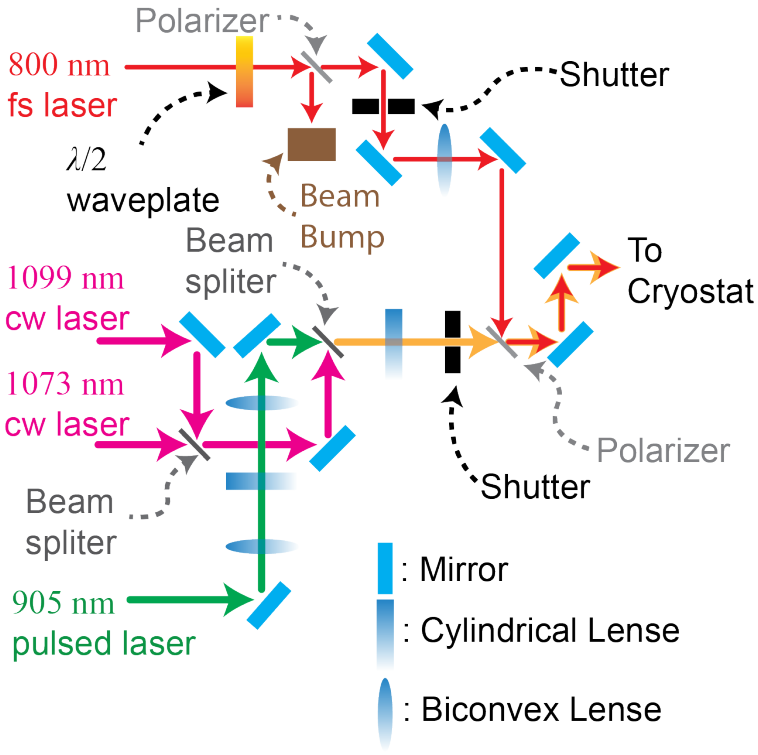

Figure 4.4: Design of the optical table

We combine multiple lasers on the optical table for the MTV visualization. The schematic of the optical table is shown in Figure 4.4. To create a femtosecond (fs) laser beam with a wavelength of 800 nm creating He_2^* molecules, we use a Spitfire Ace amplifier seeded by a Mai Tai pulsed laser and pumped by an Empower-45 laser. In addition, a pulsed laser beam with a wavelength of 905 nm and a frequency of 500 Hz is generated by an EKSPLA Nd:YAG pulsed laser to excite He_2^* molecules. To enhance the He_2^* cycling transition, we use two fiber diode continuous wave (CW) laser beams with the wavelengths of 1073 nm and 1099 nm, each with about 1W, which damp

the low-lying vibration modes $a(1)$ and $a(2)$ by exciting from $a(1)$ to $c(0)$ and $a(2)$ to $c(1)$ levels, respectively.

Laser beams expand during traveling, and the optical table is designed to adjust the focal point and the entrance beam diameter appropriately (Figure 4.4). The ideal laser intensity profile is Gaussian, corresponding to the ground transverse electromagnetic ground mode, i.e., TEM_{00}. Supposed that the wavefront is flat and the radius of the $1/e^2$ irradiance contour is w_0 at $z = 0$, the curvature radius of the wavefront after propagating a distance z is given by

$$R(z) = z\sqrt{1 + \left(\frac{\pi w_0^2}{\lambda z}\right)^2}, \tag{4.10}$$

where λ is the wavelength of the light. The radius of the $1/e^2$ contour at a distance z is then written as

$$w(z) = w_0\sqrt{1 + \left(\frac{\lambda z}{\pi w_0^2}\right)^2}. \tag{4.11}$$

In our experimental setup, the radius at the center $w(0)$ is about 60 μm. At large z, the $1/e^2$ irradiance contours approach a cone of angular radius $\lambda/\pi w_0$.

4.1.4 Cryogenics System

The design of our cryogenics system is illustrated in Figure 4.5. The system comprises a helium channel, thermal shields, and a transparent heater. The streamwise and laser directions are represented by the x- and z-direction, respectively. The helium channel is a square stainless steel channel with a cross-section dimension of roughly 9.4 mm $\times$ 9.4 mm and a length of approximately 30 cm. The top of the channel connects to a helium bath, and the temperature is accurately controlled with an accuracy of 0.1 mK by regulating the pressure. The bottom of the channel has a sapphire glass window coated with indium tin oxide (ITO) on the outside. Passing a current through the ITO coating generates heat that drives a thermal counterflow in the helium channel. The induced heat drives a thermal counterflow in the helium channel. We utilized a four-wire measurement for the resistance measurement, and the resistance is about 2.5 kΩ in our temperature range.

The channel passes through a stainless-steel cube, in which the normal fluid flow is visualized. The cube has two cylindrical side flanges featuring an indium-sealed sapphire window each. To allow for the passage of the combined laser beams, a pair of vertical slows measuring 8 mm $\times$ 12 mm is penetrated through the cube and the channel wall, minimizing laser light scattering and preventing

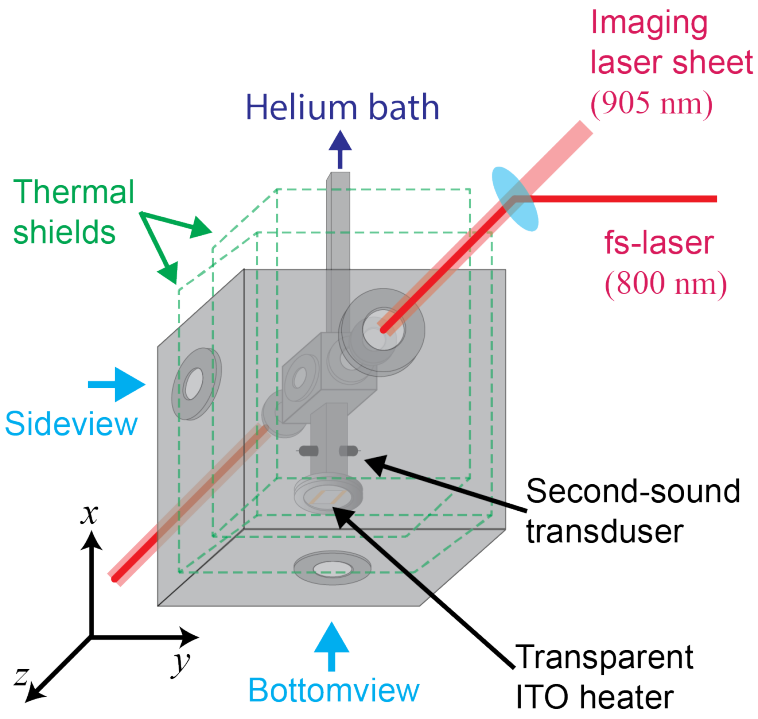

Figure 4.5: Schematic of the cryogenics system in our experimental setup.

laser-induced damage to the windows. Additionally, a sapphire view window is situated on the front side of the cube to enable the ICCD camera to capture images of the molecules being dragged in the x-direction. To pass the laser beam coming through the cryostat, the sapphire windows were installed perpendicular to the view directions; the channel has a vertical slot with a rectangle-shaped cross-section of 2.54 mm $\times$ 12.7 mm on the opposing sides. The space between the outer shell and the helium channel is vacuum, and the heat conduction between them is negligible. Hence, thermal radiation [221] is the main heat source for the helium system and can be suppressed by the two thermal shields. The outer shield is connected to liquid nitrogen ($T \sim 77$ K), and the inner shield is connected to liquid helium ($T \sim 4.15$ K).

4.1.5 Image Data Analysis

The resolution of the ICCD cameras is not high enough to tack the individual He_2^* molecules. Therefore, we apply the tracer line tracking (TLT) method utilizing a thin tracer line of triplet-state He_2^* molecules to visualize normal fluid flows in the thermal counterflow turbulence. In our experiments, we capture photos with the ICCD cameras and determine the location of the tracer line by the Newton method, in which a curved line is fitted with the fluorescence profile under

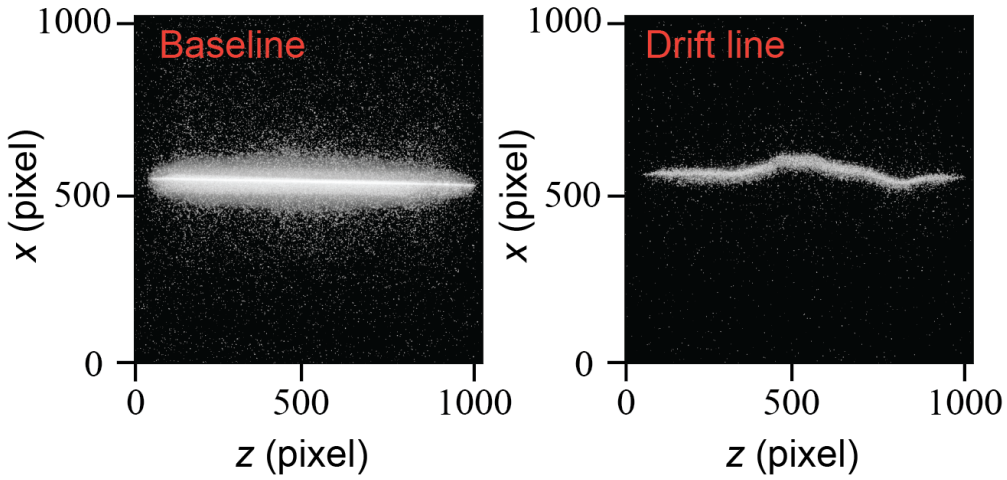

Figure 4.6: Typical Tracerlines. (Left) Baseline and (Right) drift line from the side view. The temperature is $T = 2.00$ K, the heat current is $q = 431$ mW/cm^2, and the drift time is $\Delta t_D = 20.46$ ms.

the assumption of a Gaussian noise around it [222]. The thickness of the molecular tracer line is controlled by the width of the femtosecond laser beam $w_0 = \lambda f/\pi w_f$ with the focal length of the lens f and the incident beam radius w_f. For the velocity measurement, we first take baseline images in the absence of heat current with zero drift time to determine the initial location of the tracer line. Then, tracer line images are captured after a certain drift time Δ_D. Figure 4.6 shows typical baseline and drift line pictures. By comparing them, the velocity can be calculated by

$$\boldsymbol{v}(z) = \frac{\boldsymbol{r}_{drift}(z) - \boldsymbol{r}_{base}(z)}{\Delta t_D}. \tag{4.12}$$

Analyzation of numerous samples under the same condition provides a probability density of the velocity. We typically take 100 to 150 samples for each case. The probability density function is fit with the Gaussian distribution to determine the mean speed v_a and standard deviation w_a for $a \in \{x, y\}$ (Figure 4.7). The bubbles trapping the He_2^* molecules may diffuse during the drifting, and the visualization line may be expanded. However, this effect is estimated to be negligible in our temperature range [218, 223].

4.2 Experimental Results and Discussions

At low levels of heat flux q in which the flow remains laminar, the velocity in the streamwise direction v_x is expected to be Hagen–Poiseuille-like flows (Equation 1.151). However, once the heat

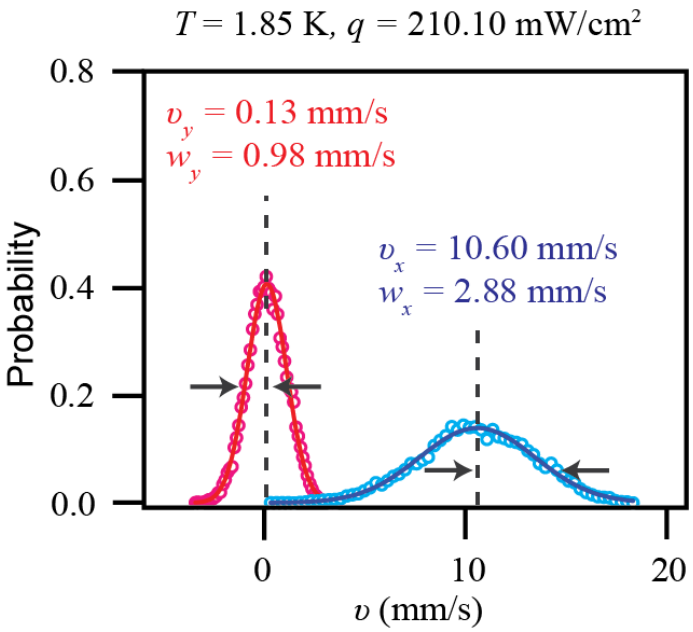

Figure 4.7: Probability density function of velocity with $T = 1.85$ K and $q = 210.10$ mW/cm^2.

flux surpasses a critical value, the superfluid flows become turbulent (i.e., T-I state). In this study, we focus on T-II states where both the normal fluid component and the superfluid component are turbulent.

Figure 4.8 shows the velocity profiles $v_a(z)$ and the compensated energy spectra $k^{5/3}\mathcal{E}_a(k)$ for $a \in \{x, y\}$. In this case, the temperature and heat flux are $T = 1.85$ K and $q = 380.58$ mW/cm^2, in which the flow is in the T-II state. To discuss the turbulent nature, we calculate the velocity fluctuation $u_a(z) = v_a(z) - \langle v_a(z)\rangle_{im}$, where $\langle\rangle_{im}$ denotes the ensemble average over the images. When examining turbulence, the energy spectrum can provide valuable insights. In isotropic 3D turbulence, the energy spectrum depends only on the amplitude of the wave number vector. However, angular dependency is present in anisotropic turbulence. To gain insight into the anisotropy of thermal counterflow turbulence, we plot the 1D energy spectra along both the streamwise and perpendicular directions given by

$$\mathcal{E}_a(k) = \sum_{k \le k' < k+\Delta k} \langle |\breve{u}_a(k')|^2 \rangle_{im}\,, \tag{4.13}$$

where $\breve{u}_a(k)$ is the 1D Fourier series of $u_a(z)$ along the tracer line in z-direction defined as

$$\breve{u}_a(k) = \frac{1}{N}\sum_z u_a(z) e^{-ikz} \tag{4.14}$$

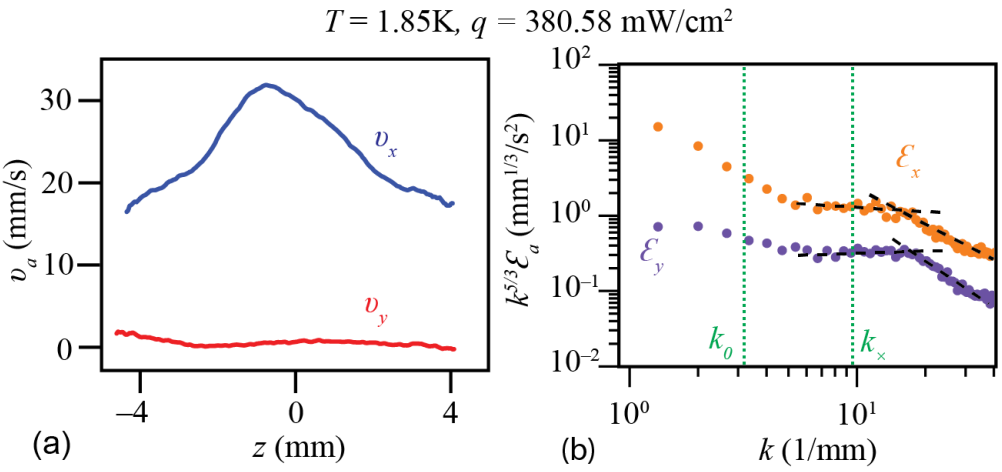

Figure 4.8: (a) Averaged velocity profile and (b) energy spectrum compensated by $k^{5/3}$ in the stream direction and perpendicular directions. The parameters are $T = 1.85$K and $q = 380.58$ mW/cm^2.

with the total grid number N. The energy spectra in Figure 4.8b confirm the anisotropic nature of thermal counterflow turbulence in He II, and the streamwise component ($a = x$) carries more turbulent energy than the perpendicular component ($a = y$).

Figure 4.9 shows the ensemble-averaged velocity $\langle v_a(z)\rangle_{im}$ and turbulent velocity defined by

$$w_a(z) = \sqrt{\langle |v_a(z) - \langle v_a(z)\rangle_{im}|^2\rangle_{im}}. \tag{4.15}$$

We obtain the profile of velocity fluctuation from these data and calculate the energy spectra and structure functions as shown in the following.

Figure 4.10 shows the energy spectra with various temperatures $T \in \{1.65\text{ K}, 1.85\text{ K}, 2.00\text{ K}\}$. The spectra can be classified into three intervals [204]: the energy-containing interval, the cascade-dominated interval, and the mutual-friction-dominated interval. The energy is injected into the turbulent flows in the outer scale of turbulence ($k < k_0$), where $k_0 := 2\pi/r_0$ with $r_0 \approx 2$ mm near the peak of the structure-function as explained later [203]. There is a competition between the mutual friction term and the convection term. The decoupling wave number $k_\times$ is estimated as $k_\times := \kappa\mathcal{L}/V_{ns}$. Below $k_\times$, the mutual friction term is small and the energy spectrum is in the cascade-dominated interval, in which the energy spectrum is expected to be similar to the classical Richardson-Kolmogorov cascade $\mathcal{E}_a(k) \propto k^{-5/3}$. Above $k_\times$, the mutual friction is the primary mechanism of energy dissipation, and the energy spectrum quickly decreases as the wavenumber k increases. This range is called the mutual-friction-dominated interval. In the case with $T = 1.85$ K

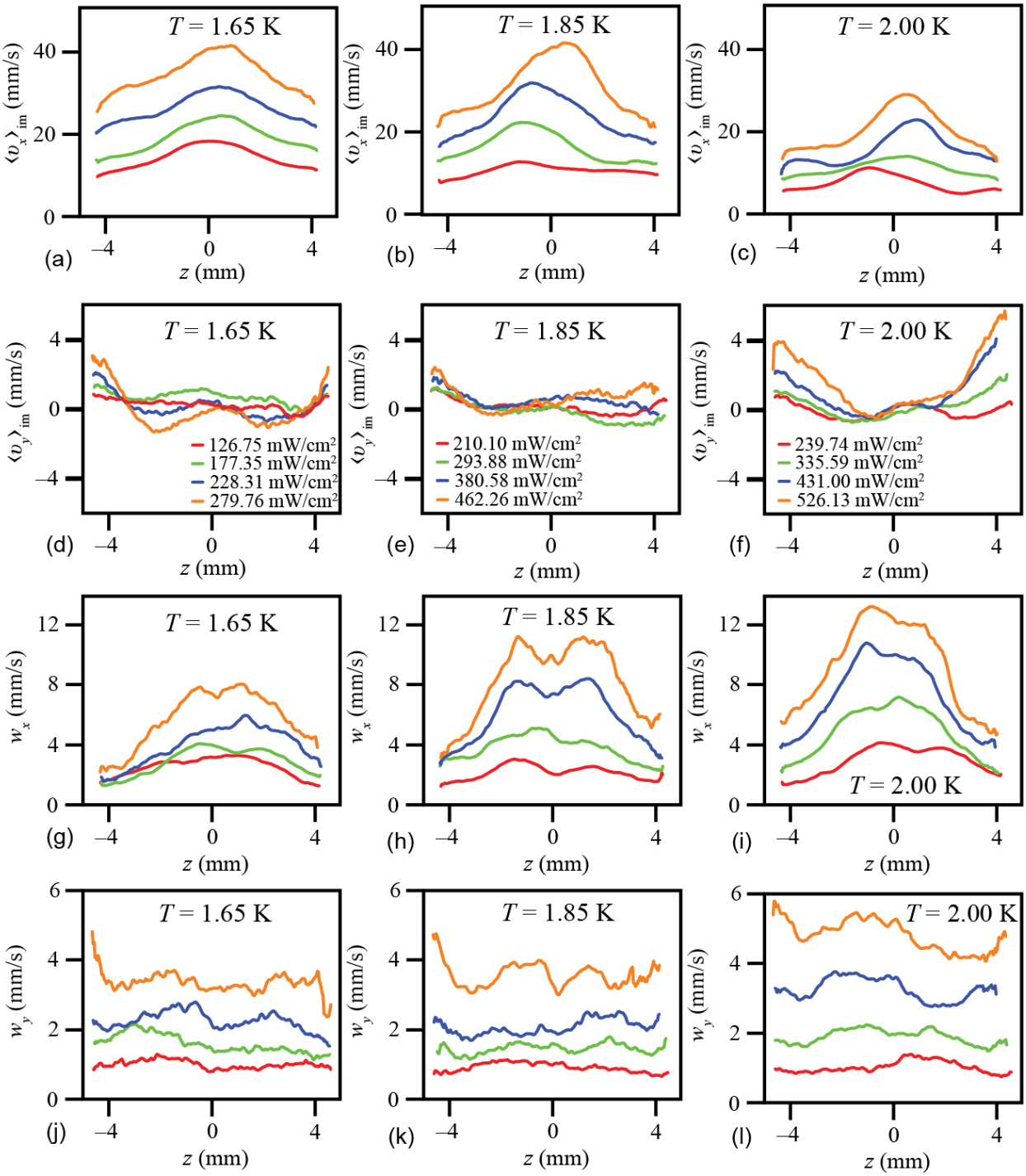

Figure 4.9: (a-c) Ensemble-averaged velocity in the streamwise direction $\langle u_x(z)\rangle_{\text{im}}$. (d-f) Ensemble-averaged velocity in the perpendicular direction $\langle u_y(z)\rangle_{\text{im}}$. (g-i) Turbulent fluctuation in the streamwise direction $w_x(z)$. (j-l) Turbulent fluctuation in the perpendicular direction $w_y(z)$.

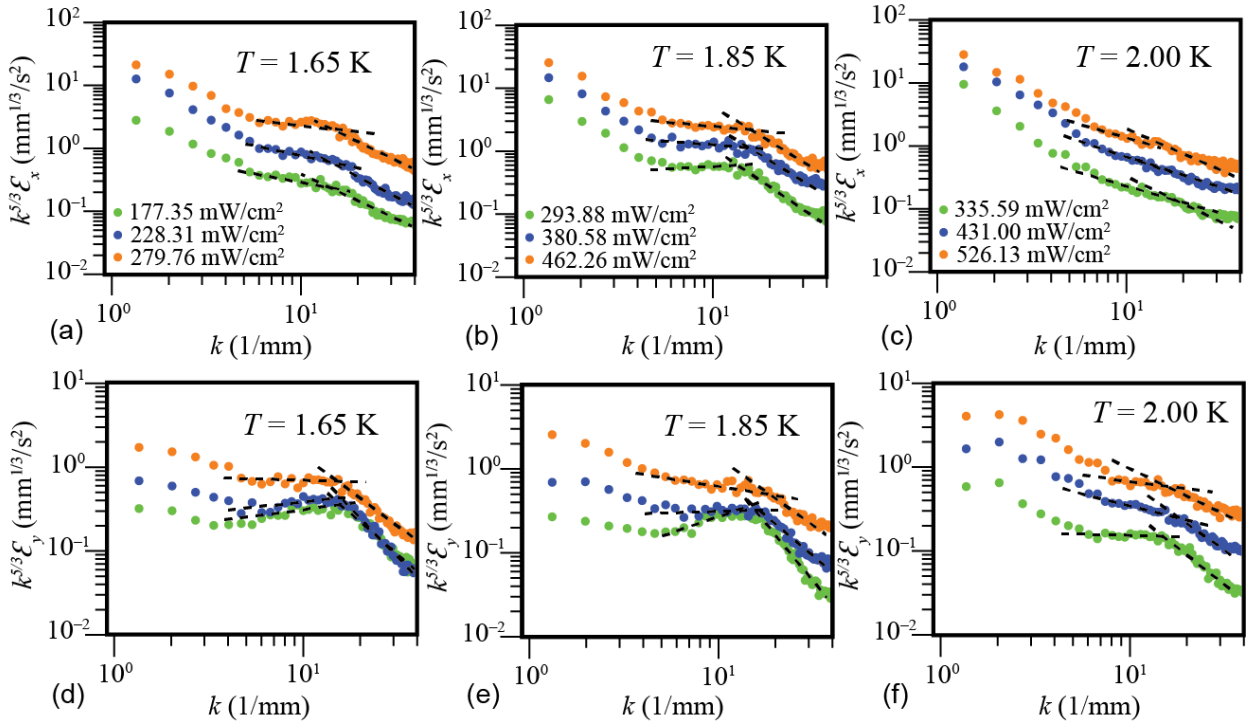

Figure 4.10: 1D energy spectra compensated by the K41 scaling $k^{5/3}\mathcal{E}_a$ in (a-c) the streamwise direction and (d-f) the perpendicular direction.

and $q = 210.10$ mW/cm^2 in Figure 4.8, these key wavenumbers are calculated as $k_0 \approx 3.14$ mm^{-1} and $k_\times \approx 9.08$ mm^{-1}. The energy spectra in each case have two cascades, denoted as $\mathcal{E} \propto k^{-m_a^C}$ in the cascade-dominated interval and $\mathcal{E} \propto k^{-m_a^F}$ in the mutual-friction-dominated interval for $a \in \{x, y\}$. Since the key wave numbers k_0 and $k_\times$ are just estimations, we choose power indexes m_a^J for $J \in \{C, F\}$ to maximize the k interval where the compensated energy spectrum $k^{-m_a^J}\mathcal{E}(k)$ is almost constant.

To probe the energy spectrum, we calculate the 1D second-order structure function defined as

$$S_a(R) = \langle [u_a(R+z) - u_a(z)]^2 \rangle_{z,im} \qquad a \in \{x, y\} \tag{4.16}$$

where $\langle\rangle_{z,im}$ indicates the combination of the spatial average with all discretized positions on the line z and the ensemble average over the images. As seen in these results, the peak exists at $z \approx 2mm$, which agrees with the primary 1D measurement [203].

Our experimental results summarized in Table 4.1 show interesting results. We anticipate that the power index of the energy spectra in the cascade-dominated interval ($m_{a,C}$ for $a \in \{x, y\}$) will conform to Kolmogorov scaling, which is roughly 1.67. Nonetheless, we have observed a

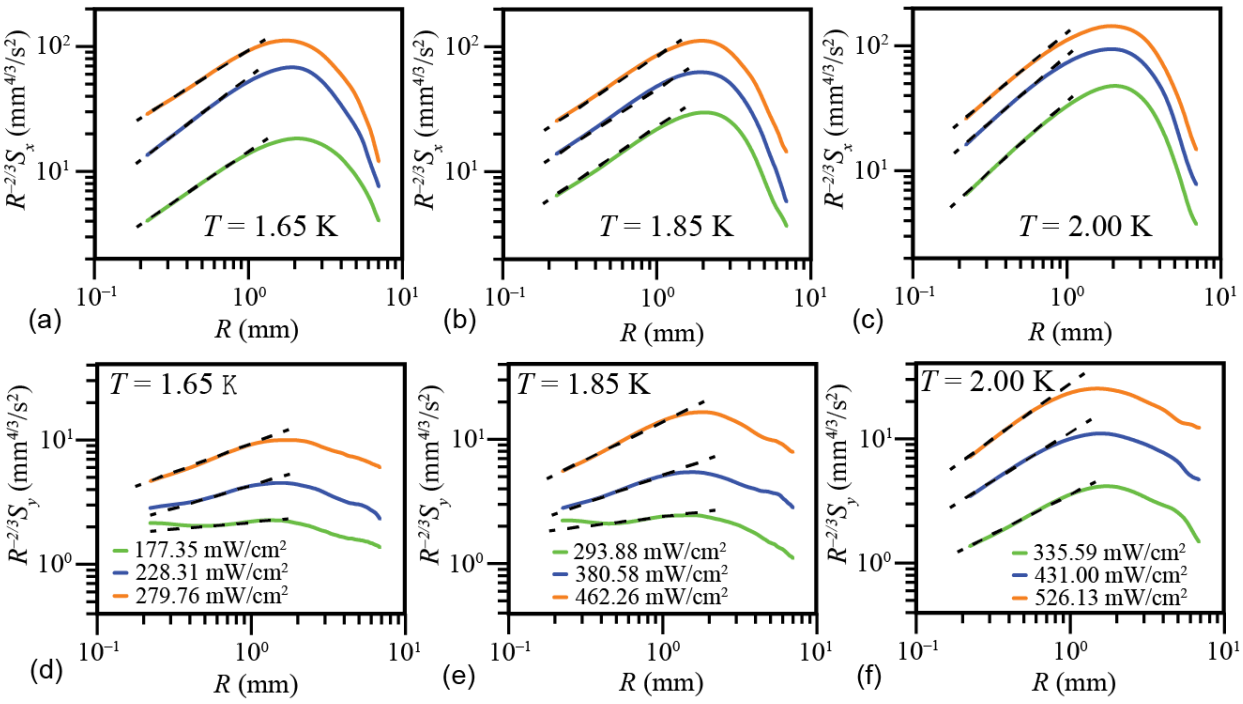

Figure 4.11: Structure function compensated by the K41 scaling $R^{-2/3}S_a(R)$ in (a-c) the streamwise direction and (d-f) the perpendicular direction.

discrepancy that progressively grows with temperature. At 2.00 K, distinguishing between the cascade-dominated interval and the mutual-friction-dominated interval based on the power indexes becomes troublesome. This variation occurs due to the dissipation of energy by mutual friction, which is clarified by the Gorter-Mellink formula (Equation 1.163). The coefficient $A_{GM}\rho_s\rho_n$ displayed in Table 4.2 climbs with temperature. Additionally, mutual friction increases cubicly as the counterflow velocity increases (i.e., v_{ns}^3). Greater mutual friction can effectively dampen the energy and influence the power index of the energy spectra in the cascade-dominated interval.

4.3 Simulation Method

To examine our experimental results, we work on the simulations with the HVBK equation (Equations 1.84, 1.156, 1.165) by the Fourier spectrum method.

4.3.1 Equations for the Thermal Counterflow Turbulence

We employ the HVBK equation (Equations 1.84, 1.156, 1.165) to simulate the velocity fields $\boldsymbol{v}_c(\boldsymbol{r}, t)$ of the superfluid component ($c = s$) and the normal fluid component ($c = n$) in the

Table 4.1: Experimental conditions and results. Columns 1-3: the experimental setups. Column 4: the estimated mutual velocity. Columns 5-8: the fitted power low of the energy spectrum. Columns 9-10: the fitted power low of the second-order structure function.

$T[K]$	$q[\mathrm{mW/cm^2}]$	Δt_D [ms]	V_{ns} [mm/s]	m_x^C	m_x^F	m_y^C	m_y^F	n_x	n_y
1.65	177.35	29.75	27.47	2.29	3.62	1.47	3.85	1.48	0.73
	228.30	19.76	35.36	2.20	3.70	1.47	4.20	1.56	0.99
	279.26	14.73	43.34	1.99	3.36	1.77	3.63	1.46	1.14
1.85	293.88	19.71	27.58	1.51	4.03	0.92	4.32	1.51	0.79
	380.57	19.84	35.72	1.89	3.43	1.57	3.81	1.52	1.10
	462.29	14.71	43.39	2.01	3.42	1.90	3.43	1.49	1.31
2.00	335,58	29.78	27.59	2.65	2.96	1.71	3.52	1.72	1.32
	430.85	19.73	35.43	2.68	2.67	2.29	3.16	1.63	1.32
	526.13	14.64	43.25	2.52	2.55	2.24	2.89	1.58	1.39

Table 4.2: Coefficient of the Gorter–Mellink formula of the mutual friction.

T [K]	$A_{\mathrm{GM}}\rho_s\rho_n[\mathrm{kg\ s/mm^5}]$
1.65	2.13×10^{-9}
1.85	4.86×10^{-9}
2.00	6.55×10^{-9}

counterflow turbulence:

$$\frac{\partial \boldsymbol{v}_c}{\partial t} + \boldsymbol{v}_c \cdot \boldsymbol{\nabla} \boldsymbol{v}_c = -\frac{\boldsymbol{\nabla} p_c}{\rho_c} + \nu_c \Delta \boldsymbol{v}_c + \boldsymbol{F}_c \tag{4.17}$$

$$\boldsymbol{\nabla} \cdot \boldsymbol{v}_c = 0 \tag{4.18}$$

with

$$p_n = \frac{\rho_n}{\rho}\left[p + \frac{\rho_s}{2}\left|\boldsymbol{v}_n - \boldsymbol{v}_s\right|^2\right] \tag{4.19}$$

$$p_s = \frac{\rho_s}{\rho}\left[p - \frac{\rho_n}{2}\left|\boldsymbol{v}_n - \boldsymbol{v}_s\right|^2\right] \tag{4.20}$$

$$\boldsymbol{F}_n = \frac{1}{\rho_n}\boldsymbol{F}_{ns} \tag{4.21}$$

$$\boldsymbol{F}_s = -\frac{1}{\rho_s}\boldsymbol{F}_{ns}. \tag{4.22}$$

Here, the velocities of both components are incompressible (i.e., $\boldsymbol{\nabla} \cdot \boldsymbol{v}_c = 0$). Decomposing the velocities into the space averaged velocity $\boldsymbol{U}_c = \langle \boldsymbol{v}_c \rangle$ and the velocity fluctuation $\boldsymbol{u}_c$ (i.e., $\boldsymbol{v}_c = \boldsymbol{U}_c + \boldsymbol{u}_c$), we obtain the equations of the velocity fluctuations:

$$\frac{\partial \boldsymbol{u}_c}{\partial t} + (\boldsymbol{U}_c + \boldsymbol{u}_c) \cdot \boldsymbol{\nabla} \boldsymbol{u}_c = -\frac{\boldsymbol{\nabla} p_c'}{\rho_c} + \nu_c \Delta \boldsymbol{u}_c + \boldsymbol{f}_c + \boldsymbol{\phi}_c \tag{4.23}$$

$$\boldsymbol{\nabla} \cdot \boldsymbol{u}_c = 0, \tag{4.24}$$

where p_c' and $\boldsymbol{f}_c$ are the fluctuation part of the pressure and the mutual friction force, respectively. Also, we introduce external forces $\boldsymbol{\phi}_c$, and the details are discussed later. Note that the fluctuation of the mutual friction forces is given by $\boldsymbol{f}_s = -(\rho_n/\rho_s)\boldsymbol{f}_n = \boldsymbol{f}_{ns}$, where $\boldsymbol{f}_{ns} = \alpha\kappa\mathcal{L}(\boldsymbol{u}_n - \boldsymbol{u}_s)$ (Equation 1.165).

Applying a curl to Equation 4.23, we obtain the equation for the vorticity fluctuation:

$$\frac{\partial \boldsymbol{\omega}_c}{\partial t} + \boldsymbol{U}_c \cdot \boldsymbol{\nabla}\boldsymbol{\omega}_c - \boldsymbol{\nabla} \times (\boldsymbol{u}_c \times \boldsymbol{\omega}_c) = \nu_c \Delta \boldsymbol{\omega}_c + \boldsymbol{g}_c + \boldsymbol{\nabla} \times \boldsymbol{\phi}_c \tag{4.25}$$

$$\boldsymbol{\nabla} \cdot \boldsymbol{\omega}_c = 0, \tag{4.26}$$

where $\boldsymbol{\omega} = \boldsymbol{\nabla} \times \boldsymbol{v} = \boldsymbol{\nabla} \times \boldsymbol{u}$ is the vorticity fluctuation and $\boldsymbol{g}_s = -(\rho_n/\rho_s)\boldsymbol{g}_n = \boldsymbol{\nabla} \times \boldsymbol{f}_s = \alpha\kappa\mathcal{L}\left(\boldsymbol{\omega}_n - \boldsymbol{\omega}_s\right)$ is the mutual friction for vorticity. Also, from a formula of the vector calculus

$$\left(\boldsymbol{u} \cdot \boldsymbol{\nabla}\right)\boldsymbol{u} = \frac{1}{2}\boldsymbol{\nabla}\boldsymbol{u}^2 - \boldsymbol{u} \times \left(\boldsymbol{\nabla} \times \boldsymbol{u}\right), \tag{4.27}$$

we obtain

$$\boldsymbol{\nabla} \times \left\{\left(\boldsymbol{u} \cdot \boldsymbol{\nabla}\right)\boldsymbol{u}\right\} = \boldsymbol{\nabla} \times \left\{\frac{1}{2}\boldsymbol{\nabla}\boldsymbol{u}^2 - \boldsymbol{u} \times \left(\boldsymbol{\nabla} \times \boldsymbol{u}\right)\right\} \tag{4.28}$$

$$= -\boldsymbol{\nabla} \times \left(\boldsymbol{u} \times \boldsymbol{\omega}\right). \tag{4.29}$$

We apply this relationship to the convection term. We use this vortex fluctuation equation (Equation 4.25) in our simulations because the pressure term does not appear, and the number of Fourier and inverse-Fourier transforms for the convection term can be reduced.

Wavenumber Space. The discretized Fourier transform is given by

$$\check{\boldsymbol{u}}\left(k_x, k_y, k_z\right) = \frac{1}{N^3}\sum_{x,y,z} \boldsymbol{u}(x,y,z)e^{-i\boldsymbol{k}\cdot\boldsymbol{r}} \tag{4.30}$$

$$\boldsymbol{u}\left(x,y,z\right) = \sum_{k_x,k_y,k_z} \check{\boldsymbol{u}}(k_x,k_y,k_z)e^{i\boldsymbol{k}\cdot\boldsymbol{r}}, \tag{4.31}$$

where N is the grid number in each direction. In this calculation, we suppose the periodic boundary conditions with system size L, and the wave number vector is given by

$$\boldsymbol{k} = \frac{2\pi}{L}\left(n_x, n_y, n_z\right). \qquad n_x, n_y, n_z \in \{0, 1, 2, \cdots, N\}. \tag{4.32}$$

Applying the Fourier transform (Equation 4.31) to the equation for the vorticity fluctuation (Equation 4.25) and the incompressible condition (Equation 4.26), we obtain

$$\begin{aligned}
\frac{\partial \check{\boldsymbol{\omega}}_s}{\partial t} &= -\left(iU_s k_x + \nu_s k^2\right)\check{\boldsymbol{\omega}}_s + \alpha\kappa\mathcal{L}\left(\check{\boldsymbol{\omega}}_n - \check{\boldsymbol{\omega}}_s\right) \\
&\quad + i\boldsymbol{k}\times\check{\boldsymbol{\phi}}_s + \frac{1}{N^3}\sum_{\boldsymbol{r}}\boldsymbol{\nabla}\times\left(\boldsymbol{u}_s\times\boldsymbol{\omega}_s\right)e^{-i\boldsymbol{k}\cdot\boldsymbol{r}} \\
&=: H_s(t), \qquad (4.33) \\
\frac{\partial \check{\boldsymbol{\omega}}_n}{\partial t} &= -\left(iU_n k_x + \nu_n k^2\right)\check{\boldsymbol{\omega}}_n + \alpha\frac{\rho_s}{\rho_n}\kappa\mathcal{L}\left(\check{\boldsymbol{\omega}}_s - \check{\boldsymbol{\omega}}_n\right) \\
&\quad + i\boldsymbol{k}\times\check{\boldsymbol{\phi}}_n + \frac{1}{N^3}\sum_{\boldsymbol{r}}\boldsymbol{\nabla}\times\left(\boldsymbol{u}_n\times\boldsymbol{\omega}_n\right)e^{-i\boldsymbol{k}\cdot\boldsymbol{r}} \\
&=: H_n(t), \qquad (4.34) \\
\mathbf{k}\cdot\check{\boldsymbol{\omega}}_{\mathbf{c}} &= 0. \qquad (4.35)
\end{aligned}$$

Since $\boldsymbol{\nabla}\times\boldsymbol{\omega} = \boldsymbol{\nabla}\times(\boldsymbol{\nabla}\times\boldsymbol{u}) = \boldsymbol{\nabla}(\boldsymbol{\nabla}\cdot\boldsymbol{u}) - \Delta\boldsymbol{u} = -\Delta\boldsymbol{u}$, the velocity fluctuation $\check{\boldsymbol{u}}(\boldsymbol{k},t)$ can be derived from the vorticity fluctuation $\check{\boldsymbol{\omega}}(\boldsymbol{k},t)$ as

$$i\boldsymbol{k}\times\check{\boldsymbol{\omega}}(\boldsymbol{k},t) = k^2\check{\boldsymbol{u}}(\boldsymbol{k},t) \qquad (4.36)$$

except at $\boldsymbol{k}=0$. The bulk velocity is supposed to be constant, so the components at $\boldsymbol{k}=\mathbf{0}$ should always be zero (i.e., $\check{\boldsymbol{u}}(0,t)=\mathbf{0}$ and $\check{\boldsymbol{\omega}}(0,t)=\mathbf{0}$).

4.3.2 Fourier-Spectrum Method

We apply the Fourier-spectrum method, evolving the fields in $\boldsymbol{k}$-space [224]. Due to the incompressible condition (Equation 4.35), the three-dimensional field has only two degrees of freedom. Corresponding to this fact, we define two variables $\check{\xi}_1(k_x,k_y,k_z)$ and $\check{\xi}_2(k_x,k_y,k_z)$ to represent the three-dimensional vorticity fluctuation field $\check{\boldsymbol{\omega}}$ as follows:

if $k_x \neq 0$

$$\check{\xi}_1 = \check{\omega}_y,\ \check{\xi}_2 = \check{\omega}_z, \qquad (4.37)$$

else if $k_y \neq 0$

$$\check{\xi}_1 = \check{\omega}_z,\ \check{\xi}_2 = \check{\omega}_x, \qquad (4.38)$$

else if $k_z \neq 0$

$$\check{\xi}_1 = \check{\omega}_x,\ \check{\xi}_2 = \check{\omega}_y, \qquad (4.39)$$

else (i.e., $k_x=0$, $k_y=0$, and $k_y=0$)

$$\check{\xi}_1 = 0,\ \check{\xi}_2 = 0. \qquad (4.40)$$

Then, the components of the velocity fluctuation field $\check{\boldsymbol{v}}$ are expressed with ξ_1 and ξ_2 as follows:
if $k_x \neq 0$

$$\check{u}_x = \frac{i}{k^2}\left(k_y\check{\xi}_2 - k_z\check{\xi}_1\right) \tag{4.41}$$

$$\check{u}_y = -\frac{i}{k^2 k_x}\left\{k_y k_z\check{\xi}_1 + \left(k_z^2 + k_x^2\right)\check{\xi}_2\right\} \tag{4.42}$$

$$\check{u}_z = \frac{i}{k^2 k_x}\left\{\left(k_x^2 + k_y^2\right)\check{\xi}_1 + k_y k_z\check{\xi}_2\right\}, \tag{4.43}$$

else if $k_y \neq 0$

$$\begin{aligned}\check{u}_x &= \frac{i}{k^2 k_y}\left\{\left(k_y^2 + k_z^2\right)\check{\xi}_1 + k_z k_x\check{\xi}_2\right\} \\ &= i\frac{1}{k_y}\check{\xi}_1 \end{aligned} \tag{4.44}$$

$$\begin{aligned}\check{u}_y &= \frac{i}{k^2}\left(k_z\check{\xi}_2 - k_x\check{\xi}_1\right) \\ &= i\frac{k_z}{k_y^2 + k_z^2}\check{\xi}_2 \end{aligned} \tag{4.45}$$

$$\begin{aligned}\check{u}_z &= -\frac{i}{k^2 k_y}\left\{k_z k_x\check{\xi}_1 + \left(k_x^2 + k_y^2\right)\check{\xi}_2\right\} \\ &= -i\frac{k_y}{k_y^2 + k_z^2}\check{\xi}_2, \end{aligned} \tag{4.46}$$

else if $k_z \neq 0$

$$\begin{aligned}\check{u}_x &= -\frac{i}{k^2 k_z}\left\{k_x k_y\check{\xi}_1 + \left(k_y^2 + k_z^2\right)\check{\xi}_2\right\} \\ &= -\frac{i}{k_z}\check{\xi}_2 \end{aligned} \tag{4.47}$$

$$\begin{aligned}\check{u}_y &= \frac{i}{k^2 k_z}\left\{\left(k_z^2 + k_x^2\right)\check{\xi}_1 + k_x k_y\check{\xi}_2\right\} \\ &= \frac{i}{k_z}\check{\xi}_1 \end{aligned} \tag{4.48}$$

$$\check{u}_z = \frac{i}{k^2}\left(k_x\check{\xi}_2 - k_y\check{\xi}_1\right) = 0. \tag{4.49}$$

The evolution equations (Equations 4.33 and 4.34) are discretized with the second-order Adams-Bashforth method [142] as

$$\check{\boldsymbol{\omega}}_s(t+\Delta t) = \check{\boldsymbol{\omega}}_s(t) + \frac{\Delta t}{2}\left(3H_s(t) - H_s(t-\Delta t)\right) \tag{4.50}$$

$$\check{\boldsymbol{\omega}}_n(t+\Delta t) = \check{\boldsymbol{\omega}}_n(t) + \frac{\Delta t}{2}\left(3H_n(t) - H_n(t-\Delta t)\right). \tag{4.51}$$

The calculation of $H_c(t)$ follows three steps:

1. We calculate the convection term associated with the zeroth order velocity, the dissipation term, and the mutual friction term (e.g., $-\left(iU_s k_x + \nu_s k^2\right)\check{\boldsymbol{\omega}}_s + \alpha\kappa\mathcal{L}\left(\check{\boldsymbol{\omega}}_n - \check{\boldsymbol{\omega}}_s\right)$ for the superfluid component)

2. A random force $\check{\boldsymbol{\phi}}_c$ is generated to calculate the random force term (i.e., $i\boldsymbol{k}\times\check{\boldsymbol{\phi}}_c$)

3. The convection term (i.e., $\sum_{\boldsymbol{r}}\boldsymbol{\nabla}\times\left(\boldsymbol{u}_c\times\boldsymbol{\omega}_c\right)e^{-i\boldsymbol{k}\cdot\boldsymbol{r}}/N^3$) is calculated.

In the third step, we calculate the convection term in real space to avoid the correlation calculation in the $\boldsymbol{k}$-space. Since the $\boldsymbol{u}\times\boldsymbol{\omega}$ term can be expressed by the velocity field as follows:

$$\begin{aligned}
\left(\boldsymbol{u}\times\boldsymbol{\omega}\right)_x &= u_y\omega_z - u_z\omega_y \\
&= u_y\left(\partial_x u_y - \partial_y u_x\right) - u_z\left(\partial_z u_x - \partial_x u_z\right) \\
&= \frac{1}{2}\partial_x\left(u_y^2 + u_z^2\right) - u_y\partial_y u_x - u_z\partial_z u_x \\
&= \frac{1}{2}\partial_x\left(u_y^2 + u_z^2\right) - \partial_y\left(u_x u_y\right) - \partial_z\left(u_z u_x\right) + u_x\left(\partial_y u_y + \partial_z u_z\right) \\
&= \frac{1}{2}\partial_x\left(u_y^2 + u_z^2 - u_x^2\right) - \partial_y\left(u_x u_y\right) - \partial_z\left(u_z u_x\right) \qquad (4.52) \\
\left(\boldsymbol{u}\times\boldsymbol{\omega}\right)_y &= \frac{1}{2}\partial_y\left(u_z^2 + u_x^2 - u_y^2\right) - \partial_z\left(u_y u_z\right) - \partial_x\left(u_x u_y\right) \qquad (4.53) \\
\left(\boldsymbol{u}\times\boldsymbol{\omega}\right)_z &= \frac{1}{2}\partial_z\left(u_x^2 + u_y^2 - u_z^2\right) - \partial_x\left(u_z u_x\right) - \partial_y\left(u_y u_z\right), \qquad (4.54)
\end{aligned}$$

we may write the $\boldsymbol{\nabla}\times\left(\boldsymbol{u}\times\boldsymbol{\omega}\right)$ term as

$$\begin{aligned}
\left(\boldsymbol{\nabla}\times\left(\boldsymbol{u}\times\boldsymbol{\omega}\right)\right)_x &= \partial_y\left(\boldsymbol{u}\times\boldsymbol{\omega}\right)_z - \partial_z\left(\boldsymbol{u}\times\boldsymbol{\omega}\right)_y \\
&= \partial_y\partial_z\left(u_y^2 - u_z^2\right) - \left(\partial_y^2 - \partial_z^2\right)\left(u_y u_z\right) + \partial_x\left(\partial_z\left(u_x u_y\right) - \partial_y\left(u_z u_x\right)\right) \qquad (4.55) \\
\left(\boldsymbol{\nabla}\times\left(\boldsymbol{u}\times\boldsymbol{\omega}\right)\right)_y &= \partial_z\partial_x\left(u_z^2 - u_x^2\right) - \left(\partial_z^2 - \partial_x^2\right)\left(u_z u_x\right) + \partial_y\left(\partial_x\left(u_y u_z\right) - \partial_z\left(u_x u_y\right)\right) \qquad (4.56) \\
\left(\boldsymbol{\nabla}\times\left(\boldsymbol{u}\times\boldsymbol{\omega}\right)\right)_z &= \partial_x\partial_y\left(u_x^2 - u_y^2\right) - \left(\partial_x^2 - \partial_y^2\right)\left(u_x u_y\right) + \partial_z\left(\partial_y\left(u_z u_x\right) - \partial_x\left(u_y u_z\right)\right) \\
&= -\partial_x\partial_y\left(\left(u_z^2 - u_x^2\right) + \left(u_y^2 - u_z^2\right)\right) \\
&\quad - \left(\partial_x^2 - \partial_y^2\right)\left(u_x u_y\right) + \partial_z\left(\partial_y\left(u_z u_x\right) - \partial_x\left(u_y u_z\right)\right). \qquad (4.57)
\end{aligned}$$

Taking the inverse Fourier series from $\check{\boldsymbol{u}}(\boldsymbol{k})$ to $\boldsymbol{u}(\boldsymbol{r})$, we can simplify the calculation by taking the Fourier series of of the independent terms (i.e., u_xu_y, u_yu_z, u_zu_x, $u_y^2-u_z^2$, and $u_z^2-u_x^2$) such as

$$\begin{aligned}
\frac{1}{N^3}\sum_{\boldsymbol{r}}\left(\boldsymbol{\nabla}\times(\boldsymbol{u}_c\times\boldsymbol{\omega}_c)\right)_x e^{-i\boldsymbol{k}\cdot\boldsymbol{r}} &= -\boldsymbol{k}_y\boldsymbol{k}_z\widetilde{\left(u_y^2-u_z^2\right)}+\left(\boldsymbol{k}_y^2-\boldsymbol{k}_z^2\right)\widetilde{(u_yu_z)} \\
&\quad -\boldsymbol{k}_x\left(\boldsymbol{k}_z\widetilde{(u_xu_y)}-\boldsymbol{k}_y\widetilde{(u_zu_x)}\right) \qquad (4.58)\\
\frac{1}{N^3}\sum_{\boldsymbol{r}}\left(\boldsymbol{\nabla}\times(\boldsymbol{u}_c\times\boldsymbol{\omega}_c)\right)_y e^{-i\boldsymbol{k}\cdot\boldsymbol{r}} &= -\boldsymbol{k}_z\boldsymbol{k}_x\widetilde{(u_z^2-u_x^2)}+\left(\boldsymbol{k}_z^2-\boldsymbol{k}_x^2\right)\widetilde{(u_zu_x)} \\
&\quad -\boldsymbol{k}_y\left(\boldsymbol{k}_x\widetilde{(u_yu_z)}-\boldsymbol{k}_z\widetilde{(u_xu_y)}\right) \qquad (4.59)\\
\frac{1}{N^3}\sum_{\boldsymbol{r}}\left(\boldsymbol{\nabla}\times(\boldsymbol{u}_c\times\boldsymbol{\omega}_c)\right)_z e^{-i\boldsymbol{k}\cdot\boldsymbol{r}} &= \boldsymbol{k}_x\boldsymbol{k}_y\left(\widetilde{(u_z^2-u_x^2)}+\widetilde{(u_y^2-u_z^2)}\right)+\left(\boldsymbol{k}_x^2-\boldsymbol{k}_y^2\right)\widetilde{(u_xu_y)} \\
&\quad -\boldsymbol{k}_z\left(\boldsymbol{k}_y\widetilde{(u_zu_x)}-\boldsymbol{k}_x\widetilde{(u_yu_z)}\right). \qquad (4.60)
\end{aligned}$$

It is worth noting that the kinetic energy per volume in $\boldsymbol{k}$-space is given by

$$\begin{aligned}
E_c &= \frac{1}{2V}\int dV u_c^2(\boldsymbol{r},t) \\
&= \frac{1}{2V}\int dV\sum_{\boldsymbol{k},\boldsymbol{k'}}\check{\boldsymbol{u}}_c^*(\boldsymbol{k})\check{\boldsymbol{u}}_c(\boldsymbol{k'})e^{i(\boldsymbol{k'}-\boldsymbol{k})\cdot\boldsymbol{r}} \\
&= \frac{1}{2}\sum_{\boldsymbol{k},\boldsymbol{k'}}\check{\boldsymbol{u}}_c^*(\boldsymbol{k})\check{\boldsymbol{u}}_c(\boldsymbol{k'})\delta\left(\boldsymbol{k'}-\boldsymbol{k}\right) \\
&= \frac{1}{2}\sum_{\boldsymbol{k}}|\check{\boldsymbol{u}}_c(\boldsymbol{k})|^2, \qquad (4.61)
\end{aligned}$$

and the energy density at $\boldsymbol{k}$ in $\boldsymbol{k}$-space can be expressed by ξ_1 and ξ_2 as

$$\frac{1}{2}|\check{\boldsymbol{u}}(\boldsymbol{k})|^2=\begin{cases}\left[\left(k_x^2+k_y^2\right)|\xi_1|^2+\left(k_z^2+k_x^2\right)|\xi_2|^2+k_yk_z\left(\xi_1^*\xi_2+\xi_1\xi_2^*\right)\right]/2k_x^2k^2 & (\text{if } k_x\neq 0)\\ \left[\left(k_y^2+k_z^2\right)|\xi_1|^2+\left(k_x^2+k_y^2\right)|\xi_2|^2+k_zk_x\left(\xi_1^*\xi_2+\xi_1\xi_2^*\right)\right]/2k_y^2k^2 & (\text{else if } k_y\neq 0)\\ \left[\left(k_z^2+k_x^2\right)|\xi_1|^2+\left(k_y^2+k_z^2\right)|\xi_2|^2+k_xk_y\left(\xi_1^*\xi_2+\xi_1\xi_2^*\right)\right]/2k_z^2k^2. & (\text{else if } k_z\neq 0)\end{cases} \qquad (4.62)$$

To compare the simulation results with our experimental results, we need to calculate the 1D Fourier series of the velocity (Equation 4.14) at $x=y=0$ given as

$$\begin{aligned}
\check{u}_a(k_z) &= \frac{1}{N}\sum_z u_a(0,0,z)e^{-ik_zz} \qquad (4.63)\\
&= \sum_{k_x,k_y}\sum_{k_z'}\frac{1}{N}\sum_z e^{-ik_zz}e^{ik_z'z}\check{u}_a(k_x,k_y,k_z') \qquad (4.64)\\
&= \sum_{k_x,k_y}\sum_{k_z'}\delta(k_z'-k_z)\check{u}_a(k_x,k_y,k_z') \qquad (4.65)\\
&= \sum_{k_x,k_y}\check{u}_a(k_x,k_y,k_z). \qquad (4.66)
\end{aligned}$$

4.3.3 External Force

External forces $\boldsymbol{\phi}_c$ for $c \in \{s, n\}$ are introduced to inject energy into the flows, and modeling external forces is not simple. Past studies usually utilized Gaussian random forces. In uniform and isotropic classical turbulence, the specific formula for the random force is not very important as long as the energy injection rate is similar. However, in He II counterflow turbulence, the random force's properties are critical due to its two-component anisotropic nature and the mutual friction.

Biferale et al. [225, 226] implemented time-varying Gaussian random forces $\phi_{c,j}$ for $c \in \{s, c\}$ and $j \in \{x, y, z\}$:

$$\langle \phi_{c,j}(\boldsymbol{k}, t)\phi^*_{c,j}(\boldsymbol{k}', t')\rangle = \frac{\sigma_k^2}{3k^3}\delta(\boldsymbol{k} - \boldsymbol{k}')\delta(t - t')f_w(k; k_{\min}, k_{\max}) \tag{4.67}$$

where σ_k is the amplitude of the random force. Also, we have introduced a function f_w to define the energy injection range as

$$f_w(k; k_{\min}, k_{\max}) = \begin{cases} 1 & (k_{\min} \le k \le k_{\max}) \\ 0. & \text{otherwise} \end{cases} \tag{4.68}$$

Polanco and Krstulovic [227] numerically demonstrated the $k^{-5/3}$ inverse cascade in thermal counterflow turbulence by utilizing the HVBK equation with time-constant Gaussian force defined as

$$\langle \phi_{c,j}(\boldsymbol{k})\phi^*_{c,j}(\boldsymbol{k}')\rangle = \sigma_L^2\delta(\boldsymbol{k} - \boldsymbol{k}')f_w(k; k_{\min}, k_{\max}). \tag{4.69}$$

where σ_L is the amplitude of the random force.

4.4 Simulation Results and Discussions

We follow some past studies with our parameters to confirm if our experimental results agree with their past simulation results. Our calculation utilized the second-order Adams–Bashforth method with the grids $N = 256^3$ [142].

Firstly, we follow the study of Polanco and Krstulovic [227], reporting the inverse cascade in low-k modes. Their parameters are provided as

$$\nu_n = 1.2 \times 10^{-4}\ \xi_{\mathrm{PK}}^2/\tau_{\mathrm{PK}}, \quad \nu_s = 1.5 \times 10^{-4}\ \xi_{\mathrm{PK}}^2/\tau_{\mathrm{PK}}$$
$$\alpha = 0.206, \quad \rho_s/\rho = 0.574468$$
$$U_{ns} = 10\ \xi_{\mathrm{PK}}/\tau_{\mathrm{PK}}, \quad L = 2\pi\ \xi_{\mathrm{PK}},$$

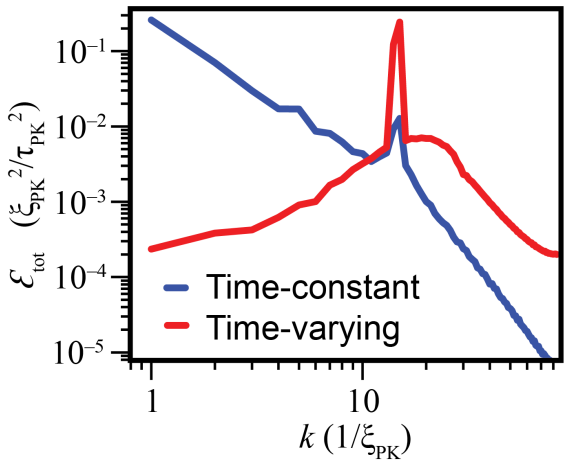

Figure 4.12: Energy spectrum $\mathcal{E}_{\rm tot}(k)$ of the steady state with the parameters of Equation 4.70. The blue and red lines correspond to the cases with time-constant and time-varying random forces, respectively.

where the corresponding temperature is $T = 1.9$ K. They also normalized the quantities by their typical length $\xi_{\rm PK}$ and time $\tau_{\rm PK}$. In their calculations, the vortex line density is estimated by $\kappa\mathcal{L} = \sqrt{\langle|\boldsymbol{\omega}_s|^2\rangle}/2$ or fixed it a value in a range $4\ \tau_{\rm PK}^{-1} \le \kappa\mathcal{L} \le 20\ \tau_{\rm PK}^{-1}$. To inject energy, they applied a time-constant Gaussian random force (Equation 4.69) only in a band $14.8\ \xi_{\rm PK}^{-1} \le k \le 15.2\ \xi_{\rm PK}^{-1}$. In this simulation, we choose $\kappa\mathcal{L} = 20\ \tau_{\rm PK}^{-1}$, and $\sigma_L = 0.06\ \xi_{\rm PK}/\tau_{\rm PK}^2$. The grid number is $N = 256^3$ and the discretized time step is $\Delta t = 5.0 \times 10^{-4}\ \tau_{\rm PK}$. Figure 4.12 shows the total energy spectrum per unit volume $\mathcal{E}_{\rm tot}(k)$ defined as

$$\mathcal{E}_{\rm tot}(k) = \frac{1}{\rho} \sum_{\substack{c=\{n,s\} \\ k \le k' < k+\Delta k}} \rho_c |\check{\boldsymbol{v}}_c(\boldsymbol{k}')|^2, \tag{4.70}$$

where $\Delta k := 2\pi/L$ is the grid size in the discretized k-space The blue curve corresponds to the case with time-constant random force, which they utilized, and the red one represents the case with time-varying random force [228]:

$$\langle \phi_{c,j}(\boldsymbol{k}, t) \phi^*_{c,j}(\boldsymbol{k}', t') \rangle = \sigma_L^2 \delta(\boldsymbol{k} - \boldsymbol{k}') \delta(t - t') f_w(k; k_{\rm min}, k_{\rm max}) \tag{4.71}$$

with $k_{\rm min} = 14.8\ \xi_{\rm PR}^{-1}$ and $k_{\rm max} = 15.2\ \xi_{\rm PR}^{-1}$. The inverse cascade appears with the steady force (i.e., blue curve). However, it does not appear in the case with the time-varying random force (i.e., red curve). These results indicate that the time-dependence of the random force is critical for the inverse cascade. It is also worth noting that the power index of the energy spectrum in the low-k interval depends on the intensity of the random force.

Furthermore, their parameters are not realistic in our system. At $T = 1.9$ K, the normal fluid viscosity is $\nu_n = 2.208 \times 10^{-2}$ mm^2/s, and the typical counterflow velocity in experiments is $U_{ns} = 30$ mm/s. Therefore, their typical length and time can be estimated as

$$\xi_{\mathrm{PK}} \approx 61 \text{ mm}, \quad \tau_{\mathrm{PK}} \approx 20 \text{ s}, \tag{4.72}$$

and the corresponding system size L and vortex line density $\mathcal{L}$ are calculated as

$$L = 2\pi\, \xi_{\mathrm{PK}} \approx 3.8 \times 10^2 \text{ mm} \tag{4.73}$$

$$\mathcal{L} \approx 10 \text{ mm}^{-2}. \tag{4.74}$$

However, in our experimental configuration, the system size is about 10 mm, and the corresponding vortex line density is about 2.5×10^3 mm^{-2}. Due to the significant discrepancy, their results cannot be directly applied to our cases.

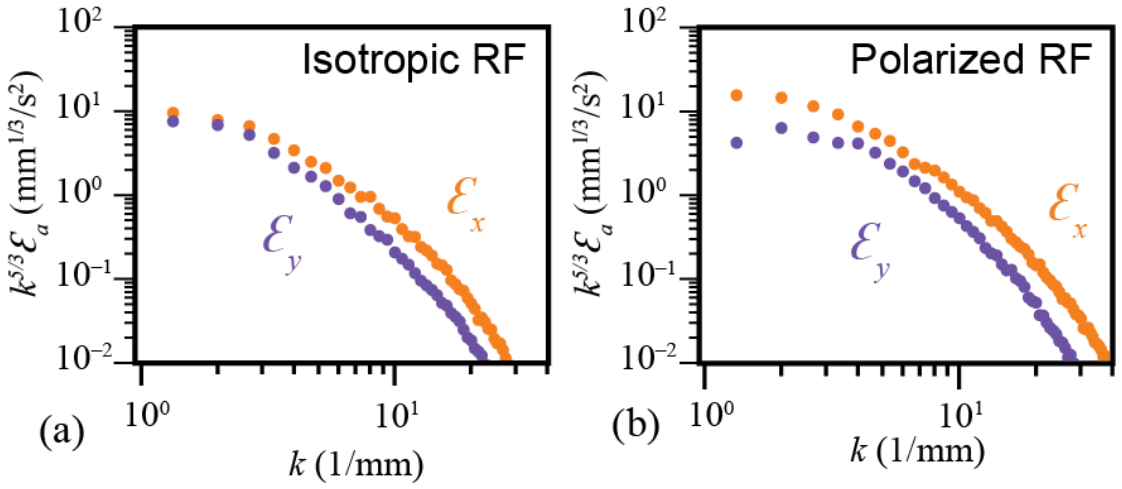

Figure 4.13: Time-averaged energy spectrum $\mathcal{E}_i(k)$ for $i \in \{x, y\}$ of the steady states. The energy is injected in the low-k region by (a) the isotropic random force and (b) the polarized random force. The orange and purple circles correspond to the energy spectra in the x and y directions, respectively. 400 samples are taken with a period of 0.1 s. The parameters correspond to the case with $T = 1.85$ K, $q = 380.57$ mW/cm^2, $\sigma_k = 15.0$ mm$^{-1/2}$s^{-2}

Next, we examine the method of Biferale et al. [202, 226]. They employed an isotropic time-varying random force (Equation 4.67) localized within a small band in low-k modes. We conduct similar simulations for our configuration. The grid number is $N = 256^3$ and the discretized time step is $\Delta t = 2.5 \times 10^{-4}$ s. The energy injection range is given by $k_{\mathrm{min}} = 0.5$ mm^{-1}, $k_{\mathrm{max}} = 3.5$ mm^{-1}.

The physical parameters correspond to the case in Figure 4.8 such as:

$$\begin{aligned}
&\nu_n = 2.5 \times 10^{-2}\ \mathrm{mm}^2/\mathrm{s}, \quad \nu_s = 2.5 \times 10^{-2}\ \mathrm{mm}^2/\mathrm{s} \\
&\alpha = 0.181, \quad \rho_s/\rho = 0.63645 \\
&L = 9.4\ \mathrm{mm}, \quad U_{ns} = 35.72\ \mathrm{mm/s}.
\end{aligned} \tag{4.75}$$

Figure 4.13 shows time-averaged 1D energy spectra $\mathcal{E}_a(k) = \langle |\breve{u}_a(k)|^2 \rangle$ in the streamwise direction ($a = x$) and the perpendicular direction ($a = y$). Figure 4.13a corresponds to the case with the isotropic random force (Equation 4.67) and confirms that the thermal counterflow spontaneously becomes anisotropic even though the energy injection is isotropic. However, the behavior in low-k modes does not agree with our experimental observation, in which $\mathcal{E}_x$ is about ten times larger than $\mathcal{E}_y$. According to our experimental results in Figure 4.10, the energy spectra are strongly anisotropic within the energy-containing interval ($k < k_0$), indicating that the energy injection should be anisotropic.

To investigate the anisotropic effects of the energy injection, we introduce the polarized Gaussian random force:

$$\begin{cases}
\langle \phi_{c,x}(\boldsymbol{k}, t) \phi_{c,x}(\boldsymbol{k}', t') \rangle = \dfrac{\sigma_k^2}{k^3} \delta(\boldsymbol{k} - \boldsymbol{k}') \delta(t - t') f_w(k; k_{\min}, k_{\max}) \\
\phi_{c,y}(\boldsymbol{k}, t) = \phi_{c,z}(\boldsymbol{k}, t) = 0.
\end{cases} \tag{4.76}$$

which has a finite value only in the streamwise direction (i.e., x-direction). With the polarized Gaussian random force (Equation 4.76) in Figure 4.13b, $\mathcal{E}_x$ becomes larger than $\mathcal{E}_y$, but the difference is smaller than our experimental observation. Hence, we need to revise the forcing method in the simulations by considering the origin of the energy injection in experiments.

The origin of the energy injection is still subtle, but one of the possible mechanisms is the instabilities of mean flow in the channel [204]. The instabilities are expected to be stronger in the mean flow direction, i.e., the x direction, and conserve the total momentum in the system (i.e., $\rho_s \boldsymbol{\phi}_s + \rho_n \boldsymbol{\phi}_n = 0$). Therefore, we introduce a polarized Gaussian random force conserving the total momentum as

$$\begin{cases}
\langle \phi_{s,x}(\boldsymbol{k}, t) \phi_{s,x}^*(\boldsymbol{k}', t') \rangle = \dfrac{\sigma_k^2}{k^3} \delta(\boldsymbol{k} - \boldsymbol{k}') \delta(t - t') f_w(k; k_{\min}, k_{\max}) \\
\phi_{n,x}(\boldsymbol{k}, t) = -\dfrac{\rho_s}{\rho_n} \phi_{s,x}(\boldsymbol{k}, t) \\
\phi_{c,y}(\boldsymbol{k}, t) = \phi_{c,z}(\boldsymbol{k}, t) = 0.
\end{cases} \tag{4.77}$$

Figure 4.14 shows the corresponding result. In this case, the flow becomes more anisotropic due to the large mutual velocity, and $\mathcal{E}_x$ becomes about 10 times larger than $\mathcal{E}_y$, which aligns with the

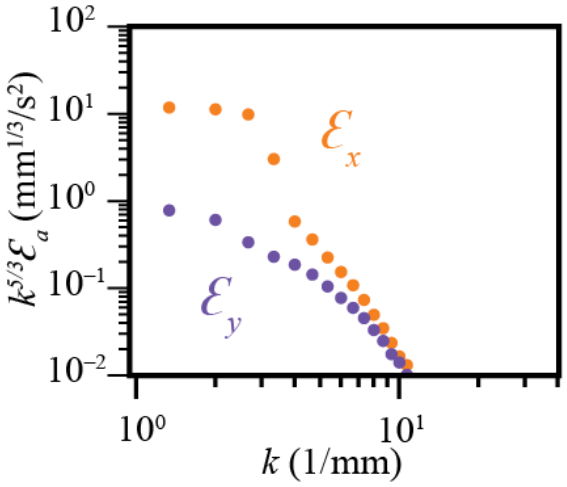

Figure 4.14: Time-averaged energy spectra $\mathcal{E}_a(k)$ of the steady states. The orange and purple circles correspond to the energy spectra in the x and y directions, respectively. The energy is injected by a time-varying 1D Gaussian random forces in the low-k modes ($0.5\ \text{mm}^{-1} \leq k \leq 3.5\ \text{mm}^{-1}$) defined as Equation 4.77. 400 samples are taken with a period of 0.1 s. The amplitude of the random forces is $\sigma_k = 15.0\ \text{mm}^{-1/2}\ \text{s}^{-2}$. The physical parameters correspond to the case with $T = 1.85\text{K}$ and $q = 380.57\text{mW/cm}^2$.

experimental observation shown in Figure 4.10. The anisotropy of the thermal counterflow comes from the mutual friction, which becomes stronger as the mutual velocity becomes larger. When the random forces $\boldsymbol{\phi}_n$ and $\boldsymbol{\phi}_s$ are opposite, as in this case (Equation 4.77), the mutual velocity is expected to be maximized, making the anisotropy stronger. However, the mutual friction dumps the energy, and the energy spectra drop more quickly than in the simulation results shown in Figure 4.13. This result is because the mutual friction term enhances the anisotropy and dissipates the energy.

Based on the above results, the energy injection should be anisotropic and conserve the total momentum. These assumptions can be justified because the energy injection is expected to arise from the instability of the mean flow, which points toward the streamwise direction. However, there is a discrepancy between the experimental observation and simulation results. The simulation's energy spectra decay much faster than those in the experiments. This difference suggests a mechanism exists to sustain the energy in the mutual-friction-dominated interval. This mechanism should originate from the mesoscopic phenomena and cannot be directly derived from the macroscopic models. One may wonder if the quantum peak is crucial in the high-k modes. In a similar fashion to the Kvov–Nazarenko–Volovik spectrum in ^{3}He-B [229], the energy spectrum of the superfluid component presumably has a quantum peak resulting from superfluid motion near

vortex cores [230]. This mechanism is expected to appear in ^{4}He. Unfortunately, we cannot directly implement the quantum contribution to the HVBK equations because the HVBK equations are valid only when the length scale is much larger than the intervortex distance l, and the quantum peak exists around the length l [230]. Mesoscopic-scale simulations, such as vortex filament simulations [201], may provide the information needed to determine the appropriate way of the energy injection in the high-k intervals.

4.5 Conclusion

We have performed experimental and numerical studies of counterflow turbulence of He II in the T-II state, in which both normal and superfluid flows are turbulent, to examine its anisotropic nature. Our experimental results show the three intervals: the energy-containing interval, the cascade interval, and the mutual-friction-dominated interval, which classification was initially introduced by Bao et al. [204] Numerical approaches proposed by past studies to examine the anisotropy of the thermal counterflow turbulence missed two critical factors. First, the energy injection must be anisotropic and conserve the total momentum. Second, a mesoscopic-scale mechanism is expected to sustain the energy even at the high k range. The energy spectra in our simulations decay faster than those in our experiments, and such a mechanism may make this decay slower. To examine this effect, mesoscopic-scale simulations, such as vortex filament simulations [201], are needed. Still, such calculations require high computational resources with our experimental parameters and are not feasible at the current stage.

CHAPTER 5

ELECTRON QUBIT FLOATING ON SOLID NEON

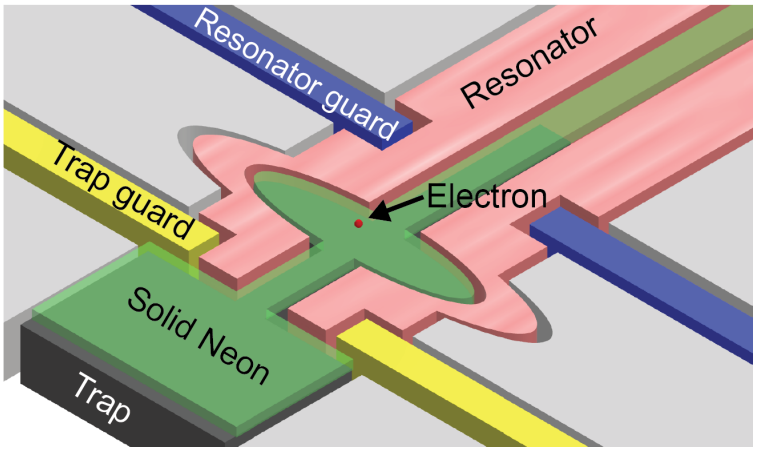

Figure 5.1: Schematic of the device. A single electron is trapped on a solid neon surface.

Electrons levitated on superfluid ^{4}He are a promising qubit system, but they suffer from decoherence caused by ripplons. Nonetheless, recent experiments have achieved a sufficiently long coherence time in an electron charge qubit trapped on a solid neon (Ne) surface (Figure 5.1), whose surface is rigid and ripplon-free [231, 232]. Yet, they observed a curious phenomenon when the electric trapping potential was reduced: the electron remained trapped, opposite to what was expected. To better understand this behavior, we carefully studied the interaction between the electron and a small protrusion on the neon surface. By meticulously assessing the image charge induced by the electron on the curved neon surface, we proficiently solve the Schrödinger equation and determine the electron states on the protrusion surface. Our findings uncover an intriguing revelation: a diminutive surface bump can spontaneously ensnare an electron, giving rise to distinctive ring-shaped quantum states that elucidate the experimental observations. Furthermore, we examined the impact of bump size and applied magnetic fields, demonstrating how the electron's excitation energy can be finely adjusted to facilitate convenient qubit operation. As a result, our study solves the mystery of the electron-on-Ne qubit's performance and provides valuable insights for optimizing the system's design.

5.1 Quantum Computing

Quantum computing has the potential to offer immense computational power by realizing quantum algorithms, which are new high-speed algorithms [233]. Despite much effort and progress in the past, realizing a quantum computer remains a significant challenge. This section explains the fundamentals of the electron qubit system floating in a vacuum above a cryogenics substrate, such as superfluid He or solid Ne.

5.1.1 Qubit

Qubit or quantum bit is the information unit in quantum computing, being represented as a linear sum (or an entangle) of two states ψ_0 and ψ_1 as

$$\psi = a_0\psi_0 + a_1\psi_1. \qquad \forall a_0, a_1 \in \mathbb{C} \tag{5.1}$$

Here, ψ_0 and ψ_1 are usually taken as the ground and first excited states. The evolution of quantum state $\psi(\boldsymbol{r}, t)$ follow the Schrödinger equation:

$$i\hbar\frac{\partial\psi}{\partial t} = -\frac{\hbar^2}{2m}\nabla^2\psi + V(\boldsymbol{r})\psi, \tag{5.2}$$

where $V(\boldsymbol{r})$ is the external potential. Experimental realization of qubits still has many challenges, and the primary issues are the decoherence and scalability of the system. A wholly isolated or closed system is ideal for qubits, but environmental interactions must exist. The qubit state is fragile with environmental noise and can easily undergo decoherence, i.e., the loss of the entangled state. Decoherence processes are usually classified into longitudinal relaxation (i.e., energy relaxation of the excited state ψ_1 to the ground state ψ_0) and transverse relaxation (i.e., dephasing). The robustness of entangled states is characterized by the coherence time, i.e., the characteristic time that the qubit sustains the entangled state, and the coherence time for the longitudinal and transverse relaxations are denoted by T_1 and T_2, respectively.

Scalable and stable qubits are pursued, and numerous qubit platforms are studied [234–236], such as superconducting circuits [237–243], semiconductor quantum dots [244–254], and trapped atoms or molecules [255–263]. We involve electron qubits floated on solid Ne. The idea of this electron qubit was initially developed by the electron-on-He system. The following briefly reviews the electron charge qubit floating on superfluid helium.

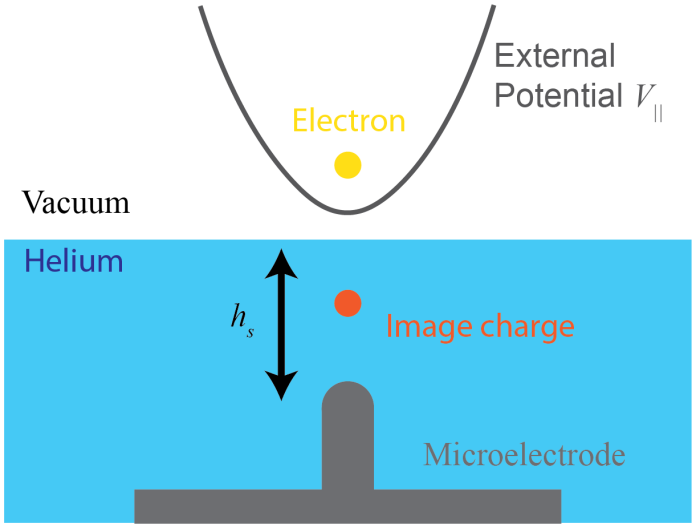

Figure 5.2: Schematic of a microelectrode submerged at the depth h_s in superfluid helium.

5.1.2 Electron Qubit on Liquid Helium

During the 1950s and 1960s, many experiments were conducted to investigate the structure and charge transport in superfluid He. The electrons hover in a vacuum over the surface of superfluid helium at the height where two opposing forces are balanced. The first force is the attractive force generated by the surface charge, while the second is the repulsive force caused by the Pauli exclusion principle between the excess electron and atomic shell electrons. Notably, these experiments led to the observation of quantized vortex rings [264, 265] and the discovery of a transition between a quasi-free electronic state to a localized electron bubble state [266]. After the discovery of the potential barrier on the superfluid helium surface to an electron [267–271], Bruschi et al., [272] first demonstrated the electrostrictive binding of electrons to the surface of liquid helium in 1966. The resulting system was among the earliest 2D electron systems [273–275] which resulted in the first realization of the Wigner crystal [276–278]. This system is ideal to study 2D quantum phenomena due to less impurities [277–284], and the development is discussed in reviews and monographs [285–287]. In 1999, Platzman and Dykman [288] proposed the electron-on-He qubit concept, which uses the Rydberg states (i.e., the motion states in the perpendicular direction to the helium surface) of an electron floated above a microelectrode submerged in helium by the depth of about $h_s \approx 0.5\mu m$ and confined in the parallel plane by an external potential $V_{||}$ (Figure 5.2). This proposal immediately caught the attention of experimentalists [289, 290].

First, let us consider the electron wave function ψ on a flat surface of dielectric material. Supposed that a charge q is placed at $\boldsymbol{r} = (0, 0, z_e)$ and dielectric material with the dielectric constant ϵ occupies the half-space $z < 0$ in the cylindrical coordinate (r, θ, z), the electric field $\boldsymbol{D}$ is given by [291]

$$\boldsymbol{D}(x, y, z) = \begin{cases} \frac{\boldsymbol{e}_z}{4\pi} \left[\frac{(z-z_e)q}{\{r^2+(z-z_e)^2\}^{3/2}} + \frac{(z+z_e)q_1}{\{r^2+(z+z_e)^2\}^{3/2}} \right] & (z > 0) \\ \frac{\boldsymbol{e}_z}{4\pi} \frac{(z-z_e)q_2}{\{r^2+(z-z_e)^2\}^{3/2}}, & (z \leq 0) \end{cases} \tag{5.3}$$

where ϵ_0 is the dielectric constants of the vacuum, $\boldsymbol{e}_z$ is the unit vector in the perpendicular direction to the substrate surface, and the image charges q_1 and q_2 are given by

$$q_1 = -\frac{\epsilon - \epsilon_0}{\epsilon + \epsilon_0} q \tag{5.4}$$

$$q_2 = \frac{2\epsilon}{\epsilon + \epsilon_0} q. \tag{5.5}$$

Here, the surface charge distribution is

$$\begin{aligned} \sigma_{\text{flat}}(r) &= [\epsilon - \epsilon_0] \, \boldsymbol{E}(z = -0) \cdot \boldsymbol{e}_z \\ &= \frac{q}{4\pi} \frac{\epsilon - \epsilon_0}{\epsilon + \epsilon_0} \frac{-2z_e}{(r^2 + z_e^2)^{3/2}}, \end{aligned} \tag{5.6}$$

and the scalar potential at the electron position is

$$\begin{aligned} \phi_e &= \frac{1}{4\pi\epsilon_0} \frac{q_1}{4z_e} \\ &= -\frac{1}{4\pi\epsilon_0} \frac{\epsilon - \epsilon_0}{\epsilon + \epsilon_0} \frac{q}{4z_e}. \end{aligned} \tag{5.7}$$

The potential is then given by [286]

$$V_e(\boldsymbol{r}) = V_0 \theta_{\text{step}}(-z) - \frac{\Lambda}{z + z_0} \theta_{\text{step}}(z) + V_{\text{ext}}(\boldsymbol{r}) \tag{5.8}$$

$$\Lambda = \frac{e^2}{16\pi\epsilon_0} \frac{\epsilon - \epsilon_0}{\epsilon + \epsilon_0} \tag{5.9}$$

where $\theta_{\text{step}}(z)$ is the unit step function and V_{ext} is the external potential. The first term is the potential barrier of the substrate, and $V_0 \approx 1.1$ eV in superfluid helium [268, 292]. The second term represents the static potential generated by the surface charge. The potential is invalid near the surface, so a cut-off z_0 is introduced. In superfluid ^{4}He, z_0 is approximately 1 Å [293]. The dielectric constant of superfluid ^{4}He is relatively small, at about $\epsilon \approx 1.0572\epsilon_0$. Therefore, the electron is located at a height about $z_e \approx 10$nm, much greater than the cut-off value z_0. In the

limit $U_0 \to \infty, z_0 \to 0$ with the absence of the external potential $V_{\rm ext}$, the energy spectrum is given by

$$\mathcal{E}_j(k_\parallel) = \mathcal{E}_j^\perp + \frac{\hbar^2 {k_\parallel}^2}{2m_e}, \qquad \forall j \in \mathbb{Z}_+ \tag{5.10}$$

$$\mathcal{E}_j^\perp = -\frac{m_e \Lambda^2}{2\hbar^2 (j+1)^2} \tag{5.11}$$

where $\boldsymbol{k}_{//}$ is the 2D wave vector parallel to the surface, l is the quantum number of the perpendicular motion, and m_e is the mass of the electron. Here, the wave function of the j-th state is written as

$$\psi_j(\boldsymbol{r}, z) = \psi_j^\perp(z)\psi^\parallel(\boldsymbol{r}) \tag{5.12}$$

$$\psi^\parallel(\boldsymbol{r}) = \frac{1}{\sqrt{S_{\rm A}}} e^{i\boldsymbol{k}_\parallel \cdot \boldsymbol{r}} \tag{5.13}$$

with the surface area $S_{\rm A}$. The energy spectrum in the perpendicular direction $\mathcal{E}_l^\perp$ is similar to the hydrogen one [293–296], hence the 1D eigenstates in the perpendicular direction $\psi_l^\perp(z)$ are called the Rydberg states. The ground and first-excited states are given by

$$\psi_0^\perp(z) = 2\gamma_e^{3/2} z e^{-\gamma_e z} \tag{5.14}$$

$$\psi_1^\perp(z) = \frac{\gamma_e^{3/2}}{\sqrt{2}} \left(1 - \frac{\gamma_e z}{2}\right) z e^{-\gamma_e z/2} \tag{5.15}$$

with $\gamma_e := m_e \Lambda / \hbar^2$ where $\langle \psi_0^\perp | \gamma_e | \psi_0^\perp \rangle \approx 114$ Å and $\langle \psi_1^\perp | \gamma_e | \psi_1^\perp \rangle \approx 456$ Å. The original system proposed by Dykman and Platzman [288,297,298] applies microwave photons and forms a coherent state by these two states χ_0 and χ_1. Next, let us estimate the penetration length λ in the substrate to validate the assumption $V_0 \to \infty$. By solving the one-dimensional (1D) Schrödinger equation with an external potential

$$V(z) = \begin{cases} 0 & (z \geq 0) \\ V_0 & (z < 0) \end{cases}, \tag{5.16}$$

the wave function ψ in $z < 0$ is obtained as

$$\psi_j^\perp(z) \propto e^{z/\lambda} \tag{5.17}$$

$$\lambda = \hbar / \sqrt{2m(V_0 - \mathcal{E}_l^\perp)} \approx \hbar / \sqrt{2mV_0} \tag{5.18}$$

where the approximation is justified because $\mathcal{E}_0 \approx 0.01$ eV $\ll V_0 \approx 1$ eV. In superfluid ^{4}He, the penetration depth is around $\lambda \approx 2$ Å, significantly shorter than the electron height γ_e. As a result, the assumption $V_0 \to \infty$ remains valid. The exact electron states above an electrode are discussed in [299–301].

The electron-on-He system is relatively resilient to surface impurities because of the electron's distance from the helium surface. Nonetheless, the electron may undergo decoherence mainly through four processes: phonon, helium vapor, ripplon, and electrode [302, 303]. The phonon effects are suppressed when the electron is localized at ultra-low temperatures, such as in the qubit system [303]. Decoherence through the elastic scattering due to helium vapor and the one-ripplon process becomes negligible at the temperatures in typical experiments ($T < 1$ K) [304–308]. However, inelastic scattering due to the two-ripplon process cannot be suppressed even at ultra-low temperatures [306–308]. The scattering can decay the excited electron states and dephase the electron qubit state [303]. Recently, Kawakami et al. measured the relaxation time through the two-ripplon process at 135 mK [309]. The decoherence through the electrode is caused by the voltage noise from an external lead or source [303]. The high-frequency noise, mostly due to sources, can be filtered out by a low-pass filter, and the low-frequency noise, mostly from thermal noise on the lead, can be suppressed by cooling down the lead temperature.

To utilize this system as a qubit, it is critical to have an experimental technique that can accurately control and determine the qubit state. The floating electrons can be moved by using a piezoelectric surface sound wave [310] or in a similar way to the charge-coupled device [311, 312]. Grimes and Brown were pioneers in measuring transitions from the ground state to the low-lying excited states using a cryogenic bolometer [293,295]. This bolometer detected microwave absorption saturation caused by the excitation of the Rydberg states. However, this method is only applicable when dealing with a sufficient number of electrons [294–296,313,314]. Platzman and Dykman [288] originally planned to use the method developed by Williams et al. [273], which measures the lifetime of the Rydberg state, but it is destructive and not ideal. Recently, Kawakami et al. [315] and Zou and Konstantinov [316] developed a novel non-destructive method detecting image-charge by measuring the image current caused in a capacitor circuit. Nonetheless, this method requires many electrons and is not applicable to a single electron qubit.

Various other qubit options are currently being developed, including in-plane orbital or spin states [317–322]. The spin qubit is expected to have a much longer coherence time, but it requires a coupling between the spin and charge states, even though the system has no such coupling inherently. Therefore, past studies introduced an artificial coupling, such as spin-photon coupling under a nonuniform magnetic field [318] and electric dipole spin resonance with a stray magnetic field [321].

Recently, an electron-on-He system with a superconducting resonator has been developed and provides a strong dipole coupling between electrons and microwave photons [246, 323–325]. This system may also achieve a strong spin-photon coupling by using a spatially varying magnetic field, enabling spin qubits [317, 326][1]. However, the decoherence rate was much higher than the theoretical estimation. It is believed that the mechanical vibration causes the fluctuations of the helium surface level, inducing the decoherence. This system has lately been applied to the solid neon system, where such a level fluctuation is suppressed.

5.1.3 Electron Qubit on Solid Neon

The potential barrier on the substance surface also exists on other substances, e.g., solid hydrogen and solid Ne [329, 330]. The solid Ne has a rigid surface, and ripplon is suppressed. The coherence time is, therefore, expected to be longer. On the other hand, the dielectric constant of the solid Ne is relatively high ($\epsilon \approx 1.244\epsilon_0$) compared with liquid helium, and the height of the electron position is low; therefore, the electron can be disturbed by surface irregularities. Recently, Zhou et al. [231, 232] developed an electron charge qubit on solid Ne with a superconducting resonator and achieved a time scale of 0.1 ms for both T_1 and T_2, which is sufficiently long for practical usage. The details are discussed in the following. Similarly to the electron-on-He system, the possibility of spin qubit on solid Ne is under discussion [331].

[1] This technique creating a strong spin-photon coupling has been developed in silicon qubit system [247, 248, 327, 328].

5.2 System Configuration

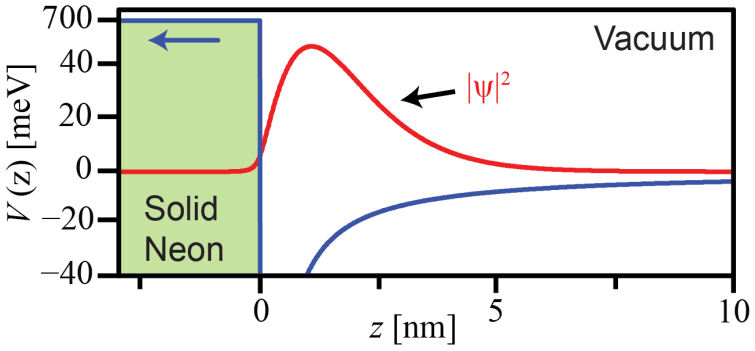

Figure 5.3: Potential and ground-state of an excess electron approaching a flat solid Ne surface. The peak of the probability density $|\psi|^2$ is located around $z = 1$ nm.

Neon can form an uncontaminated surface in a vacuum, making it an optimal substrate for ultra-low temperature experiments due to the lack of uncontrollable impurities or electromagnet noise at ultra-low temperatures. The experiments [231, 232] cool down the system to 10 mK. Electrons are thermionically emitted from a pair of tungsten filaments inside the cell. When an excess electron approaches the solid Ne surface, two forces combine to bind it at a specific height above the surface. The first is the attractive force from the surface charge, while the second is the repulsive force due to the Pauli exclusion principle between the excess electron and atomic shell electrons. Figure 5.3 shows a simulation result of a one-dimensional Schrödinger equation perpendicular to the surface, which is defined as the z-axis, with a potential

$$V(z) = \quad = \quad V_0\theta_{\text{step}}(-z) - \frac{e^2}{4\pi\epsilon_0}\frac{\epsilon-\epsilon_0}{\epsilon+\epsilon_0}\frac{1}{z}\theta_{\text{step}}(z) \tag{5.19}$$

where $V_0 = 0.7$ eV and the second term has a cut-off between $z = 0$ and 0.23nm due to the potential invalidity near the surface [292, 332–334]. The hybrid circuit quantum electrodynamics device used in the experiments is illustrated in Figure 5.1. It features a double-stripline resonator coupled with coplanar waveguides. The trap and resonator guards are applied with voltages in pairs to tune the trapping potential. The device has a tiny amount of Ne coating, estimated to be between 5 and 10 nm thick. The electron is trapped by an electric potential in the 2D surface parallel to the neon surface, and the in-plane electric potential $V_{2D}(x, y)$ can be approximated by the harmonic function around the electron at the origin as

$$V_{2D}(x, y) = \frac{1}{2}m\left(\omega_x^2 x^2 + \omega_y^2 y^2\right) \tag{5.20}$$

where ω_x and ω_y are the angular frequency on the x- and y-axes, respectively, and are determined by the electrode geometry. The angular frequency is set as $\omega_y \ll \omega_x$ so that the electron is strongly confined in the x-axis, and the orbital states in the y-axis are utilized as a qubit. Microwave photons are applied to excite the orbital ground state to the first excited state.

5.3 Numerical Method

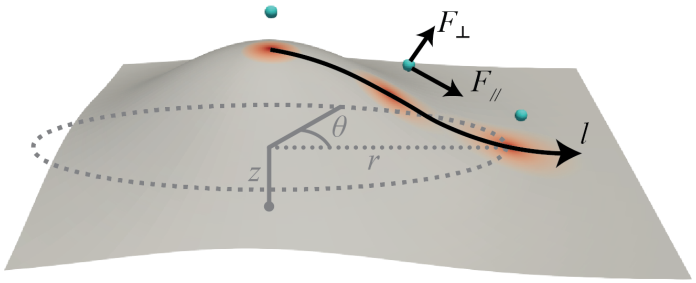

Figure 5.4: Schematic of coordinates. z is the height from the bottom, r is the distance from the z axis in the $x-y$ plane, and θ is the azimutal angle around the z axis. The light blue dots and the red distribution on the curved surface represent the electrons and the surface charge, respectively.

We have conducted numerical calculations to find the electron states around a Gaussian-shaped surface bump

$$z_\sigma(r,\theta) = H \exp\left(-\frac{r^2}{2w^2}\right) \tag{5.21}$$

where H and w are the height and standard deviation. The numerical calculations consist of the following two steps. The first step calculates the static potential acting with a test charge in the cylindrical coordinates (Figure 5.4a). Placing a test charge representing an electron at 1 nm above the surface, we calculate the surface charge generated by the test charge. We can then compute the electric field $\boldsymbol{E}$ at the position of the test charge. By taking an integral of the tangential component $E_\parallel$, the static potential ϕ_e is determined as

$$\phi_e(l) = -\int_0^l E_\parallel(l')dl' \tag{5.22}$$

where l is the distance from the z-axis on the surface. Note that l and r have a 1-to-1 correspondence on the surface.

Secondly, we solve the one-dimensional Schrödinger equation with the potential $V_e = -e\phi_e$ on the curved surface. Since the electron is supposed to be confined in a curved 2D surface

with cylindrical symmetry around the Gaussian surface deficit, the wave function has a form of $\psi^{\parallel}_{n_r,m_z}(r,\theta) = R_{n_r}(r)e^{im_z\theta}$ where n_r is the radial quantum integer and m_z is the angular quantum integer. We solve the equation for the radial component $R_{n_r}(r)$. The details of this calculation are shown later.

5.3.1 Equations for Electric Field

In dielectric systems, electric charges can be decomposed into the true charge and the induced charge as $\rho = \rho_e + \rho_\sigma$:

$$\rho_e(\boldsymbol{r}) = -e\delta(\boldsymbol{r} - \boldsymbol{r}_e) \tag{5.23}$$

$$\rho_\sigma(\boldsymbol{r}) = \sigma(x, y, z_\sigma)\delta(z - z_\sigma) \tag{5.24}$$

$$= \int_S dS_\sigma \sigma(\boldsymbol{r}_\sigma)\delta(\boldsymbol{r} - \boldsymbol{r}_\sigma) \tag{5.25}$$

where e is the elementary charge, $\boldsymbol{r}_e$ is the position of the electron, σ is the surface charge, and z_σ is the surface location. The induced charge ρ_σ can be expressed by the polarization vector $\boldsymbol{P}$ as $\rho_\sigma = -\nabla \cdot \boldsymbol{P}$ and is given in linear dielectric material (i.e., $\boldsymbol{P} = \chi\boldsymbol{E}$) by

$$\rho_\sigma = -\boldsymbol{\nabla} \cdot (\chi\boldsymbol{E}) \,. \tag{5.26}$$

In this case, Gauss's equation is written as

$$\boldsymbol{\nabla} \cdot (\epsilon\boldsymbol{E}(\boldsymbol{r})) = \rho_e \tag{5.27}$$

where $\epsilon = \epsilon_0 + \chi$. Also, the surface charge is given as

$$\sigma = \boldsymbol{P} \cdot \boldsymbol{n} = \chi\boldsymbol{E} \cdot \boldsymbol{n} \tag{5.28}$$

where $\boldsymbol{n}$ is the normal vector vertical with the dielectric surface. Here, the boundary conditions on the dielectric surface are [291]

$$\boldsymbol{D}_1 \cdot \boldsymbol{n} = \boldsymbol{D}_2 \cdot \boldsymbol{n}, \tag{5.29}$$

$$\boldsymbol{E}_1 \cdot \boldsymbol{t} = \boldsymbol{E}_2 \cdot \boldsymbol{t}, \tag{5.30}$$

where $\boldsymbol{t}$ is the normal vector tangential with the dielectric surface.

We decompose the electric field as $\boldsymbol{E}(\boldsymbol{r}) = \boldsymbol{E}_e(\boldsymbol{r}) + \boldsymbol{E}_\sigma(\boldsymbol{r})$ where $\boldsymbol{E}_e$ is the electric field by the true charge and $\boldsymbol{E}_\sigma(\boldsymbol{r})$ is the part generated by the surface charge:

$$\boldsymbol{E}_\sigma(\boldsymbol{r}) = \int_S dS_\sigma \boldsymbol{\Upsilon}_{\sigma(\boldsymbol{r}_\sigma)}(\boldsymbol{r}), \tag{5.31}$$

where $\boldsymbol{\Upsilon}_{\sigma(\boldsymbol{r}_\sigma)}(\boldsymbol{r})$ is the electric field generated by the surface charge of the position $\boldsymbol{r}_\sigma$ to the position $\boldsymbol{r}$. Then the Gauss's equation$\boldsymbol{\nabla} \cdot \boldsymbol{E}(\boldsymbol{r}) = \rho/\epsilon_0$ becomes

$$\begin{aligned} \boldsymbol{\nabla} \cdot \boldsymbol{E}_e &= \rho_e/\epsilon_0, && (5.32) \\ \boldsymbol{\nabla} \cdot \boldsymbol{E}_\sigma &= \rho_\sigma/\epsilon_0 \\ \Leftrightarrow \boldsymbol{\nabla} \cdot \int_S dS_\sigma \boldsymbol{\Upsilon}_{\sigma(\boldsymbol{r}_\sigma)}(\boldsymbol{r}) &= \frac{1}{\epsilon_0} \int_S dS_\sigma \sigma(\boldsymbol{r}_\sigma) \delta(\boldsymbol{r} - \boldsymbol{r}_\sigma) \\ \Leftrightarrow \boldsymbol{\nabla} \cdot \boldsymbol{\Upsilon}_{\sigma(\boldsymbol{r}_\sigma)}(\boldsymbol{r}) &= \frac{1}{\epsilon_0} \sigma(\boldsymbol{r}_\sigma) \delta(\boldsymbol{r} - \boldsymbol{r}_\sigma) && (5.33) \end{aligned}$$

Supposed the spherical symmetry around each surface charge, the electric field is written as

$$\begin{aligned} \boldsymbol{E}_e(\boldsymbol{r}) &= \frac{-e}{4\pi\epsilon_0} \frac{\boldsymbol{r} - \boldsymbol{r}_e}{|\boldsymbol{r} - \boldsymbol{r}_e|^3}, && (5.34) \\ \boldsymbol{\Upsilon}_{\sigma(\boldsymbol{r}_\sigma)}(\boldsymbol{r}) &= \frac{\sigma(\boldsymbol{r}_\sigma)}{4\pi\epsilon_0} \frac{\boldsymbol{r} - \boldsymbol{r}_\sigma}{|\boldsymbol{r} - \boldsymbol{r}_\sigma|^3} \qquad (\boldsymbol{r} \neq \boldsymbol{r}_\sigma) && (5.35) \\ \boldsymbol{E}_\sigma(\boldsymbol{r}) &= \int_S dS_\sigma \boldsymbol{\Upsilon}_{\sigma(\boldsymbol{r}_\sigma)}(\boldsymbol{r}) \\ &= \frac{1}{4\pi\epsilon_0} \int_S dS_\sigma \sigma(\boldsymbol{r}_\sigma) \frac{\boldsymbol{r} - \boldsymbol{r}_\sigma}{|\boldsymbol{r} - \boldsymbol{r}_\sigma|^3} && (5.36) \end{aligned}$$

5.3.2 Spacial Discretization

When we discretize the surface, since the electric field of the surface charge $\boldsymbol{\Upsilon}_{\sigma(\boldsymbol{r}_\sigma)}(\boldsymbol{r})$ diverges at $\boldsymbol{r} = \boldsymbol{r}_\sigma$ in Equation 5.35, we have to estimate $\boldsymbol{\Upsilon}_{\sigma(\boldsymbol{r}_\sigma)}(\boldsymbol{r})$ in the grid at $\boldsymbol{r} = \boldsymbol{r}_\sigma$ by another way. We may use the boundary condition (Equation 5.29) for this purpose as follows:

$$\begin{aligned} & \epsilon_0 \left(\boldsymbol{E}_e - \Delta S(\boldsymbol{r}) \boldsymbol{\Upsilon}_{\sigma(\boldsymbol{r})} + \sum_{\boldsymbol{r}' \neq \boldsymbol{r}} \Delta S(\boldsymbol{r}') \boldsymbol{\Upsilon}_{\sigma(\boldsymbol{r}')} \right) \cdot \boldsymbol{n} \\ = \; & \epsilon \left(\boldsymbol{E}_e + \Delta S(\boldsymbol{r}) \boldsymbol{\Upsilon}_{\sigma(\boldsymbol{r})} + \sum_{\boldsymbol{r}' \neq \boldsymbol{r}} \Delta S(\boldsymbol{r}') \boldsymbol{\Upsilon}_{\sigma(\boldsymbol{r}')} \right) \cdot \boldsymbol{n}, && (5.37) \\ & \Leftrightarrow \Delta S(\boldsymbol{r}) \boldsymbol{\Upsilon}_{\sigma(\boldsymbol{r})} \cdot \boldsymbol{n} = \frac{\epsilon_0 - \epsilon}{\epsilon_0 + \epsilon} \left(\boldsymbol{E}_e + \sum_{\boldsymbol{r}' \neq \boldsymbol{r}} \Delta S(\boldsymbol{r}') \boldsymbol{\Upsilon}_{\sigma(\boldsymbol{r}')} \right) \cdot \boldsymbol{n}. && (5.38) \end{aligned}$$

where $\Delta S(\boldsymbol{r})$ is the surface are of the discretized space at $\boldsymbol{r}$. The surface charge is then given by Equation (5.28) as

$$\sigma(\boldsymbol{r}) = \frac{\epsilon - \epsilon_0}{\epsilon + \epsilon_0} \frac{1}{2\pi} \left[-e \frac{\boldsymbol{r} - \boldsymbol{r}_e}{|\boldsymbol{r} - \boldsymbol{r}_e|^3} + \sum_{\boldsymbol{r}' \neq \boldsymbol{r}} \Delta S(\boldsymbol{r}') \sigma(\boldsymbol{r}') \frac{\boldsymbol{r} - \boldsymbol{r}'}{|\boldsymbol{r} - \boldsymbol{r}'|^3} \right] \cdot \boldsymbol{n} \qquad (5.39)$$

This equation contains the surface charge σ on both sides, so we iterate the equation until the values σ on both sides are close enough. The interaction term amount surface segments consume

time, and we introduce a threshold distance $r_{\rm thr}$. As a result, the equation for iteration from the old surface charge profile $\sigma_{\rm old}$ to the new profile $\sigma_{\rm new}$ is given by

$$\sigma_{\rm new}(\boldsymbol{r}) = \frac{\epsilon-\epsilon_0}{\epsilon+\epsilon_0}\frac{1}{2\pi}\left[-e\frac{\boldsymbol{r}-\boldsymbol{r}_e}{|\boldsymbol{r}-\boldsymbol{r}_e|^3}+\sum_{\boldsymbol{r}'\neq\boldsymbol{r}}\Delta S(\boldsymbol{r}')\sigma_{\rm old}(\boldsymbol{r}')\frac{\boldsymbol{r}-\boldsymbol{r}'}{|\boldsymbol{r}-\boldsymbol{r}'|^3}\right]\cdot\boldsymbol{n}, \tag{5.40}$$

and we repeat this iteration until the condition

$$\frac{|\sigma_{\rm old}(\boldsymbol{r})-\sigma_{\rm new}(\boldsymbol{r})|}{\sigma_{\rm old}(\boldsymbol{r})} < 10^{-13} \tag{5.41}$$

satisfies any location $\boldsymbol{r}$.

5.3.3 Laplacian Operator

The Schrödinger equation contains a Laplacian, and the following derives its formula on the 2D curved space. In the coordinates, whose measure is written as

$$dl^2 = \sum_j h_j^2 dx_j^2, \tag{5.42}$$

the Laplacian operator for a scalar Φ is given by [335]

$$\boldsymbol{\nabla}\cdot\boldsymbol{\nabla}\Phi = \frac{1}{h}\partial_j\left(\frac{h}{h_j^2}\partial_j\Phi\right) \tag{5.43}$$

where $h=\prod_j h_j$ [335].

On a Gaussian surface in the cylindrical coordinates, the position vector is written as

$$\boldsymbol{r}_G = \left(r\,\cos\theta, r\,\sin\theta, H\exp\left(-\frac{r^2}{2w^2}\right)\right) \tag{5.44}$$

where $r=\sqrt{x^2+y^2}$ and θ is the azimuthal angle from the x-axis. The tangent vectors are given by

$$\boldsymbol{r}_{G,r} = \left(\cos\theta, \sin\theta, -\frac{Hr}{w^2}\exp\left(-\frac{r^2}{2w^2}\right)\right) \tag{5.45}$$

$$\boldsymbol{r}_{G,\theta} = \left(-r\,\sin\theta, r\,\cos\theta, 0\right), \tag{5.46}$$

and hence,

$$h_r = \sqrt{r_{G,r}^2} = \sqrt{1+\frac{H^2r^2}{w^4}\exp\left(-\frac{r^2}{w^2}\right)}, \tag{5.47}$$

$$h_\theta = \sqrt{r_{G,\theta}^2} = r. \tag{5.48}$$

Therefore, the Laplacian is written as

$$\begin{aligned}\boldsymbol{\nabla}\cdot\boldsymbol{\nabla}\Phi &= \frac{1}{h_r r}\left[\partial_r\left(\frac{r}{h_r}\partial_r\Phi\right)+\partial_\theta\left(\frac{h_r}{r}\partial_\theta\Phi\right)\right] \\ &= \frac{1}{r^2}\left[\frac{r}{h_r}\partial_r\left(\frac{r}{h_r}\partial_r\Phi\right)+\partial_\theta^2\Phi\right]. \end{aligned} \tag{5.49}$$

5.3.4 Shape of Surface and Electron Contour

The Gaussian surface is written as

$$\boldsymbol{r}_G = \left(r\cos\theta, r\sin\theta, H\exp\left(-\frac{r^2}{2w^2}\right)\right), \tag{5.50}$$

and the electron floats on the surface described by

$$\boldsymbol{r}'_G = \boldsymbol{r}_G + h\hat{e}_n = \left(r'\cos\theta, r'\sin\theta, H\exp\left(-\frac{r^2}{2w^2}\right)+h'\right) \tag{5.51}$$

$$r' = r\left[1+\frac{\frac{Hh}{w^2}\exp\left(-\frac{r^2}{2w^2}\right)}{\sqrt{1+\frac{H^2r^2}{w^4}\exp\left(-\frac{r^2}{w^2}\right)}}\right] \tag{5.52}$$

$$h' = \frac{h}{\sqrt{1+\frac{H^2r^2}{w^4}\exp\left(-\frac{r^2}{w^2}\right)}}, \tag{5.53}$$

where $\hat{e}_n$ is the unit vector normal to the surface. The surface contour of the electron is not Gaussian, and the Laplacian operator needs a correction. However, in our configuration $Hh/w^2 \ll 1$, we may approximate $r' \approx r$ and $h' \approx h$, which lets us assume the contour has a Gaussian shape.

5.3.5 Grids in Cylindrical Coordinates

The surface charge is highly localized around the foot of the electron location (i.e., the perpendicular projection of the electron's location on the curved surface); therefore, we need a fine grid around the foot, but the grid size can be large where far away from the electron. To satisfy this configuration, we adopt the cylindrical coordinates whose center is located at the foot (Figure 5.5). The grid size linearly increases with the distance from the foot location. Supposed the electron and its foot are respectively located at

$$\boldsymbol{r}_e = \left(x_e, 0, z_e = H\exp\left(-\frac{x_e^2+y^2}{2w^2}\right)+h'\right) \tag{5.54}$$

$$\boldsymbol{r}_f = \left(x_0, 0, z_0 = H\exp\left(-\frac{x_0^2+y^2}{2w^2}\right)\right), \tag{5.55}$$

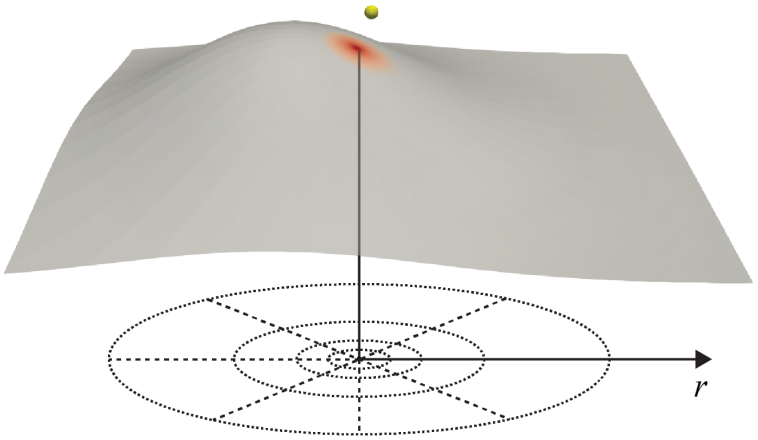

Figure 5.5: Schematic of the discretized coordinates around the foot of the electron

the position vector on the surface is expressed as

$$\boldsymbol{r}_G = \left(x - x_0, y, H \exp\left(-\frac{x^2 + y^2}{2w^2} \right) \right). \tag{5.56}$$

The space in the radial direction r is then discretized so that the step size linearly increases as $\Delta r = a + br$, where the constants a and b are determined from the fixed Δr at two locations

$$\Delta r = \Delta r_{\min} \quad @ \quad r = \Delta r_{\min}/2, \tag{5.57}$$

$$\Delta r = \Delta r_c \quad @ \quad r = r_c. \tag{5.58}$$

as

$$a = \frac{r_c - \Delta r_c/2}{r_c - \Delta r_{\min}/2} \Delta r_{\min}, \tag{5.59}$$

$$b = \frac{\Delta r_c - \Delta r_{\min}}{r_c - \Delta r_{\min}/2}. \tag{5.60}$$

In the flat case, the surface charge is given from Equation 5.6 and is expected to be confined in the order of $h = 1$ nm. For enough accuracy, we take $\Delta r_{\min} = 0.01$ nm, $\Delta r_c = 0.15$ nm, and $r_c = 50$ nm, which give $a \sim 9.986 \times 10^{-3}$ nm and $b \sim 1.502 \times 10^{-3}$ for the case with $H = 30$ nm and $w = 15$ nm. We take the grid number in the radial direction as $N_r = 1200$, which gives the maximum radius of about 99 nm for the case with $H = 30$ nm and $w = 15$ nm. Also, the grid number in the azimuthal direction is given by $N_\theta = 40$. Because of the mirror symmetry with the x-axis, we can half the calculation space and reduce the grid number N_θ to half.

5.3.6 Schrödinger Equation with External Electromagnetic Fields

In our calculations, there is an electric field from the surface charge. Also, an external magnetic field is applied to solve the degenerated states in the azimuthal direction. The following briefly explains the derivation of the Schrödinger equation with electromagnetic field.

The Dirac equation is given by [336]

$$\left[c\boldsymbol{\alpha}\cdot(\boldsymbol{p}-q\boldsymbol{A})+mc^2\beta+q\phi_e\right]\Psi=\epsilon_D\Psi, \tag{5.61}$$

where c is the speed of light, ϵ_D is the relativistic eigenvalue, m is the mass of the particle, $\boldsymbol{A}$ is the vector potential, and ϕ_e is the scalar potential. Also, $\boldsymbol{\alpha}$ and β are normalized as $(\alpha_i)^2=\beta^2=1$ and satisfy the anti-commutation relations

$$\{\alpha_i,\alpha_j\} = 0 \quad (i\neq j) \tag{5.62}$$

$$\{\alpha_i,\beta\} = 0. \tag{5.63}$$

By taking the Weyl or chiral representation

$$\alpha = \hat{s}_z\otimes\hat{\boldsymbol{s}}=\begin{pmatrix}\hat{\boldsymbol{s}} & 0\\ 0 & -\hat{\boldsymbol{s}}\end{pmatrix} \tag{5.64}$$

$$\beta = \hat{s}_x\otimes\hat{I},=\begin{pmatrix}0 & \hat{I}\\ \hat{I} & 0\end{pmatrix} \tag{5.65}$$

with the Pauli matrix $\hat{\boldsymbol{s}}$, the Dirac equation is represented as

$$\begin{pmatrix}P_t-\hat{\boldsymbol{s}}\cdot\boldsymbol{P} & -mc^2\\ -mc^2 & P_t+\hat{\boldsymbol{s}}\cdot\boldsymbol{P}\end{pmatrix}\begin{pmatrix}\Psi_R\\ \Psi_L\end{pmatrix}=0 \tag{5.66}$$

where $P_t:=(\epsilon_D-q\phi_e)/c$, $\boldsymbol{P}:=(\boldsymbol{p}-q\boldsymbol{A})$, and Ψ_R and Ψ_L are right-handed and left-handed chiral states, respectively. These equations may be written as

$$(P_t+\hat{\boldsymbol{s}}\cdot\boldsymbol{P})(P_t-\hat{\boldsymbol{s}}\cdot\boldsymbol{P})\Psi_R = m^2c^4\Psi_R \tag{5.67}$$

$$(P_t-\hat{\boldsymbol{s}}\cdot\boldsymbol{P})(P_t+\hat{\boldsymbol{s}}\cdot\boldsymbol{P})\Psi_L = m^2c^4\Psi_L. \tag{5.68}$$

Since

$$P_t\boldsymbol{P}-\boldsymbol{P}P_t = i\hbar\frac{q\boldsymbol{E}}{c} \tag{5.69}$$

$$\boldsymbol{P}\times\boldsymbol{P} = i\hbar q\boldsymbol{B}, \tag{5.70}$$

the Dirac equation can be decomposed as

$$\left(\boldsymbol{P}^2 - \hbar q\left(\boldsymbol{B} - i\frac{\boldsymbol{E}}{c}\right)\cdot\hat{\boldsymbol{s}}\right)\Psi_R = \frac{1}{c^2}\left(P_t - mc^2\right)\left(P_t + mc^2\right)\Psi_R \tag{5.71}$$

$$\left(\boldsymbol{P}^2 - \hbar q\left(\boldsymbol{B} + i\frac{\boldsymbol{E}}{c}\right)\cdot\hat{\boldsymbol{s}}\right)\Psi_L = \frac{1}{c^2}\left(P_t - mc^2\right)\left(P_t + mc^2\right)\Psi_L. \tag{5.72}$$

In the non-relativistic limit, we obtain

$$\epsilon_D = \epsilon + mc^2 \tag{5.73}$$

$$P_t + mc^2 = \epsilon - q\phi_e + 2mc^2 \approx 2mc^2, \tag{5.74}$$

and then the Dirac equations are written as

$$\left[\boldsymbol{P}^2 - \hbar q\left(\boldsymbol{B} - i\frac{\boldsymbol{E}}{c}\right)\cdot\hat{\boldsymbol{s}}\right]\Psi_R = 2m\left(\epsilon - q\phi_e\right)\Psi_R \tag{5.75}$$

$$\left[\boldsymbol{P}^2 - \hbar q\left(\boldsymbol{B} + i\frac{\boldsymbol{E}}{c}\right)\cdot\hat{\boldsymbol{s}}\right]\Psi_L = 2m\left(\epsilon - q\phi_e\right)\Psi_L. \tag{5.76}$$

Adding these equations, we obtain

$$\left(\frac{\boldsymbol{P}^2}{2m} - \frac{\hbar q}{2m}\boldsymbol{B}\cdot\hat{\boldsymbol{s}} + q\phi_e\right)\Psi_S + i\frac{\hbar q}{2mc}\boldsymbol{E}\cdot\hat{\boldsymbol{s}}\Psi_A = \epsilon\Psi_S. \tag{5.77}$$

where

$$\Psi_S := \frac{1}{\sqrt{2}}\left(\psi_R + \psi_L\right) \tag{5.78}$$

$$\Psi_A := \frac{1}{\sqrt{2}}\left(\psi_R - \psi_L\right). \tag{5.79}$$

In the non-relativistic limit, the difference between the chiral states is negligible (i.e., $\Psi_A \approx 0$) and

$$\left[\frac{\left(\boldsymbol{p} - q\boldsymbol{A}\right)^2}{2m} - \frac{\hbar q}{2m}\boldsymbol{B}\cdot\hat{\boldsymbol{s}} + q\phi_e\right]\Psi_S = \epsilon\Psi_S. \tag{5.80}$$

Taking the gauge as $\boldsymbol{A} = \frac{1}{2}\boldsymbol{B}\times\boldsymbol{r}$, the momentum term is written as

$$\left(\boldsymbol{p} - q\boldsymbol{A}\right)^2 = p^2 - q\left(\boldsymbol{p}\cdot\boldsymbol{A} + \boldsymbol{A}\cdot\boldsymbol{p}\right) + \frac{q^2}{4}\boldsymbol{B}\cdot\boldsymbol{B} \tag{5.81}$$

$$= p^2 - q\left[\left(\boldsymbol{B}\times\boldsymbol{r}\right)\cdot\boldsymbol{p} + \frac{1}{2}\left(\boldsymbol{p}\cdot\left(\boldsymbol{B}\times\boldsymbol{r}\right)\right)\right] + \frac{q^2}{4}\boldsymbol{B}\cdot\boldsymbol{B} \tag{5.82}$$

$$= p^2 - q\boldsymbol{B}\cdot\boldsymbol{L} + \frac{q^2}{4}\boldsymbol{B}\cdot\boldsymbol{B}, \tag{5.83}$$

and the Schrödinger equation in the electromagnetic field is obtained as

$$\left[\frac{\boldsymbol{p}^2}{2m} - \frac{q}{2m}\boldsymbol{B}\cdot\left(\boldsymbol{L} + 2\boldsymbol{S}\right) + q\phi_e + \frac{q^2}{4}\boldsymbol{B}\cdot\boldsymbol{B}\right]\Psi_S = \epsilon\Psi_S. \tag{5.84}$$

where $\boldsymbol{S} = \hbar\hat{\boldsymbol{s}}/2$ is the spin matrix.

We apply an external magnetic field pointing toward the z direction as $\boldsymbol{B} = -B_0\hat{e}_z$. Since the system is symmetry under the rotation around the z-axis, the parallel wavefunction has a form of

$$\psi_{\parallel} = R(r)e^{im_z\theta}, \qquad \forall m_z \in \mathbb{Z} \tag{5.85}$$

and the Schrödinger equation for our 2D system can be converted into a 1D equation

$$\begin{aligned}
\psi_{\parallel} &= R(r)e^{im_z\theta} \qquad \forall m_z \in \mathbb{Z} && (5.86)\\
\epsilon R(r) &= -\frac{\hbar^2}{2m_e}\frac{1}{r^2}\left[\frac{r}{h_r}\partial_r\left(\frac{r}{h_r}\partial_r R\right) - m_z^2 R\right] \\
&\quad + \left[V(r) - \mu_B B_0 \hbar\left(m_z + 2s\right)\right] R && (5.87)\\
V(r) &= -e\phi_e(r) + \frac{e^2 B_0^2}{8m_e}r^2, && (5.88)
\end{aligned}$$

where $\mu_B = e\hbar/2m_e$ is the Bohr magneton and $s = \pm 1/2$ represents the spin in the z-direction. The spin-up and -down states are separated with the Zeeman energy $\Delta E_{\text{Zeeman}} = g_s\mu_B B_0 \equiv \hbar\omega$. For example, when $B_0 = 0.15T$, the corresponding Zeeman frequency is $f = \omega/2\pi \approx 4.2$GHz, which lies in the microwave C band.

The scalar potential ϕ_e is evaluated as follows. There must be a potential due to the Pauli repulsive force from the electrons in the neon. However, since the repulsive force is supposed to be canceled with the perpendicular component of the attractive force, the scalar potential can be calculated by integrating the tangential component of the electric force as

$$\begin{aligned}
\boldsymbol{E}\cdot\boldsymbol{t} &= -\left(\boldsymbol{\nabla}\phi_e\right)\cdot\boldsymbol{t} && (5.89)\\
\phi_e(r) &= -\int_0^r \boldsymbol{E}\cdot\boldsymbol{t}\, d\left(\boldsymbol{r}\cdot\boldsymbol{t}\right) && (5.90)\\
&= -\int_0^r \boldsymbol{E}\cdot\boldsymbol{t}\frac{d\left(\boldsymbol{r}\cdot\boldsymbol{t}\right)}{dr}dr && (5.91)\\
&= -\int_0^r \boldsymbol{E}\cdot\boldsymbol{t}\, h_r dr && (5.92)
\end{aligned}$$

where $\boldsymbol{t} = \boldsymbol{p}_r/h_r$.

In our simulations, we apply the finite difference method to the 1D Schrödinger equation with the central difference. The system size is $L_r = 12w$, and the grid number is $N_r = 6000$. For a typical case with $H = 30$ nm and $w = 15$ nm, the grid size is $\Delta r = 3.0 \times 10^{-2}$ nm.

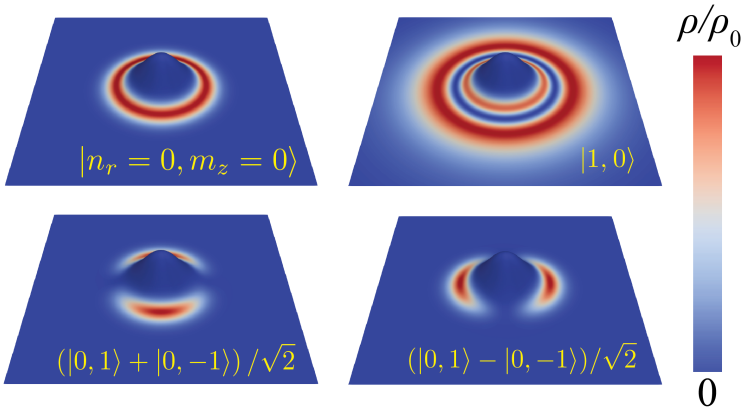

Figure 5.6: Two-dimensional probability density distribution of the electron $\langle\psi^{\parallel}|\boldsymbol{r}\rangle\langle\boldsymbol{r}|\psi^{\parallel}\rangle$ on the curved electron contour with $H = 30$ nm and $w = 15$ nm. (Left top) Ground state $|\psi^{\parallel}\rangle = |n_r = 0, m_z = 0\rangle$. (Right top) First excited state in the radial direction $|\psi^{\parallel}\rangle = |n_r = 1, m_z = 0\rangle$. (Bottom) First excited states in the angular direction, $n_r = 0$. The density is normalized by each state's maximum density ρ_0.

5.4 Results

Figure 5.6 presents the electron density of the ground and low-lying states bounded around a bump with $H = 30$ nm and $w = 15$ nm. The electron may be spontaneously bounded without an external potential and form these ring-shaped states. The electron can be excited in the radial and angular directions. Under this configuration, the energy of the second excited state in the radial direction is higher than the binding potential, and an electron in such a state or higher excited state in the radial direction may escape from the bump. The excitation energies in the right- and left-handed angular directions are degenerate, and any state of a linear combination of $|n_r, m_z\rangle = |0, 1\rangle$ and $|0, -1\rangle$ can be the first-excited states in the radial direction in the absence of the magnetic field. On the other hand, at a finite magnetic field $B_0 \neq 0$, the degeneracy between these two states $|n_r, m_z\rangle = |0, 1\rangle$ and $|0, -1\rangle$ is resolved. We propose that the states bound around the bump can be utilized as a qubit. Since the photon excitation changes the rotational motion, it may excite the electron from the ground state $|n_r = 0, m_z = 0\rangle$ to the first angular excited state $|0, 1\rangle$ or $|0, -1\rangle$, where these two excited states are degenerate in the absence of external magnetic field.

Figure 5.7 shows the radial cross-section of the lateral potential $V_e = -e\phi_e(r)$ and the electron density of the ground and first radial-excited states that are bound near a depression or protrusion on a solid neon surface. When situated above a depression (Figure 5.7a), the electron becomes

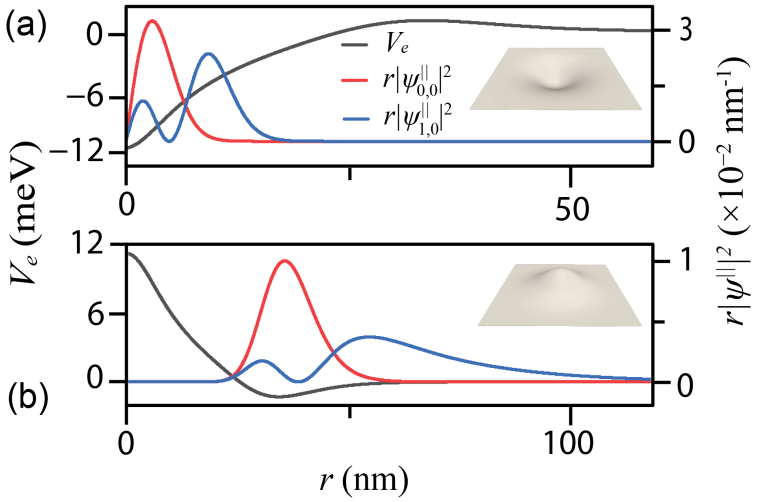

Figure 5.7: Cross-section of the potential V and the probability density profile of the electron in the r-direction $r|\psi^{\parallel}_{n_r,m_z=0}|^2$ around (a) a valley of $H = -30$ nm and $w = 15$ nm or (b) a bump of $H = 30$ nm and $w = 15$ nm.

trapped around the center. It is worth noting that the ground state has no node at the center of the valley, even though the bound states with finite $n_r \neq 0$ must be zero at the center to prevent divergence of the centrifugal potential. The node of the ground state at $r = 0$ in Figure 5.7a comes from the radius factor. Conversely, when situated near a protrusion, the electron adopts a ring-shaped geometry with a radius of about $2w$ (Figure 5.7b). The second excited state is not bound in this trapping potential.

To utilize these bound electron states as a qubit, choosing the proper bump size is crucial to ensure excitation energy matches that of the microwave photon in experiments (e.g., about 26.6 μeV [231]). Therefore, the following searches the excitation energies with various bump sizes in $H = 10$ nm to 40 nm and $w = 10$ nm to 40 nm. Figure 5.8a shows the maximum depth of the binding potential V_{bind}, which increases the bump size. Figure 5.8b displays angular excitation energy from $|n_r, m_z\rangle = |0, 0\rangle$ state to $|0, \pm 1\rangle$ state. The excitation energy primarily comes from the centrifugal potential $\hbar^2 m_z^2 / 2 m_e r^2$ and depends on the electron radius, increasing with w. Our results confirm this relationship. Based on these results, we select a pump size of $H = 30$ nm and $w = 15$ nm, providing comparable excitation energy to the typical photon energy in experiments and binding only a single electron. A single bump may trap multiple electrons if the potential is too deep.

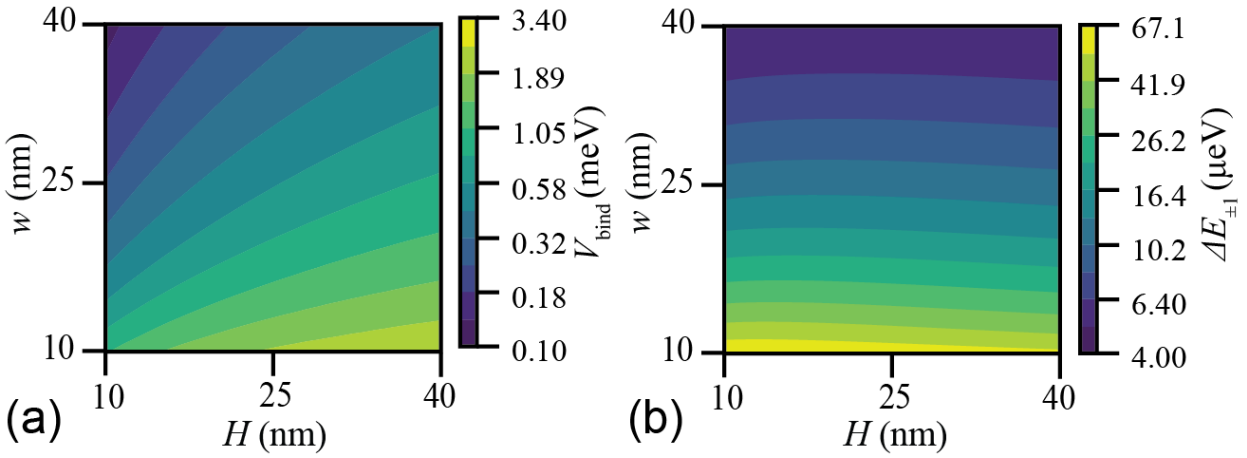

Figure 5.8: (a) Binding potential depth V_{bind}. (b) Excitation energy in the angular direction from $|n_r, m_z\rangle = |0, 0\rangle$ to $|0, 1\rangle$. The data is taken every 1 nm in both H and w directions.

Figure 5.9a shows the typical energy bands with the angular index m_z. When a finite magnetic field is present, the ground state may have a non-zero angular index, referred to as m^* in the following. ΔE_{+1} and ΔE_{-1} represent the excitation energies from the ground state $m_z = m^*$ to the neighboring states $m^* + 1$ and $m^* - 1$, respectively. Figure 5.9b illustrates the magnetic field dependence of these excitation energies. At zero magnetic field $B_0 = 0$ T, the first excited states are degenerate, and these two excitation energies are the same. Once an external magnetic field $B = -B_0\hat{\boldsymbol{z}}$ is applied, the left excitation energy ΔE_{-1} decreases and the right one ΔE_{+1} increases. The ground state shifts to $m^* = 1$ around the magnetic field $B_0 = 0.5$ T. The excitation energies change similarly as the external magnetic field increases. These results show that the external magnetic field can fine-tune the excitation energy.

5.5 Discussion

We have demonstrated that a surface bump may bind the electron, forming a ring-shaped state spontaneously. As shown in Figure 5.7a, the electron feels a repulsive force when it approaches the depression from far away. Therefore, a low-energy electron has a low chance of entering the valley. However, the bump has a bottom of the potential on the rim, and the electron may be trapped there (Figure 5.7b). The following discusses the mechanism making the potential bottom.

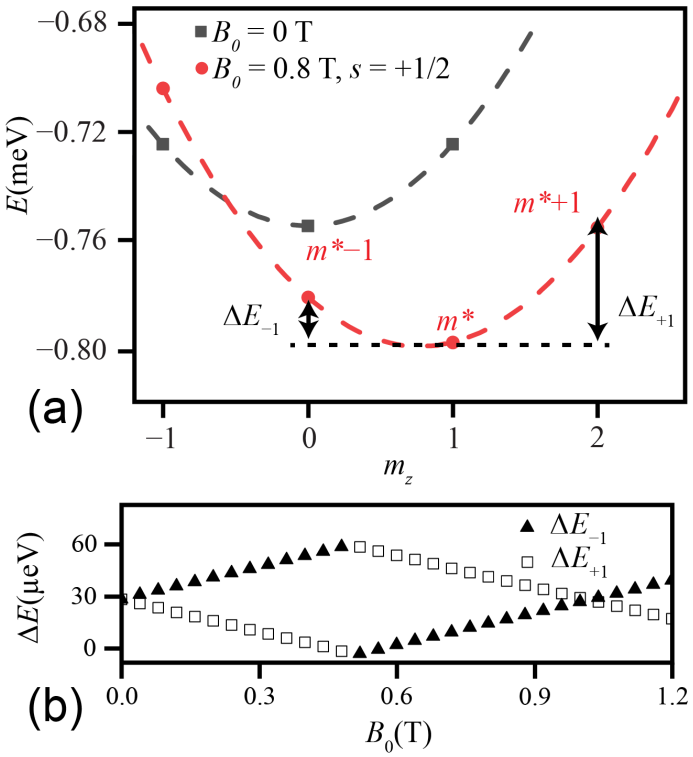

Figure 5.9: (a) Energy band and (b) excitation energies from the ground state $|n_r = 0, m_z = m^*, s = 1/2\rangle$ to the right state $|0, m^* + 1, s = 1/2\rangle$ or to the left state $|0, m^* - 1, s = 1/2\rangle$, which are denoted by ΔE_{+1} and ΔE_{-1}, respectively. The ground state m^* changes from $m^* = 0$ to $m^* = 1$ around $B_0 = 0.5$ T. The bump size is $H = 30$ nm and $w = 15$ nm

.

5.5.1 Force Acting on the Electron

One may wonder why the lateral potential V_e has a peak at the center. The reason is that the surface charge is strongly localized below the electron with a finite size, and the sign of the tangential force $F_{\|}$ depends on the local curvature. Figure 5.10 a and b show the force profile acting on the electron from the surface charge in the perpendicular and normal directions, respectively. In both figures, the force is normalized by the perpendicular component of the force acting on the electron on the flat surface F_{flat}. Near the center, the curvature radius is about 7.5 nm and is the order of the electron height $h = 1$ nm. Therefore, the perpendicular force $F_{\perp}$ becomes less with a large percentage. It is worth noting that since F_{flat} points to the negative direction, the ratio $F_{\|}/F_{\text{flat}}$ becomes negative when the parallel force $F_{\|}$ is positive and repulsive.

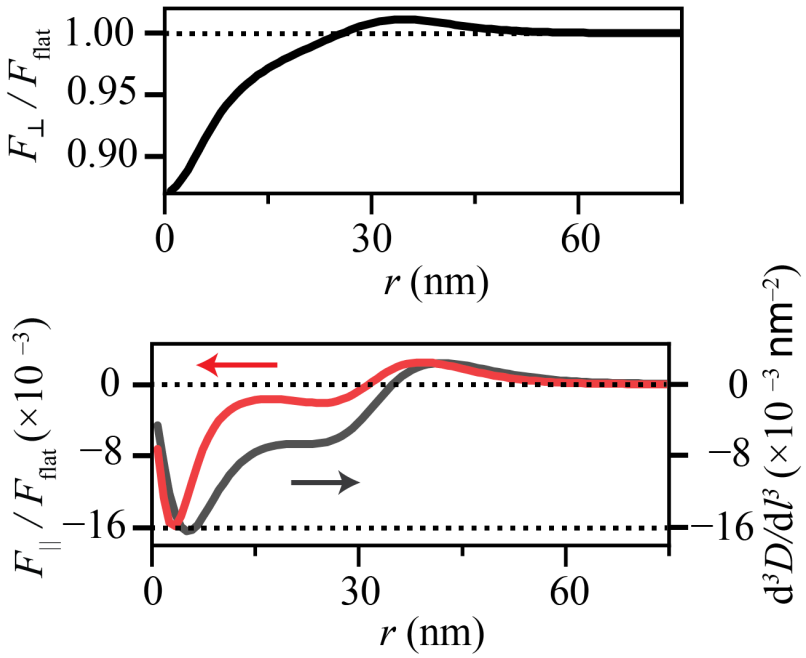

Figure 5.10: (a) Perpendicular component of the force acting on the electron $F_\perp$. (b) Parallel component of $F_\parallel$ and the third derivative of the distance function with respect to l. The bump size is $H = 30$ nm and $w = 15$ nm

Distance between electron and bump. We have carefully analyzed the distance between the electron and the Gaussian surface to discuss the dependence. On the $x-z$ surface (i.e., $y = 0$), the position vector of the bump is written by

$$\boldsymbol{r}_G = \left(x, 0, H \exp\left(-\frac{x^2}{2w^2} \right) \right). \tag{5.93}$$

Supposed the foot position is (x_0, z_0), the position of an electron is

$$(x_e, z_e) = \left(x_0 \left(1 + \frac{z_0}{w^2} h' \right), H \exp\left(-\frac{x_0^2}{2w^2} \right) + h' \right) \tag{5.94}$$

where $h' = h/\sqrt{1 + z_0^2 x_0^2 / w^4}$. The distance between the electron and a point (x, z) on the bump surface is

$$\begin{aligned} D(x) &= \sqrt{(x_e - x)^2 + (z_e - z)^2} \\ &= \sqrt{(x_e - x)^2 + \left\{ z_e - H \exp\left(-\frac{x^2}{2w^2} \right) \right\}^2}. \end{aligned} \tag{5.95}$$

Defining l as the distance from the center of the bump along the bump surface (i.e., $l(x) = \int_0^x h_l(x')dx'$), When the distance function is Taylor expanded as

$$D(l) = \sum_{n=0}^{\infty} \left. \frac{d^n D}{dl^n} \right|_{l=l_e} (l - l_e)^n, \tag{5.96}$$

here l_e is the location of the electron foot. The first two terms are zero, and the second-order term does not contribute to the tangential force because of the symmetry. Therefore, the leading contributing term is the third-order term and changes the sign around $r \approx 35$ nm, which agrees with the bottom position of the lateral potential. Here, the perpendicular component is almost the same as the force on the flat surface around the electron position around $r \approx 36$ nm. This behavior is because the local curvature radius is much larger than the electron height h far from the center.

5.5.2 Finite Thickness Effect

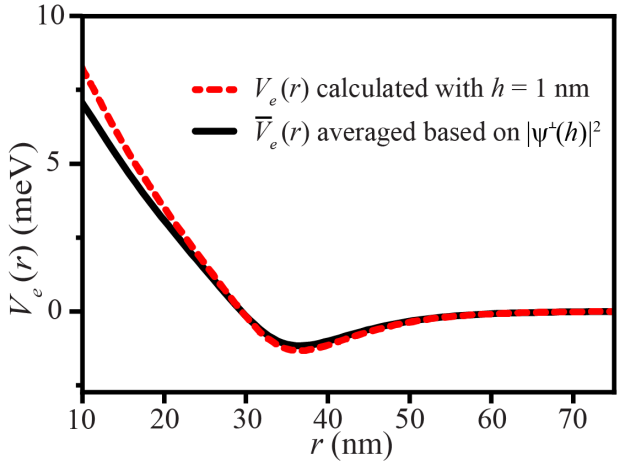

Figure 5.11: Comparison of the lateral potential $V_e(r)$ for an electron held at $h = 1$ nm above a representative neon surface versus the averaged potential $V_e(r)$ that is weighted by the electron's probability $|\psi^{\perp}(h)|^2$ shown in Figure 5.3.

We have assumed that the electron is strongly confined within the 2D space at $h = 1$ nm above the Ne surface. Nevertheless, it is not feasible to confine electrons in such a manner due to the uncertainty principle. In fact, Figure 5.3 shows that the electron's density has a finite thickness in the perpendicular direction. The finite thickness effect can be estimated by deriving the lateral potential $V_e(r) = -e\phi_e(r)$ with various floating heights of the test charge and averaging them with a weight function proportional to the electron's density. For this purpose, we denote the lateral potential V_e for an electron fixed at h as $V_e(r; h)$. Figure 5.11 shows that the lateral potential calculated with $h = 1$ nm and the weight-averaged potential based on the density $|\psi^{\perp}(h)|^2$. According to the results, the thickness effect is negligible near the potential bottom.

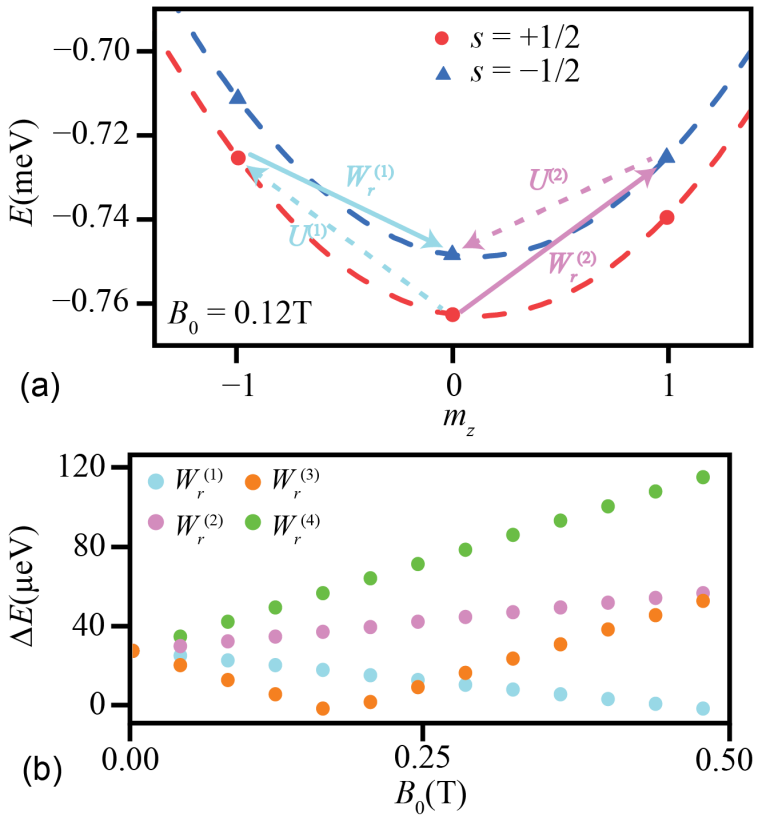

Figure 5.12: (a) Energy Band with $B_0 = 0.12$ T. (b) Excitation energies from the ground state $|n_r = 0, m_z = m^*, s = 1/2\rangle$ to the near states with different angular index m_z. The index of the transitions is described in the main text. The bump size is $H = 30$ nm and $w = 15$ nm.

5.5.3 Spin Qubit

We have discussed the charge qubit using only the spin-up state above. The following examines the possibility of spin qubits in our electron-on-Ne system. The spin qubits using the spin-up and -down states of the same orbital state are more robust, and the spin dephasing time is expected to be over 100 s for electron-on-He system [317]. Historically speaking, the electron-on-Ne system is an extension of the electron-on-He system, and there are discussions about spin qubits on liquid helium (e.g., [318, 321, 322]). The coherence time of the spin states may be longer than 100 s [317]. The orbital electron states parallel to the helium surface can be coupled with the microwave photons via a superconducting resonator, letting the spin states be coupled with the orbital states by introducing local magnetic field gradient [318]. We follow the spin manipulate method using a stray magnetic field in the electric dipole-spin resonance (EDSR) manner [337] proposed by E. Kawakami et al.,

in which the stray magnetic field makes the Rydberg transition energy depend on the spin state in the electron-on-He system [321]. We apply a static magnetic field in the z-direction and an electric field oscillating in the perpendicular direction to the neon surface with a ferromagnetic pillar placed below the solid Ne, The pillar is magnetized, creating a stray magnetic field. The center position of the electron oscillates, and the magnetic field at the electron position varies with time, allowing the excitation of the spin state. The following discusses the transition rate by this method. We apply a uniform magnetic field $B_0\boldsymbol{e}_z$ and a stray magnetic field $\mathbf{b} = b_r\boldsymbol{e}_r + b_z\boldsymbol{e}_z$ where $\boldsymbol{e}_r$ and $\boldsymbol{e}_z$ are the unit vectors in the r and z-directions, respectively. Then, the Hamiltonian is given by

$$H = H_0 + W_z + W_r, \tag{5.97}$$

here H_0 is the original Hamiltonian of the electron-on-He system with a correction of the magnetic field as $\mathbf{B} = b_r(r_e, z_e)\boldsymbol{e}_r + [B_0 + b_z(r_e, z_e)]\,\boldsymbol{e}_z$ with . Also, W_r and W_z are the terms due to the spatial gradient of stray magnetic field and are given by

$$W_z = \tfrac{1}{2}g\mu_B\left[\tfrac{\partial b_z}{\partial z}(z - z_e) + \tfrac{\partial^2 b_z}{\partial r^2}(r - r_e)^2\right]\hat{s}_z \tag{5.98}$$

$$W_r = \tfrac{1}{2}g\mu_B\tfrac{\partial b_r}{\partial r}(r - r_e)\,\hat{s}_r \tag{5.99}$$

where the stray magnetic field and its gradients on the right-hand side are estimated at the electron position (i.e., $r = r_e$ and $z = z_e$). Owing to the magnetic field gradient, the ground state may be excited to the first excited state. The transition rate is

$$\Gamma = \lim_{t\to\infty}\frac{d}{dt}\left|\frac{1}{(i\hbar)^2}\int_0^t dt''\int_0^{t''} dt'\,\langle f(t')|\,H(t')H(t'')\,|i(t'')\rangle\right|^2\delta(\omega_f - \omega_i - \omega). \tag{5.100}$$

Here,

$$\langle f(t')|\,H(t')H(t'')\,|i(t'')\rangle \tag{5.101}$$

$$= \sum_\beta \langle f(t')|\left(V(t') + W_r\right)|\beta(t')\rangle\langle\beta(t'')|\left(V(t'') + W_r\right)|i(t'')\rangle \tag{5.102}$$

$$= \sum_\beta \big[\langle f(t')|\,V(t')\,|\beta(t')\rangle\langle\beta(t'')|\,V(t'')\,|i(t'')\rangle + \langle f(t')|\,V(t')\,|\beta(t')\rangle\langle\beta(t'')|\,W_r\,|i(t'')\rangle$$
$$+ \langle f(t')|\,W_r\,|\beta(t')\rangle\langle\beta(t'')|\,V(t'')\,|i(t'')\rangle + \langle f(t')|\,W_r\,|\beta(t')\rangle\langle\beta(t'')|\,W_r\,|i(t'')\rangle\big]. \tag{5.103}$$

Under the rotational wave approximation, the transition rate can be approximated as

$$\Gamma \approx \lim_{t\to\infty}\sum_\beta\frac{d}{dt}\left|\frac{1}{(i\hbar)^2}\int_0^t dt''\int_0^{t''} dt'\,\big[\langle f(t')|\,V(t')\,|\beta(t')\rangle\langle\beta(t'')|\,W_r\,|i(t'')\rangle$$
$$+ \langle f(t')|\,W_r\,|\beta(t')\rangle\langle\beta(t'')|\,V(t'')\,|i(t'')\rangle\big]\right|^2\delta(\omega_f - \omega_i - \omega). \tag{5.104}$$

Here, the first term is written as

$$\begin{aligned}
& \frac{1}{(i\hbar)^2}\lim_{t\to\infty}\sum_\beta \frac{d}{dt}\int_0^t dt''\int_0^{t''} dt'\,\langle f(t')|\,V(t')\,|\beta(t')\rangle\,\langle\beta(t'')|\,W_r\,|i(t'')\rangle \\
= \;& \frac{1}{(i\hbar)^2}\lim_{t\to\infty}\sum_\beta \frac{d}{dt}\left[\int_0^t dt''\int_0^{t''} dt'\,\langle f|\,U\,|\beta\rangle\,e^{-i(\omega_\beta-\omega_f+\omega)t''}\,\langle\beta|\,W_r\,|i\rangle\,e^{-i(\omega_i-\omega_\beta)t'}\right. \\
& \left.\int_0^t dt''\int_0^{t''} dt'\,\langle f|\,U^\dagger\,|\beta\rangle\,e^{-i(\omega_\beta-\omega_f-\omega)t''}\,\langle\beta|\,W_r\,|i\rangle\,e^{-i(\omega_i-\omega_\beta)t'}\right] \qquad (5.105) \\
= \;& \frac{1}{(i\hbar)^2}\lim_{t\to\infty}\sum_\beta \frac{i}{\omega_i-\omega_\beta}\frac{d}{dt}\left[\langle f|\,U\,|\beta\rangle\,\langle\beta|\,W_r\,|i\rangle\int_0^t dt''\left(1-e^{-i(\omega_\beta-\omega_f+\omega)t''}\right)\right. \\
& \left.+\,\langle f|\,U^\dagger\,|\beta\rangle\,\langle\beta|\,W_r\,|i\rangle\int_0^t dt''\left(e^{-i(\omega_i-\omega_f-\omega)t''}-e^{-i(\omega_\beta-\omega_f-\omega)t''}\right)\right] \qquad (5.106) \\
\approx \;& \frac{1}{(i\hbar)^2}\sum_\beta \frac{i}{\omega_i-\omega_\beta}\,\langle f|\,U\,|\beta\rangle\,\langle\beta|\,W_r\,|i\rangle\,. \qquad (5.107)
\end{aligned}$$

Similarly, the second term may be written as

$$\begin{aligned}
& \frac{1}{(i\hbar)^2}\lim_{t\to\infty}\sum_\beta \frac{d}{dt}\int_0^t dt''\int_0^{t''} dt'\,\langle f(t')|\,W_r\,|\beta(t')\rangle\,\langle\beta(t'')|\,V(t')\,|i(t'')\rangle \\
\approx \;& \frac{1}{(i\hbar)^2}\sum_\beta \frac{i}{\omega_\beta-\omega_f}\,\langle f|\,W_r\,|\beta\rangle\,\langle\beta|\,U\,|i\rangle\,. \qquad (5.108)
\end{aligned}$$

Therefore, the transition rate may be written as

$$\gamma \approx \frac{1}{\hbar^2}\left|\sum_\beta \frac{\langle f|\,U\,|\beta\rangle\,\langle\beta|\,W_r\,|i\rangle}{\omega_i-\omega_\beta}+\frac{\langle f|\,W_r\,|\beta\rangle\,\langle\beta|\,U\,|i\rangle}{\omega_\beta-\omega_f}\right|^2\delta\left(\omega_f-\omega_i-\omega\right). \qquad (5.109)$$

By adjusting the applied magnetic field and its gradient, we can control the possible states of β. For example, we can pick up the $m=m^*+1$ and $m=m^*-1$ states for β as:

$$\begin{aligned}
|n_r=0,m_z=m^*,s=1/2\rangle \;& \underset{U^{(1)}}{\to}\; |n_r=0,m_z=m^*-1,s=1/2\rangle \\
& \underset{W_r^{(1)}}{\to}\; |n_r=0,m_z=m^*,s=-1/2\rangle \qquad (5.110) \\
|n_r=0,m_z=m^*,s=1/2\rangle \;& \underset{W_r^{(2)}}{\to}\; |n_r=0,m_z=m^*+1,s=-1/2\rangle \\
& \underset{U^{(2)}}{\to}\; |n_r=0,m_z=m^*,s=-1/2\rangle \qquad (5.111) \\
|n_r=0,m_z=m^*,s=1/2\rangle \;& \underset{U^{(3)}}{\to}\; |n_r=0,m_z=m^*+1,s=1/2\rangle \\
& \underset{W_r^{(3)}}{\to}\; |n_r=0,m_z=m^*,s=-1/2\rangle \qquad (5.112) \\
|n_r=0,m_z=m^*,s=1/2\rangle \;& \underset{W_r^{(4)}}{\to}\; |n_r=0,m_z=m^*-1,s=-1/2\rangle \\
& \underset{U^{(4)}}{\to}\; |n_r=0,m_z=m^*,s=-1/2\rangle \qquad (5.113)
\end{aligned}$$

where $U = eEx/2$. Figure 5.12a shows the first and second transition paths in the band, and Figure 5.12b shows the excitation energy corresponding to the W_r term for each path with a bump of $H = 30$ nm and $\sigma = 15$ nm.

5.6 Conclusion

We have investigated the electron states around a surface deficit, such as a bump and valley, through numerical analysis. Our results demonstrate that the ground and low-lying states can spontaneously bind around the bump without an external potential. These states may provide as a qubit. By searching the excitation energies with various bump sizes, we have determined the appropriate bump sizes in which the excitation energy matches the photon energy. Furthermore, we propose building a spin qubit with the ground state by introducing a stray magnetic field. This system can be a quantum sensor to detect magnetic fields that pass through the ring state.

We have supposed the surface is smooth, but the effectiveness of the continuous model is uncertain. It is unclear how much the atomic arrangement affects the electron state. For example, the lattice parameter is about 0.44 nm [338], close to the electron height 1 nm but sufficiently small compared with the bump sizes in our simulations. Quantum Monte Carlo calculations may provide helpful information, which will be a future topic.

BIBLIOGRAPHY

[1] T. Kanai, W. Guo, and M. Tsubota. Merging of Rotating Bose–Einstein Condensates. *Journal of Low Temperature Physics*, 195(1-2):37–50, April 2019.

[2] T. Kanai, W. Guo, M. Tsubota, and D. Jin. Torque and Angular-Momentum Transfer in Merging Rotating Bose-Einstein Condensates. *Physical Review Letters*, 124(10):105302, March 2020.

[3] T. Kanai and W. Guo. True Mechanism of Spontaneous Order from Turbulence in Two-Dimensional Superfluid Manifolds. *Physical Review Letters*, 127(9):095301, August 2021.

[4] P. A. Davidson. *Turbulence: An Introduction for Scientists and Engineers*. Oxford University Press, Oxford, second edition edition, 2015.

[5] S. Balibar. The Discovery of Superfluidity. *Journal of Low Temperature Physics*, 146(5-6):441–470, March 2007.

[6] P. Kapitza. Viscosity of Liquid Helium below the λ-Point. *Nature*, 141(3558):74–74, January 1938.

[7] J. F. Allen and A. D. Misener. Flow Phenomena in Liquid Helium II. *Nature*, 142(3597):643–644, October 1938.

[8] P. Sikivie and Q. Yang. Bose-Einstein Condensation of Dark Matter Axions. *Physical Review Letters*, 103(11):111301, September 2009.

[9] J. Dziarmaga. Dynamics of a quantum phase transition and relaxation to a steady state. *Advances in Physics*, 59(6):1063–1189, November 2010.

[10] T. Donner, S. Ritter, T. Bourdel, A. Öttl, M. Köhl, and T. Esslinger. Critical Behavior of a Trapped Interacting Bose Gas. *Science*, 315(5818):1556–1558, March 2007.

[11] W. G. Unruh. Experimental Black-Hole Evaporation? *Physical Review Letters*, 46(21):1351–1353, May 1981.

[12] N. Navon, A. L. Gaunt, R. P. Smith, and Z. Hadzibabic. Critical dynamics of spontaneous symmetry breaking in a homogeneous Bose gas. *Science*, 347(6218):167–170, January 2015.

[13] C. P. Herzog, P. K. Kovtun, and D. T. Son. Holographic model of superfluidity. *Physical Review D*, 79(6):066002, March 2009.

[14] C.-Y. Xia, H.-B. Zeng, H.-Q. Zhang, Z.-Y. Nie, Y. Tian, and X. Li. Vortex lattice in a rotating holographic superfluid. *Physical Review D*, 100(6):061901, September 2019.

[15] W.-C. Yang, C.-Y. Xia, H.-B. Zeng, M. Tsubota, and J. Zaanen. Motion of a superfluid vortex according to holographic quantum dissipation. *Physical Review B*, 107(14):144511, April 2023.

[16] D. Page, J. M. Lattimer, M. Prakash, and A. W. Steiner. Stellar Superfluids. In K.-H. Bennemann and J. B. Ketterson, editors, *Novel Superfluids*, pages 505–579. Oxford University Press, 1 edition, November 2014.

[17] A. Einstein. Quantentheorie des einatomigen idealen Gases. *Sitzungber. Kgl. Akad. Wiss.*, (261), 1924.

[18] A. Einstein. Quantentheorie des einatomigen idealen Gases: Zweite Abhandlung. *Sitzungber. Kgl. Akad. Wiss.*, (3), 1925.

[19] O. Penrose and L. Onsager. Bose-Einstein Condensation and Liquid Helium. *Physical Review*, 104(3):576–584, November 1956.

[20] A. J. Leggett. *Quantum Liquids: Bose condensation and Cooper pairing in condensed-matter systems*. Oxford graduate texts. Oxford University Press, Oxford; New York, 2006.

[21] L. D. Landau, E. M. Lifšic, L. P. Pitaevskij, and L. D. Landau. *Statistical Physics*. Number 5 in Course of theoretical physics / L. D. Landau and E. M. Lifshitz. Elsevier Butterworth Heinemann, Amsterdam Heidelberg, 3. ed., repr edition, 2011.

[22] R. P. Feynman. *Statistical Mechanics: A Set of Lectures*. Advanced book classics. Westview Press, Boulder, Colo, 1998.

[23] L. Landau. Theory of the Superfluidity of Helium II. *Physical Review*, 60(4):356–358, August 1941.

[24] H. Nishimori and G. Ortiz. *Elements of Phase Transitions and Critical Phenomena*. Oxford graduate texts. Oxford University Press, Oxford, 2015.

[25] A. L. Fetter and J. D. Walecka. *Quantum Theory of Many-Particle Systems*. Dover Publications, Mineola, N.Y, 2003.

[26] R. J. Donnelly. *Quantized Vortices in Helium II*. Number 3 in Cambridge studies in low temperature physics. Cambridge University Press, Cambridge; New York, 1991.

[27] W. F. Vinen. The detection of single quanta of circulation in liquid helium II. *Proceedings of the Royal Society of London. Series A. Mathematical and Physical Sciences*, 260(1301):218–236, February 1961.

[28] Y. Kawaguchi and T. Ohmi. Splitting instability of a multiply charged vortex in a Bose-Einstein condensate. *Physical Review A*, 70(4):043610, October 2004.

[29] M. Leadbeater, T. Winiecki, D. C. Samuels, C. F. Barenghi, and C. S. Adams. Sound Emission due to Superfluid Vortex Reconnections. *Physical Review Letters*, 86(8):1410–1413, February 2001.

[30] E. Fonda, D. P. Meichle, N. T. Ouellette, S. Hormoz, and D. P. Lathrop. Direct observation of Kelvin waves excited by quantized vortex reconnection. *Proceedings of the National Academy of Sciences*, 111(supplement_1):4707–4710, March 2014.

[31] K. W. Schwarz. Three-dimensional vortex dynamics in superfluid ^{4}He : Homogeneous superfluid turbulence. *Physical Review B*, 38(4):2398–2417, August 1988.

[32] W. F. Vinen. Decay of superfluid turbulence at a very low temperature: The radiation of sound from a Kelvin wave on a quantized vortex. *Physical Review B*, 64(13):134520, September 2001.

[33] M. Leadbeater, D. C. Samuels, C. F. Barenghi, and C. S. Adams. Decay of superfluid turbulence via Kelvin-wave radiation. *Physical Review A*, 67(1):015601, January 2003.

[34] E. Kozik and B. Svistunov. Kelvin-Wave Cascade and Decay of Superfluid Turbulence. *Physical Review Letters*, 92(3):035301, January 2004.

[35] C. J. Foot. *Atomic Physics*. Number 7. Atomic, Optical, and laser physics in Oxford master series in physics. Oxford University Press, Oxford ; New York, 2005.

[36] M. H. Anderson, J. R. Ensher, M. R. Matthews, C. E. Wieman, and E. A. Cornell. Observation of Bose-Einstein Condensation in a Dilute Atomic Vapor. *Science*, 269(5221):198–201, July 1995.

[37] K. B. Davis, M. O. Mewes, M. R. Andrews, N. J. Van Druten, D. S. Durfee, D. M. Kurn, and W. Ketterle. Bose-Einstein Condensation in a Gas of Sodium Atoms. *Physical Review Letters*, 75(22):3969–3973, November 1995.

[38] C. C. Bradley, C. A. Sackett, J. J. Tollett, and R. G. Hulet. Evidence of Bose-Einstein Condensation in an Atomic Gas with Attractive Interactions. *Physical Review Letters*, 75(9):1687–1690, August 1995.

[39] C. C. Bradley, C. A. Sackett, and R. G. Hulet. Bose-Einstein Condensation of Lithium: Observation of Limited Condensate Number. *Physical Review Letters*, 78(6):985–989, February 1997.

[40] C. Pethick and H. Smith. *Bose-Einstein Condensation in Dilute Gases*. Cambridge University Press, Cambridge, second edition edition, 2011.

[41] T. W. Neely, E. C. Samson, A. S. Bradley, M. J. Davis, and B. P. Anderson. Observation of Vortex Dipoles in an Oblate Bose-Einstein Condensate. *Physical Review Letters*, 104(16):160401, April 2010.

[42] E. Zaremba, T. Nikuni, and A. Griffin. Dynamics of Trapped Bose Gases at Finite Temperatures. *Journal of Low Temperature Physics*, 116(3/4):277–345, 1999.

[43] D. S. Jin, J. R. Ensher, M. R. Matthews, C. E. Wieman, and E. A. Cornell. Collective Excitations of a Bose-Einstein Condensate in a Dilute Gas. *Physical Review Letters*, 77(3), 1996.

[44] M.-O. Mewes, M. R. Andrews, N. J. Van Druten, D. M. Kurn, D. S. Durfee, C. G. Townsend, and W. Ketterle. Collective Excitations of a Bose-Einstein Condensate in a Magnetic Trap. *Physical Review Letters*, 77(6):988–991, August 1996.

[45] S. Choi, S. A. Morgan, and K. Burnett. Phenomenological damping in trapped atomic Bose-Einstein condensates. *Physical Review A*, 57(5):4057–4060, May 1998.

[46] J. Wilkes. *The Properties of Liquid and Solid Helium*. The International Series of Monographs on Physics. Oxford University Press, Oxford, 1967.

[47] F. London. The λ-Phenomenon of Liquid Helium and the Bose-Einstein Degeneracy. *Nature*, 141(3571):643–644, April 1938.

[48] L. D. Landau and E. M. Lifšic. *Fluid Mechanics*. Elsevier, second edition edition, 1987.

[49] I. M. Khalatnikov. *An Introduction to the Theory of Superfluidity*. Advanced book classics. Advanced Book Program, Perseus Pub, Cambridge, 2000.

[50] C. F. Barenghi, R. J. Donnelly, and W. F. Vinen, editors. *Quantized Vortex Dynamics and Superfluid Turbulence*. Number 571 in Lecture notes in physics. Springer, Berlin; New York, 2001.

[51] W. F. Vinen. Mutual friction in a heat current in liquid helium II I. Experiments on steady heat currents. *Proceedings of the Royal Society of London. Series A. Mathematical and Physical Sciences*, 240(1220):114–127, April 1957.

[52] H. R. Glyde, R. T. Azuah, and W. G. Stirling. Condensate, momentum distribution, and final-state effects in liquid 4 He. *Physical Review B*, 62(21):14337–14349, December 2000.

[53] S. Moroni, G. Senatore, and S. Fantoni. Momentum distribution of liquid helium. *Physical Review B*, 55(2):1040–1049, January 1997.

[54] D. M. Ceperley and E. L. Pollock. Path-integral computation of the low-temperature properties of liquid ^{4}He. *Physical Review Letters*, 56(4):351–354, January 1986.

[55] S. W. Van Sciver. *Helium Cryogenics*. International cryogenics monograph series. Springer, New York, 2nd ed edition, 2012.

[56] R. J. Donnelly, J. A. Donnelly, and R. N. Hills. Specific heat and dispersion curve for helium II. *Journal of Low Temperature Physics*, 44(5-6):471–489, September 1981.

[57] B. Fåk, T. Keller, M. E. Zhitomirsky, and A. L. Chernyshev. Roton-Phonon Interactions in Superfluid ^{4}He. *Physical Review Letters*, 109(15):155305, October 2012.

[58] P. Nozières. Is the Roton in Superfluid ^{4}He the Ghost of a Bragg Spot? *Journal of Low Temperature Physics*, 137(1/2):45–67, October 2004.

[59] L. Santos, G. V. Shlyapnikov, and M. Lewenstein. Roton-Maxon Spectrum and Stability of Trapped Dipolar Bose-Einstein Condensates. *Physical Review Letters*, 90(25):250403, June 2003.

[60] S. S. Natu, L. Campanello, and S. Das Sarma. Dynamics of correlations in a quasi-two-dimensional dipolar Bose gas following a quantum quench. *Physical Review A*, 90(4):043617, October 2014.

[61] R. M. Wilson, S. Ronen, and J. L. Bohn. Critical Superfluid Velocity in a Trapped Dipolar Gas. *Physical Review Letters*, 104(9):094501, March 2010.

[62] M. Jona-Lasinio, K. Łakomy, and L. Santos. Roton confinement in trapped dipolar Bose-Einstein condensates. *Physical Review A*, 88(1):013619, July 2013.

[63] P. B. Blakie, D. Baillie, and R. N. Bisset. Roton spectroscopy in a harmonically trapped dipolar Bose-Einstein condensate. *Physical Review A*, 86(2):021604, August 2012.

[64] N. G. Parker, C. Ticknor, A. M. Martin, and D. H. J. O'Dell. Structure formation during the collapse of a dipolar atomic Bose-Einstein condensate. *Physical Review A*, 79(1):013617, January 2009.

[65] J. L. Bohn, R. M. Wilson, and S. Ronen. How does a dipolar Bose-Einstein condensate collapse? *Laser Physics*, 19(4):547–549, April 2009.

[66] S. Ronen, D. C. E. Bortolotti, and J. L. Bohn. Radial and Angular Rotons in Trapped Dipolar Gases. *Physical Review Letters*, 98(3):030406, January 2007.

[67] L. Chomaz, R. M. W. Van Bijnen, D. Petter, G. Faraoni, S. Baier, J. H. Becher, M. J. Mark, F. Wächtler, L. Santos, and F. Ferlaino. Observation of roton mode population in a dipolar quantum gas. *Nature Physics*, 14(5):442–446, May 2018.

[68] W. F. Saam. Damping of Ripplons in Superfluid ^{4}He at $T = 0$. *Physical Review A*, 8(4):1918–1920, October 1973.

[69] H. Gould and V. K. Wong. Ripplon damping in superfluid He 4 at low temperatures. *Physical Review B*, 18(5):2124–2126, September 1978.

[70] R. C. Jones, A. J. E. Williams, W. F. Vinen, and P. A. Ewbank. The lifetime of interacting ripplons on the surface of superfluid helium. *Journal of Low Temperature Physics*, 92(3-4):239–261, August 1993.

[71] A. Kolmogorov. Dissipation of energy in the locally isotropic turbulence. *Proceedings of the Royal Society of London. Series A: Mathematical and Physical Sciences*, 434(1890):15–17, July 1991.

[72] A. Kolmogorov. The local structure of turbulence in incompressible viscous fluid for very large Reynolds numbers. *Proceedings of the Royal Society of London. Series A: Mathematical and Physical Sciences*, 434(1890):9–13, July 1991.

[73] H. Tennekes and J. L. Lumley. *A First Course in Turbulence*. MIT press, Cambridge; London, 1992.

[74] A. Bejan. *Convection Heat Transfer*. Wiley, Hoboken, fourth edition edition, 2013.

[75] K. R. Sreenivasan. On the universality of the Kolmogorov constant. *Physics of Fluids*, 7(11):2778–2784, November 1995.

[76] U. Frisch. *Turbulence: The Legacy of A. N. Kolmogorov*. Cambridge University Press, Cambridge; New York, 1995.

[77] A. N. Kolmogorov. A refinement of previous hypotheses concerning the local structure of turbulence in a viscous incompressible fluid at high Reynolds number. *Journal of Fluid Mechanics*, 13(1):82–85, May 1962.

[78] S. A. Orszag. Analytical theories of turbulence. *Journal of Fluid Mechanics*, 41(2):363–386, April 1970.

[79] B. B. Mandelbrot. Intermittent turbulence in self-similar cascades: divergence of high moments and dimension of the carrier. *Journal of Fluid Mechanics*, 62(2):331–358, January 1974.

[80] R. H. Kraichnan. On Kolmogorov's inertial-range theories. *Journal of Fluid Mechanics*, 62(2):305–330, January 1974.

[81] R. M. McMullen, M. C. Krygier, J. R. Torczynski, and M. A. Gallis. Navier-Stokes Equations Do Not Describe the Smallest Scales of Turbulence in Gases. *Physical Review Letters*, 128(11):114501, March 2022.

[82] E. Gkioulekas and K. K. Tung. A new proof on net upscale energy cascade in two-dimensional and quasi-geostrophic turbulence. *Journal of Fluid Mechanics*, 576:173–189, April 2007.

[83] C. E. Leith. Diffusion Approximation for Two-Dimensional Turbulence. *The Physics of Fluids*, 11(3):671–672, March 1968.

[84] E. Gkioulekas and K. K. Tung. On the double cascades of energy and enstrophy in two dimensional turbulence. Part 2. Approach to the KLB limit and interpretation of experimental evidence. *Discrete and Continuous Dynamical Systems - Series B*, 5(1):103–124, February 2005.

[85] G. I. Taylor. Statistical theory of turbulence. *Proceedings of the Royal Society of London. Series A - Mathematical and Physical Sciences*, 151(873):421–444, September 1935.

[86] A. Pumir and B. I. Shraiman. Persistent Small Scale Anisotropy in Homogeneous Shear Flows. *Physical Review Letters*, 75(17):3114–3117, October 1995.

[87] A. Pumir. Turbulence in homogeneous shear flows. *Physics of Fluids*, 8(11):3112–3127, November 1996.

[88] X. Shen and Z. Warhaft. The anisotropy of the small scale structure in high Reynolds number ($R_\lambda \sim 1000$) turbulent shear flow. *Physics of Fluids*, 12(11):2976–2989, November 2000.

[89] J. Schumacher, K. R. Sreenivasan, and P. K. Yeung. Derivative moments in turbulent shear flows. *Physics of Fluids*, 15(1):84–90, January 2003.

[90] J. Schumacher. Relation between shear parameter and Reynolds number in statistically stationary turbulent shear flows. *Physics of Fluids*, 16(8):3094–3102, August 2004.

[91] L. Biferale and I. Procaccia. Anisotropy in turbulent flows and in turbulent transport. *Physics Reports*, 414(2-3):43–164, July 2005.

[92] A. P. Finne, T. Araki, R. Blaauwgeers, V. B. Eltsov, N. B. Kopnin, M. Krusius, L. Skrbek, M. Tsubota, and G. E. Volovik. An intrinsic velocity-independent criterion for superfluid turbulence. *Nature*, 424(6952):1022–1025, August 2003.

[93] J. T. Tough. Chapter 3: Superfluid Turbulence. *Progress in Low Temperature Physics*, 8:133–219, 1982. ISSN: 0079-6417.

[94] D. J. Melotte and C. F. Barenghi. Transition to Normal Fluid Turbulence in Helium II. *Physical Review Letters*, 80(19):4181–4184, May 1998.

[95] A. Marakov, J. Gao, W. Guo, S. W. Van Sciver, G. G. Ihas, D. N. McKinsey, and W. F. Vinen. Visualization of the normal-fluid turbulence in counterflowing superfluid ^{4}He. *Physical Review B*, 91(9):094503, March 2015.

[96] H. E. Hall and W. F. Vinen. The rotation of liquid helium II II. The theory of mutual friction in uniformly rotating helium II. *Proceedings of the Royal Society of London. Series A. Mathematical and Physical Sciences*, 238(1213):215–234, December 1956.

[97] B. V. Svistunov. Superfluid turbulence in the low-temperature limit. *Physical Review B*, 52(5):3647–3653, August 1995.

[98] W. F. Vinen. Classical character of turbulence in a quantum liquid. *Physical Review B*, 61(2):1410–1420, January 2000.

[99] W. F. Vinen and J. J. Niemela. Quantum Turbulence. *Journal of Low Temperature Physics*, 128(5/6):167–231, 2002.

[100] W. F. Vinen. Mutual friction in a heat current in liquid helium II III. Theory of the mutual friction. *Proceedings of the Royal Society of London. Series A. Mathematical and Physical Sciences*, 242(1231):493–515, November 1957.

[101] W. F. Vinen. Mutual friction in a heat current in liquid helium II. II. Experiments on transient effects. *Proceedings of the Royal Society of London. Series A. Mathematical and Physical Sciences*, 240(1220):128–143, April 1957.

[102] W. F. Vinen. Mutual friction in a heat current in liquid heliumn. II. IV. Critical heat currents in wide channels. *Proceedings of the Royal Society of London. Series A. Mathematical and Physical Sciences*, 243(1234):400–413, January 1958.

[103] C. Gorter and J. Mellink. On the irreversible processes in liquid helium II. *Physica*, 15(3-4):285–304, May 1949.

[104] R. J. Donnelly and C. F. Barenghi. The Observed Properties of Liquid Helium at the Saturated Vapor Pressure. *Journal of Physical and Chemical Reference Data*, 27(6):1217–1274, November 1998.

[105] S. K. Nemirovskii. Quantum turbulence: Theoretical and numerical problems. *Physics Reports*, 524(3):85–202, March 2013.

[106] S. K. Nemirovskii. On the Closure Problem of the Coarse-Grained Hydrodynamics of Turbulent Superfluids. *Journal of Low Temperature Physics*, 201(3-4):254–268, November 2020.

[107] A. D. Mcewan. Angular momentum diffusion and the initiation of cyclones. *Nature*, 260(5547):126–128, March 1976.

[108] J. C. B. Papaloizou and D. N. C. Lin. Theory of Accretion Disks I: Angular Momentum Transport Processes. *Annual Review of Astronomy and Astrophysics*, 33(1):505–540, September 1995.

[109] S. A. Balbus. Enhanced Angular Momentum Transport in Accretion Disks. *Annual Review of Astronomy and Astrophysics*, 41(1):555–597, September 2003.

[110] G. Falkovich. *Fluid mechanics*. Cambridge University Press, Cambridge; New York, second edition edition, 2018.

[111] M. R. Andrews, C. G. Townsend, H.-J. Miesner, D. S. Durfee, D. M. Kurn, and W. Ketterle. Observation of Interference Between Two Bose Condensates. *Science*, 275(5300):637–641, January 1997.

[112] Y. Shin, M. Saba, T. A. Pasquini, W. Ketterle, D. E. Pritchard, and A. E. Leanhardt. Atom Interferometry with Bose-Einstein Condensates in a Double-Well Potential. *Physical Review Letters*, 92(5):050405, February 2004.

[113] Z. Hadzibabic, S. Stock, B. Battelier, V. Bretin, and J. Dalibard. Interference of an Array of Independent Bose-Einstein Condensates. *Physical Review Letters*, 93(18):180403, October 2004.

[114] Y. Shin, C. Sanner, G.-B. Jo, T. A. Pasquini, M. Saba, W. Ketterle, D. E. Pritchard, M. Vengalattore, and M. Prentiss. Interference of Bose-Einstein condensates split with an atom chip. *Physical Review A*, 72(2):021604, August 2005.

[115] W.-M. Liu, B. Wu, and Q. Niu. Nonlinear Effects in Interference of Bose-Einstein Condensates. *Physical Review Letters*, 84(11):2294–2297, March 2000.

[116] T. Yang, B. Xiong, and K. A. Benedict. Dynamical excitations in the collision of two-dimensional Bose-Einstein condensates. *Physical Review A*, 87(2):023603, February 2013.

[117] X. Zhang, M. H. Chan, T. Harko, S.-D. Liang, and C. S. Leung. Slowly rotating Bose Einstein condensate galactic dark matter halos, and their rotation curves. *The European Physical Journal C*, 78(4):346, April 2018.

[118] C. L. Vicente, C. Kim, H. J. Maris, and G. M. Seidel. Coalescence of Levitated He II Drops. *Journal of Low Temperature Physics*, 121(5/6):627–632, 2000.

[119] J. M. Escartín, F. Ancilotto, M. Barranco, and M. Pi. Vorticity and quantum turbulence in the merging of superfluid helium nanodroplets. *Physical Review B*, 99(14):140505, April 2019.

[120] J. M. Escartín, F. Ancilotto, M. Barranco, and M. Pi. Merging of superfluid helium nanodroplets with vortices. *Physical Review B*, 105(2):024511, January 2022.

[121] S. Stock, Z. Hadzibabic, B. Battelier, M. Cheneau, and J. Dalibard. Observation of Phase Defects in Quasi-Two-Dimensional Bose-Einstein Condensates. *Physical Review Letters*, 95(19):190403, November 2005.

[122] D. R. Scherer, C. N. Weiler, T. W. Neely, and B. P. Anderson. Vortex Formation by Merging of Multiple Trapped Bose-Einstein Condensates. *Physical Review Letters*, 98(11):110402, March 2007.

[123] B. Xiong, T. Yang, and K. A. Benedict. Distortion of interference fringes and the resulting vortex production of merging Bose-Einstein condensates. *Physical Review A*, 88(4):043602, October 2013.

[124] S.-J. Yang, Q.-S. Wu, S.-N. Zhang, S. Feng, W. Guo, Y.-C. Wen, and Y. Yu. Generating ring dark solitons in an evolving Bose-Einstein condensate. *Physical Review A*, 76(6):063606, December 2007.

[125] S.-J. Yang, Q.-S. Wu, S. Feng, Y.-C. Wen, and Y. Yu. Solitons and vortices in an evolving Bose-Einstein condensate. *Physical Review A*, 77(3):035602, March 2008.

[126] L. A. Toikka, O. Kärki, and K.-A. Suominen. Creation and revival of ring dark solitons in an annular Bose–Einstein condensate. *Journal of Physics B: Atomic, Molecular and Optical Physics*, 47(2):021002, January 2014.

[127] C. N. Weiler, T. W. Neely, D. R. Scherer, A. S. Bradley, M. J. Davis, and B. P. Anderson. Spontaneous vortices in the formation of Bose–Einstein condensates. *Nature*, 455(7215):948–951, October 2008.

[128] R. Carretero-González, B. P. Anderson, P. G. Kevrekidis, D. J. Frantzeskakis, and C. N. Weiler. Dynamics of vortex formation in merging Bose-Einstein condensate fragments. *Physical Review A*, 77(3):033625, March 2008.

[129] G. Lamporesi, S. Donadello, S. Serafini, F. Dalfovo, and G. Ferrari. Spontaneous creation of Kibble–Zurek solitons in a Bose–Einstein condensate. *Nature Physics*, 9(10):656–660, October 2013.

[130] L. Corman, L. Chomaz, T. Bienaimé, R. Desbuquois, C. Weitenberg, S. Nascimbène, J. Dalibard, and J. Beugnon. Quench-Induced Supercurrents in an Annular Bose Gas. *Physical Review Letters*, 113(13):135302, September 2014.

[131] T. Kibble. Phase-transition dynamics in the lab and the universe. *Physics Today*, 60(9):47–52, September 2007.

[132] W. Zurek. Cosmological experiments in condensed matter systems. *Physics Reports*, 276(4):177–221, November 1996.

[133] T. Kanai, W. Guo, and M. Tsubota. Flows with fractional quantum circulation in Bose-Einstein condensates induced by nontopological phase defects. *Physical Review A*, 97(1):013612, January 2018.

[134] G. Volovik and V. Mineev. Line and point singularities in superfluid He3. *JETP Letters*, 24:561–563, January 1976.

[135] S. Autti, V. V. Dmitriev, J. Mäkinen, A. Soldatov, G. Volovik, A. Yudin, V. Zavjalov, and V. Eltsov. Observation of Half-Quantum Vortices in Topological Superfluid He 3. *Physical Review Letters*, 117(25):255301, December 2016.

[136] S. Burger, K. Bongs, S. Dettmer, W. Ertmer, K. Sengstock, A. Sanpera, G. V. Shlyapnikov, and M. Lewenstein. Dark Solitons in Bose-Einstein Condensates. *Physical Review Letters*, 83(25):5198–5201, December 1999.

[137] A. Görlitz, J. M. Vogels, A. E. Leanhardt, C. Raman, T. L. Gustavson, J. R. Abo-Shaeer, A. P. Chikkatur, S. Gupta, S. Inouye, T. Rosenband, and W. Ketterle. Realization of Bose-Einstein Condensates in Lower Dimensions. *Physical Review Letters*, 87(13):130402, September 2001.

[138] F. Jendrzejewski, S. Eckel, N. Murray, C. Lanier, M. Edwards, C. Lobb, and G. Campbell. Resistive Flow in a Weakly Interacting Bose-Einstein Condensate. *Physical Review Letters*, 113(4):045305, July 2014.

[139] W. J. Kwon, J. H. Kim, S. W. Seo, and Y. Shin. Observation of von Kármán Vortex Street in an Atomic Superfluid Gas. *Physical Review Letters*, 117(24):245301, December 2016.

[140] T. C. Killian, D. G. Fried, L. Willmann, D. Landhuis, S. C. Moss, T. J. Greytak, and D. Kleppner. Cold Collision Frequency Shift of the $1S-2S$ Transition in Hydrogen. *Physical Review Letters*, 81(18):3807–3810, November 1998.

[141] A. L. Gaunt, T. F. Schmidutz, I. Gotlibovych, R. P. Smith, and Z. Hadzibabic. Bose-Einstein Condensation of Atoms in a Uniform Potential. *Physical Review Letters*, 110(20):200406, May 2013.

[142] W. H. Press, editor. *Numerical Recipes: the Art of Scientific Computing*. Cambridge University Press, Cambridge; New York, 3rd ed edition, 2007.

[143] I. Shomroni, E. Lahoud, S. Levy, and J. Steinhauer. Evidence for an oscillating soliton/vortex ring by density engineering of a Bose–Einstein condensate. *Nature Physics*, 5(3):193–197, March 2009.

[144] A. D. Jackson, G. M. Kavoulakis, and C. J. Pethick. Solitary waves in clouds of Bose-Einstein condensed atoms. *Physical Review A*, 58(3):2417–2422, September 1998.

[145] M. J. Ku, B. Mukherjee, T. Yefsah, and M. W. Zwierlein. Cascade of Solitonic Excitations in a Superfluid Fermi gas: From Planar Solitons to Vortex Rings and Lines. *Physical Review Letters*, 116(4):045304, January 2016.

[146] A. V. Mamaev, M. Saffman, and A. A. Zozulya. Propagation of Dark Stripe Beams in Nonlinear Media: Snake Instability and Creation of Optical Vortices. *Physical Review Letters*, 76(13):2262–2265, March 1996.

[147] G. Theocharis, D. J. Frantzeskakis, P. G. Kevrekidis, B. A. Malomed, and Y. S. Kivshar. Ring Dark Solitons and Vortex Necklaces in Bose-Einstein Condensates. *Physical Review Letters*, 90(12):120403, March 2003.

[148] C. Spengel. *Emergent Nonlinear Phenomena in Bose-Einstein Condensates*. Springer, Heidelberg, 2010.

[149] M. Ma, R. Carretero-González, P. G. Kevrekidis, D. J. Frantzeskakis, and B. A. Malomed. Controlling the transverse instability of dark solitons and nucleation of vortices by a potential barrier. *Physical Review A*, 82(2):023621, August 2010.

[150] V. Bretin, P. Rosenbusch, F. Chevy, G. V. Shlyapnikov, and J. Dalibard. Quadrupole Oscillation of a Single-Vortex Bose-Einstein Condensate: Evidence for Kelvin Modes. *Physical Review Letters*, 90(10):100403, March 2003.

[151] T. P. Simula, T. Mizushima, and K. Machida. Kelvin Waves of Quantized Vortex Lines in Trapped Bose-Einstein Condensates. *Physical Review Letters*, 101(2):020402, July 2008.

[152] R. Blaauwgeers, V. B. Eltsov, G. Eska, A. P. Finne, R. P. Haley, M. Krusius, J. J. Ruohio, L. Skrbek, and G. E. Volovik. Shear Flow and Kelvin-Helmholtz Instability in Superfluids. *Physical Review Letters*, 89(15):155301, September 2002.

[153] G. E. Volovik. On the Kelvin-Helmholtz instability in superfluids. *Journal of Experimental and Theoretical Physics Letters*, 75(8):418–422, April 2002.

[154] S. Eckel, F. Jendrzejewski, A. Kumar, C. Lobb, and G. Campbell. Interferometric Measurement of the Current-Phase Relationship of a Superfluid Weak Link. *Physical Review X*, 4(3):031052, September 2014.

[155] N. Navon, A. L. Gaunt, R. P. Smith, and Z. Hadzibabic. Emergence of a turbulent cascade in a quantum gas. *Nature*, 539(7627):72–75, November 2016.

[156] B. Mukherjee, Z. Yan, P. B. Patel, Z. Hadzibabic, T. Yefsah, J. Struck, and M. W. Zwierlein. Homogeneous Atomic Fermi Gases. *Physical Review Letters*, 118(12):123401, March 2017.

[157] A. Kumar, R. Dubessy, T. Badr, C. De Rossi, M. De Goër De Herve, L. Longchambon, and H. Perrin. Producing superfluid circulation states using phase imprinting. *Physical Review A*, 97(4):043615, April 2018.

[158] H. Kellay and W. I. Goldburg. Two-dimensional turbulence: a review of some recent experiments. *Reports on Progress in Physics*, 65(5):845–894, May 2002.

[159] A. Adriani, A. Mura, G. Orton, C. Hansen, F. Altieri, M. L. Moriconi, J. Rogers, G. Eichstädt, T. Momary, A. P. Ingersoll, G. Filacchione, G. Sindoni, F. Tabataba-Vakili, B. M. Dinelli, F. Fabiano, S. J. Bolton, J. E. P. Connerney, S. K. Atreya, J. I. Lunine, F. Tosi, A. Migliorini, D. Grassi, G. Piccioni, R. Noschese, A. Cicchetti, C. Plainaki, A. Olivieri, M. E. O'Neill, D. Turrini, S. Stefani, R. Sordini, and M. Amoroso. Clusters of cyclones encircling Jupiter's poles. *Nature*, 555(7695):216–219, March 2018.

[160] L. Onsager. Statistical hydrodynamics. *Il Nuovo Cimento*, 6(2):279–287, March 1949.

[161] G. L. Eyink and K. R. Sreenivasan. Onsager and the theory of hydrodynamic turbulence. *Reviews of Modern Physics*, 78(1):87–135, January 2006.

[162] G. Boffetta and R. E. Ecke. Two-Dimensional Turbulence. *Annual Review of Fluid Mechanics*, 44(1):427–451, January 2012.

[163] S. P. Johnstone, A. J. Groszek, P. T. Starkey, C. J. Billington, T. P. Simula, and K. Helmerson. Evolution of large-scale flow from turbulence in a two-dimensional superfluid. *Science*, 364(6447):1267–1271, June 2019.

[164] G. Gauthier, M. T. Reeves, X. Yu, A. S. Bradley, M. A. Baker, T. A. Bell, H. Rubinsztein-Dunlop, M. J. Davis, and T. W. Neely. Giant vortex clusters in a two-dimensional quantum fluid. *Science*, 364(6447):1264–1267, June 2019.

[165] Y. P. Sachkou, C. G. Baker, G. I. Harris, O. R. Stockdale, S. Forstner, M. T. Reeves, X. He, D. L. McAuslan, A. S. Bradley, M. J. Davis, and W. P. Bowen. Coherent vortex dynamics in a strongly interacting superfluid on a silicon chip. *Science*, 366(6472):1480–1485, December 2019.

[166] E. Varga, V. Vadakkumbatt, A. Shook, P. Kim, and J. Davis. Observation of Bistable Turbulence in Quasi-Two-Dimensional Superflow. *Physical Review Letters*, 125(2):025301, July 2020.

[167] T. Simula, M. J. Davis, and K. Helmerson. Emergence of Order from Turbulence in an Isolated Planar Superfluid. *Physical Review Letters*, 113(16):165302, October 2014.

[168] T. Billam, M. Reeves, B. Anderson, and A. Bradley. Onsager-Kraichnan Condensation in Decaying Two-Dimensional Quantum Turbulence. *Physical Review Letters*, 112(14):145301, April 2014.

[169] X. Yu, T. P. Billam, J. Nian, M. T. Reeves, and A. S. Bradley. Theory of the vortex-clustering transition in a confined two-dimensional quantum fluid. *Physical Review A*, 94(2):023602, August 2016.

[170] A. J. Groszek, T. P. Simula, D. M. Paganin, and K. Helmerson. Onsager vortex formation in Bose-Einstein condensates in two-dimensional power-law traps. *Physical Review A*, 93(4):043614, April 2016.

[171] A. Skaugen and L. Angheluta. Origin of the inverse energy cascade in two-dimensional quantum turbulence. *Physical Review E*, 95(5):052144, May 2017.

[172] M. T. Reeves, T. P. Billam, X. Yu, and A. S. Bradley. Enstrophy Cascade in Decaying Two-Dimensional Quantum Turbulence. *Physical Review Letters*, 119(18):184502, October 2017.

[173] A. J. Groszek, M. J. Davis, D. M. Paganin, K. Helmerson, and T. P. Simula. Vortex Thermometry for Turbulent Two-Dimensional Fluids. *Physical Review Letters*, 120(3):034504, January 2018.

[174] R. Pakter and Y. Levin. Nonequilibrium Statistical Mechanics of Two-Dimensional Vortices. *Physical Review Letters*, 121(2):020602, July 2018.

[175] D. Maestrini and H. Salman. Entropy of Negative Temperature States for a Point Vortex Gas. *Journal of Statistical Physics*, 176(4):981–1008, August 2019.

[176] M. T. Reeves, K. Goddard-Lee, G. Gauthier, O. R. Stockdale, H. Salman, T. Edmonds, X. Yu, A. S. Bradley, M. Baker, H. Rubinsztein-Dunlop, M. J. Davis, and T. W. Neely. Turbulent Relaxation to Equilibrium in a Two-Dimensional Quantum Vortex Gas. *Physical Review X*, 12(1):011031, February 2022.

[177] A. Tononi and L. Salasnich. Bose-Einstein Condensation on the Surface of a Sphere. *Physical Review Letters*, 123(16):160403, October 2019.

[178] A. Tononi, F. Cinti, and L. Salasnich. Quantum Bubbles in Microgravity. *Physical Review Letters*, 125(1):010402, June 2020.

[179] K. Padavić, K. Sun, C. Lannert, and S. Vishveshwara. Vortex-antivortex physics in shell-shaped Bose-Einstein condensates. *Physical Review A*, 102(4):043305, October 2020.

[180] N. S. Móller, F. E. A. Dos Santos, V. S. Bagnato, and A. Pelster. Bose–Einstein condensation on curved manifolds. *New Journal of Physics*, 22(6):063059, June 2020.

[181] S. J. Bereta, M. A. Caracanhas, and A. L. Fetter. Superfluid vortex dynamics on a spherical film. *Physical Review A*, 103(5):053306, May 2021.

[182] O. Zobay and B. M. Garraway. Two-Dimensional Atom Trapping in Field-Induced Adiabatic Potentials. *Physical Review Letters*, 86(7):1195–1198, February 2001.

[183] Y. Colombe, E. Knyazchyan, O. Morizot, B. Mercier, V. Lorent, and H. Perrin. Ultracold atoms confined in rf-induced two-dimensional trapping potentials. *Europhysics Letters*, 67(4):593–599, August 2004.

[184] T. L. Harte, E. Bentine, K. Luksch, A. J. Barker, D. Trypogeorgos, B. Yuen, and C. J. Foot. Ultracold atoms in multiple radio-frequency dressed adiabatic potentials. *Physical Review A*, 97(1):013616, January 2018.

[185] E. R. Elliott, M. C. Krutzik, J. R. Williams, R. J. Thompson, and D. C. Aveline. NASA's Cold Atom Lab (CAL): system development and ground test status. *npj Microgravity*, 4(1):16, August 2018.

[186] N. Lundblad, R. A. Carollo, C. Lannert, M. J. Gold, X. Jiang, D. Paseltiner, N. Sergay, and D. C. Aveline. Shell potentials for microgravity Bose–Einstein condensates. *npj Microgravity*, 5(1):30, December 2019.

[187] R. A. Carollo, D. C. Aveline, B. Rhyno, S. Vishveshwara, C. Lannert, J. D. Murphree, E. R. Elliott, J. R. Williams, R. J. Thompson, and N. Lundblad. Observation of ultracold atomic bubbles in orbital microgravity. *Nature*, 606(7913):281–286, June 2022.

[188] T. W. Neely, A. S. Bradley, E. C. Samson, S. J. Rooney, E. M. Wright, K. J. H. Law, R. Carretero-González, P. G. Kevrekidis, M. J. Davis, and B. P. Anderson. Characteristics of Two-Dimensional Quantum Turbulence in a Compressible Superfluid. *Physical Review Letters*, 111(23):235301, December 2013.

[189] S. J. Rooney, P. B. Blakie, B. P. Anderson, and A. S. Bradley. Suppression of Kelvon-induced decay of quantized vortices in oblate Bose-Einstein condensates. *Physical Review A*, 84(2):023637, August 2011.

[190] M. L. Chiofalo, S. Succi, and M. P. Tosi. Ground state of trapped interacting Bose-Einstein condensates by an explicit imaginary-time algorithm. *Physical Review E*, 62(5):7438–7444, November 2000.

[191] S. Nazarenko and M. Onorato. Freely decaying Turbulence and Bose–Einstein Condensation in Gross–Pitaevski Model. *Journal of Low Temperature Physics*, 146(1-2):31–46, January 2007.

[192] W. J. Kwon, G. Moon, J.-y. Choi, S. W. Seo, and Y.-i. Shin. Relaxation of superfluid turbulence in highly oblate Bose-Einstein condensates. *Physical Review A*, 90(6):063627, December 2014.

[193] A. Cidrim, F. E. A. Dos Santos, L. Galantucci, V. S. Bagnato, and C. F. Barenghi. Controlled polarization of two-dimensional quantum turbulence in atomic Bose-Einstein condensates. *Physical Review A*, 93(3):033651, March 2016.

[194] A. W. Baggaley and C. F. Barenghi. Decay of homogeneous two-dimensional quantum turbulence. *Physical Review A*, 97(3):033601, March 2018.

[195] R. H. Kraichnan and D. Montgomery. Two-dimensional turbulence. *Reports on Progress in Physics*, 43(5):547, May 1980.

[196] V. A. Bogomolov. Dynamics of vorticity at a sphere. *Fluid Dynamics*, 12(6):863–870, November 1977.

[197] D. G. Dritschel, M. Lucia, and A. C. Poje. Ergodicity and spectral cascades in point vortex flows on the sphere. *Physical Review E*, 91(6):063014, June 2015.

[198] J. A. Viecelli. Equilibrium properties of the condensed states of a turbulent two-dimensional neutral vortex system. *Physics of Fluids*, 7(6):1402–1417, June 1995.

[199] J. Gao, W. Guo, and W. F. Vinen. Determination of the effective kinematic viscosity for the decay of quasiclassical turbulence in superfluid ^{4}He. *Physical Review B*, 94(9):094502, September 2016.

[200] J. Gao, W. Guo, S. Yui, M. Tsubota, and W. F. Vinen. Dissipation in quantum turbulence in superfluid ^{4}He above 1 K. *Physical Review B*, 97(18):184518, May 2018.

[201] S. Yui, H. Kobayashi, M. Tsubota, and W. Guo. Fully Coupled Two-Fluid Dynamics in Superfluid ^{4}He : Anomalous Anisotropic Velocity Fluctuations in Counterflow. *Physical Review Letters*, 124(15):155301, April 2020.

[202] L. Biferale, D. Khomenko, V. L'vov, A. Pomyalov, I. Procaccia, and G. Sahoo. Superfluid Helium in Three-Dimensional Counterflow Differs Strongly from Classical Flows: Anisotropy on Small Scales. *Physical Review Letters*, 122(14):144501, April 2019.

[203] J. Gao, E. Varga, W. Guo, and W. F. Vinen. Energy spectrum of thermal counterflow turbulence in superfluid helium-4. *Physical Review B*, 96(9):094511, September 2017.

[204] S. Bao, W. Guo, V. S. L'vov, and A. Pomyalov. Statistics of turbulence and intermittency enhancement in superfluid ^{4}He counterflow. *Physical Review B*, 98(17):174509, November 2018.

[205] J. Gao, A. Marakov, W. Guo, B. T. Pawlowski, S. W. Van Sciver, G. G. Ihas, D. N. McKinsey, and W. F. Vinen. Producing and imaging a thin line of He_2^* molecular tracers in helium-4. *Review of Scientific Instruments*, 86(9):093904, September 2015.

[206] J. Gao, W. Guo, V. S. L'vov, A. Pomyalov, L. Skrbek, E. Varga, and W. F. Vinen. Decay of counterflow turbulence in superfluid ^{4}He. *JETP Letters*, 103(10):648–652, May 2016.

[207] J. Gao, E. Varga, W. Guo, and W. F. Vinen. Statistical Measurement of Counterflow Turbulence in Superfluid Helium-4 Using He_2^* Tracer-Line Tracking Technique. *Journal of Low Temperature Physics*, 187(5-6):490–496, June 2017.

[208] E. Varga, J. Gao, W. Guo, and L. Skrbek. Intermittency enhancement in quantum turbulence in superfluid ^{4}He. *Physical Review Fluids*, 3(9):094601, September 2018.

[209] R. A. Sherlock and D. O. Edwards. Oscillating Superleak Second Sound Transducers. *Review of Scientific Instruments*, 41(11):1603–1609, November 1970.

[210] L. Skrbek and K. R. Sreenivasan. Developed quantum turbulence and its decay. *Physics of Fluids*, 24(1):011301, January 2012.

[211] C. F. Barenghi, R. J. Donnelly, and W. F. Vinen. Friction on quantized vortices in helium II. A review. *Journal of Low Temperature Physics*, 52(3-4):189–247, August 1983.

[212] A. V. Benderskii, R. Zadoyan, N. Schwentner, and V. A. Apkarian. Photodynamics in superfluid helium: Femtosecond laser-induced ionization, charge recombination, and preparation of molecular Rydberg states. *The Journal of Chemical Physics*, 110(3):1542–1557, January 1999.

[213] P. C. Hill. Ultraviolet continua of helium molecules. *Physical Review A*, 40(9):5006–5016, November 1989.

[214] D. N. McKinsey, C. R. Brome, J. S. Butterworth, S. N. Dzhosyuk, P. R. Huffman, C. E. H. Mattoni, J. M. Doyle, R. Golub, and K. Habicht. Radiative decay of the metastable $He_2\left(a^3\Sigma_u^+\right)$ molecule in liquid helium. *Physical Review A*, 59(1):200–204, January 1999.

[215] D. R. Poole, C. F. Barenghi, Y. A. Sergeev, and W. F. Vinen. Motion of tracer particles in He II. *Physical Review B*, 71(6):064514, February 2005.

[216] Y. A. Sergeev and C. F. Barenghi. Particles-Vortex Interactions and Flow Visualization in ^{4}He. *Journal of Low Temperature Physics*, 157(5-6):429–475, December 2009.

[217] D. E. Zmeev, F. Pakpour, P. M. Walmsley, A. I. Golov, W. Guo, D. N. McKinsey, G. G. Ihas, P. V. E. McClintock, S. N. Fisher, and W. F. Vinen. Excimers He_2^* as Tracers of Quantum Turbulence in ^{4}He in the $T = 0$ Limit. *Physical Review Letters*, 110(17):175303, April 2013.

[218] D. N. McKinsey, W. H. Lippincott, J. A. Nikkel, and W. G. Rellergert. Trace Detection of Metastable Helium Molecules in Superfluid Helium by Laser-Induced Fluorescence. *Physical Review Letters*, 95(11):111101, September 2005.

[219] W. G. Rellergert, S. B. Cahn, A. Garvan, J. C. Hanson, W. H. Lippincott, J. A. Nikkel, and D. N. McKinsey. Detection and Imaging of He_2 Molecules in Superfluid Helium. *Physical Review Letters*, 100(2):025301, January 2008.

[220] W. Guo, M. La Mantia, D. P. Lathrop, and S. W. Van Sciver. Visualization of two-fluid flows of superfluid helium-4. *Proceedings of the National Academy of Sciences*, 111(supplement_1):4653–4658, March 2014.

[221] H. R. N. Jones. *Radiation Heat Transfer*. Number 89 in Oxford chemistry primers. Oxford University Press, Oxford, 2007.

[222] S. Pulkkinen, M. M. Mäkelä, and N. Karmitsa. A generative model and a generalized trust region Newton method for noise reduction. *Computational Optimization and Applications*, 57(1):129–165, January 2014.

[223] W. Guo, D. N. McKinsey, A. Marakov, K. J. Thompson, G. G. Ihas, and W. F. Vinen. Visualization Technique for Determining the Structure Functions of Normal-Fluid Turbulence in Superfluid Helium-4. *Journal of Low Temperature Physics*, 171(5-6):497–503, June 2013.

[224] C. Canuto, editor. *Spectral Methods: Evolution to Complex Geometries and Applications to Fluid Dynamics*. Scientific computation. Springer, Berlin; New York, 2007.

[225] L. Biferale, D. Khomenko, V. L'vov, A. Pomyalov, I. Procaccia, and G. Sahoo. Turbulent statistics and intermittency enhancement in coflowing superfluid ^{4}He. *Physical Review Fluids*, 3(2):024605, February 2018.

[226] L. Biferale, D. Khomenko, V. S. L'vov, A. Pomyalov, I. Procaccia, and G. Sahoo. Strong anisotropy of superfluid ^{4}He counterflow turbulence. *Physical Review B*, 100(13):134515, October 2019.

[227] J. I. Polanco and G. Krstulovic. Counterflow-Induced Inverse Energy Cascade in Three-Dimensional Superfluid Turbulence. *Physical Review Letters*, 125(25):254504, December 2020.

[228] P. E. Kloeden and E. Platen. *Numerical Solution of Stochastic Differential Equations*. Number 23 in Applications of mathematics. Springer, Berlin ; New York, corr. 3rd print edition, 1999.

[229] V. S. L'vov, V. Nazarenko, and G. E. Volovik. Energy spectra of developed superfluid turbulence. *Journal of Experimental and Theoretical Physics Letters*, 80(7):479–483, October 2004.

[230] D. Khomenko, V. S. L'vov, A. Pomyalov, and I. Procaccia. Counterflow-induced decoupling in superfluid turbulence. *Physical Review B*, 93(1):014516, January 2016.

[231] X. Zhou, G. Koolstra, X. Zhang, G. Yang, X. Han, B. Dizdar, X. Li, R. Divan, W. Guo, K. W. Murch, D. I. Schuster, and D. Jin. Single electrons on solid neon as a solid-state qubit platform. *Nature*, 605(7908):46–50, May 2022.

[232] X. Zhou, X. Li, Q. Chen, G. Koolstra, G. Yang, B. Dizdar, Y. Huang, C. S. Wang, X. Han, X. Zhang, D. I. Schuster, and D. Jin. Electron charge qubit with 0.1 millisecond coherence time. *Nature Physics*, October 2023.

[233] M. A. Nielsen and I. L. Chuang. *Quantum Computation and Quantum Information*. Cambridge University Press, Cambridge ; New York, 10th anniversary ed edition, 2010.

[234] N. P. De Leon, K. M. Itoh, D. Kim, K. K. Mehta, T. E. Northup, H. Paik, B. S. Palmer, N. Samarth, S. Sangtawesin, and D. W. Steuerman. Materials challenges and opportunities for quantum computing hardware. *Science*, 372(6539):eabb2823, April 2021.

[235] R. Hanson, L. P. Kouwenhoven, J. R. Petta, S. Tarucha, and L. M. K. Vandersypen. Spins in few-electron quantum dots. *Reviews of Modern Physics*, 79(4):1217–1265, October 2007.

[236] A. J. Heinrich, W. D. Oliver, L. M. K. Vandersypen, A. Ardavan, R. Sessoli, D. Loss, A. B. Jayich, J. Fernandez-Rossier, A. Laucht, and A. Morello. Quantum-coherent nanoscience. *Nature Nanotechnology*, 16(12):1318–1329, December 2021.

[237] A. Wallraff, D. I. Schuster, A. Blais, L. Frunzio, R.-S. Huang, J. Majer, S. Kumar, S. M. Girvin, and R. J. Schoelkopf. Strong coupling of a single photon to a superconducting qubit using circuit quantum electrodynamics. *Nature*, 431(7005):162–167, September 2004.

[238] A. Blais, A. L. Grimsmo, S. Girvin, and A. Wallraff. Circuit quantum electrodynamics. *Reviews of Modern Physics*, 93(2):025005, May 2021.

[239] Y. Nakamura, Y. A. Pashkin, and J. S. Tsai. Coherent control of macroscopic quantum states in a single-Cooper-pair box. *Nature*, 398(6730):786–788, April 1999.

[240] R. J. Schoelkopf and S. M. Girvin. Wiring up quantum systems. *Nature*, 451(7179):664–669, February 2008.

[241] J. Clarke and F. K. Wilhelm. Superconducting quantum bits. *Nature*, 453(7198):1031–1042, June 2008.

[242] F. Arute, K. Arya, R. Babbush, D. Bacon, J. C. Bardin, R. Barends, R. Biswas, S. Boixo, F. G. S. L. Brandao, D. A. Buell, B. Burkett, Y. Chen, Z. Chen, B. Chiaro, R. Collins, W. Courtney, A. Dunsworth, E. Farhi, B. Foxen, A. Fowler, C. Gidney, M. Giustina, R. Graff, K. Guerin, S. Habegger, M. P. Harrigan, M. J. Hartmann, A. Ho, M. Hoffmann, T. Huang, T. S. Humble, S. V. Isakov, E. Jeffrey, Z. Jiang, D. Kafri, K. Kechedzhi, J. Kelly, P. V. Klimov, S. Knysh, A. Korotkov, F. Kostritsa, D. Landhuis, M. Lindmark, E. Lucero, D. Lyakh, S. Mandrà, J. R. McClean, M. McEwen, A. Megrant, X. Mi, K. Michielsen, M. Mohseni, J. Mutus, O. Naaman, M. Neeley, C. Neill, M. Y. Niu, E. Ostby, A. Petukhov, J. C. Platt, C. Quintana, E. G. Rieffel, P. Roushan, N. C. Rubin, D. Sank, K. J. Satzinger, V. Smelyanskiy, K. J. Sung, M. D. Trevithick, A. Vainsencher, B. Villalonga, T. White, Z. J. Yao, P. Yeh, A. Zalcman, H. Neven, and J. M. Martinis. Quantum supremacy using a programmable superconducting processor. *Nature*, 574(7779):505–510, October 2019.

[243] P. Krantz, M. Kjaergaard, F. Yan, T. P. Orlando, S. Gustavsson, and W. D. Oliver. A quantum engineer's guide to superconducting qubits. *Applied Physics Reviews*, 6(2):021318, June 2019.

[244] A. Chatterjee, P. Stevenson, S. De Franceschi, A. Morello, N. P. De Leon, and F. Kuemmeth. Semiconductor qubits in practice. *Nature Reviews Physics*, 3(3):157–177, February 2021.

[245] E. Kawakami, P. Scarlino, D. R. Ward, F. R. Braakman, D. E. Savage, M. G. Lagally, M. Friesen, S. N. Coppersmith, M. A. Eriksson, and L. M. K. Vandersypen. Electrical control of a long-lived spin qubit in a Si/SiGe quantum dot. *Nature Nanotechnology*, 9(9):666–670, September 2014.

[246] X. Mi, J. V. Cady, D. M. Zajac, P. W. Deelman, and J. R. Petta. Strong coupling of a single electron in silicon to a microwave photon. *Science*, 355(6321):156–158, January 2017.

[247] X. Mi, M. Benito, S. Putz, D. M. Zajac, J. M. Taylor, G. Burkard, and J. R. Petta. A coherent spin–photon interface in silicon. *Nature*, 555(7698):599–603, March 2018.

[248] N. Samkharadze, G. Zheng, N. Kalhor, D. Brousse, A. Sammak, U. C. Mendes, A. Blais, G. Scappucci, and L. M. K. Vandersypen. Strong spin-photon coupling in silicon. *Science*, 359(6380):1123–1127, March 2018.

[249] A. J. Landig, J. V. Koski, P. Scarlino, U. C. Mendes, A. Blais, C. Reichl, W. Wegscheider, A. Wallraff, K. Ensslin, and T. Ihn. Coherent spin–photon coupling using a resonant exchange qubit. *Nature*, 560(7717):179–184, August 2018.

[250] L. Petit, H. G. J. Eenink, M. Russ, W. I. L. Lawrie, N. W. Hendrickx, S. G. J. Philips, J. S. Clarke, L. M. K. Vandersypen, and M. Veldhorst. Universal quantum logic in hot silicon qubits. *Nature*, 580(7803):355–359, April 2020.

[251] G. Burkard, M. J. Gullans, X. Mi, and J. R. Petta. Superconductor–semiconductor hybrid-circuit quantum electrodynamics. *Nature Reviews Physics*, 2(3):129–140, January 2020.

[252] L. R. Schreiber and H. Bluhm. Silicon comes back. *Nature Nanotechnology*, 9(12):966–968, December 2014.

[253] T. Cubaynes, M. R. Delbecq, M. C. Dartiailh, R. Assouly, M. M. Desjardins, L. C. Contamin, L. E. Bruhat, Z. Leghtas, F. Mallet, A. Cottet, and T. Kontos. Highly coherent spin states in carbon nanotubes coupled to cavity photons. *npj Quantum Information*, 5(1):47, July 2019.

[254] P. Stano and D. Loss. Review of performance metrics of spin qubits in gated semiconducting nanostructures. *Nature Reviews Physics*, 4(10):672–688, August 2022.

[255] C. Monroe, D. M. Meekhof, B. E. King, W. M. Itano, and D. J. Wineland. Demonstration of a Fundamental Quantum Logic Gate. *Physical Review Letters*, 75(25):4714–4717, December 1995.

[256] D. Kielpinski, C. Monroe, and D. J. Wineland. Architecture for a large-scale ion-trap quantum computer. *Nature*, 417(6890):709–711, June 2002.

[257] D. Leibfried, R. Blatt, C. Monroe, and D. Wineland. Quantum dynamics of single trapped ions. *Reviews of Modern Physics*, 75(1):281–324, March 2003.

[258] C. D. Bruzewicz, J. Chiaverini, R. McConnell, and J. M. Sage. Trapped-ion quantum computing: Progress and challenges. *Applied Physics Reviews*, 6(2):021314, June 2019.

[259] J. M. Pino, J. M. Dreiling, C. Figgatt, J. P. Gaebler, S. A. Moses, M. S. Allman, C. H. Baldwin, M. Foss-Feig, D. Hayes, K. Mayer, C. Ryan-Anderson, and B. Neyenhuis. Demonstration of the trapped-ion quantum CCD computer architecture. *Nature*, 592(7853):209–213, April 2021.

[260] G. K. Brennen, C. M. Caves, P. S. Jessen, and I. H. Deutsch. Quantum Logic Gates in Optical Lattices. *Physical Review Letters*, 82(5):1060–1063, February 1999.

[261] D. Jaksch, J. I. Cirac, P. Zoller, S. L. Rolston, R. Côté, and M. D. Lukin. Fast Quantum Gates for Neutral Atoms. *Physical Review Letters*, 85(10):2208–2211, September 2000.

[262] M. Saffman, T. G. Walker, and K. Mølmer. Quantum information with Rydberg atoms. *Reviews of Modern Physics*, 82(3):2313–2363, August 2010.

[263] Y. Wang, A. Kumar, T.-Y. Wu, and D. S. Weiss. Single-qubit gates based on targeted phase shifts in a 3D neutral atom array. *Science*, 352(6293):1562–1565, June 2016.

[264] G. W. Rayfield and F. Reif. Evidence for The Creation and Motion of Quantized Vortex Rings in Superfluid Helium. *Physical Review Letters*, 11(7):305–308, October 1963.

[265] G. W. Rayfield and F. Reif. Quantized Vortex Rings in Superfluid Helium. *Physical Review*, 136(5A):A1194–A1208, November 1964.

[266] J. L. Levine and T. M. Sanders. Mobility of Electrons in Low-Temperature Helium Gas. *Physical Review*, 154(1):138–149, February 1967.

[267] G. Careri, U. Fasoli, and F. S. Gaeta. Experimental behaviour of ionic structures in liquid helium — II. *Il Nuovo Cimento*, 15(5):774–783, March 1960.

[268] W. T. Sommer. Liquid Helium as a Barrier to Electrons. *Physical Review Letters*, 12(11):271–273, March 1964.

[269] M. A. Woolf and G. W. Rayfield. Energy of Negative Ions in Liquid Helium by Photoelectric Injection. *Physical Review Letters*, 15(6):235–237, August 1965.

[270] J. Jortner, N. R. Kestner, S. A. Rice, and M. H. Cohen. Study of the Properties of an Excess Electron in Liquid Helium. I. The Nature of the Electron—Helium Interactions. *The Journal of Chemical Physics*, 43(8):2614–2625, October 1965.

[271] K. Hiroike, N. R. Kestner, S. A. Rice, and J. Jortner. Study of the Properties of an Excess Electron in Liquid Helium. II. A Refined Description of Configuration Changes in the Liquid. *The Journal of Chemical Physics*, 43(8):2625–2632, October 1965.

[272] L. Bruschi, B. Maraviglia, and F. E. Moss. Measurement of a Barrier for the Extraction of Excess Electrons from Liquid Helium. *Physical Review Letters*, 17(13):682–684, September 1966.

[273] R. Williams, R. S. Crandall, and A. H. Willis. Surface States of Electrons on Liquid Helium. *Physical Review Letters*, 26(1):7–9, January 1971.

[274] W. T. Sommer and D. J. Tanner. Mobility of Electrons on the Surface of Liquid ^{4}He. *Physical Review Letters*, 27(20):1345–1349, November 1971.

[275] T. R. Brown and C. C. Grimes. Observation of Cyclotron Resonance in Surface-Bound Electrons on Liquid Helium. *Physical Review Letters*, 29(18):1233–1236, October 1972.

[276] E. Wigner. On the Interaction of Electrons in Metals. *Physical Review*, 46(11):1002–1011, December 1934.

[277] C. C. Grimes and G. Adams. Evidence for a Liquid-to-Crystal Phase Transition in a Classical, Two-Dimensional Sheet of Electrons. *Physical Review Letters*, 42(12):795–798, March 1979.

[278] D. S. Fisher, B. I. Halperin, and P. M. Platzman. Phonon-Ripplon Coupling and the Two-Dimensional Electron Solid on a Liquid-Helium Surface. *Physical Review Letters*, 42(12):798–801, March 1979.

[279] C. C. Grimes and G. Adams. Observation of Two-Dimensional Plasmons and Electron-Ripplon Scattering in a Sheet of Electrons on Liquid Helium. *Physical Review Letters*, 36(3):145–148, January 1976.

[280] M. I. Dykman and L. S. Khazan. Effect of the interaction between nondegenerate electrons localized in a thin surface layer on the cyclotron resonance and on the magnetoconductance. *JETP*, 50(4):747, October 1979.

[281] M. I. Dykman, M. J. Lea, P. Fozooni, and J. Frost. Magnetoresistance in 2D electrons on liquid helium: Many-electron versus single-electron kinetics. *Physical Review Letters*, 70(25):3975–3978, June 1993.

[282] D. Konstantinov, M. I. Dykman, M. J. Lea, Y. Monarkha, and K. Kono. Resonant Correlation-Induced Optical Bistability in an Electron System on Liquid Helium. *Physical Review Letters*, 103(9):096801, August 2009.

[283] H. Ikegami, H. Akimoto, D. G. Rees, and K. Kono. Evidence for Reentrant Melting in a Quasi-One-Dimensional Wigner Crystal. *Physical Review Letters*, 109(23):236802, December 2012.

[284] D. G. Rees, N. R. Beysengulov, J.-J. Lin, and K. Kono. Stick-Slip Motion of the Wigner Solid on Liquid Helium. *Physical Review Letters*, 116(20):206801, May 2016.

[285] E. Y. Andrei, F. Lévy, and E. Mooser, editors. *Two-Dimensional Electron Systems: on Helium and other Cryogenic Substrates*, volume 19 of *Physics and Chemistry of Materials with Low-Dimensional Structures*. Springer Netherlands, Dordrecht, 1997.

[286] Y. Monarkha and K. Kono. *Two-Dimensional Coulomb Liquids and Solids*. Springer Berlin Heidelberg, Heidelberg, 2004.

[287] Y. Z. Kovdrya. One-dimensional and zero-dimensional electron systems on liquid helium (Review). *Low Temperature Physics*, 29(2):77–104, February 2003.

[288] P. M. Platzman and M. I. Dykman. Quantum Computing with Electrons Floating on Liquid Helium. *Science*, 284(5422):1967–1969, June 1999.

[289] M. Lea, P. Frayne, and Y. Mukharsky. Could we Quantum Compute with Electrons on Helium? *Fortschritte der Physik*, 48(9-11):1109–1124, September 2000.

[290] A. J. Dahm, J. M. Goodkind, I. Karakurt, and S. Pilla. Using Electrons on Liquid Helium for Quantum Computing. *Journal of Low Temperature Physics*, 126(1/2):709–718, 2002.

[291] J. D. Jackson. *Classical electrodynamics*. Wiley, New York, 3rd ed edition, 1999.

[292] D. Jin. Quantum electronics and optics at the interface of solid neon and superfluid helium. *Quantum Science and Technology*, 5(3):035003, May 2020.

[293] C. C. Grimes, T. R. Brown, M. L. Burns, and C. L. Zipfel. Spectroscopy of electrons in image-potential-induced surface states outside liquid helium. *Physical Review B*, 13(1):140–147, January 1976.

[294] A. P. Volodin and V. S. Edel'man. Photoresonance and mobility of electrons localized over liquid helium. *JETP*, 54(1):198, July 1981.

[295] C. C. Grimes and T. R. Brown. Direct Spectroscopic Observation of Electrons in Image-Potential States Outside Liquid Helium. *Physical Review Letters*, 32(6):280–283, February 1974.

[296] D. K. Lambert and P. L. Richards. Measurement of Local Disorder in a Two-Dimensional Electron Fluid. *Physical Review Letters*, 44(21):1427–1429, May 1980.

[297] M. I. Dykman and P. M. Platzman. Quantum Computing Using Electrons Floating on Liquid Helium. *Fortschritte der Physik*, 48(9-11):1095–1108, September 2000.

[298] M. I. Dykman and P. Platzman. Quantum computing with electrons floating on liquid helium. *Quantum Information and Computation*, 1(Special):102–107, December 2001.

[299] E. Cheng, M. W. Cole, and M. H. Cohen. Binding of electrons to the surface of liquid helium. *Physical Review B*, 50(2):1136–1142, July 1994. Erratum Phys. Rev. B 50, 16134 (1994).

[300] M. M. Nieto. Electrons above a helium surface and the one-dimensional Rydberg atom. *Physical Review A*, 61(3):034901, February 2000.

[301] S. H. Patil. Electron near a helium liquid surface. *Physical Review A*, 64(6):064902, November 2001.

[302] M. I. Dykman. Theory of cyclotron resonance of two-dimensional electrons interacting with surface and volume phonons. *Physica Status Solidi (b)*, 88:463, 1978.

[303] M. I. Dykman, P. M. Platzman, and P. Seddighrad. Qubits with electrons on liquid helium. *Physical Review B*, 67(15):155402, April 2003.

[304] T. Ando. Broadening of Inter-Subband Transitions in Image-Potential-Induced Surface States outside Liquid Helium. *Journal of the Physical Society of Japan*, 44(3):765–773, March 1978.

[305] M. Saitoh and T. Aoki. Theory of Hot Electrons on the Liquid ^{4}He Surface. *Journal of the Physical Society of Japan*, 44(1):71–79, January 1978.

[306] Y. P. Monarkha and S. S. Sokolov. Decay rate of the excited surface electron states on liquid helium. *Low Temperature Physics*, 32(10):970–972, October 2006.

[307] Y. P. Monarkha and S. S. Sokolov. Decay Rate of the Excited States of Surface Electrons over Liquid Helium. *Journal of Low Temperature Physics*, 148(3-4):157–161, June 2007.

[308] Y. P. Monarkha, S. S. Sokolov, A. V. Smorodin, and N. Studart. Decay of excited surface electron states in liquid helium and related relaxation phenomena induced by short-wavelength ripplons. *Low Temperature Physics*, 36(7):565–575, July 2010.

[309] E. Kawakami, A. Elarabi, and D. Konstantinov. Relaxation of the Excited Rydberg States of Surface Electrons on Liquid Helium. *Physical Review Letters*, 126(10):106802, March 2021.

[310] H. Byeon, K. Nasyedkin, J. R. Lane, N. R. Beysengulov, L. Zhang, R. Loloee, and J. Pollanen. Piezoacoustics for precision control of electrons floating on helium. *Nature Communications*, 12(1):4150, July 2021.

[311] G. Sabouret, F. R. Bradbury, S. Shankar, J. A. Bert, and S. A. Lyon. Signal and charge transfer efficiency of few electrons clocked on microscopic superfluid helium channels. *Applied Physics Letters*, 92(8):082104, February 2008.

[312] F. R. Bradbury, M. Takita, T. M. Gurrieri, K. J. Wilkel, K. Eng, M. S. Carroll, and S. A. Lyon. Efficient Clocked Electron Transfer on Superfluid Helium. *Physical Review Letters*, 107(26):266803, December 2011.

[313] E. Collin, W. Bailey, P. Fozooni, P. G. Frayne, P. Glasson, K. Harrabi, M. J. Lea, and G. Papageorgiou. Microwave Saturation of the Rydberg States of Electrons on Helium. *Physical Review Letters*, 89(24):245301, November 2002.

[314] D. Konstantinov, H. Isshiki, Y. Monarkha, H. Akimoto, K. Shirahama, and K. Kono. Microwave-Resonance-Induced Resistivity: Evidence of Ultrahot Surface-State Electrons on Liquid He 3. *Physical Review Letters*, 98(23):235302, June 2007.

[315] E. Kawakami, A. Elarabi, and D. Konstantinov. Image-Charge Detection of the Rydberg States of Surface Electrons on Liquid Helium. *Physical Review Letters*, 123(8):086801, August 2019.

[316] S. Zou and D. Konstantinov. Image-charge detection of the Rydberg transition of electrons on superfluid helium confined in a microchannel structure. *New Journal of Physics*, 24(10):103026, October 2022.

[317] S. A. Lyon. Spin-based quantum computing using electrons on liquid helium. *Physical Review A*, 74(5):052338, November 2006.

[318] D. I. Schuster, A. Fragner, M. I. Dykman, S. A. Lyon, and R. J. Schoelkopf. Proposal for Manipulating and Detecting Spin and Orbital States of Trapped Electrons on Helium Using Cavity Quantum Electrodynamics. *Physical Review Letters*, 105(4):040503, July 2010.

[319] G. Koolstra, G. Yang, and D. I. Schuster. Coupling a single electron on superfluid helium to a superconducting resonator. *Nature Communications*, 10(1):5323, November 2019.

[320] M. I. Dykman, O. Asban, Q. Chen, D. Jin, and S. A. Lyon. Spin dynamics in quantum dots on liquid helium. *Physical Review B*, 107(3):035437, January 2023.

[321] E. Kawakami, J. Chen, M. Benito, and D. Konstantinov. Blueprint for quantum computing using electrons on helium, October 2023. arXiv:2303.03688 [cond-mat, physics:quant-ph].

[322] M. Zhang and L. F. Wei. Spin-orbit couplings between distant electrons trapped individually on liquid helium. *Physical Review B*, 86(20):205408, November 2012.

[323] S. Kotler, R. W. Simmonds, D. Leibfried, and D. J. Wineland. Hybrid quantum systems with trapped charged particles. *Physical Review A*, 95(2):022327, February 2017.

[324] A. Stockklauser, P. Scarlino, J. Koski, S. Gasparinetti, C. Andersen, C. Reichl, W. Wegscheider, T. Ihn, K. Ensslin, and A. Wallraff. Strong Coupling Cavity QED with Gate-Defined Double Quantum Dots Enabled by a High Impedance Resonator. *Physical Review X*, 7(1):011030, March 2017.

[325] G. Yang, A. Fragner, G. Koolstra, L. Ocola, D. Czaplewski, R. Schoelkopf, and D. Schuster. Coupling an Ensemble of Electrons on Superfluid Helium to a Superconducting Circuit. *Physical Review X*, 6(1):011031, March 2016.

[326] M. Pioro-Ladrière, T. Obata, Y. Tokura, Y.-S. Shin, T. Kubo, K. Yoshida, T. Taniyama, and S. Tarucha. Electrically driven single-electron spin resonance in a slanting Zeeman field. *Nature Physics*, 4(10):776–779, October 2008.

[327] J. J. Viennot, M. C. Dartiailh, A. Cottet, and T. Kontos. Coherent coupling of a single spin to microwave cavity photons. *Science*, 349(6246):408–411, July 2015.

[328] P. Peng, C. Matthiesen, and H. Häffner. Spin readout of trapped electron qubits. *Physical Review A*, 95(1):012312, January 2017.

[329] A. Troyanovskii, A. Volodin, and M. Khaikin. Electron localization over a liquid hydrogen surface. *JETP Letters*, 29(1):65, November 1978.

[330] A. Troyanovskii, A. Volodin, and M. Khaikin. Electron localization over the surface of crystalline hydrogen and neon. *JETP Letters*, 29(7):421, February 1979.

[331] Q. Chen, I. Martin, L. Jiang, and D. Jin. Electron spin coherence on a solid neon surface. *Quantum Science and Technology*, 7(4):045016, October 2022.

[332] M. W. Cole and M. H. Cohen. Image-Potential-Induced Surface Bands in Insulators. *Physical Review Letters*, 23(21):1238–1241, November 1969.

[333] M. W. Cole. Properties of Image-Potential-Induced Surface States of Insulators. *Physical Review B*, 2(10):4239–4252, November 1970.

[334] M. W. Cole. Electronic Surface States of a Dielectric Film on a Metal Substrate. *Physical Review B*, 3(12):4418–4422, June 1971.

[335] T. Y. Thomas. *Concepts from Tensor Analysis and Differential Geometry.* Academic Press, London, 1961.

[336] J. J. Sakurai and J. Napolitano. *Modern Quantum Mechanics.* Cambridge University Press, Cambridge, 3rd ed edition, 2020.

[337] Y. Tokura, W. G. Van Der Wiel, T. Obata, and S. Tarucha. Coherent Single Electron Spin Control in a Slanting Zeeman Field. *Physical Review Letters*, 96(4):047202, January 2006.

[338] D. G. Henshaw. Atomic Distribution in Liquid and Solid Neon and Solid Argon by Neutron Diffraction. *Physical Review*, 111(6):1470–1475, September 1958.

BIOGRAPHICAL SKETCH

Toshiaki Kanai holds a B.S. in Physics and an M.S. in Mathematics and Physics from Osaka City University and joined Florida State University in the Fall of 2018 to pursue his Ph.D. degree in Physics.

Publications

1. T. Kanai, D. Jin, and W. Guo, "Ring quantum states of surface-bound electrons on solid neon for quantum computing", (under review)
2. S. Inui, M. Hulse, T. Kanai, and W. Guo, "Boiling peak heat flux for steady inhomogeneous heat transfer in superfluid ^{4}He", *Phys. Rev. B* **108**, 174509 (2023)
3. Y. Tang, W. Guo, H. Kobayashi, S. Yui, M. Tsubota, and T. Kanai, "Imaging quantized vortex rings in superfluid helium to decipher quantum dissipation", *Nat Commun* **14**, 2941 (2023)
4. W. Guo and T. Kanai, "Vinen's Latest Thoughts on the "Bump" Puzzle in Decaying He II Counterflow Turbulence", *J. Low Temp. Phys.* (2023)
5. T. Kanai and W. Guo, "True Mechanism of Spontaneous Order from Turbulence in Two-Dimensional Superfluid Manifolds" *Phys. Rev. Lett.* **127**, 095301 (2021)
6. S. Bao, T. Kanai, Y. Zhang, L. N. Cattafesta III, and W. Guo, "Stereoscopic detection of hot spots in superfluid 4He (He II) for accelerator-cavity diagnosis" *Int. J. Heat Mass Transf.* **161**, 120259 (2020)
7. Y. Tang, S. Bao, T. Kanai, and W. Guo, "Statistical properties of homogeneous and isotropic turbulence in He II measured via particle tracking velocimetry" *Phys. Rev. Fluids* **5**, 084602 (2020)
8. T. Kanai, W. Guo, M. Tsubota, and D. Jin, "Torque and Angular-Momentum Transfer in Merging Rotating Bose–Einstein Condensates" *Phys. Rev. Lett.* **124**, 105302 (2020)
9. T. Kanai, W. Guo, and M. Tsubota, "Merging of Rotating Bose–Einstein Condensates" *J. Low Temp. Phys.* **5**, 084602 (2019)